

2003

Analysis of grinding wheel loading for electroplated cubic boron nitride wheels used with water-based lubricating fluids

Frank C. Gift
Lehigh University

Follow this and additional works at: <http://preserve.lehigh.edu/etd>

Recommended Citation

Gift, Frank C., "Analysis of grinding wheel loading for electroplated cubic boron nitride wheels used with water-based lubricating fluids" (2003). *Theses and Dissertations*. Paper 788.

This Thesis is brought to you for free and open access by Lehigh Preserve. It has been accepted for inclusion in Theses and Dissertations by an authorized administrator of Lehigh Preserve. For more information, please contact preserve@lehigh.edu.

Gift, Frank C. Jr.

Analysis of
Grinding Wheel
Loading for
Electroplated
Cubic Boron
Nitride Wheels...

May 2003

**Analysis of Grinding Wheel Loading for Electroplated Cubic Boron
Nitride Wheels Used with Water-based Lubricating Fluids**

by

Frank C. Gift Jr.

A Thesis

Presented to the Graduate and Research Committee

of Lehigh University

in Candidacy for the Degree of

Master of Science

in

Materials Science and Engineering

Lehigh University

May, 2003

This thesis is accepted and approved in partial fulfillment of the requirements for the Master of Science.

4/22/2003

Date

Dr. Wojciech Z. Misiolek
Thesis Advisor

Dr. Alwyn Eades
Assistant Department Chairperson

ACKNOWLEDGEMENTS

This research project and my experience at Lehigh University as a graduate student would not have been possible without the guidance and leadership of my advisor, Dr. Wojciech Z. Misiolek. As my advisor, he has helped me to stay focused and develop the skills necessary to complete my graduate work. As a mentor, he has helped me understand the finer points of business, politics, and scientific research, and the interplay between the three. As my boss and employer, he has provided me with an outstanding model for how to successfully manage people and resources. My sincere thanks and appreciation goes to him.

Edwin Force II was instrumental in both conceptualizing and developing the experimental testing system used to complete the grinding fluid trials. His experience with and knowledge of metal machining was extremely helpful in organizing the experimental plan for the fluid performance tests. Without his dedication and patience, both in the system development as well as “working in the trenches” with me to carry out the experimental tests, this project would never have reached completion. I am truly indebted to Ed for his benevolence and assistance with this project.

Muge Caglar, Dr. Quentin Craft, Dr. Robert Evans, Pat Grogan, John Hufnal, Ed Platt, and Dr. Edward Trauffer (all from Quaker Chemical Corporation) were truly supportive of this project. Their role in the project development stage was critical in terms of assessing Quaker Chemical’s research goals and ensuring that the experimental plan would target those areas. I am especially grateful to Muge and Bob, who were continuously involved with the project from beginning to end. Their insight and behind-the-scenes efforts are truly appreciated. Without the financial support of Quaker Chemical, this project and my graduate program would not have proceeded in the successful manner it has.

Alex Bandar’s unparalleled enthusiasm in troubleshooting the data acquisition system used in the research project, as well as helping me write MATLAB code to sort the acquired data, is also greatly appreciated. I’m truly thankful for his help,

along with the informal discussions and lab assistance from the other members of my research group – Heather Browne, Steve Claves, Mario Epler, Mike Giunta, Neil Hurley, Panya Kansuwan, Dr. Pawel Kazanowski, Kai Lorcharoensery, and Will Van Geertruyden. Dave Ackland and Bill Mushock aided me in the analysis of my samples through the training I received on the Philips XL30 ESEM, as well as their reliable support in keeping it running and keeping me from breaking it. John Gregoris and Mike Rex helped me develop methods for creating samples from the CBN grinding wheels and with creating a support structure for stereoscope observations of the wheel surface. Arlan Bencoter facilitated the metallurgical preparation of the most difficult samples I have yet encountered – cross-sectioned specimens of a CBN grinding wheel. His patience and tutelage in this regard are highly recognized.

I would like to thank Stephan Koknat and Mike Love from Abrasive Technologies for their cooperation in designing and selecting the electroplated CBN wheels, as well as their discussion regarding the manufacture and consistency of the wheels. Thanks goes to Al Carius from GE Superabrasives for his generous contribution of several carats of CBN control crystals for analysis and use as a standard. I'd also like to thank Ed Guptil from Pratt & Whitney, who gave me valuable insight into the operations that our experimental tests were simulating and the type of problems currently being faced by the industry.

Lastly, I'd like to thank my mother, father, and younger sister for their continued support of all my endeavors. They have provided me with the financial means to complete my degrees, as well as the impetus to strive to do my best at all times. They have been truly amazing. Their love and support will never be forgotten. My gratitude also goes to my girlfriend Amy, who has patiently listened to my boring tirades about my research troubles. She has given me confidence when it was most needed, and the means to persevere over difficult times. Her love, kindness, and encouragement have been inspirational.

TABLE OF CONTENTS

ACKNOWLEDGEMENTS.....	iii
TABLE OF CONTENTS.....	v
LIST OF TABLES.....	vii
LIST OF FIGURES.....	viii
LIST OF VARIABLES / TERMS.....	xiii
ABSTRACT.....	1
1.0 INTRODUCTION.....	2
2.0 BACKGROUND.....	5
2.1 Grinding Wheels	
2.2 Cubic Boron Nitride	
2.3 Mechanics of Grinding	
2.4 Specific Grinding Applications	
2.5 Grinding Wheel Failure Mechanisms	
3.0 EXPERIMENTAL PROCEDURE.....	45
3.1 Foreword	
3.2 Fluid Preparation and Circulation System	
3.3 Material Selection and Sample Generation	
3.4 Grinding System	
3.5 Power Measurements	
3.6 Force Measurements	
3.7 Collection of Grinding Swarf	
3.8 Profilometer Measurements	
3.9 Analytical Techniques	
3.10 Stereoscope Observations	
3.11 Grinding Wheel Specimens	
3.12 Grinding Chip Specimens	
3.13 CBN Control Crystal Specimens	
4.0 RESULTS.....	69
4.1 Performance Evaluation	
4.2 Water-based Fluid Trials	
4.3 Profilometer Analysis	
4.4 Power Measurements	
4.5 Force Measurements	
4.6 PMC-9259 Fluid Trial	

4.7 Grinding Swarf	
4.8 Grinding Wheels	
4.9 CBN Abrasive Grains	
5.0 DISCUSSION.....	128
5.1 Foreword	
5.2 Fluid Performance	
5.3 Improvements to the Grinding Tests	
5.4 Analysis of Failure	
5.5 Grinding Swarf	
5.6 Grinding Wheel Loading	
5.7 Fluid Effects	
5.8 Preventative Measures	
6.0 CONCLUSIONS.....	149
APPENDIX.....	152
REFERENCES.....	153
CURRICULUM VITAE.....	156

LIST OF TABLES

- Table I:** Selected physical properties of common abrasive materials.
- Table II:** Relation between ANSI grit size and the mean particle diameter of the abrasive grains.
- Table III:** Relative assessment of general grinding fluid categories.
- Table IV:** Measurements of internal porosity of a M509 block.
- Table V:** Bulk elemental composition of GTD-222 alloy used in the experiment.
- Table VI:** System parameters used in the experimental trials.
- Table VII:** Grind length for each wheel tested in the water-base fluid trials.
- Table VIII:** Mean depth measurements (mm) for the entry side of the work block for Wheel #2, Water-based A fluid.
- Table IX:** Mean depth measurements (mm) for the exit side of the work block for Wheel #2, Water-based A fluid.
- Table X:** Calculation of average cut depth (mm) for each groove and the work block for Wheel #2, Water-based A fluid.
- Table XI:** Mean cut depth (mm) calculated of each groove for all water-based fluid trials.
- Table XII:** Mean cut depth of each work piece for all water-based fluid trials.

LIST OF FIGURES

- Figure 1:** Schematic of an electroplated CBN grinding wheel, manufactured by Abrasive Technology Inc., used in the research project.
- Figure 2:** SEM image of Borazon CBN 500 grain displaying a faceted blocky structure.
- Figure 3:** Jagged Borazon CBN 500 particles are in much greater number than the well-defined faceted grains.
- Figure 4:** Morphology and scale of fine-scale structure present on fractured surfaces of CBN abrasive particles.
- Figure 5:** Simple cutting model illustrating the mechanics of chip formation and the uniformity of the operation across the width (w) of the tool.
- Figure 6:** Two dimensional orthogonal cutting model.
- Figure 7:** Relation of rake angle to chip flow direction and the resultant frictional force vector, R .
- Figure 8:** Orthogonal model showing the secondary shear zone, sliding region, and direction of chip curl after it breaks contact with the tool.
- Figure 9:** Schematic of radial slot grinding of a ceramic coated part.
- Figure 10:** Illustration of the system setup developed for the grinding tests.
- Figure 11:** Light optical microscope images of internal porosity within the M509 machined blocks.
- Figure 12:** Schematic (two viewing angles) of GTD-222 material stock geometry.
- Figure 13:** Light optical micrograph of the GTD-222 alloy, showing a cellular morphology typical in castings.
- Figure 14:** EDS plots for the GTD-222 alloy's (a) matrix and (b) secondary phase. (Acc. Voltage: 20 KeV)
- Figure 15:** Brown & Sharp 618 Micromaster Surface Grinding Machine with enclosure to contain mist and debris generated during laboratory tests.
- Figure 16:** Illustration of internal assembly and force data collection system.
- Figure 17:** Illustration of upgrinding (feed and wheel rotation are in opposite directions) and layout of fluid delivery system.

- Figure 18:** Two dimensional grid of measured points and the corresponding three dimensional image obtained from the optical profilometer scan. The sample scanned is the block machined by Wheel #3 using Water-based A.
- Figure 19:** Profile trace along the center of the fifth groove cut by Wheel #2, Water-based A, and showing fine scale fluctuations in elevation along its length.
- Figure 20:** Perpendicular profile trace and computerized measurements of cut depth for the beginning of the work block ground by Wheel #2, XR-82438.
- Figure 21:** Plot of grind length (representing grinding wheel life) vs. the average depth of cut in the work block.
- Figure 22:** Power measurements for Wheel #1, Water-based A Fluid.
- Figure 23:** Power measurements for Wheel #2, Water-based A Fluid.
- Figure 24:** Power measurements for Wheel #3, Water-based A Fluid.
- Figure 25:** Power measurements for Wheel #1, Water-based B Fluid.
- Figure 26:** Power measurements for Wheel #2, Water-based B Fluid.
- Figure 27:** Power measurements for Wheel #3, Water-based B Fluid.
- Figure 28:** Power measurements for Wheel #1, Water-based C Fluid.
- Figure 29:** Power measurements for Wheel #2, Water-based C Fluid.
- Figure 30:** Power measurements for Wheel #3, Water-based C Fluid.
- Figure 31:** Graphical output of tangential force data (prior to corrections of signal drift) for Groove 3, Wheel #1, Water-based B Fluid.
- Figure 32:** Graphical output of corrected tangential force data for Groove 3, Wheel #1, Water-based B Fluid.
- Figure 33:** Normal force measurements for Wheel #1, Water-based A Fluid.
- Figure 34:** Tangential force measurements for Wheel #1, Water-based A Fluid.
- Figure 35:** Normal force measurements for Wheel #2, Water-based A Fluid.
- Figure 36:** Tangential force measurements for Wheel #2, Water-based A Fluid.
- Figure 37:** Normal force measurements for Wheel #3, Water-based A Fluid.
- Figure 38:** Tangential force measurements for Wheel #3, Water-based A Fluid.

- Figure 39:** Normal force measurements for Wheel #1, Water-based B Fluid.
- Figure 40:** Tangential force measurements for Wheel #1, Water-based B Fluid.
- Figure 41:** Normal force measurements for Wheel #2, Water-based B Fluid.
- Figure 42:** Tangential force measurements for Wheel #2, Water-based B Fluid.
- Figure 43:** Normal force measurements for Wheel #3, Water-based B Fluid.
- Figure 44:** Tangential force measurements for Wheel #3, Water-based B Fluid.
- Figure 45:** Normal force measurements for Wheel #1, Water-based C Fluid.
- Figure 46:** Tangential force measurements for Wheel #1, Water-based C Fluid.
- Figure 47:** Normal force measurements for Wheel #2, Water-based C Fluid.
- Figure 48:** Tangential force measurements for Wheel #2, Water-based C Fluid.
- Figure 49:** Normal force measurements for Wheel #3, Water-based C Fluid.
- Figure 50:** Tangential force measurements for Wheel #3, Water-based C Fluid.
- Figure 51:** Comparison of the normal forces using Water-based A Fluid.
- Figure 52:** Comparison of the tangential forces using Water-based A Fluid.
- Figure 53:** Comparison of the normal forces using Water-based B Fluid.
- Figure 54:** Comparison of the tangential forces using Water-based B Fluid.
- Figure 55:** Comparison of the normal forces using Water-based C Fluid.
- Figure 56:** Comparison of the tangential forces using Water-based C Fluid.
- Figure 57:** Power measurements for the four days of testing with neat oil.
- Figure 58:** Plots of normal force and tangential force for neat oil fluid trial.
- Figure 59:** Comparison of tangential forces between the neat oil fluid and the water-based fluids.
- Figure 60:** Grinding chips recovered from test trials of the grinding system with blocks of M509 alloy.
- Figure 61:** Wheel deposit from dry machining tests with M509, showing the underside (a), and topside (b), of the deposit.

- Figure 62:** Smear deposit of M509 material, comprised of grinding chips shown extending from all sides of the deposit's perimeter.
- Figure 63:** Clustered mass of grinding chips from the Water-based B fluid trial.
- Figure 64:** Collection of grinding chips with various shapes and sizes.
- Figure 65:** Serrated and smooth sides of grinding chips.
- Figure 66:** Curled chips with serration morphology visible for (a) Water-based A, (b) Water-based B, (c) Water-based C, and (d) Oil Baseline fluids.
- Figure 67:** Large wheel deposit on the grinding wheel surface.
- Figure 68:** Image of a deposit showing grinding tracks in the direction of rotation.
- Figure 69:** Encapsulation of a single CBN grain by adhering material.
- Figure 70:** Chip adhesion on a single CBN abrasive grain.
- Figure 71:** Deposit build-up at the abrasive grain's rake face.
- Figure 72:** Intimate contact of the deposit at the rake face; track lines visible on top.
- Figure 73:** Self-supporting, trailing edge of a wheel deposit with chip morphology.
- Figure 74:** Deposit tail is not resting on abrasive grains or wheel bond.
- Figure 75:** Material flow over the non-cutting face of the CBN grain.
- Figure 76:** Material flow over grains encapsulated in a large deposit.
- Figure 77:** Build-up at the rake face showing the direction of material flow.
- Figure 78:** Layered morphology of the deposit visible.
- Figure 79:** Profile view of a medium-sized wheel deposit, circled in red.
- Figure 80:** Grinding chip visibly coming from the deposit, circled in red.
- Figure 81:** Chip morphology in the underside of deposit without direct contact with lower height CBN abrasive grains.
- Figure 82:** Wheel deposit with chip morphology on the underside, no damage to the CBN electroplated matrix layer is visible.
- Figure 83:** Grinding wheel used in the neat oil study shows no signs of loading.
- Figure 84:** Clear surface of the grinding wheel used in the oil fluid trial, some abrasive grains missing on the surface are circled in red.

- Figure 85:** Sharp abrasive grains are observed on the surface of the wheel used with the oil, despite its completion of 120 grinding passes.
- Figure 86:** New wheel showing clean surface with regions, circled in red, where significant numbers of CBN grains are missing.
- Figure 87:** New wheel with a region of missing and/or overplated CBN grains.
- Figure 88:** The surface of many CBN grains have finely spaced ridges.
- Figure 89:** CBN control grain possessing what could appear to be a wear flat.
- Figure 90:** CBN control grain with a micro-fractured top surface.
- Figure 91:** Schematic cross-section of three CBN abrasive grains on the wheel surface that function as cutting tools in grinding.
- Figure 92:** Schematic of cutting action displaying chip formation and adhesion.
- Figure 93:** Illustration of scrubber jet spray against the individual cutting grains.
- Figure 94:** Adhesion of a grinding chip on the cutting face of a CBN grain.
- Figure 95:** Deformation of adhering chips onto the cutting face and across the clearance face of the CBN grain.
- Figure 96:** Deposit growth begins with buildup on the clearance face of the CBN grain.
- Figure 97:** Continued growth leads the deposit to flow along the backside of the CBN grain and form self-supporting tails.
- Figure 98:** Bridging to adjacent grains occurs when the trailing edge of the deposit grows to a significant size.
- Figure 99:** Deposit growth continues laterally around the sides of the CBN grain, with continued adherence and growth on adjacent grains.
- Figure 100:** Illustration of a wear flat (clearance angle = 0°) sliding along the work piece surface.
- Figure 101:** Temperature increases associated with frictional rubbing of wear flats.
- Figure 102:** Fluid directions that would be more effective in wheel cleaning.
- Figure 103:** Scrubber nozzles would be oriented as shown on both sides of the wheel for high pressure fluid delivery that is effective in wheel cleaning.

LIST OF VARIABLES / TERMS:

α	- rake angle
β	- friction angle
ϕ	- shear plane angle
w	- width of cut
d	- depth of cut
v	- cutting velocity
MRR	- material removal rate
r	- chip thickness ratio
t_0	- undeformed chip thickness
t_c	- deformed chip thickness
F_P	- cutting force
F_Q	- thrust force
R'	- resultant vector of cutting and thrust force
R	- frictional force vector

ABSTRACT

Adhesion wear on the surface of grinding wheels, known as wheel loading, is responsible for several deleterious effects in industrial grinding operations. Among them is a reduction in tool life associated with increased cutting forces, increased power consumption, thermal damage, and tolerance variations in the process. Wheel loading is most prominent in operations using water-based lubricating fluids, and has become a leading problem to solve for integrating these fluids into manufacturing operations that previously utilized petroleum oils. Petroleum oils, despite their longevity in grinding performance, are being replaced in industrial operations with fluids that are less hazardous in the workplace (flammability issues) and more environmentally friendly.

This research project evaluated the performance of three water-based fluids and a straight oil fluid when grinding a nickel-based superalloy with electroplated cubic boron nitride grinding wheels. Parameters used in the experiments were chosen to simulate industrial creep-feed grinding of superalloy components for aero-engine manufacture. Analysis of the grinding wheel surface, grinding chips, and the quantitative data gathered from the experiments was used to develop a model for material deposition on the wheel's surface. The deposition mechanism was then examined to assess the functionality of the different physical and chemical properties of the grinding fluids. These properties were used to resolve why wheel loading occurs with the water-based fluids and as a framework for developing future generations of fluids. Also proposed were improvements to the scrubber nozzle layout that would reduce or eliminate wheel loading based on the mechanism of deposition that was developed.

1.0 INTRODUCTION:

Developing a new water-based grinding fluid technology capable of competing with existing petroleum-based lubricating fluids was the motivation behind this research project. The research was centered on evaluating the performance of the fluids when grinding difficult to machine Ni/Co superalloys used in the aerospace industry with electroplated cubic boron nitride (CBN) grinding wheels. Ultimately, the performance of a fluid would be determined by the life of the grinding tool for a given machining operation and the quality and integrity of the final machined part. Fluid properties such as thermal conductivity, viscosity, and dynamic wetting (among others) are responsible for establishing a cutting fluid's functionality, including its ability to conduct heat away from the grinding zone and lubricate the wheel surface to minimize wheel wear. Grinding fluids are therefore held accountable for the efficiency and productivity levels that can be achieved in manufacturing operations involving grinding and machining.

The Lehigh project team was responsible for: 1) Designing the grinding experiment and methods for analyzing the grinding wheels and workpieces, 2) Evaluating the performance of the fluids tested, and 3) Characterizing the mechanism of metal deposition and fluid effect on the binding material of the wheel. Quaker Chemical Corporation selected three water-based fluids and a straight petroleum oil (see **Appendix**) to be evaluated in the baseline study. After reviewing the findings of this research project, specific fluid properties were to be selected and ranked according to the role they play in the fluid's grinding performance. Tailoring the

chemistry of the lubricating fluid to achieve an optimal balance of the physical properties needed to machine these aerospace alloys effectively and efficiently was the final project objective.

Petroleum oils (neat oils) have been used extensively in many applications because they are an established technology with exceptional performance in grinding and machining, generally considered being due to their high lubricity characteristics. Petroleum oils, therefore, provide the benchmark of performance that replacement fluids must match to be considered viable alternatives. Such petroleum fluids, however, are not ideal for safe use in most high-speed manufacturing processes. Oil delivered to the tool-work interface can be aerosolized by high-velocity pressure jets and by the geometry and rotation of the manufacturing process itself. Aerosolized oil becomes an explosion hazard that puts the operator, surrounding workers, and manufacturing facility in jeopardy. Combining this inherent danger of using petroleum oils with the stigma associated with using such environmentally unfriendly lubricating fluids, manufacturing operations could potentially benefit from eliminating petroleum oils and replacing them with water-based, environmentally friendly lubricating fluids.

Water-based lubricating fluids are a very attractive alternative because they are economic, low maintenance coolants that do not create the same amount of pollution as straight petroleum oils. The water-based fluids are subject to the same high-velocity pressure jets used in the neat oil delivery systems. As a result of these conditions, these water-based fluids are also aerosolized and create a problem with misting. They do not pose fire hazards, but their acceptance is dependent on the

sensitivity of the operator to the fluid vapor. The Occupational Safety and Health Administration (OSHA) has established regulations for allowable concentrations of airborne chemicals. Grinding operations without complete enclosures are specifically susceptible to these standards. Any changes to fluid chemistry to enhance its performance in grinding applications must therefore satisfy OSHA regulations and be acceptable to the machine operators.

Presently, water-based lubricating fluids have had difficulty matching the performance of the neat oils currently being used in industrial practice. One problem that is typical for grinding wheels used in water-based fluid applications is a phenomenon known as loading. Material that has been removed from the workpiece during the cutting process will adhere to the surface of the grinding wheel. Adhesion wear such as this is uncharacteristic of machining operations which utilize neat oil technology. Wheel loading severely decreases the life of the grinding tool, making water-based fluids a less appealing alternative to the existing neat oil technology. Pressures to simultaneously improve productivity levels, reduce cost, and eliminate the hazards associated with straight petroleum oil grinding have spurred interest in water-based fluid research.

2.0 BACKGROUND:

2.1 Grinding Wheels:

Grinding and machining are both terms for material removal processes, sometimes being used interchangeably. The term grinding could more appropriately be referred to as abrasive machining. Grinding utilizes hard abrasive particles affixed to a substrate (belt, cup, wheel, etc.) to remove material at high cutting speeds. All grinding completed in this research project was accomplished using electroplated cubic boron nitride (CBN) grinding wheels (see Figure 1).

WHEEL SPECIFICATIONS

Abrasive Technology Inc.

Electroplated Cubic Boron Nitride Wheel

Fin Width: 0.060"

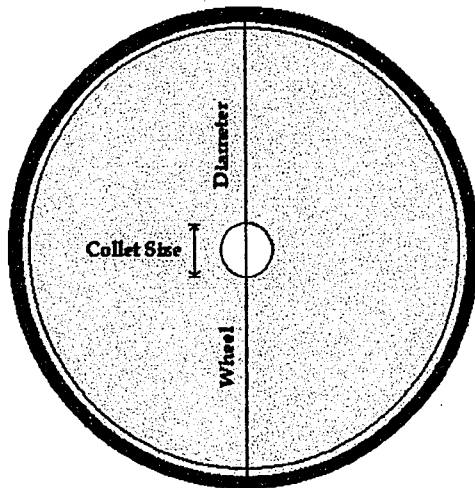
Full Tip Radius

Fin Depth: 0.25"

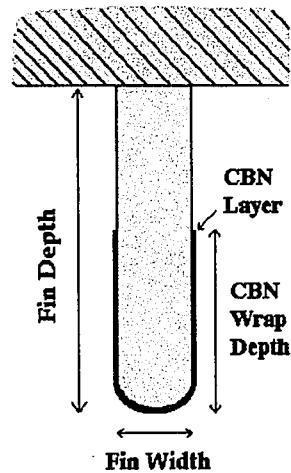
Wheel Diameter: 10"

Collet Size: 1.25"

Wrap Depth: 0.125"



Cross-section of Wheel Fin



Abrasive: GE Type 500, 120 mesh size

Bond: ABK2 Bond, ATI

Figure 1: Schematic of an electroplated CBN grinding wheel, manufactured by Abrasive Technology Inc., used in the research project.

Grinding wheels are manufactured in many shapes and a variety of styles to suit the needs of the customer. The various styles for wheel manufacture reflect the abrasive type, abrasive grain size, bond material, wheel grade, and wheel structure. Parameters such as these are controlled by the grinding wheel manufacturer to conform to application requirements related to workpiece material, component geometry, surface finish specifications and severity of the operation.

Increased levels of production during the industrial revolution resulted in, among other things, the need for improvements in grinding technology. At the turn of the 19th century, grinding wheels were designed for manufacture with what are known today as conventional abrasive materials, such as aluminum oxide (Al_2O_3) and silicon carbide (SiC) to machine a myriad of material types including cast iron, marble, copper, plastics, and wood [1]. These abrasive materials were widely used for all sorts of grinding operations through the early part of the 20th century, especially since there were few alternatives. Eventually, synthetic diamond and cubic boron nitride (CBN) abrasive materials were developed that were harder and more wear resistant than their conventional abrasive counterparts. Diamond and CBN, materials known as superabrasives, emerged as synthetic abrasives for machining ultra-hard materials and were used to create grinding instruments with an exceptionally long tool life. The General Electric Company first introduced diamond as a grinding abrasive in the United States in 1957, followed by CBN in 1969 [1]. Aluminum oxide, silicon carbide, cubic boron nitride and diamond are the four most commonly used abrasive materials and are of the greatest commercial importance [2].

Selection of abrasive type will depend on the economics of the manufacturing operation and the material that must be machined. Aluminum oxide is the most common and will be used to grind a variety of materials, particularly ferrous alloys. Silicon carbide is also a common abrasive material, and is used to grind both soft and brittle materials, but will not be used typically to grind steel due to the affinity of the carbon in the SiC for iron. Both of these abrasives are cheaper to manufacture than the superabrasive materials, so conventional abrasive grinding wheels are often selected because of a lower up-front tool cost. Economics works against conventional abrasive grinding wheels only for manufacturing operations that can offset the higher tool costs of superabrasive grinding wheels with lower time costs [3]. Lower time costs refer to a reduction in overall production time and costs associated with manufacturing. Superabrasive grinding wheels are more durable and often will not require multiple dressing or truing procedures, so they can be used for more severe grinds and last for longer periods of time. Production time can be reduced with an increased material removal rate for the grinding operation, decreased setup time, and fewer tool changeovers – all common to superabrasive grinding wheels. Costs per part will then decrease as production rates are increased and direct/indirect labor hours are reduced. Under these general circumstances a superabrasive grinding wheel would be a justified selection.

Diamond is the hardest known material and will be employed for many grinding processes, including the hardest materials classes like glasses and ceramics. Similar to silicon carbide, diamond will not normally be used to grind ferrous alloys since it is comprised entirely of carbon and will break down at an accelerated rate

when grinding such materials. Cubic boron nitride is the second hardest known material and has been commercially successful in machining hard ferrous alloys and some superalloys used in the aerospace industry. CBN is generally used in grinding operations that would benefit from a longer lasting tool (i.e. superabrasive grinding wheels) and where diamond is not a suitable choice. Presented in **Table I** are some of the physical properties for each of the above-mentioned abrasive materials.

Table I: Selected physical properties of common abrasive materials [4].

PHYSICAL PROPERTIES (AMBIENT)	ALUMINUM OXIDE (AL₂O₃)	SILICON CARBIDE (SiC)	DIAMOND (C)	CUBIC BORON NITRIDE (BN)
Density (g/cm³)	3.92	3.21	3.52	3.48
Thermal Conductivity (W/m·K)	33.5	41.5	2,092	1,300
Threshold Degradation Temperature (°C)	1,750	1,500	800	1,400
Knoop Hardness	2100	2400	7000	4700

Abrasive grain size is a critical factor in grinding wheel design and usage. Grain size, or *grit size*, is related to the average diameter of the abrasive particles bonded to the grinding tool. Abrasive grains typically have faceted, blocky shapes that only slightly resemble spheres, however they are roughly equiaxed and generally do not have one disproportionately long axis or direction. The average diameter of the abrasive grains is determined using a sieving process. Mesh screens used to sort the grains have incrementally smaller openings that allow the abrasive grains to pass.

The screen number represents the number of openings per linear inch, which is correspondingly related to the average particle diameter.

A larger mesh number, or grit size, corresponds to smaller abrasive particle diameters (see **Table II**). The sieving process is not absolute, thus a range of particle sizes exist that are associated with the mesh screen number. Grit size designations are specified largely by two classification systems – The American National Standards Institute (ANSI) standard is used in the United States and the Federation Européenne des Fabricants de Produits Abrasifs (FEPA) is used throughout Europe [5, 6].

Table II: Relation between ANSI grit size and the mean particle diameter of the abrasive grains [7].

ANSI Grit Size	Average Particle Diameter	ANSI Grit Size	Average Particle Diameter
	μm		μm
18	1000	100	150
20	850	120	125
25	710	140	106
30	600	170	90
35	500	200	75
40	425	230	63
45	355	270	53
50	300	325	45
60	250	400	38
70	212	450	32
80	180	500	25

ANSI standards were used by General Electric Superabrasives in the manufacture and sorting of the CBN type-500 abrasive grits, as well as by Abrasive Technology Inc. in manufacturing the electroplated CBN grinding wheels used in this research project. In an attempt to confine the size distribution as much as possible,

Abrasive Technology Inc. uses a secondary sizing procedure on the GE abrasive material before bonding the selected abrasives to the grinding wheel hub [8]. Confining the size distribution will reduce variation in grinding wheel performance and create a more consistent surface finish on the ground part surface.

Grit size is important because the requirements of both the production process and final component are dictated by the condition of the abrasives and the grinding parameters employed. Small abrasive particles are referred to as fine-grained, while large abrasive particles are referred to as coarse-grained. Small grit sizes (large abrasive particle diameter) in the ranges of 8 – 30 are employed for heavy stock removal or roughing operations. Larger material removal rates are necessary for stock removal, in order to complete the operation in a timely manner. The fraction of the abrasive grain size that penetrates and cuts the material during a grind is small, but proportionately the material removed is related to the cut depth of the abrasive grain. Therefore, larger abrasive grains cut deeper and are needed to achieve higher material removal rates for a given workpiece material and set of machining parameters. Brittle materials do not permit large penetration depths for the abrasive grits, so that fine-grained abrasives are used to allow more cutting edges access to the workpiece [9]. This allows a similar material removal rate to be achieved on brittle workpiece materials without high grinding forces and excessive wear of the grinding wheel. In contrast to roughing operations, larger grit sizes (smaller abrasive grain diameter) are utilized for finishing operations where close tolerances and good surface finish are requirements.

Bond material is another important criterion in grinding wheel manufacture. Several options exist for bonding the selected abrasive grains to the grinding wheel surface. The three general bond-type groups are organic, vitrified, and metallic bonding systems [10]. Organic bond systems are represented by the following bond-type subgroups: rubber, rubber reinforced, resinoid, resinoid reinforced, and shellac bonds. The organic bond materials are somewhat elastic, but are limited in their durability and heat resistance. Vitrified bond systems are the most commonly used; they include vitrified ceramic-clay and silicate bonds. These amorphous bonding materials are hard and do not degrade at elevated temperatures. Typically they are used for heat sensitive grinding applications. Disadvantages of this bond system include brittle fracture and wear of the bond material during use. These two bond systems (organic and vitrified) have been adopted for grinding wheel manufacture as primarily monolithic wheel structures, where the abrasive grains are enveloped in the bond material throughout the wheel, or a significant portion of the wheel periphery.

Metallic bonds operate differently, being used primarily for bonding diamond and cubic boron nitride abrasive grains in a thin layer on the periphery of the wheel. They have higher heat resistance than organic bonds and higher fracture toughness than vitrified bonds [10]. This technique allows a single layer of the expensive superabrasive material to be bonded to a wheel substrate, usually through electroplating processes. Metallic bonds are strong enough to hold the abrasive grains onto the wheel despite only 40% (approximately) of the abrasive grain surface actually being in contact with the matrix bond. This bond type creates a sharp cutting surface capable of extensive grinding uses. Once the cutting surface is rendered

ineffective after significant use, the remaining abrasive is stripped away and a fresh layer is applied, allowing the grinding wheel hubs to be recycled.

Wheel grade is a relative measure of the grinding wheel's hardness. Hardness in this sense does not mean the hardness of the abrasive grain, rather the effective hardness of the bond system. More accurately, wheel grade represents the strength which the bonding material holds the abrasive grains in the grinding wheel [11]. Wheel grade is marked by an alphabetic ranking system, where A represents a very soft grade and Z represents a very hard grade. Differences in wheel grade exist to reflect changes in the way abrasive materials will perform in various grinding operations. Worn abrasive grains will be ineffective at cutting the work material; it is therefore desirable that they be removed from the wheel bond to expose fresh cutting abrasive grains. A very hard wheel grade would continue to hold the abrasive grain despite its inability to effectively cut and subsequent build-up of grinding forces (to be discussed later). Balance in grade selection is optimized by choosing softer grades to machine hard work materials for continuous exposure of fresh cutting grains and choosing harder wheel grades for softer materials since the abrasive grains stay sharp for longer periods of time.

Relative measure of hardness was used to describe the wheel grade marking for the reason that workpiece material properties and grinding parameters will cause the grinding wheel to appear *harder* or *softer* than its original designation. Changes in working conditions that cause an increase in the depth of cut for the abrasive grains will tend to amplify grinding forces that pull the abrasive grains out of the wheel, causing it to perform as if it were a softer grade grinding wheel [11].

Recommendations for increasing grinding wheel grade or hardness according to the “grain depth of cut” theory would be to reduce feed rate, increase wheel speed, and increase wheel diameter [11]. Superabrasive grinding wheels primarily utilize metallic, vitrified, and hard resin bonding systems, so grades for these wheels are almost exclusively in the medium to hard ranges for most grinding applications.

Grinding wheel structure is the last parameter manipulated by wheel manufacturers to suit the customers’ needs. Wheel structure is a term used to describe the density of abrasive grains in the grinding wheel. Abrasive grains, bond material, and voids comprise the entirety of the wheel structure for conventional grinding wheels. Large concentrations of abrasive grains and a low percentage of voids (or pores) would be considered a *dense* wheel structure. An *open* wheel structure would consist of the opposite – a large fraction of voids and low percentage of abrasive grains. Dense wheel structures are optimal for grinding precision parts with a good surface finish. Open wheels allow for better chip clearance and better access of grinding fluid to the cutting zone, resulting in less wheel loading and cooler cutting conditions. Numerical markings between 1 and 15 are used to distinguish structure types for conventional grinding wheels [2]. A very dense structure would be rated as 1 and a very open structure rated as 15.

Diamond and CBN wheels do not follow the structure marking system as with conventional abrasive grinding wheels. Instead, a concentration number indicating the volumetric amount of abrasive in the wheel is used. A concentration of 100 is the highest, and values typically represented for superabrasive wheels are 25, 50, 75, or 100. Concentration is related to expense of the wheel, as for the case of diamond a

100 concentration is equal to 72 carats per cubic inch of matrix [11]. Higher concentrations are expected to have a higher grit density, hence concentration for superabrasive wheels and structure for conventional wheels are related.

2.2 Cubic Boron Nitride:

Cubic boron nitride is the second hardest material known to man, hence its classification as a superabrasive material. Diamond and CBN have been extensively developed for all types of applications within the realm of grinding and machining. They do not compete head-to-head for most applications, so they have been successfully introduced to mutually exclusive markets. Diamond is used extensively to grind and machine ceramic materials and many nonferrous alloys, while CBN is used for grinding ferrous, high-cobalt and high-nickel alloys since these elements are better carbide formers than nitride formers.

Despite their service in different markets, CBN was introduced as a result of commercial success by engineers at GE Superabrasives with the synthesis of artificial diamond. Synthetic production of diamond allowed for wide-spread utilization of this material for grinding and machining applications. Graphite is the stable form of the carbon structure at ambient temperatures and pressure. Application of high pressure and temperature to hexagonal graphite, usually in the presence of catalysts to speed up the reaction, causes a polymorphic transformation to the cubic diamond structure. The diamond allotrope has a higher density and higher coordination number (from 3 to 4) than graphite. Rapid decompression and cooling rate allow the cubic phase to be retained as a metastable phase at ambient temperature. In order for diamond to

revert from the cubic phase back to its hexagonal phase (graphite), the kinetic hindrance must be overcome with suitable thermal energy for bond-breaking and atomic redistribution of the carbon atoms [12]. Diamond is subject to this reversion process at temperatures approaching 750°C [4].

CBN was first synthesized by GE in 1959, and given the trade name Borazon®. Its potential use as a grinding abrasive was recognized, and within 10 years it was being sold commercially as a grinding superabrasive. Development of CBN was directly related to the successful production of artificial diamond. Two suppliers have dominated the markets in CBN manufacture - GE selling CBN under the trade name Borazon® and De Beers who provided the trade name Ambrorite, with the associated abbreviation changing to ABN. This abrasive is still sold in different product families and varieties; however it is universally referred to today as CBN.

Synthesis of CBN requires some similar processing techniques as those used to form diamond, specifically high-pressure high-temperature (HPHT) processing and explosive shock synthesis [13]. Hexagonal boron nitride is the starting material, which is converted to the metastable cubic form (zinc-blende crystal structure) under extreme pressure and temperature. Alkali metals and alkaline earth metals are excellent catalysts for the reaction. Lithium nitride, first used as a catalyst by De Beers to produce amber colored abrasives, seems to perform the best. Pressures between 5 – 9 GPa and temperatures between 1500-2000°C are used industrially to synthesize CBN, which will typically appear as either a dark brown / black color due to excess boron or an amber color due to excess lithium nitride [14]. The cubic structure of boron nitride is also a metastable phase in ambient conditions. Back

conversion to its hexagonal form occurs at temperatures approaching 1700°C, a much higher temperature than for diamond [4].

As listed in **Figure 1**, the CBN abrasive material used for manufacturing the grinding wheels in this research project was supplied by General Electric Superabrasives. The abrasive type, as specified by the manufacturer, was GE Type 500 Borazon. Borazon CBN 500 was selected because it has the highest fracture strength of any monocrystalline CBN product available and has proven to give long-life performance in grinding nickel and cobalt-based materials, in addition to hardened steels [15]. Control samples of Borazon CBN 500, 80/100 mesh size, were obtained for analysis of characteristic X-ray signature (discussed later) and morphological features. This variety of CBN is a golden orange color that is blocky in shape. Ideally shaped, faceted abrasive crystals are sometimes observed, as in **Figure 2**.

Generally, however, the population of abrasive particles that are utilized in the wheel manufacture will not exhibit such well-defined surfaces. Rather, the particles appear jagged across an entire face for many of the abrasive grains, as in **Figure 3**. These features are not an intended part of the synthesis process, but are a result of fracture during extraction of the abrasive particles from the catalyst mass. Fractured edges are sharp and durable for cutting, but their shape is more complex than is given in most treatments of metal cutting and grinding, since they deviate substantially from the ideal cutting tool morphology (discussed later).

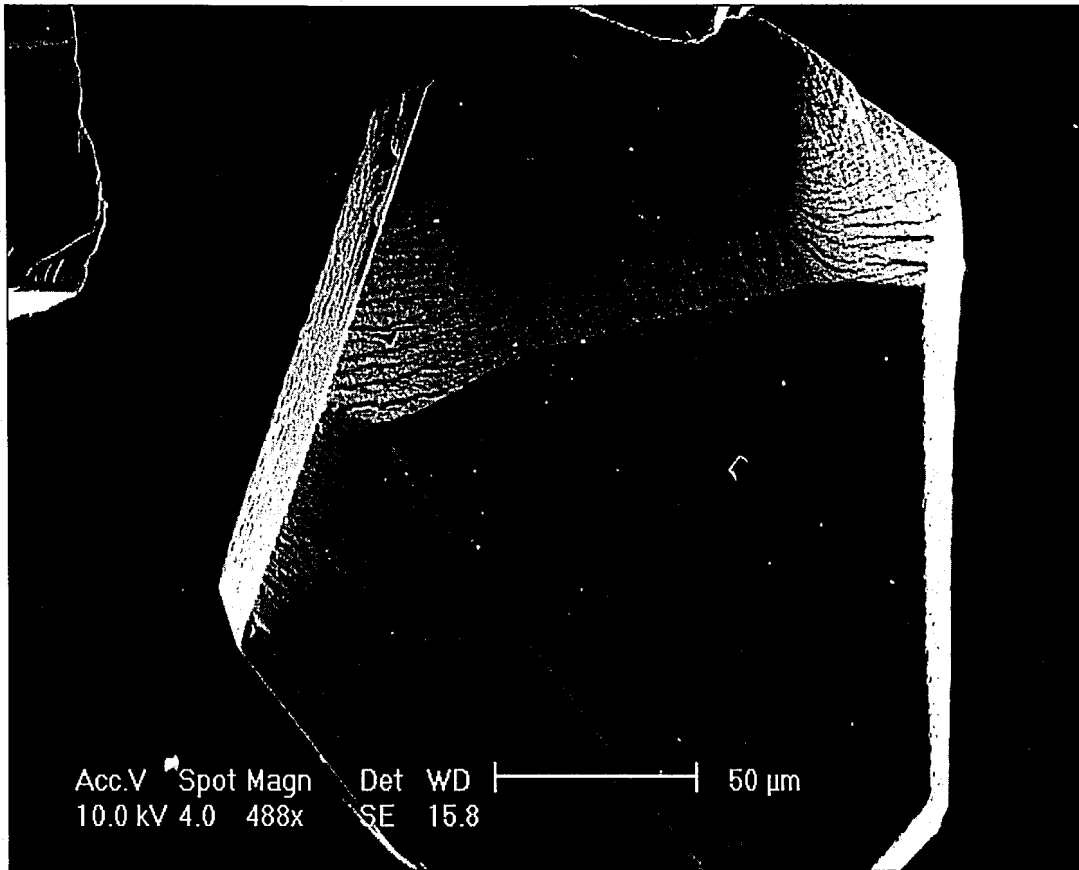


Figure 2: SEM image of Borazon CBN 500 grain displaying a faceted blocky structure.

Further complicating the mechanics of chip formation and chip flow from an ideal treatment is the presence of fine fracture lines along the surface of both faceted and jagged particles. The scale and morphology of these fracture lines varies for a given particle surface. **Figure 4** demonstrates this variability in fine-scale surface structure. Combining the variation in particle size, growth morphology, and fine-scale structure with the inherent distribution of orientations present for a given grain plated to a grinding wheel, the number of possible cutting tool geometries (for a grain) approaches infinity.

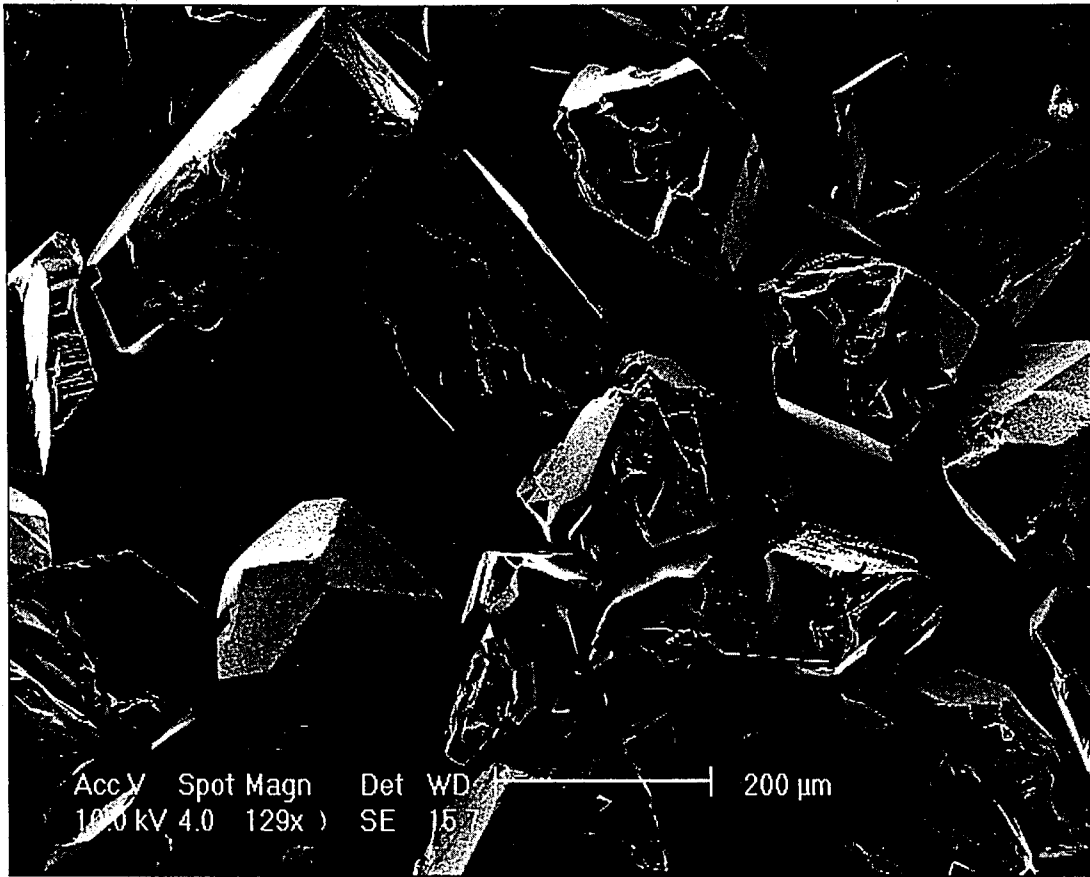


Figure 3: Jagged Borazon CBN 500 particles are in much greater number than the well-defined faceted grains.

Variation of abrasive particles (all aspects) can also be combined with manufacturing disparities between batches of grinding wheels manufactured and slight differences in grinding conditions to give an expected range of performance for most grinding wheels. Abrasive Technology, Inc. has been regarded as one of the most consistent wheel manufacturers in the industry and was therefore selected as the supplier for this project. A 10% variation in wheel performance has been observed for industrial use of ATI's electroplated CBN grinding wheels [8].

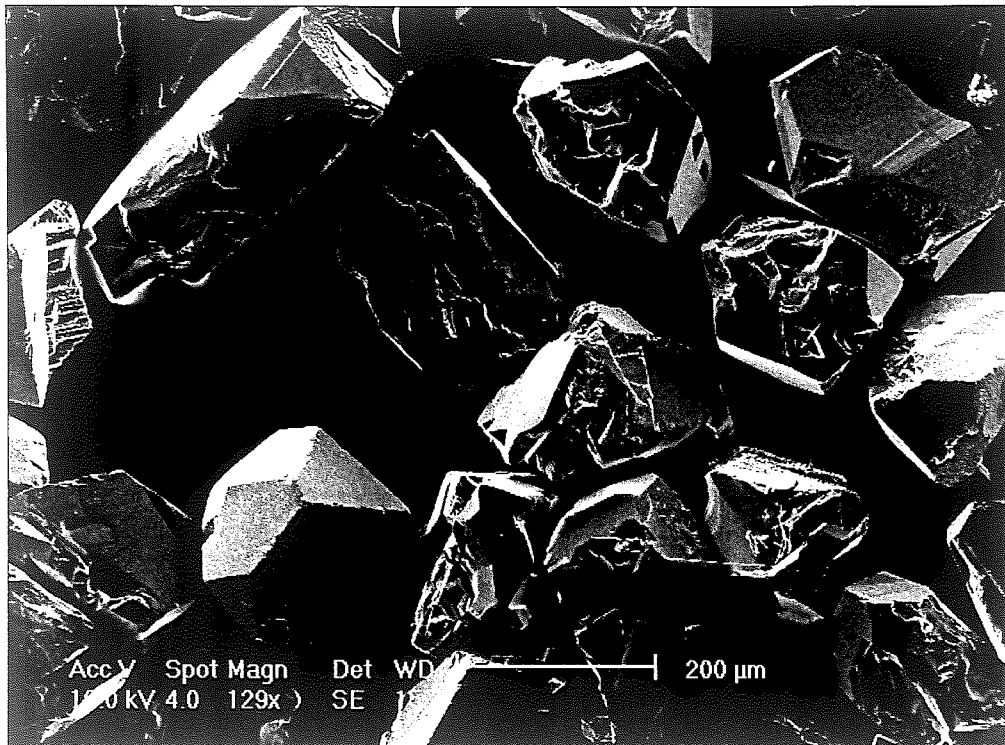


Figure 3: Jagged Borazon CBN 500 particles are in much greater number than the well-defined faceted grains.

Variation of abrasive particles (all aspects) can also be combined with manufacturing disparities between batches of grinding wheels manufactured and slight differences in grinding conditions to give an expected range of performance for most grinding wheels. Abrasive Technology, Inc. has been regarded as one of the most consistent wheel manufacturers in the industry and was therefore selected as the supplier for this project. A 10% variation in wheel performance has been observed for industrial use of ATI's electroplated CBN grinding wheels [8].



Figure 4: Morphology and scale of fine-scale structure present on fractured surfaces of CBN abrasive particles.

2.3 Mechanics of Grinding:

Analysis of grinding operations should begin with a complete understanding of less dynamic machining operations. Metal cutting operations involving single-point cutting tools are ideally suited for a theoretical treatment of cutting forces, grinding temperatures, coolant flow, and material response. Grinding wheels have an extraordinary number of cutting points with an infinite number of orientations and complexities, as described earlier, making analytical treatments much more complex. Single-point cutting operations use one tool face for all cutting operations, removing the uncertainty in chip formation conditions. Grinding processes must abide by the



Figure 4: Morphology and scale of fine-scale structure present on fractured surfaces of CBN abrasive particles.

2.3 Mechanics of Grinding:

Analysis of grinding operations should begin with a complete understanding of less dynamic machining operations. Metal cutting operations involving single-point cutting tools are ideally suited for a theoretical treatment of cutting forces, grinding temperatures, coolant flow, and material response. Grinding wheels have an extraordinary number of cutting points with an infinite number of orientations and complexities, as described earlier, making analytical treatments much more complex. Single-point cutting operations use one tool face for all cutting operations, removing the uncertainty in chip formation conditions. Grinding processes must abide by the

same principles governing much simpler metal cutting operations, so a fundamental understanding of them is prudent.

Orthogonal cutting tool models are often used for mathematical treatment of material flow and cutting forces. It simplifies an analysis of the single-point cutting process by removing unnecessary complexities such as chip breakers or tool asymmetries, and reduces the simplified three-dimensional operation (Figure 5) to two dimensions (Figure 6). The third dimension lies out of the plane of the page in the orthogonal cutting model and is assumed uniform across the width of the cutting tool. This simple model, however, is sufficient to accurately describe the mechanics of material removal for less complex machining operations such as turning and planing.

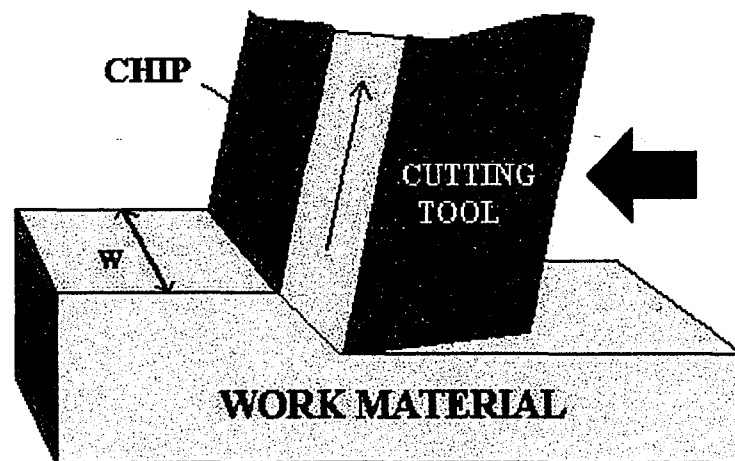


Figure 5: Simple cutting model illustrating the mechanics of chip formation and the uniformity of the operation across the width (w) of the tool.

Chip formation is the method by which material that is cut from the surface of the work piece becomes deformed and exits the cutting zone. As the cutting tool moves along the surface of the workpiece at some cutting velocity (v) and depth of

cut (d), material is forced to flow across the rake face of the tool. Constancy across the width of the tool allows the volumetric amount of material removed per unit time, otherwise known as the material removal rate (MRR), to be calculated as follows:

$$\text{MRR} = v * d * w$$

Workpiece material is separated or cut at the nose of the tool. The material layer just below the cut point passes under the clearance face of the tool and comprises the newly machined surface of the workpiece. Material above the cut point is plastically deformed into chips that subsequently move away from the cutting zone and out of the system.

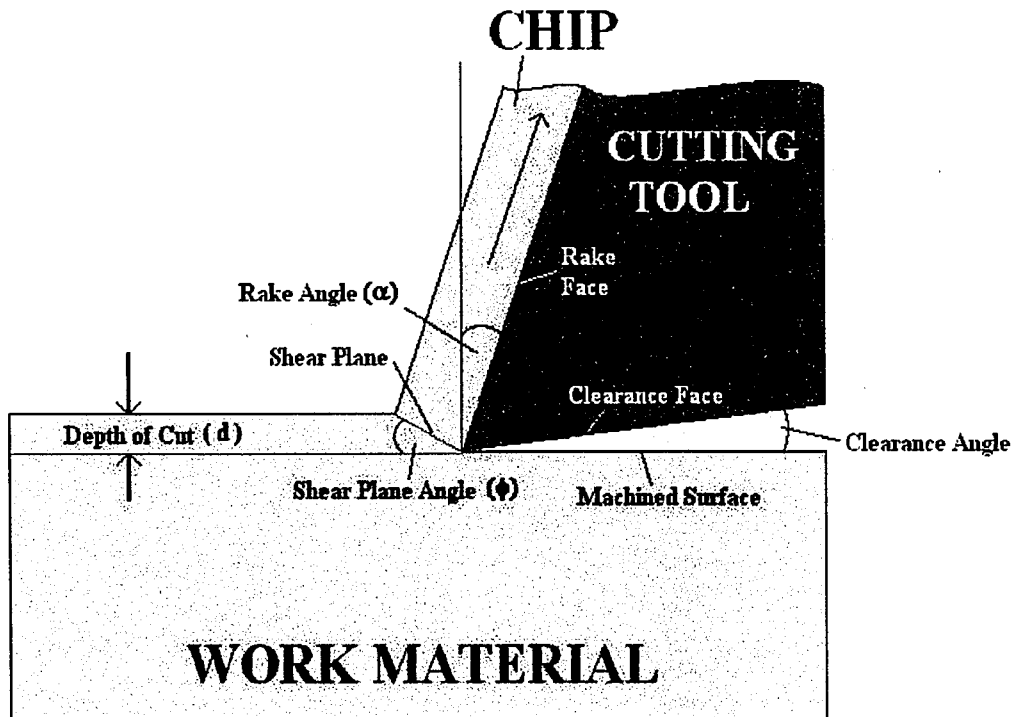


Figure 6: Two dimensional orthogonal cutting model.

Shear deformation ahead of the cutting tool allows material to initially form the chip at an angle, called the shear plane angle (ϕ), from the direction of cutting, which in the case of the orthogonal cutting model is parallel to the workpiece surface.

This shear deformation occurs in what is termed the primary shear zone; the shear plane in **Figure 6** delineates this extremely thin zone just ahead of the cutting tool where primary shear takes place. Through simple trigonometry it can be seen that for a constant depth of cut and all other parameters remaining equivalent, higher values of the shear plane angle will cause a reduction in the chip thickness.

The tool's rake face is at an angle, known as the rake angle (α), to a line drawn perpendicular to the work surface at the nose of the tool. Material flow is directed by the rake face, such that the shear plane angle and the rake angle are related. Abrasive grains of various sizes and orientations are the cutting tools in grinding operations. These grains are much stronger in compression, and as such are grown and embedded into the surface of grinding wheels such that they are loaded in compression. Positive rake angles (around 6°) are utilized in many metal cutting operations, while the abrasive grains on grinding wheels typically have negative rake angles approximately 30° to 45° . The effect on the direction of chip flow based on rake angle can be seen in **Figure 7**.

Chip thickness ratio (r) represents the ratio of the undeformed chip thickness (t_o), equivalent to the depth of cut in the orthogonal cutting model, to the thickness of the deformed chip (t_c). The relationship between the shear plane angle, rake angle, and chip thickness ratio based on the geometry of the orthogonal cutting model is shown below:

$$\tan \phi = \frac{r \cos \alpha}{1 - r \sin \alpha}$$

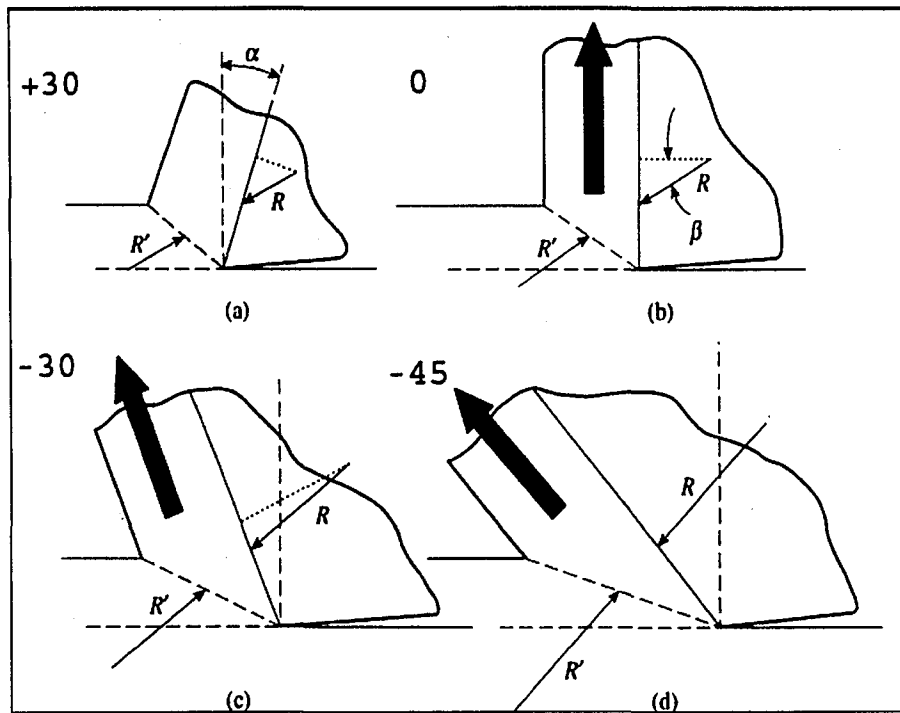


Figure 7: Relation of rake angle to chip flow direction and the resultant frictional force vector, R. [6]

The equation above unrealistically ignores the effect of friction, which is directly responsible for additional shear along the rake face of the cutting tool. Secondary shear occurs in a zone, known as the secondary shear zone, within the chip body along the rake face of the tool (see **Figure 8**). As the chip slides along the rake face, frictional forces resist that motion and give rise to a velocity gradient in material flow within the chip. Sticking friction and high shear strain in the chip causes seizure at the interface between the chip and tool [16]. Following the seizure region is sometimes a sliding region of the chip just before it curls and breaks contact with the tool interface. Large compressive stresses during chip formation develop for all metal cutting operations; with pressures comparable to those in friction welding processes causing seizure and bonding of the work material to the tool face [17].

Forces in metal cutting and grinding are often broken down into vector components that can be measured or easily defined. The cutting force is parallel to the cutting direction and the thrust force perpendicular to it (orthogonal cutting model), labeled F_P and F_Q respectively in Figure 8. A piezoelectric dynamometer can be used as a fixture for the workpiece and properly integrated to provide accurate measurements of these forces. Frictional forces between the chip and tool can be overly simplified to give a relationship between the frictional force acting parallel to the tool face and the normal force to friction acting perpendicular to the tool face.

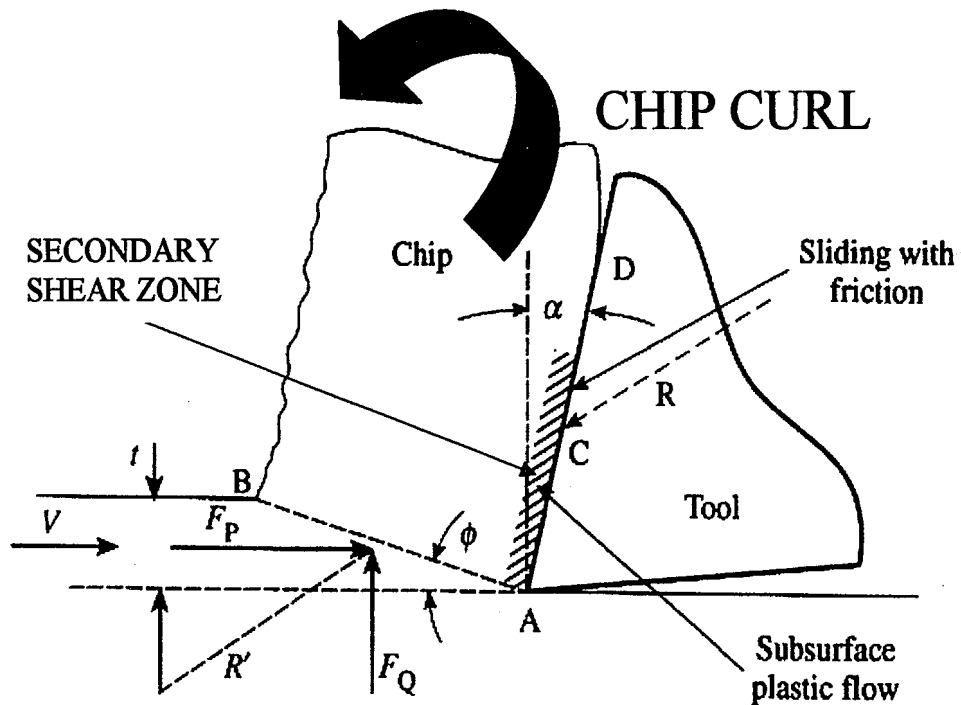


Figure 8: Orthogonal model showing the secondary shear zone, sliding region, and direction of chip curl after it breaks contact with the tool. [6]

The resultant force vector (R , equal and opposite to R' , in Figure 8) is at an angle, called the friction angle (β), to the normal force to friction. A relation known as the Merchant Equation exists between the rake angle, friction angle, and shear plane angle assuming that the shear plane angle is oriented such that shear stress is

maximized, shear strength of the material does not change with temperature and/or strain rate, and the classical friction model is accurate. The Merchant Equation is:

$$2\phi + \beta - \alpha = C$$

where $C = 90^\circ$ when the shear strength of the material is independent of the compressive stress acting on it [18].

These conditions are not realistically met in actual cutting operations, but are adequately satisfied for the usual range of strain and rate of shear encountered in less severe cutting processes [18]. Merchant's equation has been utilized for roughly assessing the function of rake angle and friction conditions on the shear plane angle in metal cutting. Higher rake angles and reduced friction at the chip-tool interface (lower friction angle) will cause the shear plane angle to increase. Increasing the shear plane angle is generally favorable in the sense that the deformed chip thickness and the shear stress required to form the chip are both reduced. Reducing the shear stress required for chip formation causes a reduction in metal cutting forces and energy required to complete the process.

Energy considerations in grinding are important, since the indication of wheel failure is often marked by a rise in forces during grinding or an overall rise in power consumption for the grinding equipment. Specific energy, the energy per unit volume of material removed, will account for all effects in the process by which energy is consumed. Increases in rake angle and use of lubricants have been shown to reduce the specific energy of machining processes. Reductions in the undeformed chip thickness have been shown to increase the specific energy for cutting. Grinding and metal cutting operations with extremely small depths of cut for the abrasive grains or

tools have extraordinarily high values for the specific grinding energy. This “size effect” is purportedly related to shearing of low dislocation density segments of material, however results of TEM studies on the grinding chips have shown high dislocation densities that would indicate this premise of the size effect is incorrect [5]. In light of the force analysis previously discussed, it seems likely to the authors that the frictional forces along the cutting face become increasingly more significant as the chip thickness decreases – hence a higher specific energy for such cutting processes to remove equivalent amounts of material. Also, abrasive grains have a large negative rake angle, such that grinding operations begin to resemble an extrusion process with large specific energy values due to high strain and increasing strain rate as the undeformed chip thickness decreases [6].

Chips will assume different forms and geometries of deformation depending on the general characteristics of the material being machined and the process itself. The four distinguishable categories of chips are: continuous, continuous with a built-up edge (BUE), discontinuous, and shear localized. Continuous chips are chips that have a relatively uniform cross-section and experience nearly homogeneous strain along the length of chip (direction of chip flow). Ductile metals machined at normal to high cutting speeds with sharp, smooth cutting tools and lower friction conditions will tend to form this chip geometry. The BUE occurs with the continuous chip formation for lower cutting speeds with materials that adhere to the nose of the cutting tool. Worn edges and higher friction conditions promote the formation of the built-up edge. Discontinuous chips are formed when brittle materials are machined at higher feed rates and depth of cut. The chip is separated across the thickness of the

chip into sections so that the surface is irregular and broken. Shear-localized chips are a compromise between continuous and discontinuous chip morphologies. There are segments with high shear strain that slip and form a ridge adjacent to regions of low strain. High cutting speeds are the primary criteria for this chip form, usually in difficult to machine alloys like nickel-base superalloys. Teeth (like those in a saw) are visible on the free surface side of the chip, while the face that flows along the rake face of the tool is roughly flat.

Energy consumption in cutting and grinding can be attributed to more than the plastic deformation associated with the cutting action that forms chips. Sliding of the cutting tool along the work surface can result in plowing and frictional rubbing. Plowing occurs when the tool fails to cut the material and instead causes deformation without material removal. Frictional rubbing occurs when the tool, specifically the clearance face, contacts the newly generated workpiece surface and slides during cutting. The area of contact between the tool and workpiece is exacerbated by wear along the clearance face. The cutting, plowing, and rubbing forces all contribute to the energy consumption of the cutting operation, which for grinding (with small chips and grains having negative rake angles) is realized in its characteristically high specific energy.

Only one tool is utilized for machining in the orthogonal cutting model. All material that is removed from the specimen must therefore pass across the rake face of this tool alone. Grinding, however, is an interrupted cutting operation (from the single-point tool perspective) where cutting occurs at high speeds and with an arc-shaped cut for grinding wheels. Material removed from the workpiece is cut by and

flows across thousands of different abrasive grains on the grinding tool. Clearly, this is a significant difference between single-point cutting operations and multi-point cutting operations like grinding. Approximately 97% of the energy consumed in metal cutting operations appears as heat that is convected away by the chips, work piece, tool and cutting fluid [19]. If the cutting fluid is assumed to extract a nominal fraction of the heat generated in the cutting zone, then the distribution of energy would be approximately 90% to the chips, 5% to the tool, and 5% to the work [6].

Heat generated inside the chip is due to shear deformation (internal friction). Metal cutting without lubrication allows heat the possibility of being conducted back into the workpiece, the cutting tool, or remaining entirely in the chip (adiabatic process). In single-point cutting operations like turning, continuous contact between the tool and chip material can allow steady-state heat flow conditions to be reached. Tool temperatures in dry turning of AISI 52100 steel with sharp carbide tools have exceeded 1000°C at the face of the tool, the highest temperatures being found at the approximate center of the chip-tool contact length [20]. Additional heating during cutting occurs as a result of frictional sliding at the chip-tool interface, along with frictional heating due to rubbing of the tool along the freshly cut workpiece surface. Tools exhibiting significant wear will generate higher cutting temperatures, a consequence of increased contact area between the clearance face and the workpiece surface. Generally, increasing the material removal rate for a metal cutting operation causes more rapid deformation and strain, which also increases the temperatures in the cutting zone.

Thermal energy generated in cutting that flows into the workpiece can cause thermal softening of that material. Thermal softening of the workpiece material is related to the reduced flow stress, which can result in a decrease in the energy consumed in chip formation. Negative effects of this thermal softening include increased frictional forces and adhesion wear on the tool. Both effects are a result of larger effective chip-tool contact area due to the flattening and welding of asperities on the chip face as it is formed along the rake face of the tool. Heating of the work material may also induce residual stresses and tolerance variations after the machining process. In severe cases, thermal damage like burning and surface cracking can render the machined part unusable. The maximum temperature in the work piece in surface grinding (up-grinding mode) will be at the entry of the cut, with temperatures gently trailing off behind the entry point and a steeper gradient from entry to the exit point of the grinding wheel [21].

Heat that flows into the cutting tool may cause accelerated attritious wear of the rake face or clearance face. Chemical wear resulting from high temperature interaction with the gaseous environment, cutting fluid, and/or work piece material can also occur, leading to a degradation of properties. The possibility of thermal shock damage to the tool from rapid heating and cooling in multipoint cutting operations is also a problem, especially those where a chilled coolant is employed.

Heat flow during machining can be reasonably controlled by careful selection of setup parameters, use of coolants, and proper maintenance or replacement of the cutting tools. Grinding will not have chip-tool interface temperatures as high as turning operations, if all machining parameters remain equivalent where possible.

Largely, this is because an abrasive grit on the grinding tool will spend only a fraction of the time engaged in the work piece, while the remaining time it is exposed to the atmosphere and/or coolant if applied. Use of coolants (lubricating fluids) is widely accepted and provides machinists with another field of parameters to manipulate in order to tailor their applications for achieving optimal working conditions, best part quality, and the most economical means of completing the process.

Fluids function as a heat sink for some of the cutting energy, as a lubricant to reduce friction in the cutting zone, and to assist with chip removal from the cutting zone and cutting (grinding) tool surface. There are four general categories which metalworking fluids fall under: straight cutting oils, emulsions (soluble oil), synthetic fluids, and semi-synthetic fluids. Straight oils (also called neat oils) are derived from oil from petroleum (mineral, paraffinic, or naphthenic base), animal, or vegetable origin, utilized alone or in combination to achieve a range of viscosity, wetting ability, and lubricating characteristics [19]. Emulsions are water-based fluids with a suspension of oil droplets through the use of emulsifying agents. Synthetic fluids are water-based solutions containing dissolved substances (no oil) that act as rust inhibitors, stabilizers, water softeners, and wetting agents. Semi-synthetic fluids are a combination of emulsions and synthetic fluids, generally having lower oil contents than ordinary emulsified fluids. All of these fluids may also contain biocides to prevent the growth of mold and bacteria, ester additives for increased lubricity, and extreme pressure additives (sulfur, chlorine, and phosphorous compounds) that are surface active, preventing or reducing adhesion (welding) between the freshly cut work material and the cutting tool surface.

The general performance of these fluid categories in relative terms of function and viability in a manufacturing setting were assessed by GE Superabrasives, and are listed in **Table III**. Each of these fluid categories will contain both technologically-advanced and poorly formulated fluids that do not conform to the assessment score; however it provides a rough measure of their benefits and limitations.

Application (or delivery) and maintenance of metal working fluids is just as critical as selection of fluid type to the level of performance that can be achieved for a given machining process. Fluids must be applied in a suitable volume and with appropriate pressures and velocities to be effective in: entering the cutting zone, providing the capacity to cool the cutting tool, and cleaning the tool face (grinding wheel). Metalworking fluids can be applied in various ways. Misting (low volume, high velocity) and manual application of the fluids by the operator are appropriate in some metal cutting operations, but not typically for grinding. Grinding requires significant cooling and lubrication, so that high volume, high pressure, and high velocity delivery are customary. Immersion of the grinding process in the fluid or flooding the cutting zone (low pressure, high volume) is sufficient for cooling and lubricating, but does not provide any mechanism for cleaning the grinding wheel of adhering material. High-pressure, high-velocity jets are capable of high volume delivery that adds this cleaning capability.

Table III: Relative assessment of general grinding fluid categories [22].

	SYNTHETICS	SEMI-SYNTHETICS	SOLUBLE OILS (EMULSION)	STRAIGHT OIL
HEAT REMOVAL	4	3	2	1
LUBRICITY	1	2	3	4
MAINTENANCE	3	2	1	4
FILTER ABILITY	4	3	2	1
ENVIRONMENTAL	4	3	2	1
COST	4	3	2	1
WHEEL LIFE	1	2	3	4

1 = POOR 4 = BEST

In one case, increasing the bulk fluid volume delivery rate from 2 gallons per minute to 5 gallons per minute (7.6 – 18.9 L/min) in an internal plunge grind using vitrified CBN grinding wheels was shown to reduce wheel wear, reduce power consumed, and improve the surface finish for all fluids tested [23]. Not all of the fluid, however, delivered to the entry point will flow through the grinding zone. The fraction of fluid delivered that reaches the grinding zone (percent utilization) will significantly increase with increasing wheel porosity (lower grain concentration), closer positioning of the delivery nozzle to the grinding zone, and proper orientation of the delivery nozzle [24],[25].

High pressure fluid delivery has been generally applied using nozzles near the entry point of the grinding wheel to allow the rotation of the wheel to pull the fluid into the cutting zone. It is critical that the fluid must be delivered at a velocity that approximately matches or exceeds the cutting velocity of the grinding wheel, with a

pressure capable of penetrating the rotational air barrier surrounding the grinding wheel. Velocities and pressures that are significantly lower will fail to deliver adequate amounts of fluid to the cutting zone, resulting in increased temperatures and cutting forces and an overall decrease in machining performance. Additional nozzles can be utilized for high pressure cleaning and high pressure cooling (fluid not expected to enter the cutting zone), which has been shown to increase grinding performance through improved surface finish, lower wheel wear, lower power requirements, and reduced thermal damage [22].

Fluid maintenance will ensure consistency of process performance. Filtration or removal of dirt is necessary to prevent residue buildup, poor surface finish, reduced tool life, and microbial growth [26]. Bacteria and mold must be kept in check to prevent clogging of fluid lines and offensive odor buildup, while pH must be stabilized to control rancidity, mix uniformity, and ferrous corrosion (too low pH) or nonferrous corrosion (too high pH) [26].

2.4 Specific Grinding Applications:

Finishing operations are generally completed by surface grinding with low depth of cut, due to the close tolerances and fine finishes that can be attained with tools utilizing fine-grained abrasives. Grinding can also be used to complete more severe material removal operations involving larger depths of cut and higher material removal rates (MRR), often referred to as creep feed grinding. The advantages of creep feed grinding include closer tolerances on formed surfaces due to lower feed rates and reduced lost-work time due to grinding completion occurring without the

need for multiple reciprocations of the work tool [2]. Creep feed grinding is a more demanding process than surface grinding, therefore creep feed grinders are designed differently to handle the extra stress. Creep feed grinding machines require higher spindle power, high static and dynamic stability, accurate slide ways to reduce stick-slip, consistent table speeds for low infeed rates, and high pressure fluid delivery systems [27].

Creep feed grinding of superalloys with CBN tooling is extensively employed in the aerospace industry in the manufacture of aero-engine parts. Reducing in-process inventory, lowering capital equipment investment costs, and improving part quality has spurred the aerospace industry to develop advanced grinding technology and machine tool design for processing components from nickel-based superalloys [28].

The parts are cast from superalloys that have excellent mechanical properties (including high temperature strength), and often times are coated with a protective ceramic layer for thermal protection. Grinding through both materials simultaneously with the same tool is required. Components may have odd geometries such that form grinding, radial slot grinding, and creep feed slot grinding is used to generate the required profile on the part with one grinding step. Turbine assemblies for jet engines require components that are ground to extremely close tolerances for mating surfaces. This becomes an extraordinarily challenging process to balance necessary parameters for machining both materials correctly and effectively. Damage to the component resulting from a final machining step can create scrap that is a significant loss in the manufacturer's investment in the part. This is completely unacceptable, and must be

considered when assessing the practicality of the machining process. Increased abrasive costs or processing costs per part may be readily offset by a reduction in the amount of scrap or rework.

Grinding superalloys with electroplated CBN wheels has been utilized because of certain advantages over conventional grinding wheel and non-electroplated CBN wheel processes. Electroplated CBN wheels have a generous exposure of abrasive grains on the wheel surface (approximately 40% of the particles being exposed) that allow these wheels to “act sharper”, requiring less power and being capable of higher material removal rates [29]. Electroplated CBN wheels have also been shown empirically to grind cooler (reduced thermal damage) and produce more consistent cuts and parts (excellent profile retention) [29]. Special form shapes and the elimination of dressing steps have made these grinding tools ideally suited for turbine component grinding applications.

2.5 Grinding Wheel Failure Mechanisms:

Failure of the grinding tool utilized in a machining operation can be generally considered as the point at which any one parameter in the process varies to a significant degree outside of acceptable bounds of the specified tolerances for that operation. This vague description of tool failure is comprehensive enough to include most of the reasons for tool replacement in industrial grinding. Decreases in the material removal rate or cutting velocity that can be maintained for a given machining operation may be justification for tool changeover. Increased cutting forces and power consumption above some pre-determined threshold value may indicate tool

failure and the need for replacement. Thermal damage, such as work piece burning or adverse changes in mechanical properties of the material, will also be an indicator of tool failure. Unacceptable variations in form tolerance or surface finish are also valid criteria for determination of the acceptable life of a machining tool.

The rationale for deeming a grinding wheel unusable (due to tool failure) can be expansive, as just described. Assessing the mode of tool failure can be done with a wide range of specificity. For instance, thermal damage to the workpiece surface could be regarded as: 1) A result of increased frictional heating due to tool wear and accumulated thermal energy in the work piece, or 2) A result of attritious wear and chemical wear (due to fluid interaction) of the abrasive grits, causing the formation of wear flats on the abrasive grains that generate higher rubbing forces and increased frictional contact with the work piece - hence the observed thermal damage. Regardless of the failure assessment, the mechanism of failure for the individual cutting tools (the abrasive grains for grinding) has not been rigorously identified such that a preventative or corrective treatment can be prescribed.

Mechanism of failure is extremely specific to a given process and the entire array of operational parameters that were employed, since no single parameter can be considered to operate in isolation from the others. Topographical, physical, mechanical, chemical and metallurgical properties of the work piece and tool, combined with the properties of the lubricating fluids, delivery, and selected process parameters must be considered [30]. The complex, simultaneous interaction of all known parameters makes an analysis of metal machining operations (specifically grinding) and its mode of failure extremely difficult.

Electroplated grinding wheels can be considered as a circular hub with a large number of individual cutting tools embedded on the periphery, as described earlier. From this perspective, the mode of failure can be evaluated in terms of individual “tool failures” accumulating sequentially to the point of malfunction, or the collective degradation of all the cutting edges leading to progressively poorer performance and ultimately tool breakdown. Either line of reasoning would be appropriate; the mechanisms leading to the failure, however, will lead to different tribological properties of the system being labeled as the root cause. Overlap of properties and function will inexorably exist between the different failure modes and the identifiable mechanisms being considered as responsible.

Ignoring the complexity and dynamic action of the grinding process to assume that each abrasive grain is equivalent and experiences the same forces, temperature, environment, etc., the dominant tool wear mechanisms acting collectively on the CBN grits would be: abrasion wear, chemical wear, thermal wear, and impact wear [31]. Abrasive wear, sometimes referred to as attritious wear, occurs as a result of continued contact and sliding between the tool and work material(s). Over time, the tool body is reduced in size and form due to removal of material from the tool surface. This form of wear is an inevitable consequence of tool usage in machining operations.

Chemical wear of CBN can be attributed to interfacial interactions between the tool (abrasive grain) and the work piece material, gaseous atmosphere, and lubricating fluid. As an example, CBN is held to be far superior to diamond tools in machining hardened M2 tool steel due to a lower chemical affinity for the steel during

operation [32]. Variations in material chemistry may also present a noticeable change in machining performance. Gray cast iron produced in different foundries with nominal differences in alloy chemistry was found to affect the tool life of polycrystalline CBN inserts by orders of magnitude in machinability studies [31]. Fluids used in the process can cause chemical wear of the abrasive grains and the matrix that holds them into the wheel periphery. CBN has been observed to break down in the presence of steam at high temperatures to form boric oxide, B_2O_3 . The chemical reaction has been observed in laboratory studies, but never clearly identified in machining studies due to the complex interactions of other variables. Water-based fluids have been theorized to interact with CBN tools and grains during grinding to produce the following chemical reactions:



where the boric oxide product dissolves in water at high temperatures, chemically eroding the CBN material [22].

Thermal wear is a result of temperature cycling within the cutting tool that prematurely causes breakdown and failure. Temperature cycling occurs as the abrasive grain heats up during its length of contact with the work piece and cools off during the remaining part of the wheel rotation before it reenters the work piece. Repeated fluctuations in temperature due to this interrupted cutting can cause thermal shock or fatigue of the abrasive particles. Microfracture of the grains leads to an accelerated reduction in the particle volume and in edge sharpness.

Impact wear is the product of repeated impact loading. Chipping of CBN tools that are involved with interrupted cutting processes leads to worn edges that are

dull and are ineffective at cutting. These worn tools cause increases in cutting forces that eventually lead to thermal damage, increased power consumption, and unacceptable surface finish. Abrasive grains on grinding wheels undergo the same impact loading, suffering a similar fate. As the grains chip (microfracture), the wheel loses form and approaches the failure criterion for the operation.

Wear of electroplated CBN grinding wheels may also occur by failure mechanisms specific to electroplated grinding wheels: attritious grit wear (including chemical wear), grit pull-out and bond erosion, grit fracture, and wheel loading [33]. Each of these mechanisms may act independently or in combination, and are relevant to all grinding wheels in which the abrasive grains are electroplated in a single layer on the wheel periphery. These electroplated wheel wear mechanisms are redundant in some respects with the wear mechanisms of CBN tooling; however they do encompass the observed range of failure modes for electroplated CBN wheels and deserve some extended explanation.

Attritious grit wear was already discussed previously in the description of abrasive wear. This definition of wear (adapted from *Stokes, et. al.*) suggests that it occurs as a result of erosive interaction between the tool, work piece, and loose abrasive particles, including the wear effects of chemical interactions. Hard work materials will result in increased rates of attritious wear. Diamond is used to machine the hardest work materials since it is the hardest abrasive material and has been empirically shown to take the longest to wear. Other abrasive materials of lower hardness will wear away at an increased rate directly related to the difference in hardness between work and tool. Chemical interactions between the tool and material

may accelerate the wear process as previously described, such that the difference in hardness will not always be proportionally related to tool life. Diamonds ability to machine hard ceramics does not explain its accelerated rate of wear when machining softer and relatively ductile ferrous alloys. This behavior is only explained in terms of chemical interactions between the carbon (diamond) and iron. Similarly, CBN has been selected as the tool of choice for machining nickel- and cobalt-based alloys based on lower chemical interaction between the tool and work piece.

Grit pullout is the process whereby abrasive particles are forcibly removed from the periphery of the grinding wheel. Dulled cutting edges may increase the cutting forces that an individual abrasive grain experiences to the point that they exceed the bond strength of the matrix and the particle is detached. Errors in manufacture may result in underplating, where the grit retention strength is not sufficient for machining. Softer work materials may allow plastic deformation to the extent that the abrasive particle is equally or more deeply embedded in the work piece than its matrix bond. In such cases, the abrasive particle may be mechanically gripped by the work material and ripped from the wheel hub, left embedded in the work block to be cut out later by subsequent passes of other abrasive grits. Bond erosion due to chemical attack or attritious wear by chips and free-floating abrasives can also occur. This will result in the weakening of the grit retention strength of the bond during service until eventually the forces pulling on the abrasive particles succeed in removing it from the wheel surface.

Grit fracture is the process by which the grains are reduced in size by the removal of sizable portions of the abrasive particle volume. The cause for fracture

can be related to high cutting forces, impact loading, thermal cycling, or leaching of the binder in the case of polycrystalline abrasive grains. Grit fracture has been incorporated into the design of many electroplated grinding tools. As the tool wears and becomes an inefficient cutting edge, microfracture allows the grain to strip away the worn face and once again become used as a sharp tool. Fracture of the particle at the matrix bond level is termed macrofracture. This is an undesirable process wherein the effective cutting ability of the abrasive grain has been eliminated.

Wheel loading is the last mechanism of failure for electroplated CBN grinding wheels. This mechanism is currently at the forefront of problems to be solved in the effort to incorporate water-based fluid technology into industrial practice. Wheel loading is the phenomenon of adhesion of work piece material onto the surface of the grinding tool. Material removed from the work piece attaches itself to the abrasive grains, or embeds itself in the voids in the wheel surface, reducing the effective cutting ability of the grinding wheel. The process of increasing wheel loading due to adhesion will generally be offset to some degree by the dislodging of adhered lumps of work material due to grain fracture [34]. As the surface of the grinding wheel becomes loaded, contact area between the work piece and the grinding wheel in its arc of cut is increased. Increased frictional rubbing and higher cutting temperatures combine to prematurely end the life of the grinding tool.

Metal adhesion can be viewed as the precursor to grit fracture or grit pullout, or as an aftereffect of dulled cutting edges and wear flat formation due to attritious and chemical wear. A pressure welding process is commonly agreed to be an accurate description of the process, whereby the chips adhere to the individual cutting

grains to form the surface deposits. Adherent lumps are comprised of chips that adhere to the abrasive grains as well as each other to form the compacted mass, which upon reaching significant size may spall off (causing grit fracture or pullout) or cause the wheel to fail [35]. The deposit morphology has been characterized, but the literature is not in full agreement on the cause(s) of wheel loading, especially since variation in experimental design and chosen parameters between research groups can have important repercussions in determining the mechanisms responsible.

A medium carbon heat-treated C-45 steel ground with aluminum oxide wheels was shown to have insignificant levels of wheel loading after 130 passes at a 0.01mm depth of cut, but heavy loading was observed for the same material after 16 passes at a 0.04mm depth of cut [36]. Material removal rate was suggested to be an important parameter in discerning the likelihood of wheel loading. The same parameters were also used to grind both 316 stainless steel and Ti-6Al-4V at a 0.01mm depth of cut, where a substantial amount of wheel loading was observed on the wheel surface in different patterns of accumulation [36]. In another study of grinding medium steel with aluminum oxide wheels, it was shown that material removal rate was not a critical parameter in assessing wheel loading. In this study, table speed had little effect on wheel loading since there were competing processes resulting in equivalent amounts of accumulated loaded mass, but increasing depth of cut (resulting in large grain grinding distance) causes increased wheel loading [34].

No solid state chemical reaction between Al_2O_3 and SiC grains with T15 steel and Ti-6Al-4V work materials was shown to exist [37]. A chemical reaction or diffusional process in the boundary layer between the chip and tool is proposed to

exist, but it provides an insignificant fraction of the bonding strength of the deposit in most cases due to the extremely short duration of contact [34]. The chemistry of work material and tool material is clearly important (as has been discussed with diamond grinding of ferrous alloys), and does not correlate well with these observations. Adhesion problems are more noticeable with materials of lower hardness, which concurs with the pressure welding mechanism of deposit formation. Hardness is not, however, a direct indicator of the material's machinability or tendency towards wheel loading. Oxidation resistance of the work material has also been reported to play an important role in wheel loading. Increasing oxidation resistance of the work material is shown to reduce the degree of wheel loading that will occur for a given operation [38]. The oxygen reactions on the surface may prevent adhesion of the chips to the workpiece, which is in harmony with the function of sulfur and chlorine extreme-pressure (EP) additives (along with other Group VI and VII compounds) that react with the surface of the work material to prevent adhesion [39]. Undoubtedly, chemical interactions between the chip and tool have a greater importance than is currently understood.

Agreement has been reached that different mechanisms of adhesion will prevail if different work material, tool material, and processing parameters are chosen. Universal treatment of wheel loading from one process to another is therefore futile. The evidence gathered suggests that applying general principals to accurately describe the phenomenon in many processes must be done with care. Development of solutions to prevent wheel loading must logically account for

material interactions with the tool and all processing parameters that can be adjusted in order to correctly attempt a counteraction.

3.0 EXPERIMENTAL PROCEDURE:

3.1 Foreword:

The research project is centered on grinding tests carried out in a laboratory setting that simulates industrial machining conditions. All the tests were executed with electroplated CBN grinding wheels, see **Figure 1** for specifications, and run until failure so that the performance of the different lubricating fluids (see **Appendix**) could be evaluated. Performance of each grinding fluid was gauged by measurements of power, grinding forces, and life of the grinding wheel. Grinding wheel failure was identified as the point at which the wheel became ineffective at cutting the material and seized itself in the work block. Prior to experimentation, wheel life was determined to be the primary indicator of fluid performance. Data collected from the power meter and dynamometer would augment the assessment of wheel failure with quantitative measurements up to the point of failure.

After completion of the grinding performance tests, each wheel was removed from the system and analyzed to determine the modes of wear. Wheels were preliminarily examined using an optical stereoscope. These observations provided information regarding the extent and morphology of material adhering to the surface of the grinding wheel. Sections of the wheels were cut to provide specimens for scanning electron microscope (SEM) analysis and to prepare cross-sectioned samples for light optical microscope (LOM) analysis. These samples were utilized in determining if abrasive grit wear existed, if wear of the matrix bond existed, and to analyze the deposited material on the surface of the grinding wheels. Grinding swarf

collected from the fluid run-off was similarly examined to determine any correlation between the fluid used and the morphology of the grinding chips. Surface roughness measurements and profile traces of the ground blocks were completed using an optical profilometer system to provide information regarding the integrity of the ground surface and the control of the machining process parameters.

In order to accurately simulate industrial grinding conditions, an experimental testing laboratory was developed that would closely represent the manufacturing setup in an aerospace engine production facility. To that end, the specific operation that was replicated in the experiment was a type of creep feed process known as groove grinding, commonly employed in the aerospace industry. Groove grinding, or slot grinding, is an application where grinding wheels as narrow as 0.635mm (0.025") in width are used to cut deep slots in the work piece. These deep slots serve as a seal (sometimes referred to as a feather seal) for control leakage when the mating half of the adjoining component in the turbine assembly is put into place. Groove grinding operations are often completed using a form wheel that completes the slot while grinding a smooth surface in the adjacent material for the mating edge. **Figure 9** shows a complex radial slot grinding operation on a curved component, which requires a form grinding wheel to grind through the ceramic coating layer on the one edge, grind the entire face of the part with the required surface finish, and complete the slot (or groove) with the required tolerances. Groove grinding of the slot, one of the functionally distinct processes in this complex operation, became the focus for the project due to its severity and history with adhesion wear problems. This allowed the

adhesion phenomenon to be characterized without the extraneous steps of grinding through a ceramic layer or generation of a large, flat face with surface grinding.

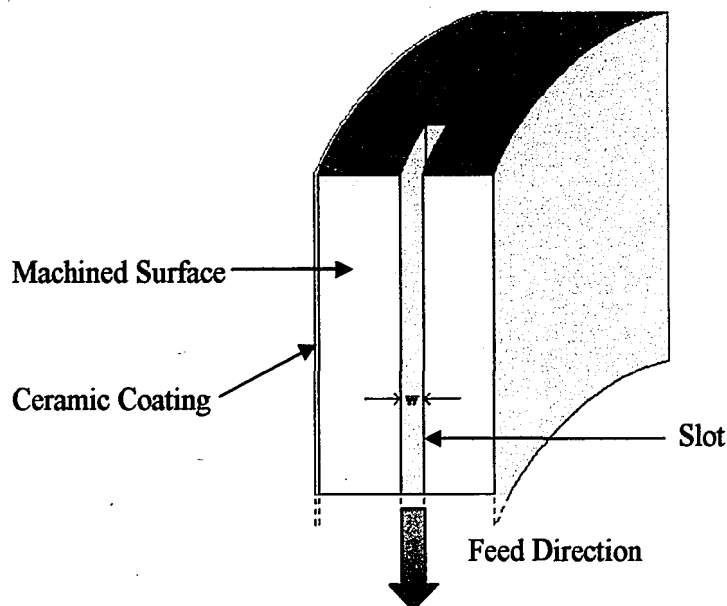


Figure 9: Schematic of radial slot grinding of a ceramic coated part.

3.2 Fluid Preparation and Circulation System:

The system used for the grinding experiments is illustrated in Figure 10. Four different fluids were tested in the experimental trials. The water-based fluids were the first fluids to be tested, ending the trials with the neat oil fluid. Prior to any fluid being tested, a 5% concentration cleaning solution in water with rust inhibitor (Ferrocut 118) was pumped through the entire system for two hours (both sets of relief piping open) to remove any debris or residue that might be present in the grinding chamber and piping. Following the cleaning schedule, the cleaning solution was removed and plain tap water was pumped through the system for another two hours before removal. This process was completed before introducing any new fluid into the system to ensure the starting conditions were consistent. Air was circulated through the entire system for ten days prior to introducing the Oil Baseline fluid (neat

oil) into the tank. Small amounts of water remaining in the pipes were considered to be detrimental to the performance of the oil, so evaporating out any water in the system was crucial.

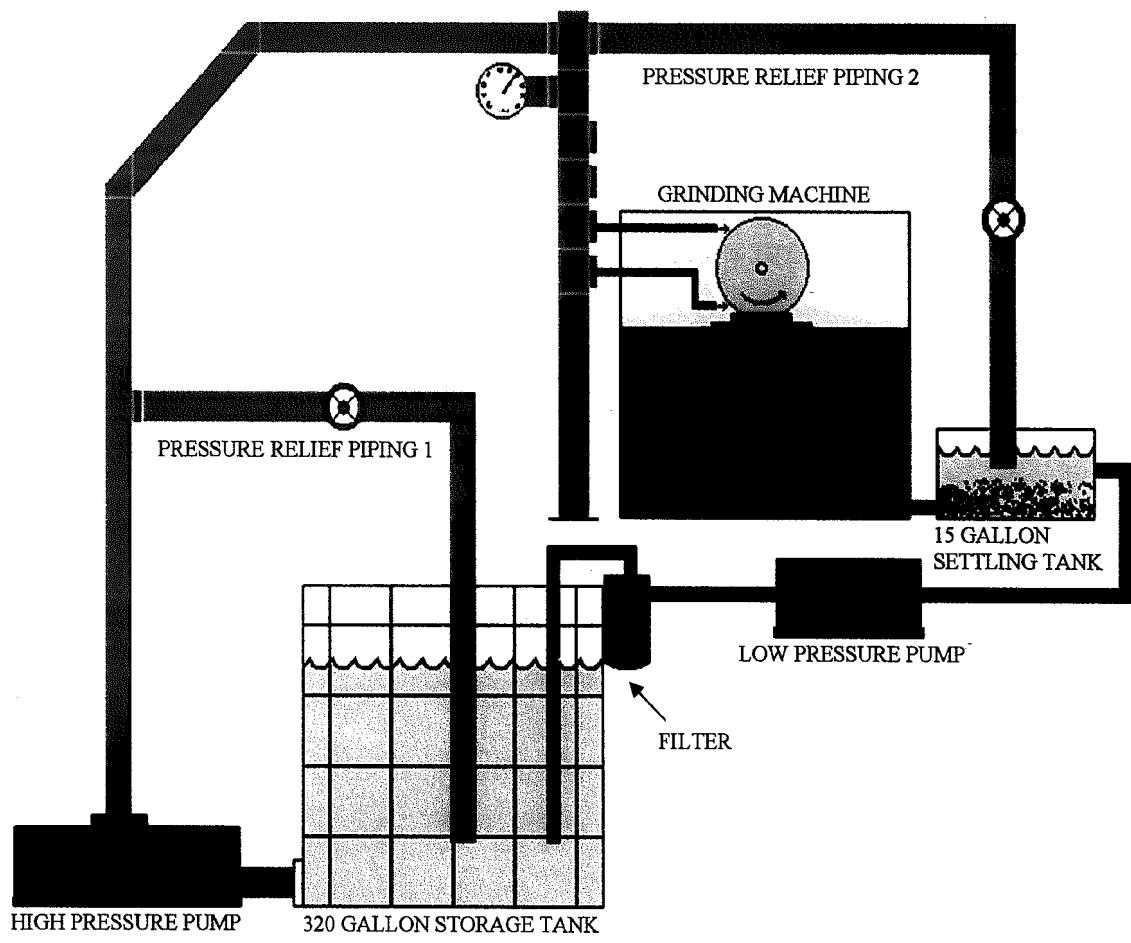


Figure 10: Illustration of the system setup developed for the grinding tests.

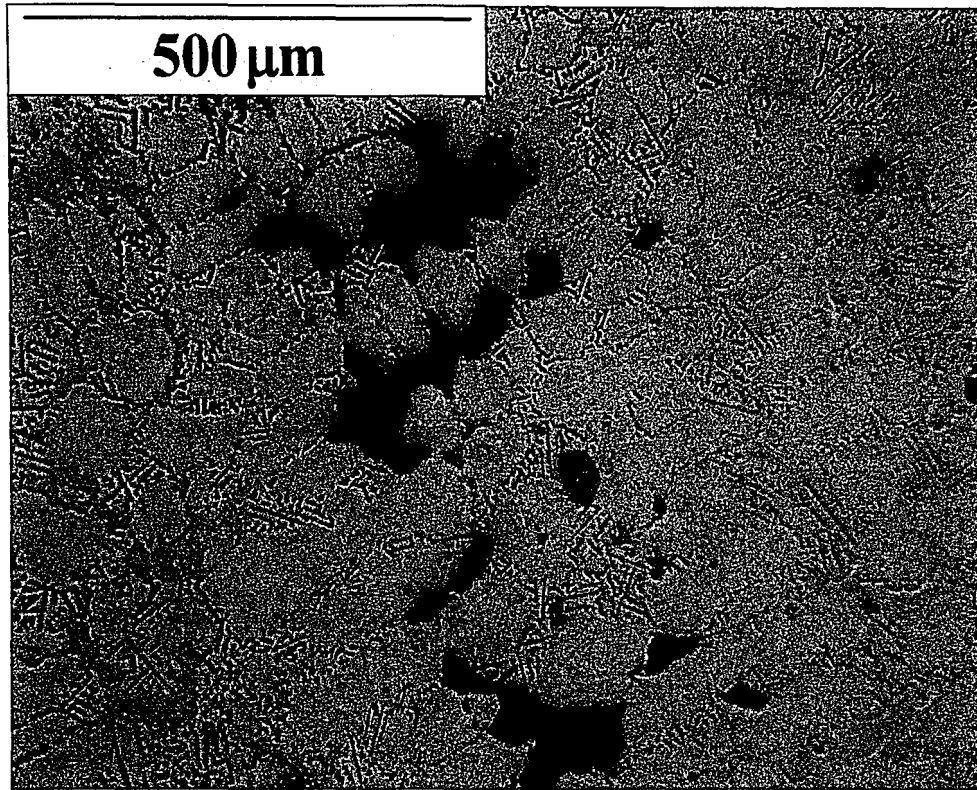
The water-based fluids were used in 8% concentrations, while the Oil Baseline fluid was used in its original form. Mixing was required for the water-based fluids to obtain a homogeneous solution. Six-hundred ninety seven liters (184 gallons) of tap water were put into the system first, followed by 60.6 liters (16 gallons) of the concentrated solute. After both components were added, the fluid was circulated out of the large storage tank through the high pressure pump and back into the large storage tank via *Pressure Relief Piping 1* (all other piping was closed) for one hour prior to testing.

Seven-hundred fifty-seven liters (200 gallons) of fluid were used for each experimental trial to ensure there was sufficient time between recirculation to accurately simulate an industrial process. Increased time between recirculation avoided problems such as unnecessary temperature increases, fluid shearing, and excessive foaming. Fluid held in the large storage tank was drawn out and pressurized to 6.89 MPa (1000 psi) by a high pressure pump before it flowed through the piping system. Fluid was delivered into the enclosed grinding assembly at 83.3 liters (22 gallons) per minute by two fire hose nozzles (coolant delivery and cleaning) rated for 2.76 MPa (400 psi) fluid pressure each. Fluid run-off from the grinding table was run through a 5-micron filter bag and collected in a 56.8 liter (15 gallon) holding tank that allowed any remaining sediment in the fluid to fall to the bottom. A low pressure pump, internal to the grinding machine, was used to pull the fluid from the top of the settling tank and pump it through a larger fluid filtering unit before returning to the large storage tank. Filter bags were changed between each wheel

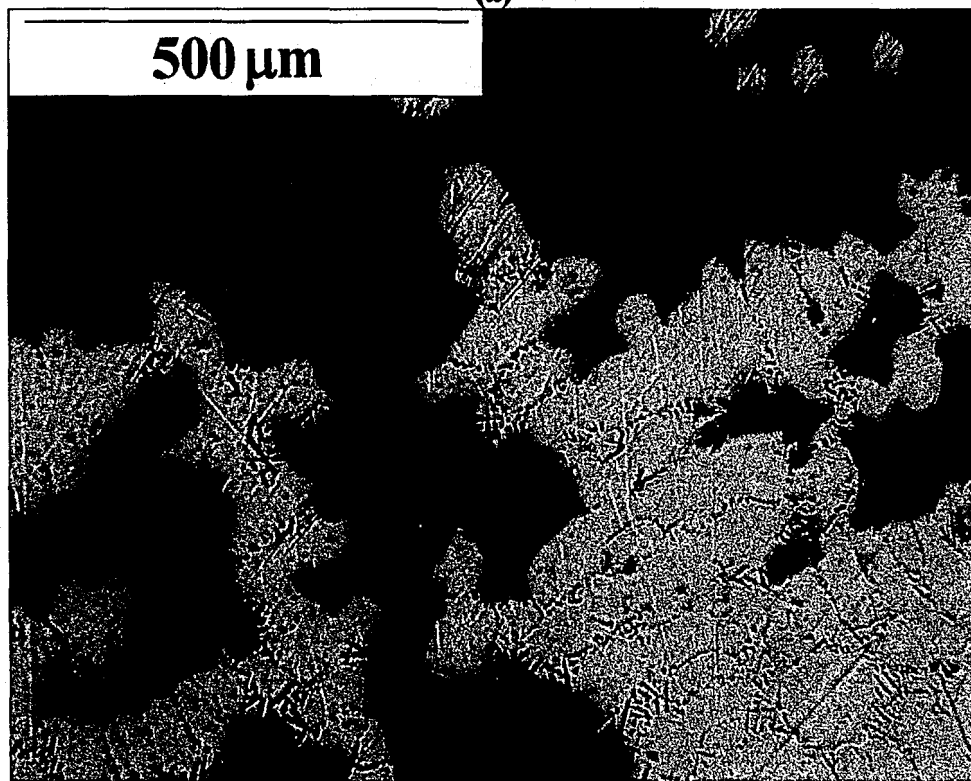
tested, while the settling tank was cleaned out and the fluid filtering units replaced between each fluid trial.

3.3 Material Selection and Sample Generation:

Cobalt-based and nickel-based superalloys are among the most difficult materials to machine. These high-temperature high-strength alloys are notorious for adhesive wear problems during grinding and cutting. Based on this criterion alone, these alloys made excellent candidates for this research project. The material first selected for the study was a cobalt-based superalloy – MAR-M509 used in the aerospace industry for turbine part manufacture. Cubic blocks (101.6mm x 76.2mm x 12.7mm) were prepared by an external machine shop from a large cylindrical specimen of cast material stock. Upon receipt of the prepared blocks, large internal shrinkage pores from an improper casting process were visible. The nature of this shrinkage porosity can be seen in **Figure 11** and was quantified for one sacrificial work block using light optical microscopy and computerized analysis (see **Table IV**). After consideration of the sample integrity and the adverse effect it might have on the consistency of grinding performance, this alloy was eliminated as the work material for the experiment and replaced with a nickel-based superalloy – trade name GTD-222.

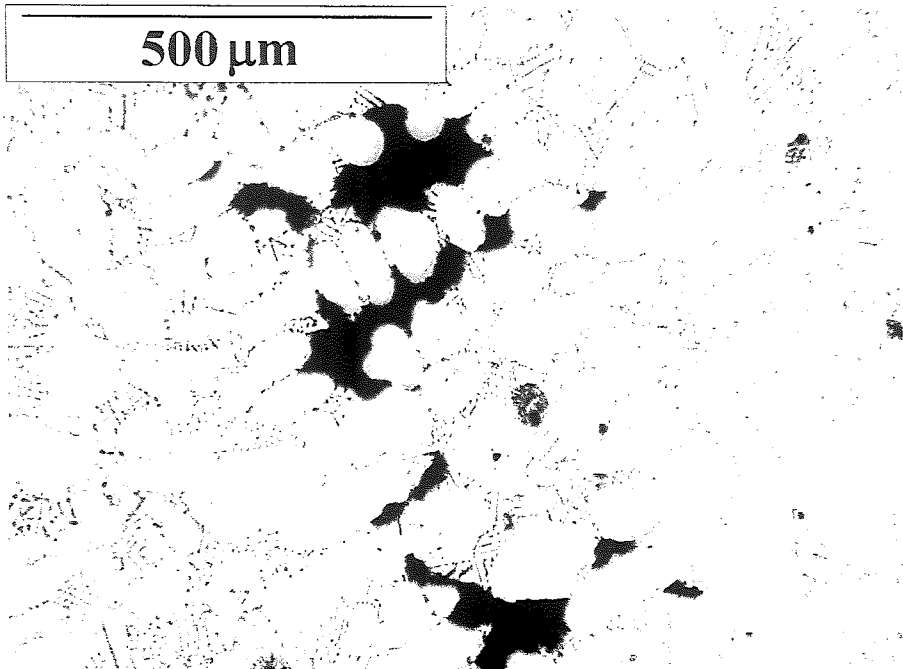


(a)

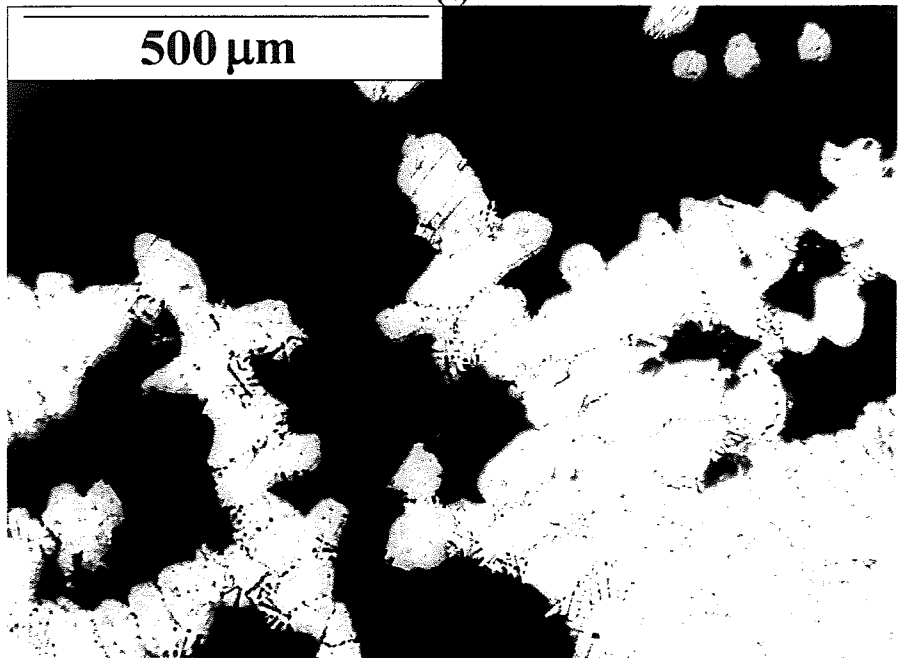


(b)

Figure 11: Light optical microscope images of internal porosity within the M509 machined blocks.



(a)



(b)

Figure 11: Light optical microscope images of internal porosity within the M509 machined blocks.

Table IV: Measurements of internal porosity of a M509 block.

POROSITY MEASUREMENTS OF M509 ALLOY SAMPLE NO. 1
 LECO IMAGE ANALYSIS 3001 **AVERAGE POROSITY – 5.46%**

FIELD	AREA%	FIELD	AREA%	FIELD	AREA%	FIELD	AREA%
1	0.01	31	0.07	61	0.00	91	14.42
2	0.02	32	35.57	62	0.04	92	0.05
3	0.19	33	62.42	63	0.01	93	0.02
4	0.03	34	6.63	64	0.02	94	0.04
5	1.26	35	0.06	65	1.33	95	0.01
6	2.43	36	0.02	66	10.38	96	0.00
7	13.53	37	0.01	67	0.10	97	0.01
8	9.73	38	0.03	68	29.49	98	0.03
9	0.02	39	0.05	69	76.89	99	0.03
10	1.08	40	0.02	70	55.42	100	1.41
11	3.94	41	0.04	71	20.94	101	0.03
12	21.41	42	0.05	72	0.13	102	0.03
13	0.23	43	0.05	73	0.05	103	0.04
14	0.06	44	0.06	74	0.02	104	0.04
15	0.07	45	1.34	75	0.12	105	0.50
16	0.24	46	0.09	76	0.00	106	1.82
17	0.25	47	0.17	77	0.06	107	11.18
18	1.11	48	21.07	78	0.06	108	3.91
19	3.43	49	19.80	79	0.22	109	3.82
20	4.71	50	19.12	80	0.26	110	0.02
21	0.01	51	42.04	81	0.04	111	6.93
22	0.01	52	2.78	82	0.02	112	51.06
23	0.02	53	2.04	83	0.03	113	0.34
24	0.04	54	0.00	84	0.03	114	0.06
25	0.05	55	0.01	85	2.34	115	0.01
26	0.01	56	0.01	86	30.43	116	0.03
27	1.01	57	0.03	87	4.17	117	0.04
28	9.66	58	0.04	88	1.68	118	0.03
29	0.90	59	0.05	89	19.19	119	0.07
30	0.02	60	0.01	90	11.33	-	-

The nickel-based superalloy chosen to replace the M509 alloy is also an aerospace alloy used in turbine part manufacture. Chemistry of the nickel-based superalloy was verified at an independent laboratory testing facility; the results being

summarized in **Table V**. This material, like the previous, was obtained in cast form. Geometry of the starting material (**Figure 12**) was much less convenient to work with than the previous material stock, so sample preparation was more difficult. Wire electrical discharge machining (EDM) was used to cut through the material and fabricate rectangular shaped work blocks for experimental testing. Based on the geometry of the material stock it was possible to specify a block length of 101.6mm (4 inches) and height of 9.53mm (0.375 inches), but the width of the blocks was variable, between approximately two and six inches, in order to utilize as much of the stock as possible in sample preparation. Approximately 16 work blocks could be fabricated from each bar of material stock. Alloy material left over after cutting the work blocks was used to make specimens (standard metallurgical preparation) for microstructure analysis and determination of X-ray signature. The stock has a cellular microstructure (**Figure 13**) typical of cast material, with a second phase (script morphology) present, both of which were examined using an energy dispersive spectroscopy (EDS) system at 20 KeV to determine which elements (excluding tungsten) were present in the matrix and secondary phase (**Figure 14**).

Table V: Bulk elemental composition of GTD-222 alloy used in the experiment.

ELEMENT	WEIGHT PERCENT
Chromium	22.43%
Cobalt	19.50%
Titanium	2.48%
Tungsten	1.98%
Aluminum	1.11%
Niobium	0.79%
Tantalum	0.35%
Nickel	Balance

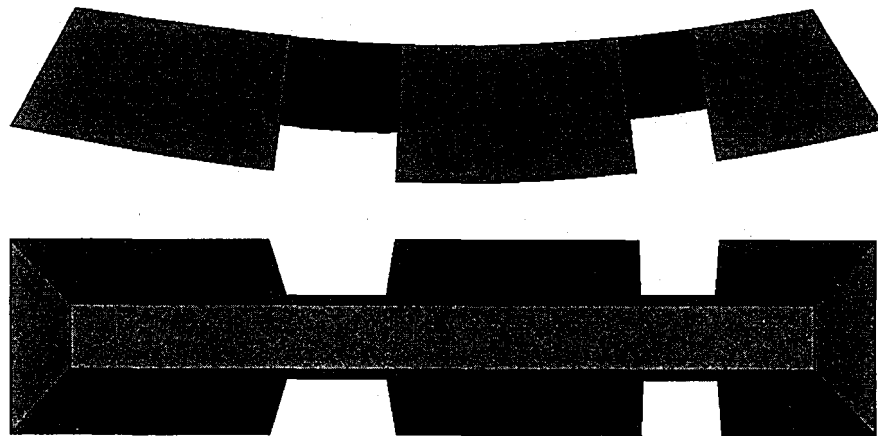


Figure 12: Schematic (two viewing angles) of GTD-222 material stock geometry.

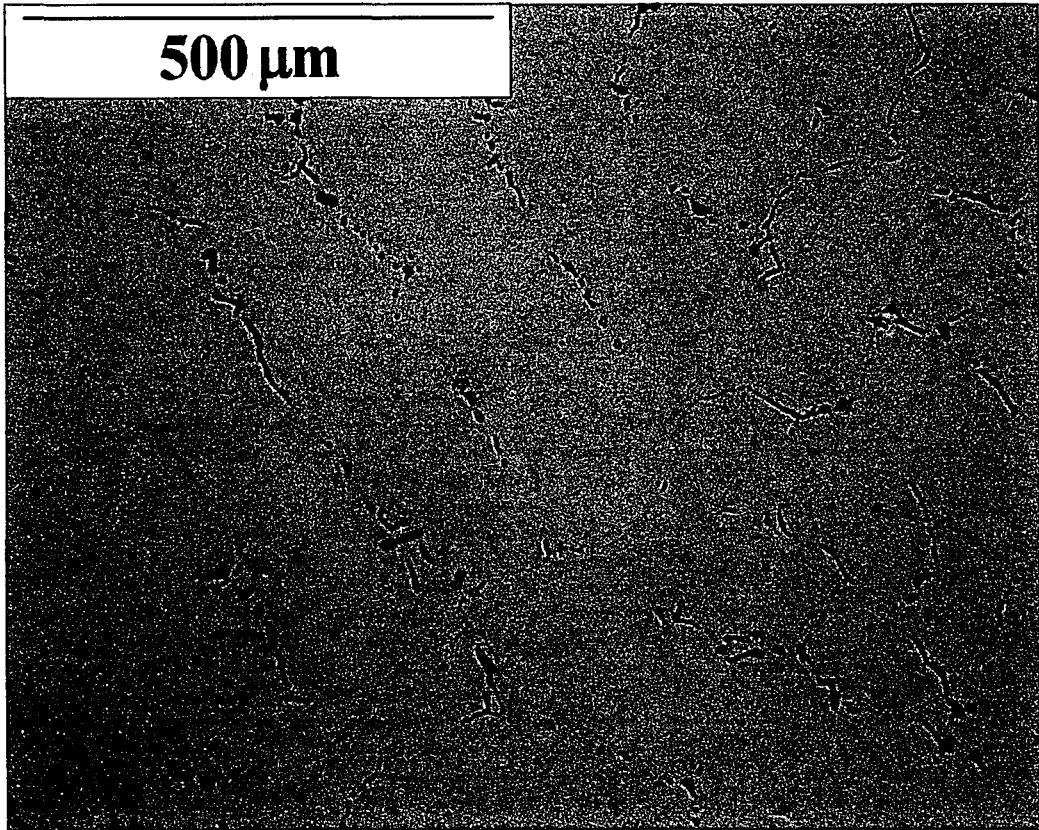


Figure 13: Light optical micrograph of the GTD-222 alloy, showing a cellular morphology typical in castings.

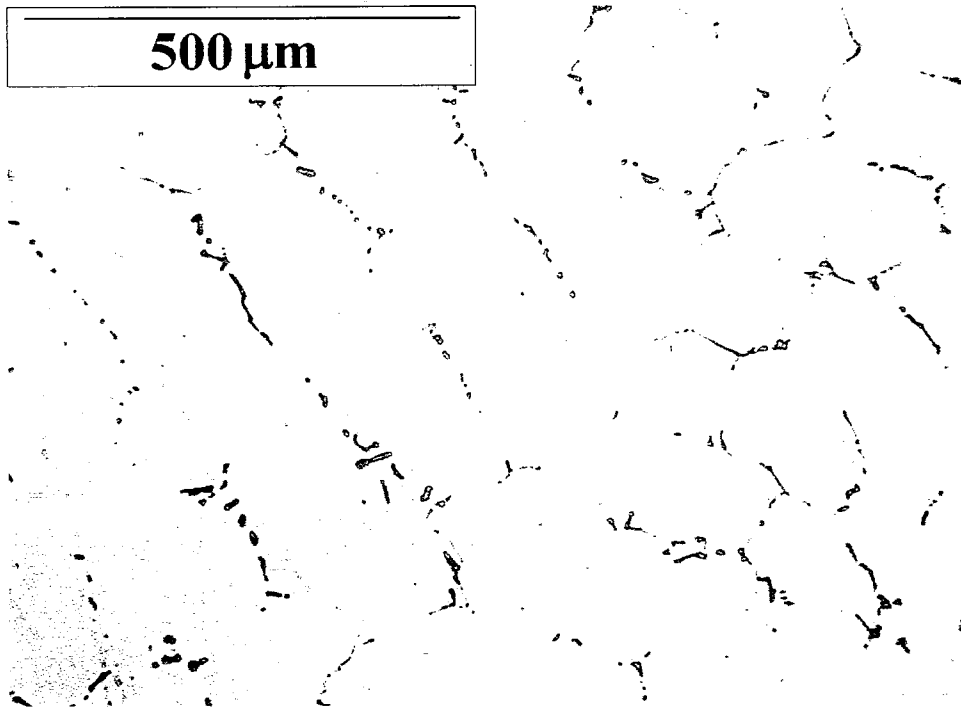
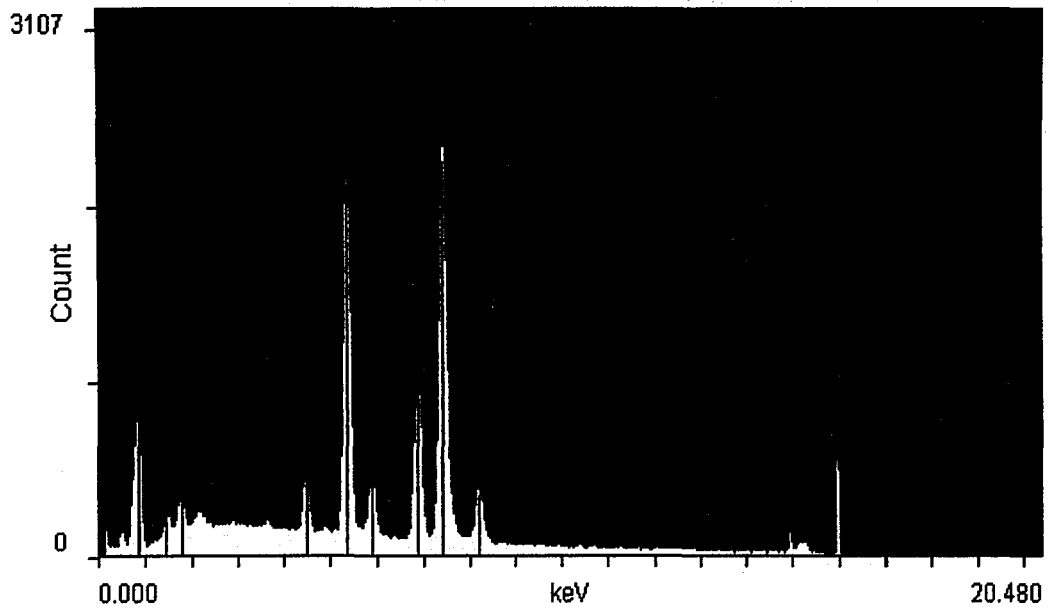
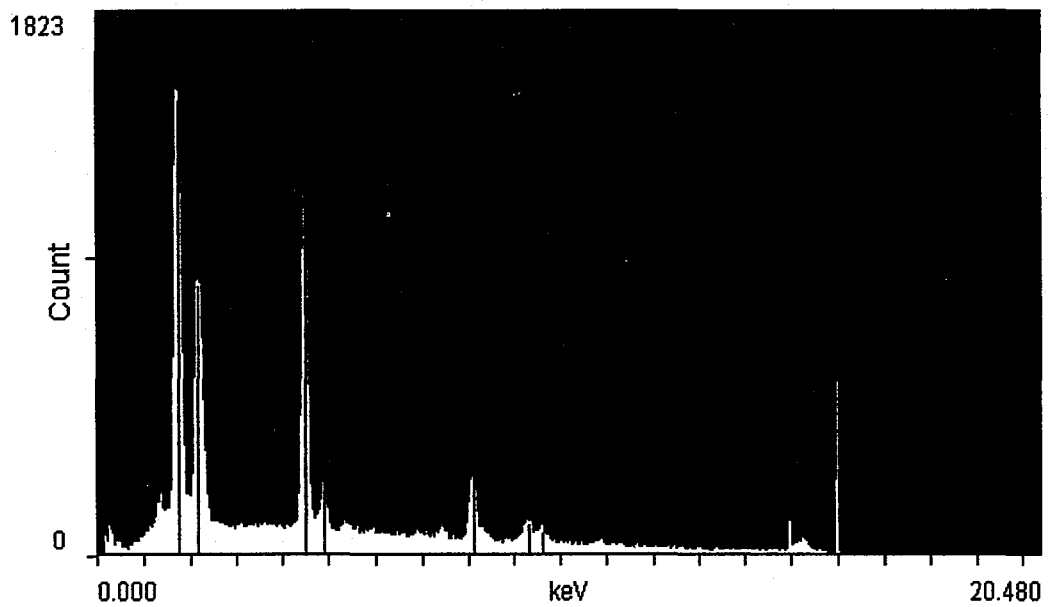


Figure 13: Light optical micrograph of the GTD-222 alloy, showing a cellular morphology typical in castings.

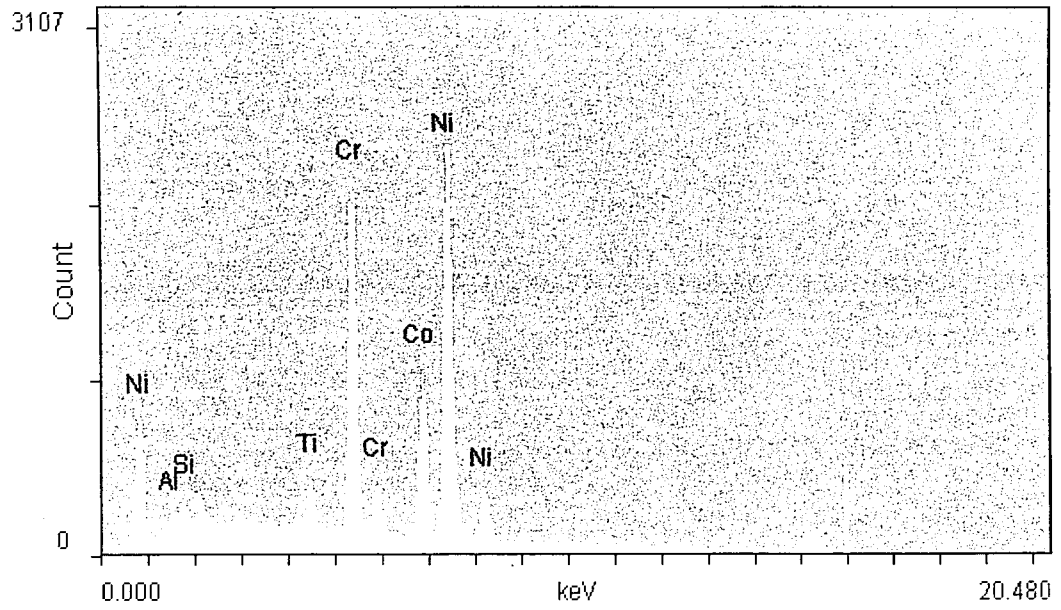


(a)

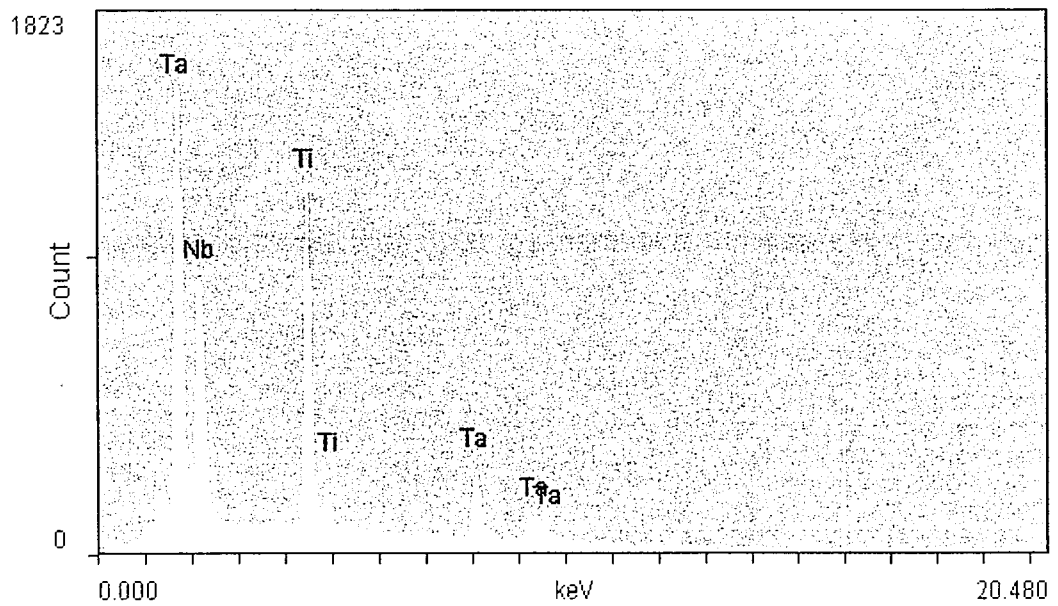


(b)

Figure 14: EDS plots for the GTD-222 alloy's (a) matrix and (b) secondary phase. (Acc. Voltage: 20 KeV)



(a)



(b)

Figure 14: EDS plots for the GTD-222 alloy's (a) matrix and (b) secondary phase. (Acc. Voltage: 20 KeV)

3.4 Grinding System:

Grinding was completed using a Brown & Sharp 618 Micromaster Surface Grinding Machine. The original machine design was improved with the use of rubber floor pads to reduce harmonic vibrations and chatter, and outfitted with a custom built enclosure (Figure 15) to contain fluid mist and grinding swarf. The experimental test blocks of the Ni-base superalloy were mounted directly onto a three-axis Kistler dynamometer (type 9257a). A Velmex NF90 Series motorized feed table was integrated into the grinding assembly to allow external digital control of the operation. The feed table served as the support structure for the dynamometer and work block. Signals from the dynamometer were sent through a charge amplifier before being collected by a data acquisition system. A schematic of the internal assembly and data collection system is shown in Figure 16.

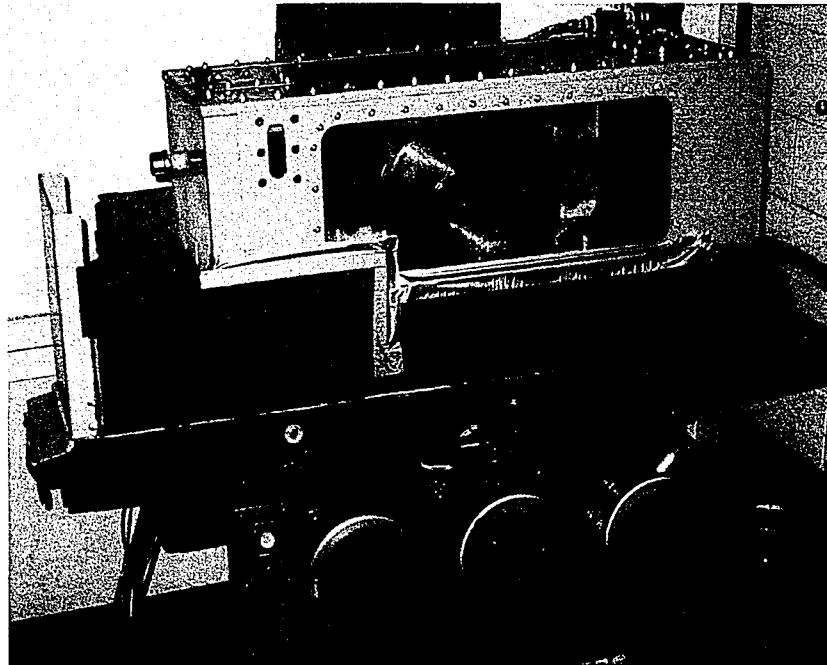


Figure 15: Brown & Sharp 618 Micromaster Surface Grinding Machine with enclosure to contain mist and debris generated during laboratory tests.

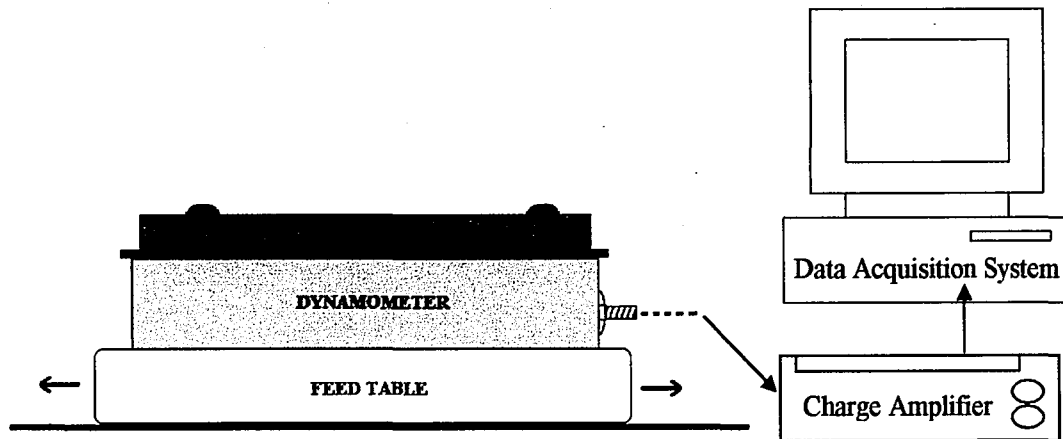


Figure 16: Illustration of internal assembly and force data collection system.

Variations in block width related to the initial stock material geometry did not allow a consistent mechanism to be used to secure work blocks to the dynamometer. Pieces were secured using either a clamping system on both edges of the block (smaller width pieces) or direct screw mounts through the work piece into the dynamometer face (larger width pieces). The clamps or screws that secured the work piece to the dynamometer restricted the width of actual grinding surface that could be utilized in testing. The 12.7mm (0.5") wide grinding wheel hub had to be safely aligned so that it would not impinge on the clamps or screws mounted on either side during testing.

Three electroplated CBN grinding wheels were tested for each fluid to evaluate its performance in terms of tool life. Grinding was completed in the upgrinding mode (feed direction opposite to wheel rotation) for all tests, with a conventional layout used for the fluid delivery nozzle and scrubber nozzle, see **Figure 17**. Grinding passes were completed on each work block until either the grinding wheel failed or the test block had to be replaced to continue testing.

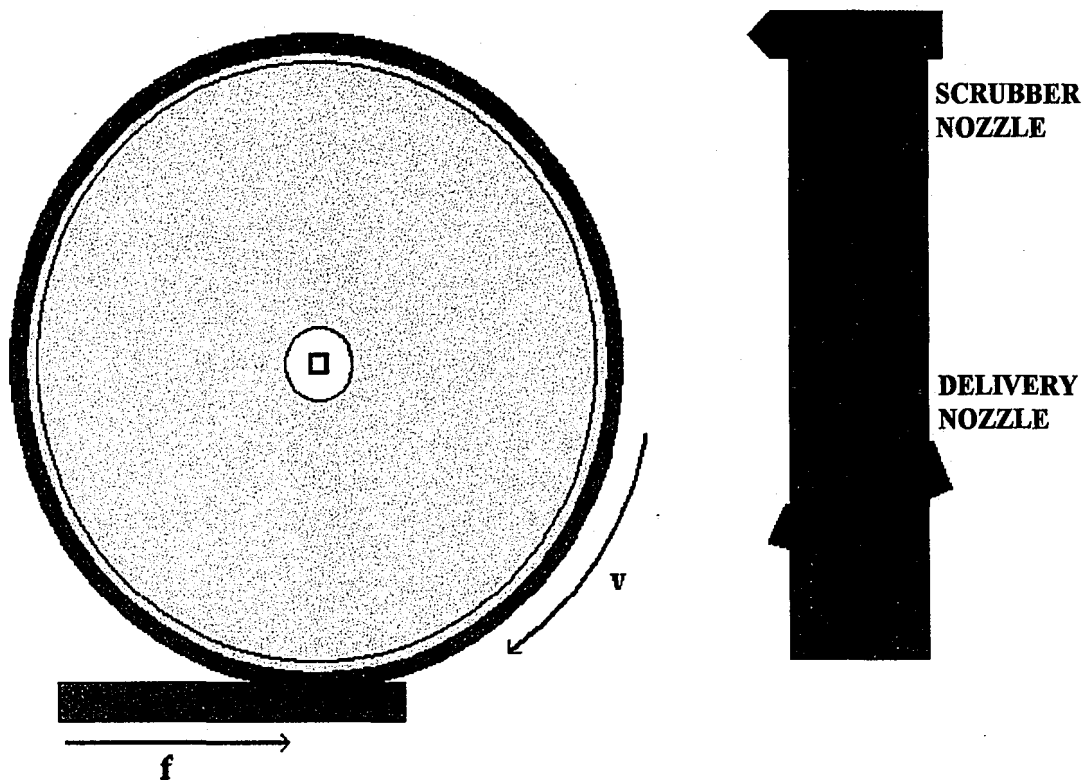


Figure 17: Illustration of upgrinding (feed and wheel rotation are in opposite directions) and layout of fluid delivery system.

As mentioned previously, the failure condition was reached when the grinding wheel stalled (seized itself in the work block) during cutting. Use of an anti-friction bearing-type spindle with an Oriflex Drive allowed the spindle to stall during the grind without damaging the 1.12 kW (1.5 hp) motor. Impedance to wheel rotation increased as the wheel became loaded with adherent material to the point of seizure in the work block. Grinding wheel life was the benchmark of fluid performance and was gauged by the total length the wheel was able to grind before failure.

Grinding passes were made along the surface of the work by using a feed table to traverse the work block past the rotating grinding wheel held in fixed position on the machine's armature. The wheel was set to the base height (zeroed) by traversing

the work block past the grinding wheel while simultaneously lowering the rotating wheel until it just began to grind a track along the top surface of the piece. Once the fluid was properly mixed, the work block secured, and the base height set, the grinding tests were run according to the system parameters listed in **Table VI** until the wheel failed.

Table VI: System parameters used in the experimental trials.

GRINDING SYSTEM PARAMETERS	
Grinding Wheel	Electroplated CBN, 120 grit, ABX2 bond
Grinding Machine	Brown & Sharp 618 Micromaster Surface Grinding Machine
Spindle Speed	3056 rpm
Cutting Speed	8000 SFM (1600 m/s)
Feed Rate	4 in./min. (1.69 m/s)
Grinding Pass Length	4 inches (10.16 cm)
Depth of Cut	0.04 inches (1.02 mm)
Maximum Metal Removal Rate (MRR)	0.0081 in. ³ /min. (0.0022 cm ³ /s)
Fluid Volume	200 gallons (757.1 L)
Fluid Flow Rate	22 gal./min. (83.3 L/min)
Delivery Pressure	400 psi (2.76 MPa)

3.5 Power Measurements:

Power being drawn by the grinding machine during testing was measured using a Monitech Systems Power Monitor (Model PPC-1). This device was capable of displaying the power readings in a digital display window and showing the percent load on the motor with a metered dial. Power measurements in horsepower units were manually recorded from the digital display window every six seconds for 90 seconds during a grinding test. The measurement time allotted was sufficient to capture the baseline power drawn from the motor at idle, as well as its engagement cycle in the work piece. Six second intervals were chosen so that recording could be managed accurately by the testing operator with sufficient attention to the other emergency motor controls during each pass. Sensitivity of the equipment was limited to 74.6 W (0.1 hp), so readings were only accurate to within +/- 37.3 W (0.05 hp). Small oscillations in power consumption were present due to the dynamic nature of the grinding operation. Peak emphasis and a maximum time delay were employed by the measuring equipment to reduce fluctuations in the measurements and provide stable values for recording. Power measurements are used in industry to gauge tool wear and as criterion for tool replacement. In this research experiment they were used to correlate with wheel performance and estimate the approach of wheel failure.

3.6 Force Measurements:

Forces in three orthogonal directions (x, y, and z) were measured over three separate channels by a Kistler dynamometer (type 9257a) to which each work block was secured. The y-direction measurements corresponded to the cutting force

(tangential force), the z-direction measurements corresponded to the thrust force (normal force), and the x-direction measurements acted as the trigger for the acquisition software to begin collecting data. A software program written in BASIC programming code and developed earlier for drill-tap torque measurements was modified to collect the force data. Initialization of the program was possible only from a DOS-based operating system, so an IBM compatible computer (8088 processor) was used for acquisition and storage of the files. Measurements were taken nine times a second, the maximum sampling rate the acquisition software would allow, for a total measurement time of 110 seconds. Measurement time was limited by the memory capacity of the computer, such that longer sampling times would crash the software. The measurement time of 110 seconds was the largest sampling time possible, and was deemed to be long enough to acquire data prior to, during, and after the grinding wheel's engagement in the work block. This ensured a baseline measurement with nominal fluctuations in the force readings (due to fluid spray and machine vibrations) was obtained both before and after the grinding pass.

The system was calibrated in the z-direction using static weights to determine the calibration factor required by the software to convert the voltage signal to units of force in lb.-force units. Spring-scales were used in the y-direction to ensure the calibration factor determined for the z-direction was accurately converting the signal to lb-force in the y-direction as well. The resolution of the force data measurements is 0.565 N (0.127 lb).

Differences in absolute time were nominal between when the acquisition software and feed table were initialized, as two operators were running the testing and

simultaneously activated each respective operation. Odd geometries of the work pieces, however, caused slight changes in the orientation and location of how each block was fixtured to the dynamometer. These variations created force plots for each sample that had different time values for when the wheel engaged and exited the work piece within the 110-second measurement time frame. Time values for the entry and exit point, (corresponding to the measurement bounds used to calculate the average tangential and normal force) were therefore manually determined by analysis of each graphical force plot, both tangential and normal force, for each grinding pass.

3.7 Collection of Grinding Swarf:

Fluid delivered to the grinding zone and sprayed on the surface of the grinding wheel by the scrubber nozzle carried the grinding chips out of the grinding chamber. The fluid runoff from the grinding table was therefore channeled through a 5-micron filter bag to capture these chips from each grinding test. Filter bags were changed with each new grinding wheel or change of work piece (whichever was first), so that multiple grinding swarf samples were collected for each fluid trial. Chip deposits and abrasive grains removed from the grinding wheel were also collected in the filter bags. After testing was completed, these bags were removed and allowed to dry, subsequently being cut and examined at higher magnification with an optical stereoscope. The swarf contained within the filter cloth was also utilized in making samples for SEM analysis.

3.8 Profilometer Measurements:

After the testing was completed, and the work blocks were removed from the system, an optical profilometer was used to characterize the surface roughness within the grooves and measure the system control over the depth of cut. Surface scans of each block were completed using a Micromesure CHR-150 Optical Profilometer System. This system utilizes white light and an optical sensor to obtain measurements of height (based on the wavelength that is in focus) to create a two-dimensional grid of points representing different elevations, hence the generation of a three-dimensional surface map. Surface maps generated for this research project were accomplished using a probe with a 10mm depth of field and a light frequency of 300 Hz. This probe has a z-axis resolution of 300nm and a lateral resolution of 25 μ m. Points on the grid were spaced 5 μ m apart in the x- and y-direction.

Profile traces along the length of the grooves were used to characterize the extent of spindle deflection during the grinding pass. Profile traces perpendicular to the groove direction were used to determine the maximum and mean groove depth for each pass; hence the system control over depth of cut for a given work block and between fluid trials could be ascertained. Analysis of each surface scan was accomplished using the software package (Mountains Universal Software, v3.0.8) accompanying the profilometer system.

3.9 Analytical Techniques:

Determining the mechanism for adhesion of ground material to the grinding wheel surface was one of the primary goals of the research project. Analysis of both

the grinding wheel surface and the grinding swarf obtained from each experimental trial was accomplished using both scanning electron microscopy and light optical microscopy. These analytical tools were used to characterize the exterior and interior morphology of the deposits, the integrity of the wheel surface, the extent of wear of the abrasive grains and matrix bond, and the nature of adhesion between the deposit and wheel surface. Visual observations of the wheel surface using an optical stereoscope accompanied the other analyses, and aided in sample preparation of both grinding chips for SEM investigation and grinding wheel sections for LOM study.

3.10 Stereoscope Observations:

An Olympus SZH10 Research Stereoscope was used to observe the surface of each grinding wheel at higher magnification prior to sectioning for sample preparation. Wheels were placed on a fixed spindle and rotated under the stereoscope to examine the external morphology of the material deposited on the grinding nib. The filter bags used to capture grinding swarf were cut open and its contents initially inspected using the stereoscope. Work blocks were also examined for visible surface damage or other irregularities visible with the stereoscope. Notes were taken on all observations, while images from the stereoscope were recorded using a Nikon Coolpix 995 Digital Camera.

3.11 Grinding Wheel Specimens:

Specimens were prepared for both SEM analysis and LOM analysis. Sectioning of the grinding wheels was completed by using a band saw to cut through the exterior nib and cut directly through to the interior bore in the wheel hub. Two

cuts were made in the wheel like this to remove approximately a 1/4 pie slice. Pie slices were removed from one grinding wheel from each fluid set, as well as one new, un-used grinding wheel which was used as a reference. The steel hub was subsequently cut away to create self-supporting samples that could be set inside the SEM chamber and analyzed from the top or at an angle. Additional cuts were made to some of these specimens to remove more of the steel hub so that only the grinding nib remained. This nib was then set into an epoxy mount and metallographically prepared using special diamond grinding wheel plates and polishing wheels to grind through the side of the CBN nib and create a flat surface. These cross-sectioned samples were analyzed using LOM to reveal the interior morphology of the wheel deposits.

3.12 Grinding Chip Specimens:

Specimens were also created to analyze the morphology of the grinding chips. Carbon tape was applied to standard SEM stubs to provide a surface that the grinding chips would adhere to. This stub was gently pressed into the inside of the filter bags in random locations to collect the chips. Stubs with grinding chips were prepared in this manner for each fluid. Each individual chip was first confirmed to be from the GTD-222 alloy before taking images by comparing it to the X-ray signature of the material stock. This eliminated the possibility of contaminant grinding chips being included in the study.

3.13 CBN Control Crystal Specimens:

Control CBN crystals (80/100 grit) from General Electric Superabrasives were also examined with the SEM. These samples were used as a reference for the starting morphology of abrasive grits prior to wheel manufacture and/or machining operations. Copper tape was applied to standard SEM stubs to provide a tacky surface (more so than carbon tape) that the CBN control crystals would adhere to. The non-conducting CBN crystals and the thick layer of adhesive glue on the copper tape were problematic for SEM analysis. A thin layer of carbon was coated onto these samples to reduce the charging effect. Combining the carbon coating with a reduction in accelerating voltage and spot size allowed imaging of these particles to be accomplished with good resolution.

4.0 RESULTS:

4.1 Performance Evaluation:

Three electroplated CBN grinding wheels were tested for each fluid in the baseline study. Grinding tests were run until the grinding wheel failed and stalled in the work block. After wheel failure was reached, the grinding wheel, work block, and 5 μ m filter bag were removed from the system and labeled for later study. Three different water-based fluid trials (Water-based A, Water-based B, and Water-based C) were run in succession before any analysis of the grinding wheels, work blocks, or grinding swarf was completed. Testing of the Oil Baseline fluid (petroleum oil) began two months afterwards, while analysis of the materials from the previous testing was underway.

Length of grind before failure was the metric used to gauge tool life for the electroplated CBN grinding wheels. Determining a G-ratio (ratio of volume of work material removed to volume of wheel material worn away) for electroplated grinding wheels was not practical. The single layer of abrasive grains on the wheel surface acted as permanent tools when compared to other wheel types with bond materials that wear away and expose fresh grains. With the machining parameters remaining constant between fluid trials, the grind length was determined to be an accurate measure of tool life for the specific operating conditions utilized in the experiment. These tool life values would not be absolute, but could be compared relatively among the different fluids used in the experiment to provide a performance indicator for CBN groove grinding of nickel-based superalloys with each fluid.

4.2 Water-based Fluid Trials:

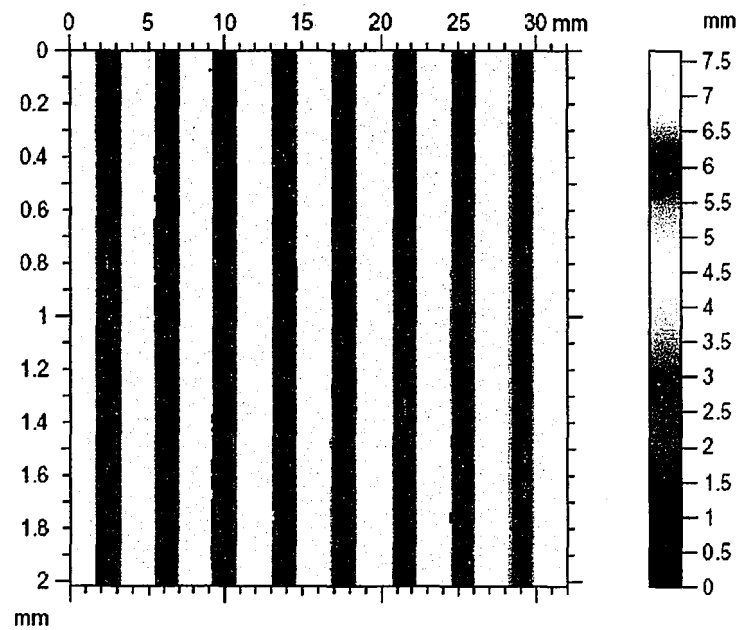
The length of each grinding pass was measured and tallied to give the total grind length of that wheel for the specific fluid. The results of the water-based fluid trials can be seen below in **Table VII**. Clearly, the data shows considerable deviation in grind length for a given fluid trial, even when the accepted 10% variation in wheel life due to manufacturing discrepancies between wheels is taken into account. From this data, it seems the trials are not consistent and do not provide any indication of differences in operating performance for the different fluids.

Table VII: Grind length for each wheel tested in the water-base fluid trials.

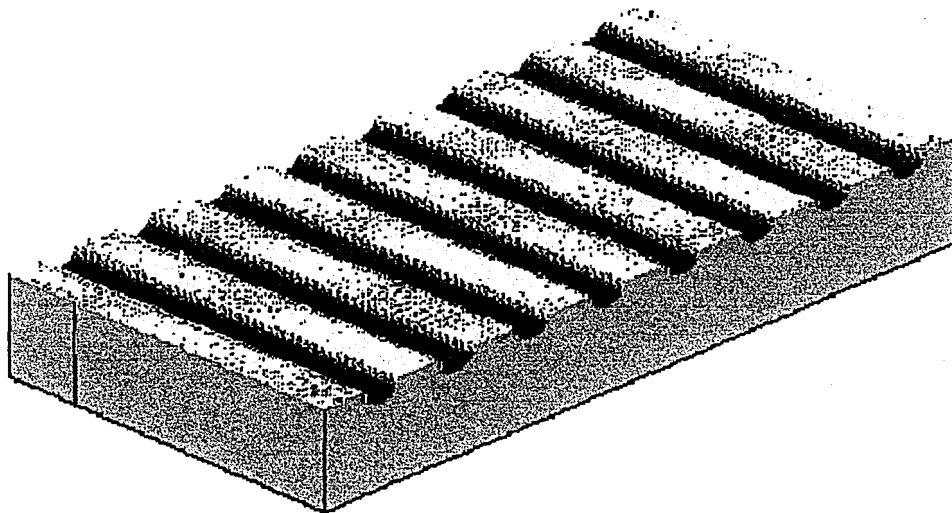
TESTING DESIGNATION	GRIND LENGTH (mm)
Water-based A – Wheel 1	380
Water-based A – Wheel 2	705
Water-based A – Wheel 3	835
Water-based B – Wheel 1	581
Water-based B – Wheel 2	575
Water-based B – Wheel 3	455
Water-based C – Wheel 1	457
Water-based C – Wheel 2	493
Water-based C – Wheel 3	777

4.3 Profilometer Analysis:

In order to understand the differences in grind length for a given fluid, it was necessary to verify the control over the system parameters maintained during the experimental trials. To that end, surface scans were completed using an optical profilometer system to measure the depth of cut for a given block and compare the actual values between all the grinding wheels tested. Initial measurements indicated significant differences in depth of cut existed between different grinding wheels.



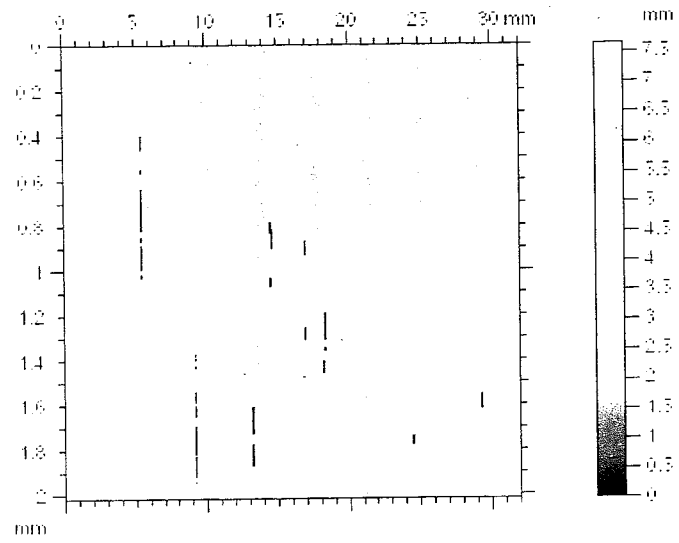
(a)



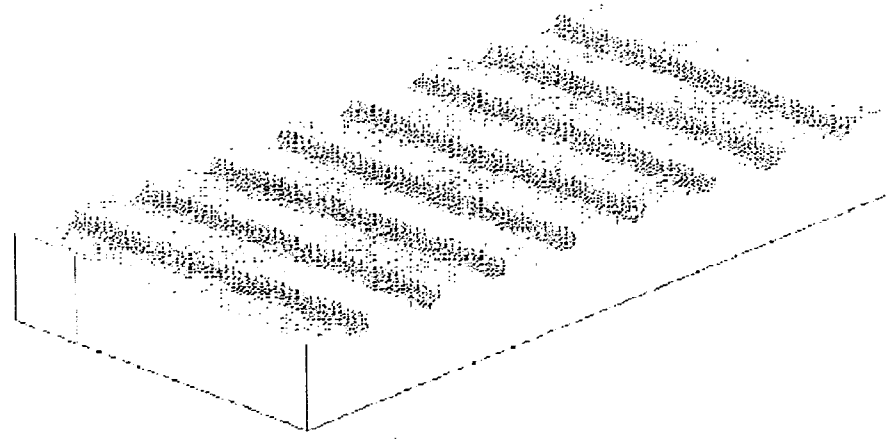
(b)

Figure 18: Two dimensional grid of measured points and the corresponding three dimensional image obtained from the optical profilometer scan. The sample scanned in this figure is the block machined by Wheel #3 using Water-based A.

An example of the grid of points developed from a surface scan and its corresponding three-dimensional image is shown in **Figure 18**. The two-dimensional



(a)



(b)

Figure 18: Two dimensional grid of measured points and the corresponding three dimensional image obtained from the optical profilometer scan. The sample scanned in this figure is the block machined by Wheel #3 using Water-based A.

An example of the grid of points developed from a surface scan and its corresponding three-dimensional image is shown in **Figure 18**. The two-dimensional

array of points is really a rectangular grid scan compressed into a square shape, as can be seen from the length scale markings along the top and left side of the scan. Height values for each point are assigned according to the chromatic scale, with zero being the bottom point of focus for the 10mm probe. Regions of black coloration in this particular scan, corresponding to zero on the chromatic scale, are not holes in the sample, but rather are “dropped points”. These points were not read correctly by the optical probe, and are assigned a value that is outside the range of focus for the probe.

Profile traces along the length of the grooves showed considerable fluctuations in the depth of cut. An example of these fluctuations is displayed in **Figure 19**. Fine scale fluctuations in the profile made it difficult to determine the average value for depth of cut for a given point along the length of the groove. If the cut depth was evaluated at the points marked in red circles, a difference of 0.5mm in depth of cut would be observed. This irregularity, presumed to be related to spindle deflection, had to be accounted for when determining the actual groove depth.

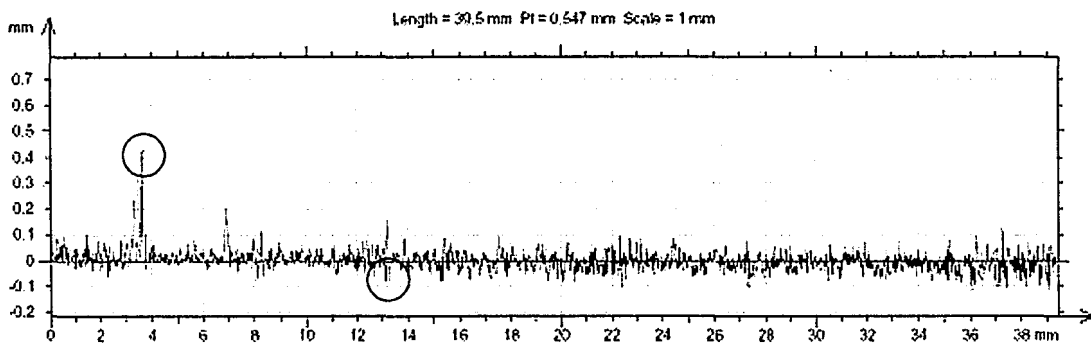


Figure 19: Profile trace along the center of the fifth groove cut by Wheel #2, Water-based A, showing fine scale fluctuations in elevation along its length.

Preliminary scans indicated that the depth of cut varied along the groove, between grinding passes, and between work blocks. A system of analyzing these

samples was developed to measure and characterize these variations. Scans of the beginning (entry side) and end (exit side) of each work block were completed to assess the change in depth both parallel and perpendicular to the grooves. Assuming that variation in depth of cut between the entry and exit point of the work block was linear, scans were completed at each end of the block to capture the maximum difference in cut depth for the pass. The scan grid was set to be 2mm in length at either end of the block. This grid length was deemed appropriate to account for changes in cut depth along the groove due to spindle deflection, but small enough to provide a value for cut depth representing the entry point or exit point for the particular pass.

Twenty-one profiles in each grid scan perpendicular to the groove direction, taken 0.1mm apart, were extracted for analysis of the groove depth. **Figure 20** shows one such profile scan and the computerized analysis of cut depth. The *Height Measurement* feature in the Mountains Universal Software automatically indexes the grooves, creates baseline positions on either side of the grooves for reference, and calculates the maximum depth and mean depth for each groove in the profile trace. The two valleys in grooves 3 and 5 represent dropped points during the scan. If the grooves were hemispherically smooth, the maximum depth would be the ideal value to use for analysis. The maximum depth measured by the software, however, is sensitive to dropped points or irregularities in the central region of the groove, such that the values obtained are less consistent and prone to error. Mean depth provides a measurement that averages the irregular points and surface roughness into the

calculation. These measurements are less sensitive to surface abnormalities, and so were used for cut depth analysis instead.

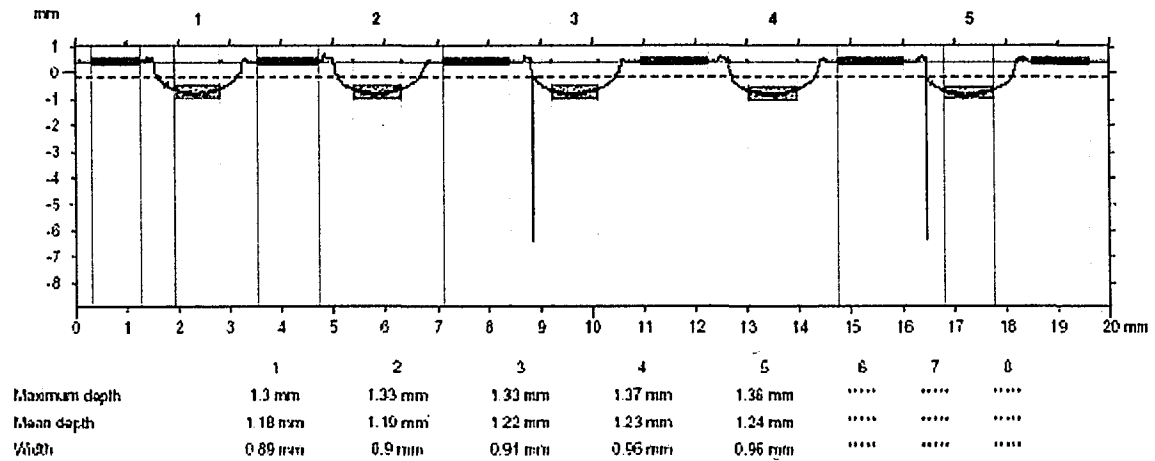


Figure 20: Perpendicular profile trace and computerized measurements of cut depth for the beginning of the work block ground by Wheel #2, XR-82438.

Mean depth measurements were obtained for the beginning and end of each work block that was part of the experimental trials. The twenty-one mean depth measurements from each grid were averaged together to provide one value for the groove depth at either the beginning or end of the pass. In this manner, the scans and analysis were completed for all work blocks, with the data being tabulated in a spreadsheet to determine the average depth of cut for each groove and the entire work block. Groove depth was determined by averaging the measurement of depth at the beginning and end of the pass. Average work block depth was determined by taking the average of each groove depth that was completed on the work piece. Examples of the spreadsheet calculations are shown in **Tables VIII – X**. All depth of cut measurements for each groove are listed in **Table XI**, and the average depth of cut for each work block is listed in **Table XII**.

Table VIII: Mean depth measurements (mm) for the entry side of the work block for Wheel #2, Water-based A fluid.

Profile Trace	Groove 1	Groove 2	Groove 3	Groove 4	Groove 5	Groove 6	Groove 7
1	1.10	1.14	1.14	1.17	1.18	1.20	1.19
2	1.08	1.11	1.15	1.17	1.18	1.20	1.18
3	1.11	1.10	1.13	1.17	1.19	1.20	1.18
4	1.10	1.12	1.14	1.18	1.20	*	1.19
5	1.08	1.11	1.15	1.16	1.20	1.24	1.19
6	1.09	1.15	1.14	1.18	1.17	*	1.21
7	1.11	1.11	1.18	1.17	1.17	1.21	1.19
8	1.09	1.11	1.17	1.17	1.18	1.20	1.17
9	1.08	1.10	1.14	1.17	1.18	1.21	1.19
10	1.08	1.14	1.15	1.17	1.19	1.18	1.21
11	1.09	1.08	1.17	1.16	1.19	1.19	1.18
12	1.08	1.09	1.13	1.18	1.16	1.18	1.19
13	1.09	1.13	1.13	1.19	1.18	1.20	1.21
14	1.09	1.11	1.16	1.14	1.18	1.18	1.18
15	1.08	1.11	1.18	1.15	1.20	1.19	1.17
16	1.11	1.11	1.16	1.18	1.18	1.17	1.17
17	1.09	1.09	1.16	1.16	1.17	1.21	1.20
18	1.09	1.12	1.13	1.18	1.16	1.20	1.16
19	1.07	1.13	1.14	1.15	1.18	1.18	1.17
20	1.10	1.10	1.18	1.16	1.17	1.18	1.15
21	1.10	1.12	1.14	1.18	1.18	1.18	1.23
Average:	1.091	1.113	1.151	1.169	1.18	1.195	1.186

* indicates an erroneous measurement due to dropped points or surface irregularities

Table IX: Mean depth measurements (mm) for the exit side of the work block for Wheel #2, Water-based A fluid.

Profile Trace	Groove 1	Groove 2	Groove 3	Groove 4	Groove 5	Groove 6	Groove 7
1	1.21	1.30	1.26	1.27	1.24	1.27	1.20
2	1.17	1.23	1.23	1.25	1.27	1.29	1.23
3	1.21	1.25	1.23	1.27	1.28	1.26	1.19
4	1.19	1.26	1.24	1.24	1.25	1.26	1.21
5	1.18	1.20	1.22	1.27	1.27	1.28	1.22
6	1.20	1.20	1.24	1.25	1.25	1.27	1.23
7	1.20	1.21	1.22	1.28	1.25	1.29	1.20
8	1.22	1.21	1.22	1.25	1.27	1.27	1.17
9	1.20	1.22	1.23	1.24	1.27	1.24	1.17
10	1.23	1.22	1.23	1.25	1.28	1.25	1.18
11	1.18	1.20	1.20	1.26	1.28	1.28	1.19
12	1.19	1.21	1.25	1.23	1.26	1.28	1.19
13	1.21	1.21	1.23	1.26	1.28	1.27	*
14	1.19	1.20	1.23	1.25	1.27	1.29	1.23
15	1.20	1.21	1.24	1.25	1.30	1.24	*
16	1.21	1.21	1.22	1.25	1.25	1.26	1.23
17	1.19	1.20	1.24	1.27	1.24	1.26	1.21
18	1.21	1.20	1.21	1.24	1.26	1.26	1.21
19	1.17	1.19	1.24	1.25	1.26	1.25	1.18
20	1.20	1.20	1.23	1.24	1.25	1.27	1.20
21	1.20	1.20	1.23	1.25	*	1.26	1.19
Average:	1.198	1.216	1.23	1.253	1.264	1.267	1.202

* indicates an erroneous measurement due to dropped points or surface irregularities

Table X: Calculation of average cut depth (mm) for each groove and the work block for Wheel #2, Water-based A fluid.

Depth	Groove 1	Groove 2	Groove 3	Groove 4	Groove 5	Groove 6	Groove 7	Work Block
Entry	1.091	1.113	1.151	1.169	1.18	1.195	1.186	
Exit	1.198	1.216	1.23	1.253	1.264	1.267	1.202	
Average	1.145	1.164	1.191	1.211	1.222	1.231	1.194	1.194

**Table XI: Mean cut depth (mm) calculated of each groove
for all water-based fluid trials.**

Designation	Groove 1	Groove 2	Groove 3	Groove 4	Groove 5	Groove 6	Groove 7	Groove 8
Wheel 1 - Fluid A	1.267	1.271	1.271	1.292				
Wheel 2 - Fluid A	1.145	1.164	1.191	1.211	1.222	1.231	1.194	
Wheel 3 - Fluid A	1.011	1.045	1.067	1.071	1.099	1.118	1.146	1.142
Wheel 1 - Fluid B	1.200	1.193	1.211	1.225	1.243	1.27*		
Wheel 2 - Fluid B	1.175	1.208	1.243	1.268	1.310	1.314		
Wheel 3 - Fluid B	1.327	1.354	1.340	1.409	1.441			
Wheel 1 - Fluid C	1.342	1.375	1.372	1.397	1.439			
Wheel 2 - Fluid C	1.305	1.317	1.339	1.355	1.378			
Wheel 3 - Fluid C	1.146	1.167	1.188	1.238	1.249	1.272	1.293	1.23**

* Value was estimated due to errors in measuring cut depth on exit side

** Groove 8 had to be completed on a different work block, all other water-based fluid tests were finished using one work block per grinding wheel.

Table XII: Mean cut depth of each work piece for all water-based fluid trials.

Designation	Mean Cut Depth for the Block
Wheel 1 - Water-based A	1.28 mm
Wheel 2 - Water-based A	1.19 mm
Wheel 3 - Water-based A	1.09 mm
Wheel 1 - Water-based B	1.22 mm
Wheel 2 - Water-based B	1.25 mm
Wheel 3 - Water-based B	1.38 mm
Wheel 1 - Water-based C	1.39 mm
Wheel 2 - Water-based C	1.34 mm
Wheel 3 - Water-based C	1.22 mm

The mean depth measurements for all work blocks tested in the water-based fluid trials confirmed that the depth of cut parameter varied significantly between work blocks. Mean groove depths calculated at the beginning and end of the different work blocks indicated that changes in depth were not consistent. Some work blocks seemed to have similar cut depths at the entry and exit side of the block, while other blocks indicated the depth of cut increased or decreased from beginning to end. Differences in cut depth measurements between the entry side and exit side are attributed to both deflection of the spindle and variation in the mode of securing the work blocks to the dynamometer, based on the variation in work block geometry.

Analysis of the groove depth measurements listed in **Table XI** indicates that the support structure for the work blocks was off-level. Fairly consistent increases in cut depth from the initial pass to the final pass reflect this error in the experimental testing apparatus. Some final passes show a final cut depth which seems to decrease. This is an effect of the increased cutting forces causing oscillations and increased deflection in the spindle arm.

Mean cut depth values for each work block (**Table XII**) provide insight into the reason the grind length for each wheel differed for a given lubricating fluid trial. Plotting the grind length for each wheel against the average depth of cut the wheel experienced in the work block helps to explain the variations in tool life (see **Figure 21**). Differences in the average cut depth for different work blocks was attributed to the lack of precision in the method used to set the initial height of the grinding wheel.

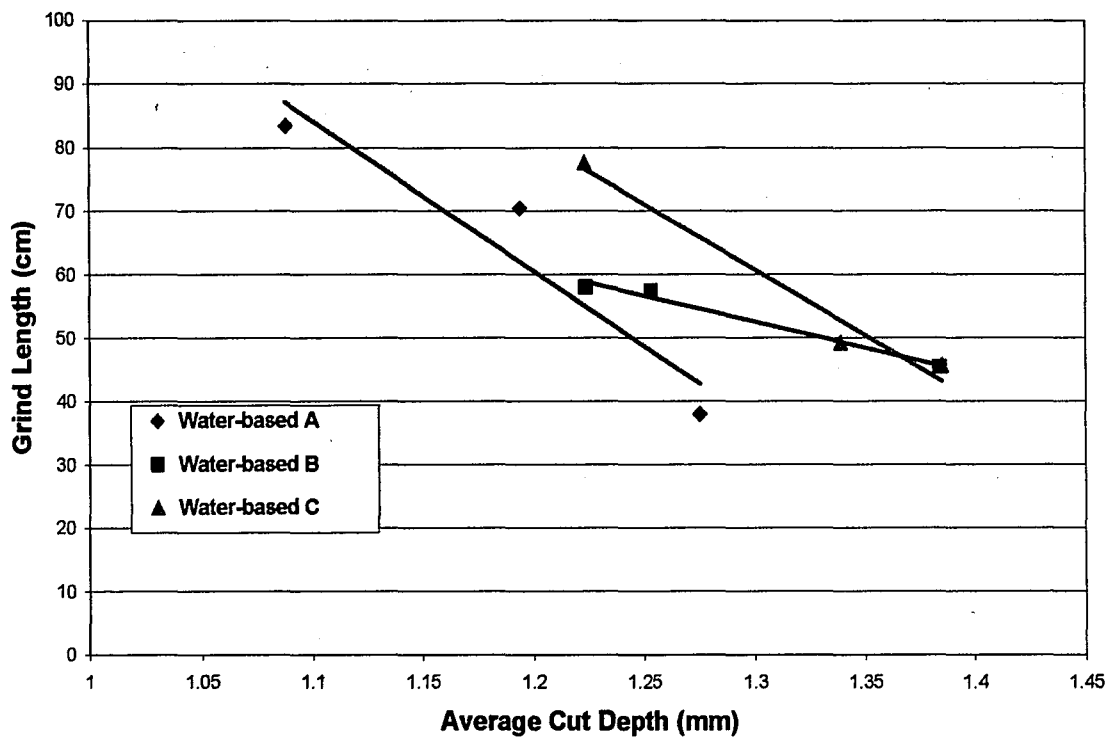


Figure 21: Plot of grind length (representing grinding wheel life) vs. the average depth of cut in the work block.

4.4 Power Measurements:

Power measurements recorded using the *Monitech Systems Power Monitor* were manually recorded during the experiment and then entered into a spreadsheet to display the power consumption trends in graphical form. Baseline power measurements during non-engagement times were omitted from the graphical displays. Power measurements from each engagement cycle were sequentially strung together to provide one graph representing the power drawn by the grinding machine throughout the life of the grinding wheel. **Figures 22 – 30** show the power measurement data collected for the water-based fluid trials.

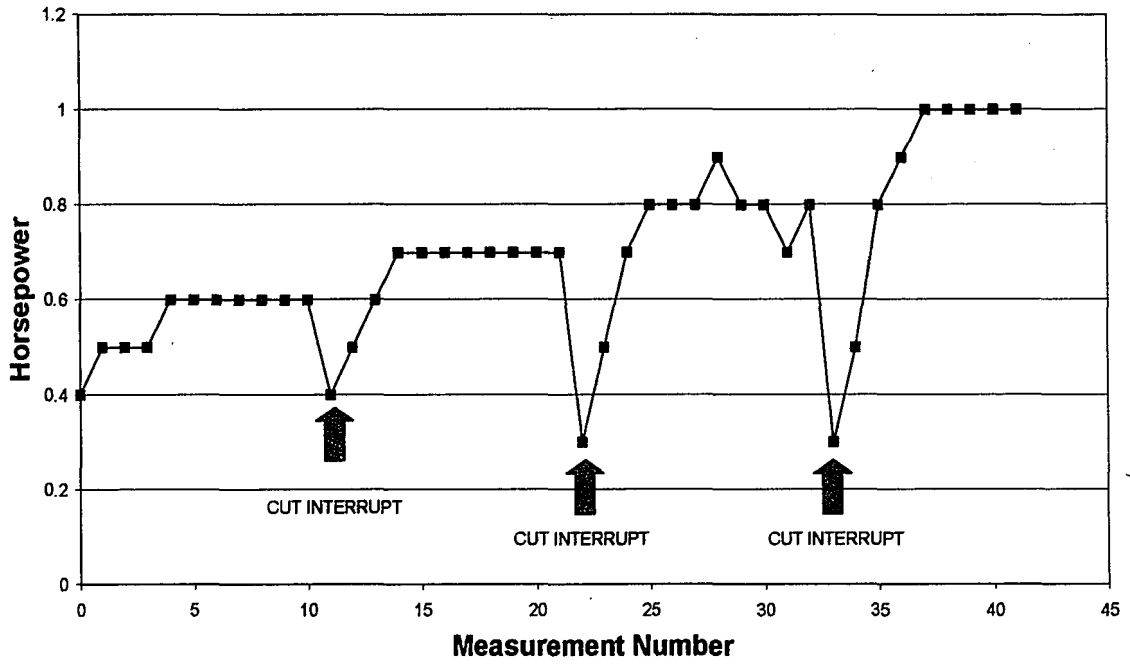


Figure 22: Power measurements for Wheel #1, Water-based A Fluid.

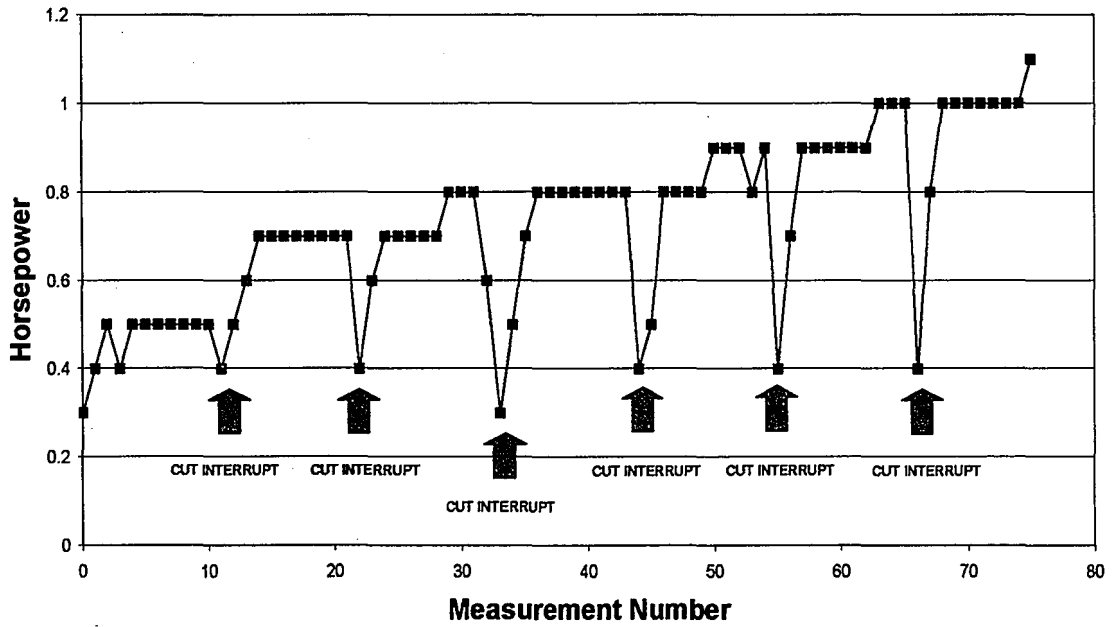


Figure 23: Power measurements for Wheel #2, Water-based A Fluid.

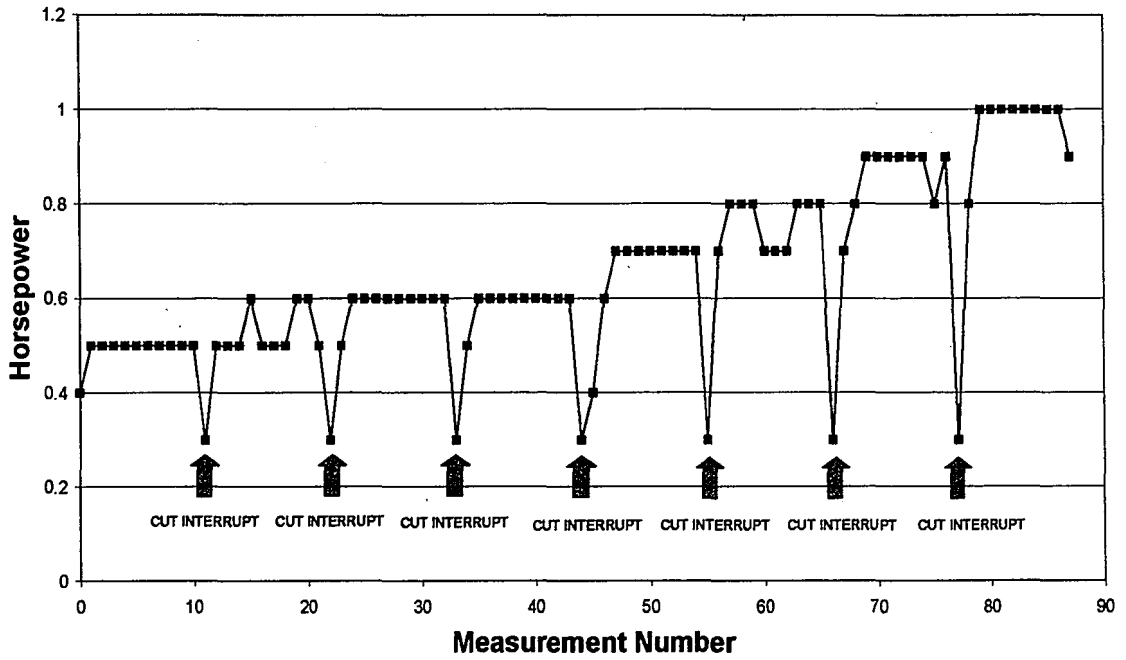


Figure 24: Power measurements for Wheel #3, Water-based A Fluid.

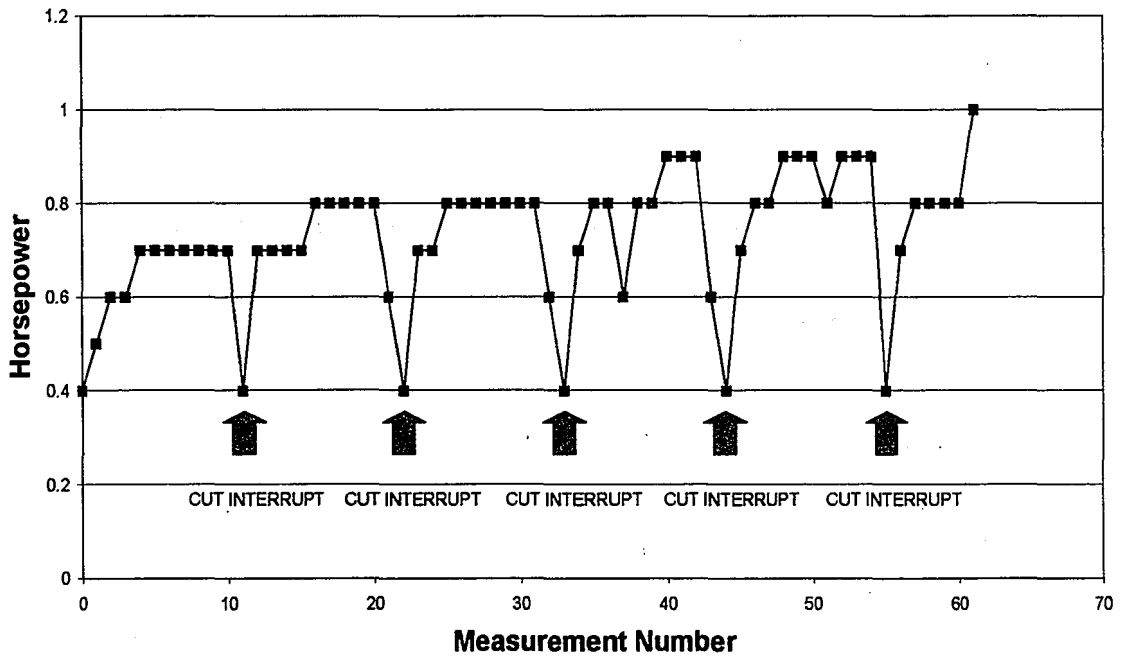


Figure 25: Power measurements for Wheel #1, Water-based B Fluid.

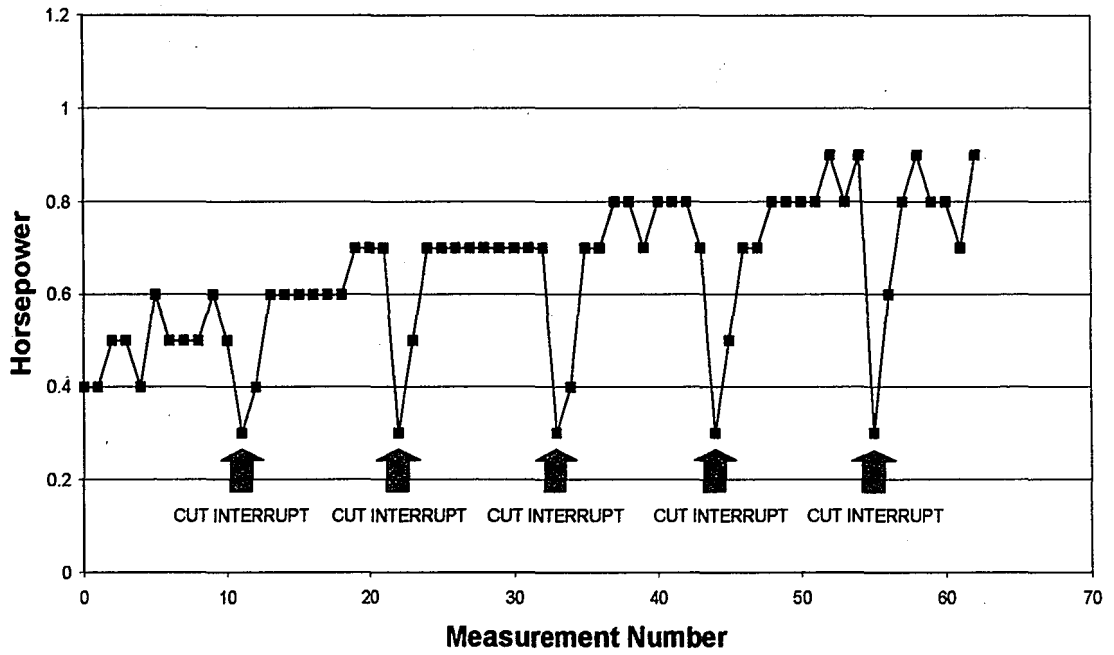


Figure 26: Power measurements for Wheel #2, Water-based B Fluid.

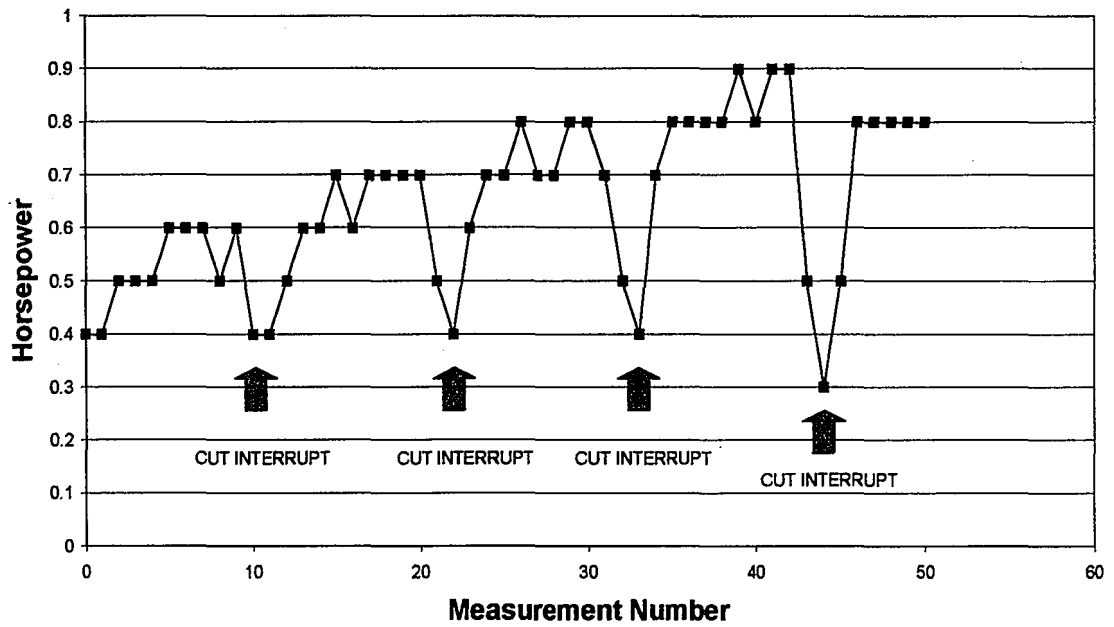


Figure 27: Power measurements for Wheel #3, Water-based B Fluid.

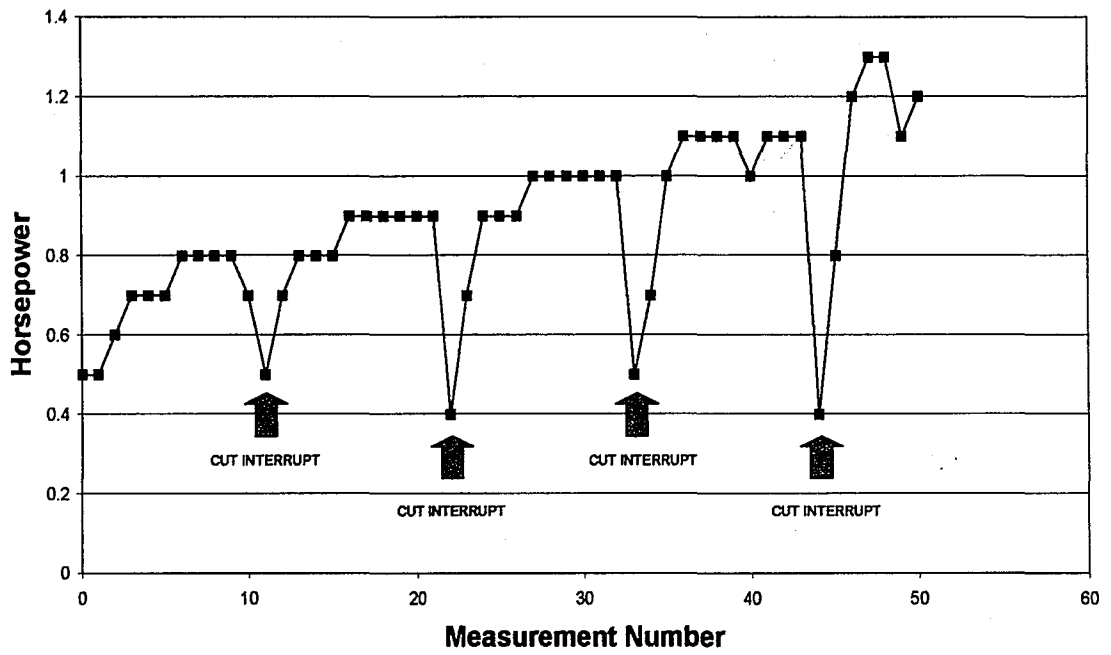


Figure 28: Power measurements for Wheel #1, Water-based C Fluid.

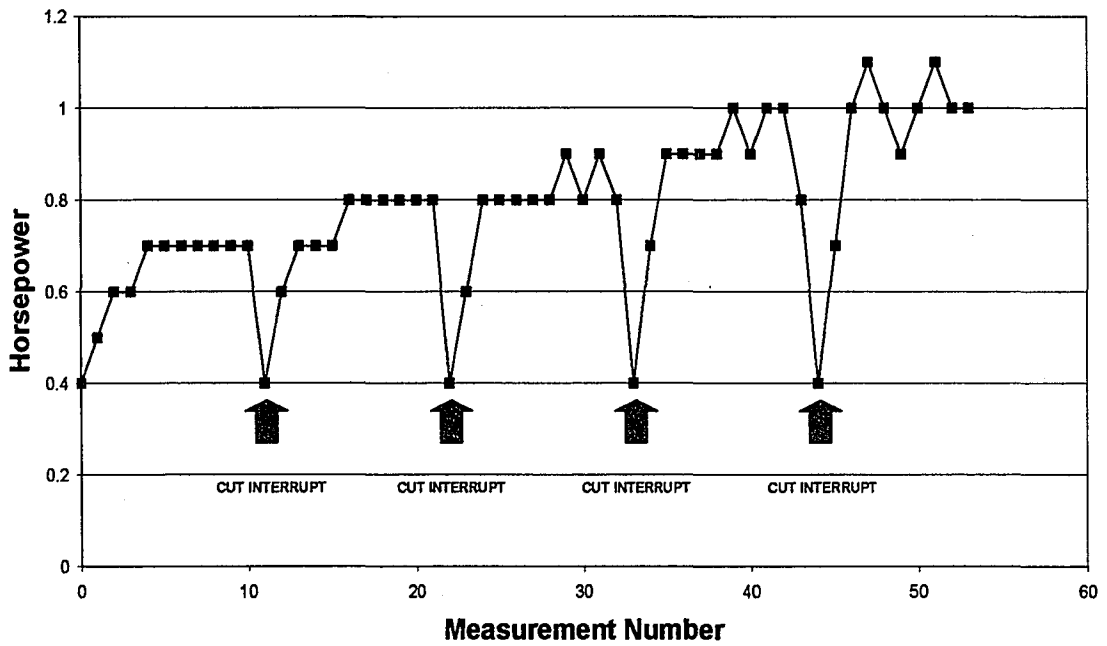


Figure 29: Power measurements for Wheel #2, Water-based C Fluid.

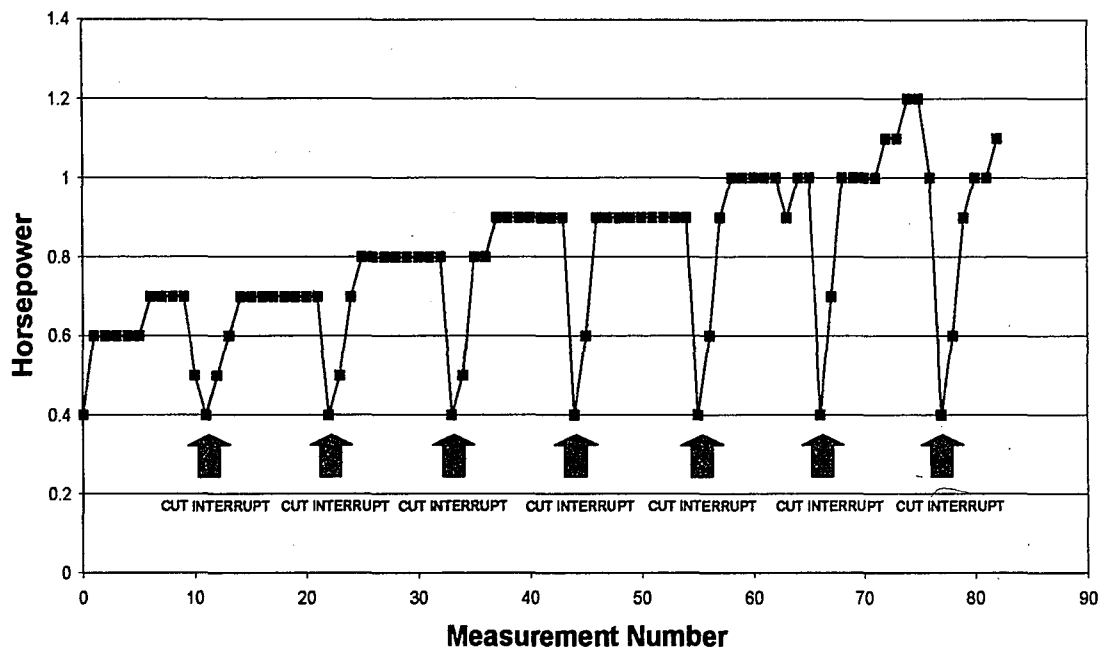


Figure 30: Power measurements for Wheel #3, Water-based C Fluid.

Each of the power graphs has several arrows marked 'cut interrupt'. These arrows serve to indicate the location of the initial non-engagement power measurement of the subsequent grinding pass. The trend in power consumption for a given pass is that it is lowest when the wheel is not engaged in the work block followed by a climb to some peak value once the wheel is fully engaged in the material. This trend repeats itself for each grinding pass, with the peak value obtained for the pass increasing steadily until failure. The last measurement recorded in each graph represents the power drawn at failure. Power measurements at failure never reach the 1.12 kW (1.5 hp) capacity of the machine due to the transmission (turning the spindle) slipping and allowing the wheel to stall in the work block without damaging the motor.

4.5 Force Measurements:

Measurements of tangential and normal forces acting on the work piece were collected with the use of a Kistler (type 9257a) piezoelectric dynamometer. Tangential forces are parallel to the feed direction and normal forces are perpendicular to the work piece surface. All signal data was collected by a data acquisition system that converted the signals to lb-force units. MATLAB software was used to remove extraneous channel information and separate the valid data into arrays corresponding to the tangential and normal force measurements. These arrays were saved as ASCII text files and imported into a spreadsheet. They were then sequentially strung together to display the trends in force (from the initial pass to failure) in graphical form.

Initial grinding trials both without fluid and with plain tap water in the fluid delivery system were completed to test the functionality and accuracy of the motorized feed table and measurement equipment. All tests had positive results, and the decision to begin testing was marked by beginning the aforementioned cleaning process to remove debris out of the system from the chamber and piping. Unexpected and unexplained errors in force data collection began after the cleaning solution entered the system prior to actual fluid trials. It is assumed that the silicone sealant used to protect the interface (inside the grinding assembly) between the dynamometer and the cables carrying the signals for the x-, y- and z-direction force measurements was damaged by the cleaning solution. All attempts to prevent or correct this interruption in signal carrying failed. Reapplication of the sealant was periodically

performed, but rapid degradation by the cleaning solution and the experimental fluids was inevitable.

Drift in the signal was therefore accepted in order to continue with the experimental fluid trials. Force data from each pass experienced this drift from the beginning to end of the sampling period. Resetting the charge amplifier after each test normalized the signal back to zero. In this way, each data set initially oscillated around zero and slowly decayed with time. In order for the data to be properly interpreted, manual corrections to each force plot (both tangential and normal force) for each groove had to be made prior to them being assembled into one master plot. An example of the graphical output that was obtained after sorting in MATLAB is shown in **Figure 31**.

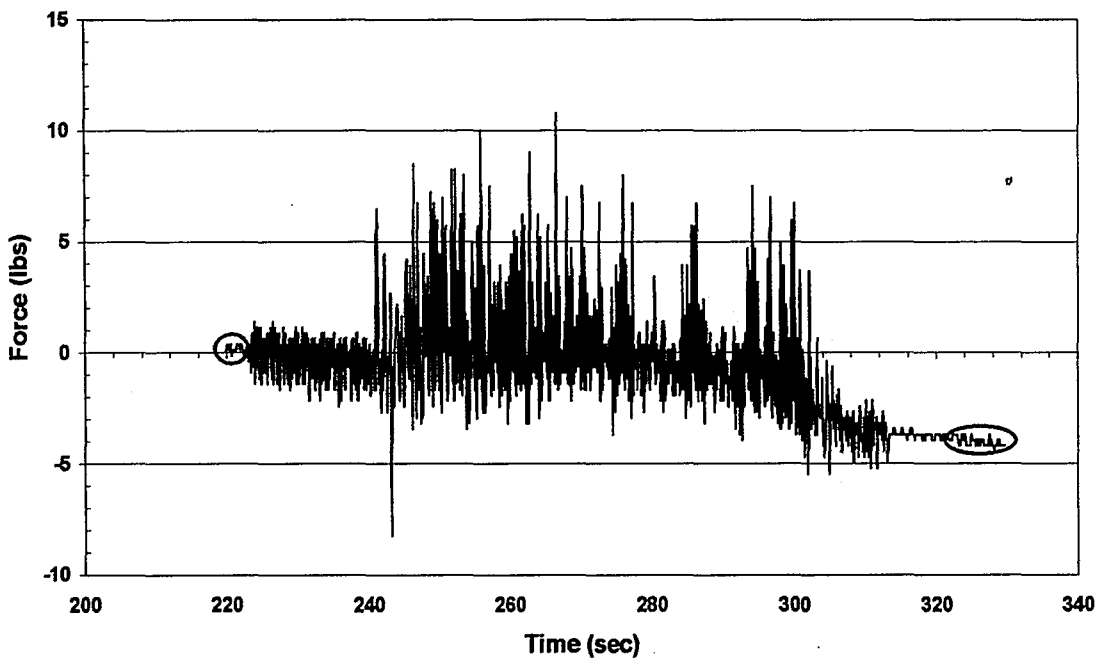


Figure 31: Graphical output of tangential force data (prior to corrections of signal drift) for Groove 3, Wheel #1, Water-based B Fluid.

The circled regions at the beginning and end of the plot are force measurements recorded when the grinding wheel was not engaged in the work block. Small oscillations in force readings are a result of harmonic vibrations in the system picked up by the dynamometer. Both regions should have oscillated around zero since the grinding wheel was no longer in contact with the work block / dynamometer fixture. Correcting the measurements for this signal drift involved interpolation of the data (with the assumption that the drift was linear) from the beginning to end of the test. Points representing the nominal force value at the beginning and end of each measurement set were determined graphically from each individual force plot. The slope between the points was calculated and incremental additions were made to the entire data set (based on the calculated slope) to normalize the data. The corrected output from Figure 31 is displayed in Figure 32. This procedure was carried out on all data sets, irrespective of the degree of signal drift.

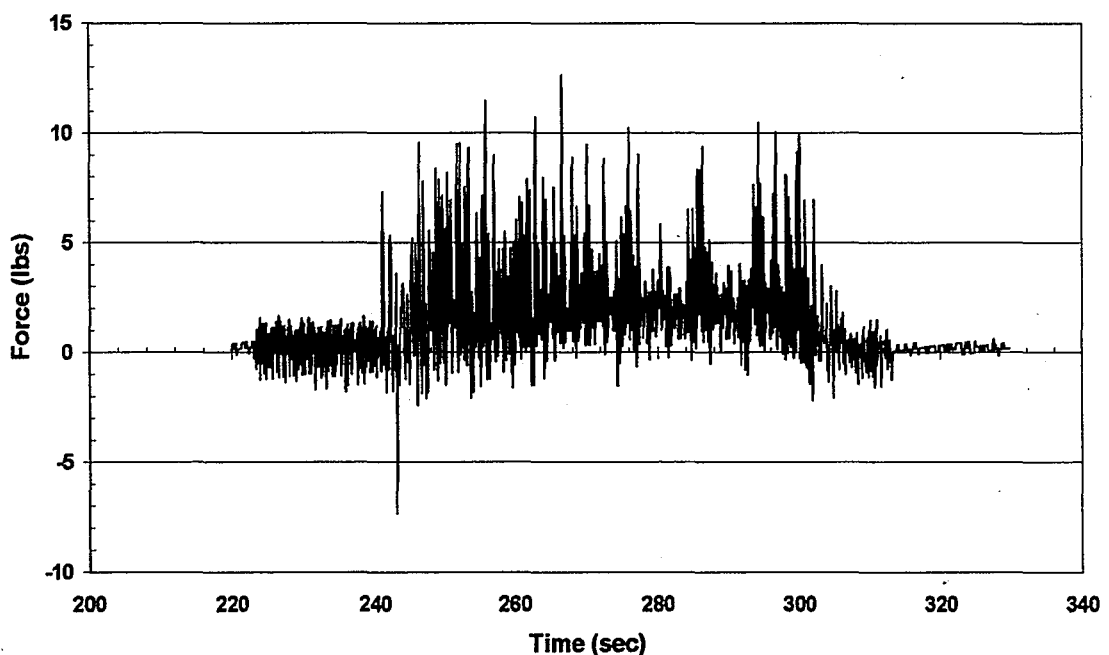


Figure 32: Graphical output of corrected tangential force data for Groove 3, Wheel #1, Water-based B Fluid.

After corrections were made, the individual data sets were strung together to create the force plots (both tangential and normal force) for each wheel. All the corrected force data collected in the water-based fluid trials are displayed in **Figures 33-50**. Trends in force are similar to those observed in the power measurement graphs. During periods of non-engagement between the wheel and work piece, the force readings are nominal. As the wheel enters the work block the force readings increase to some peak value and drop off again as the wheel exits the work block. The peak values obtained generally increase with each subsequent pass until the wheel reaches failure. Large spikes in the force readings at the end of some plots are due to slower reaction times for disengaging the feed table after wheel stall. At failure, the grinding wheel would quickly drop its rotational speed to zero. If the feed table was not immediately disengaged, the wheel was continually fed into the work block without cutting, causing the significant increase (or spike) in the force reading.

Comparison of forces between different grinding wheels for each fluid was made by determining the average force per pass for each wheel and plotting that data on one graph. Averaging was accomplished by graphically determining the entry point and exit point of full wheel engagement, and computing the mathematical mean of all the force measurements between those bounds. **Figures 51 – 56** show the comparisons of tangential and normal force between wheels for each of the three water-based fluid trials. All grinding wheels for all fluids show an increase in both normal force and tangential force from the initial pass to the final pass at failure.

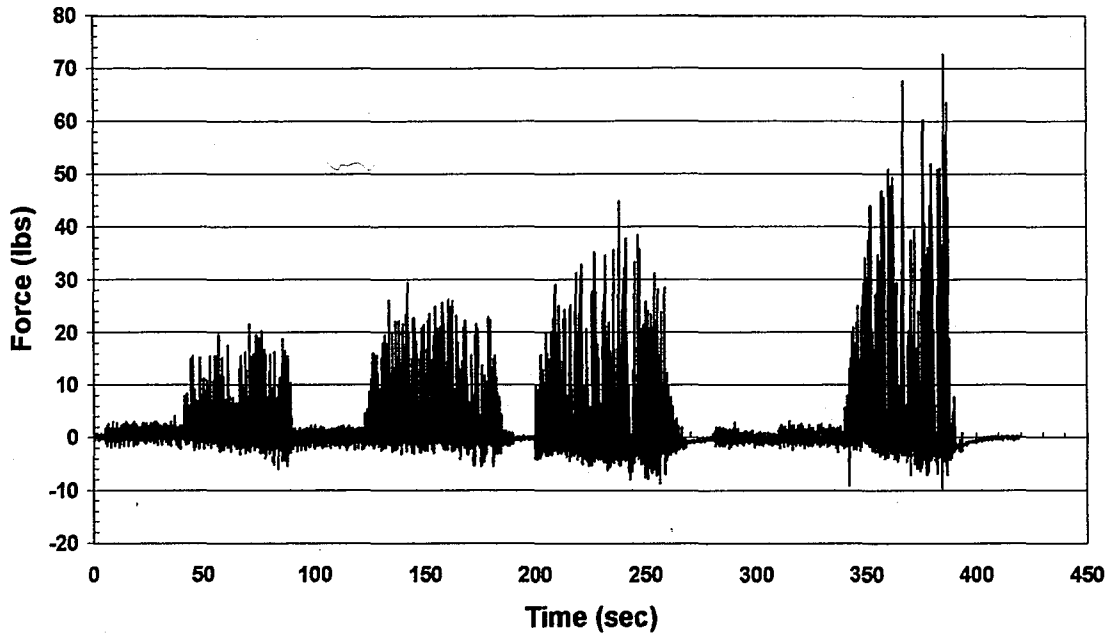


Figure 33: Normal force measurements for Wheel #1, Water-based A Fluid.

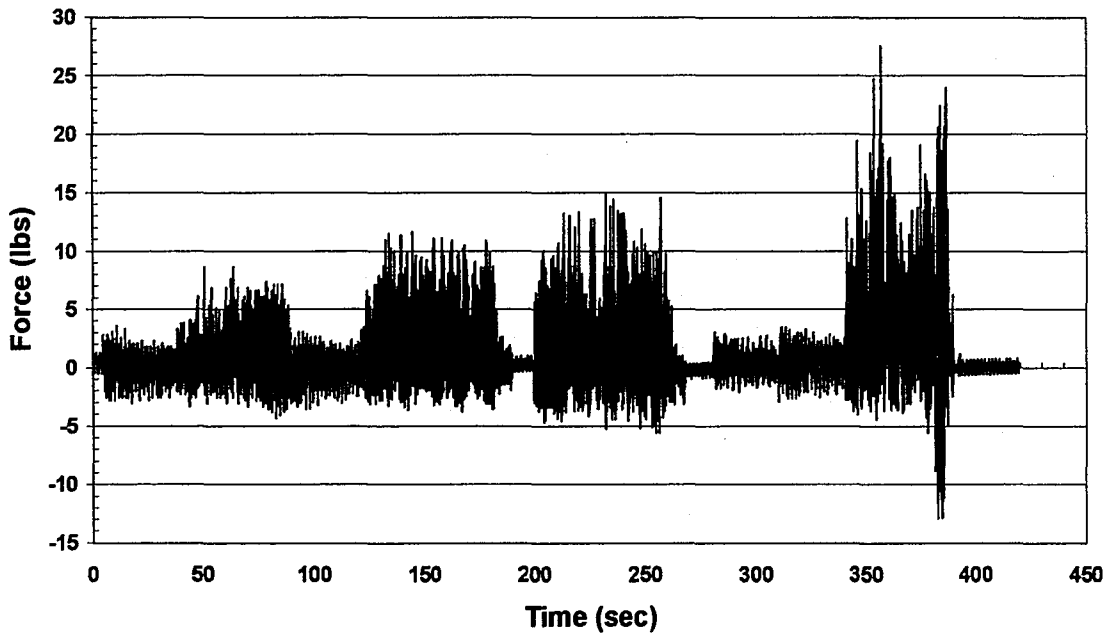


Figure 34: Tangential force measurements for Wheel #1, Water-based A Fluid.

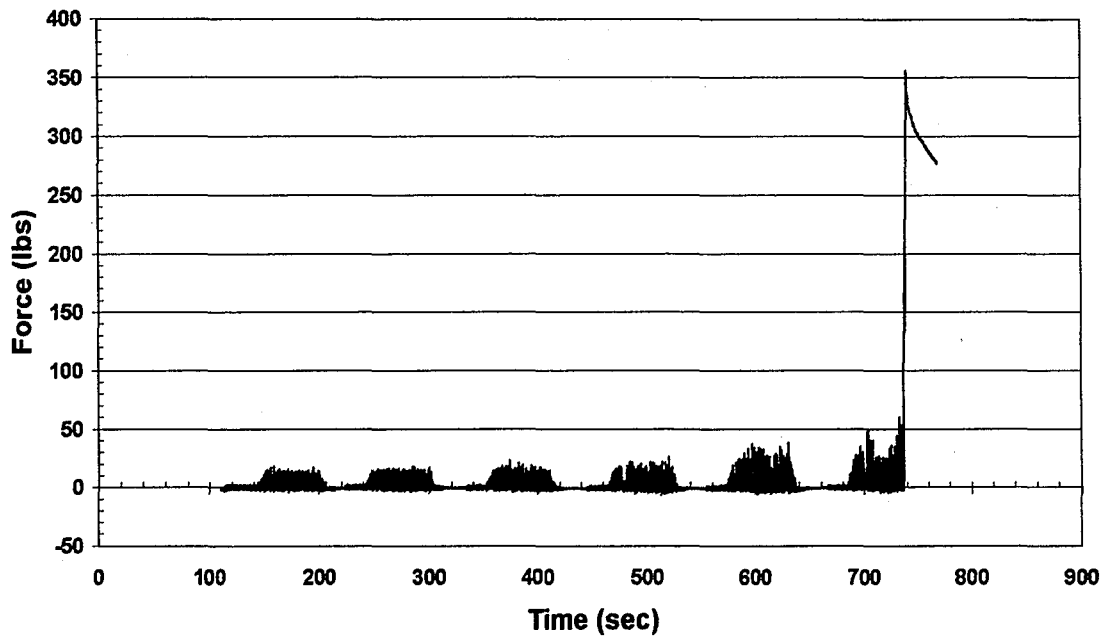


Figure 35: Normal force measurements for Wheel #2, Water-based A Fluid.

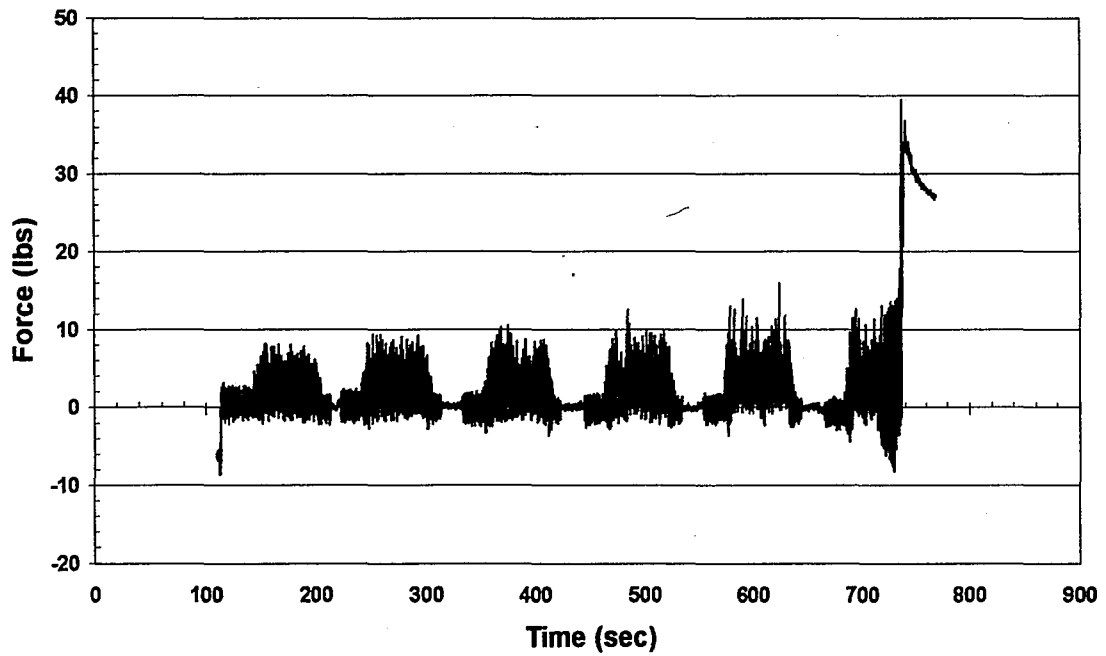


Figure 36: Tangential force measurements for Wheel #2, Water-based A Fluid.

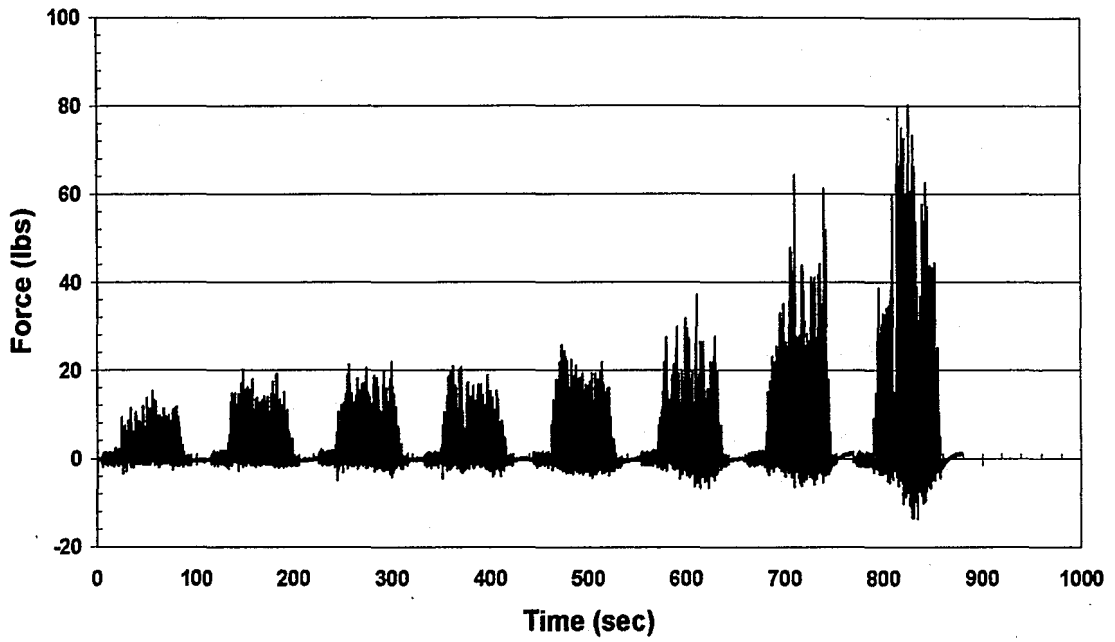


Figure 37: Normal force measurements for Wheel #3, Water-based A Fluid.

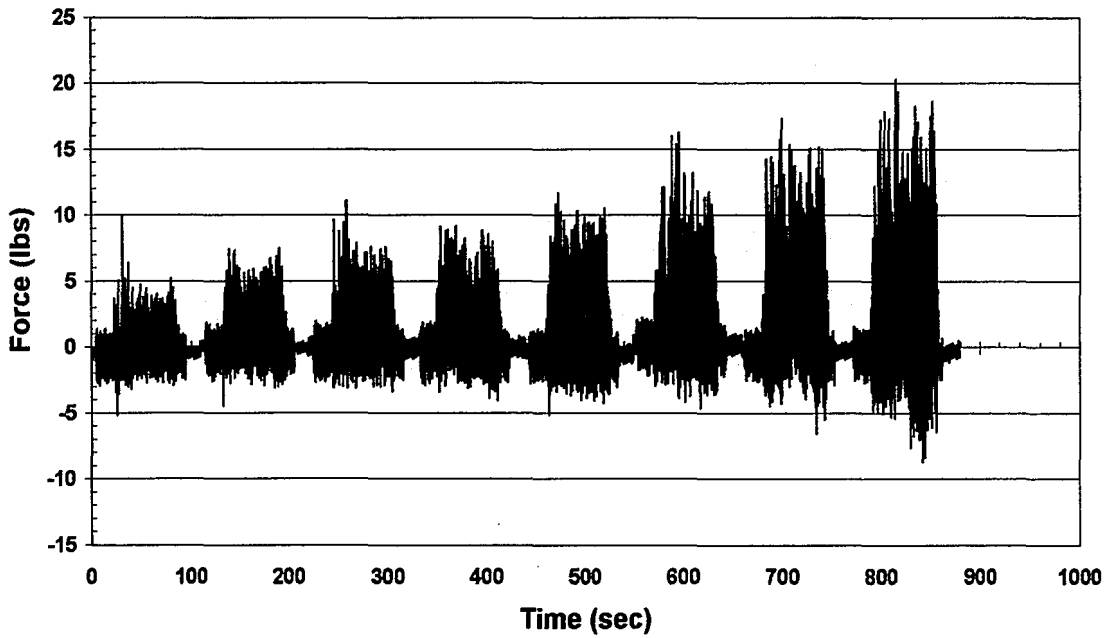


Figure 38: Tangential force measurements for Wheel #3, Water-based A Fluid.

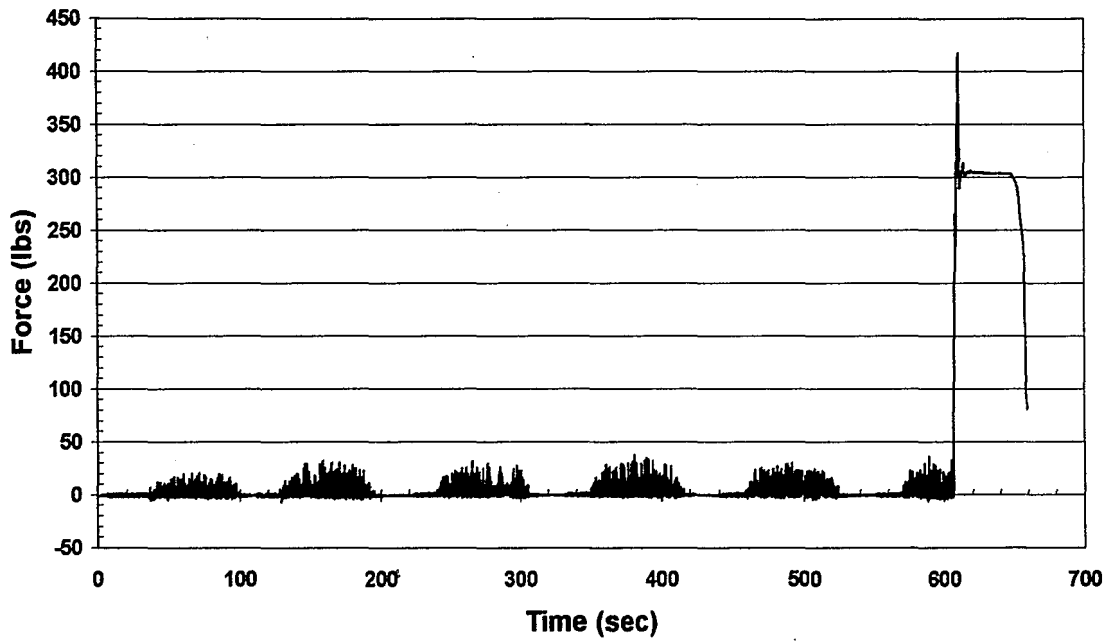


Figure 39: Normal force measurements for Wheel #1, Water-based B Fluid.

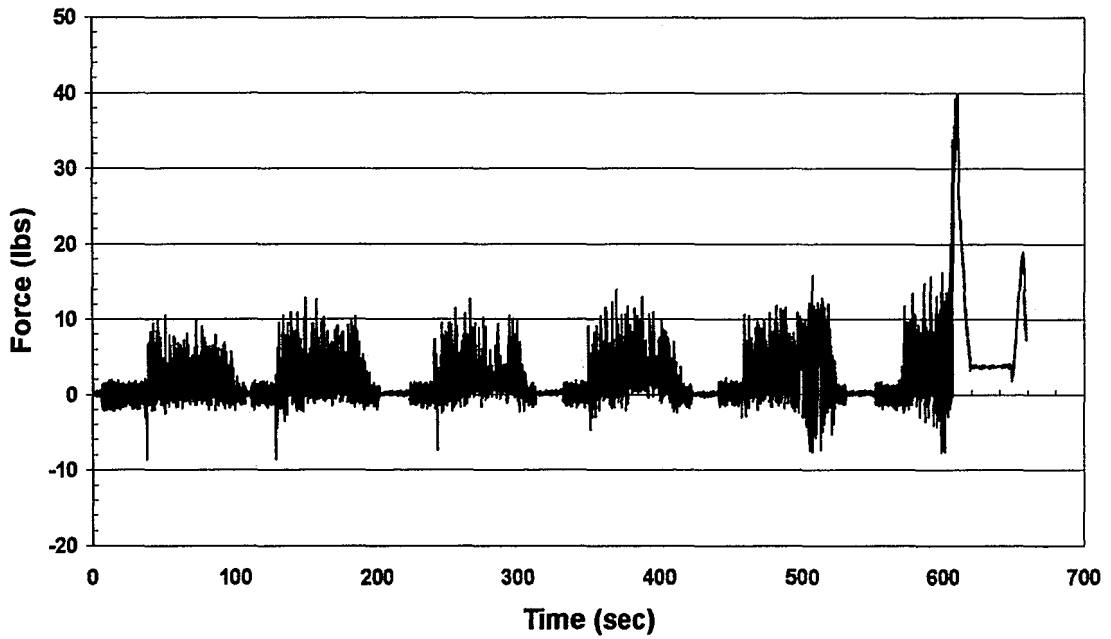


Figure 40: Tangential force measurements for Wheel #1, Water-based B Fluid.

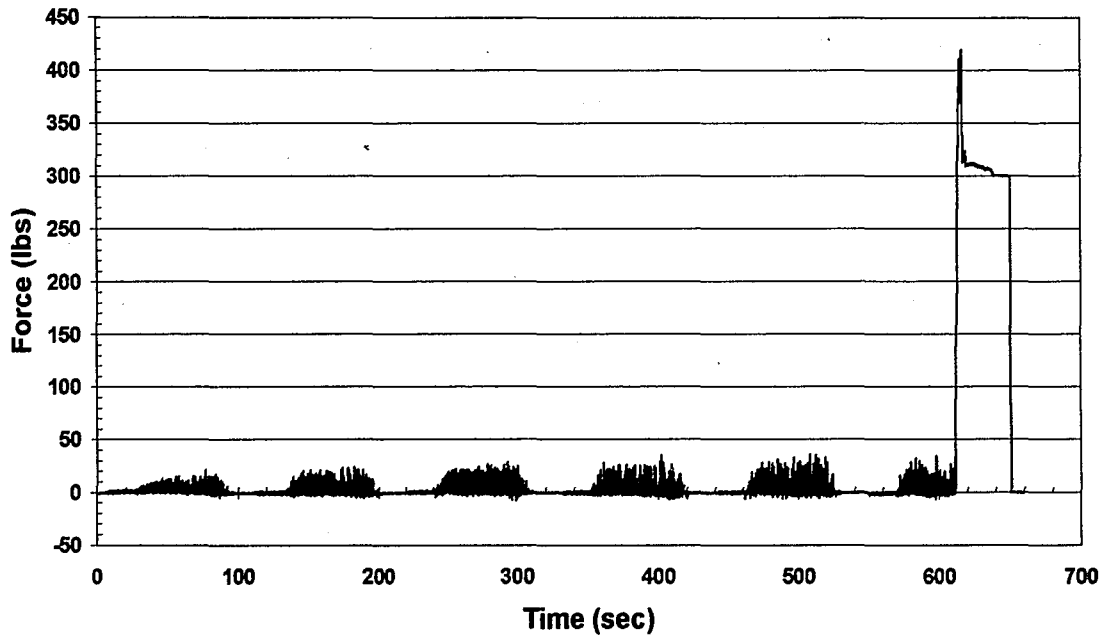


Figure 41: Normal force measurements for Wheel #2, Water-based B Fluid.

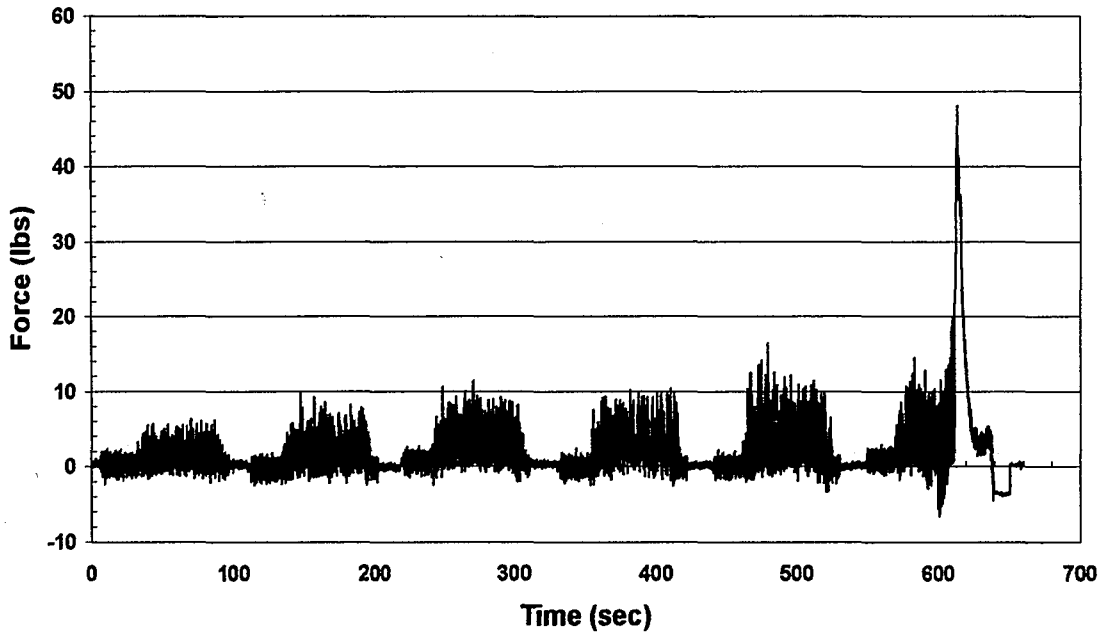


Figure 42: Tangential force measurements for Wheel #2, Water-based B Fluid.

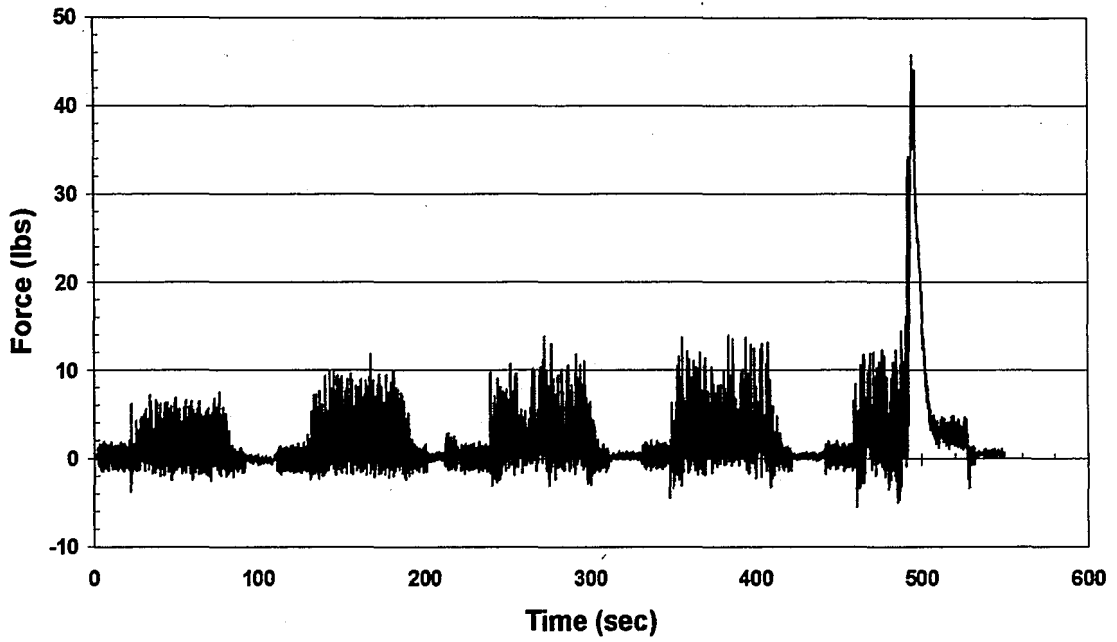


Figure 43: Normal force measurements for Wheel #3, Water-based B Fluid.

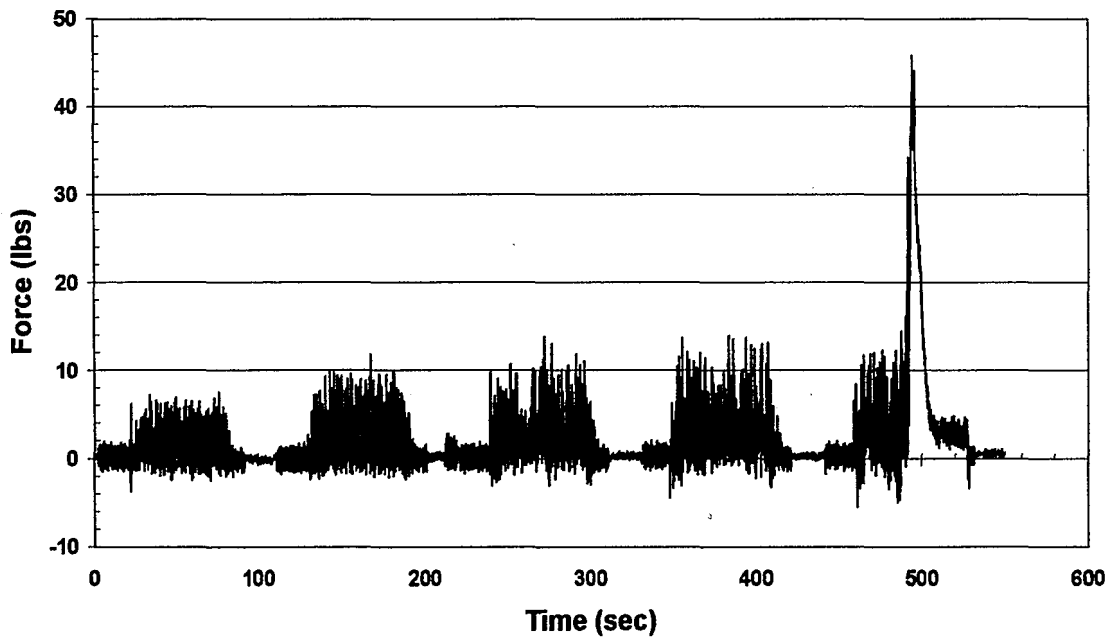


Figure 44: Tangential force measurements for Wheel #3, Water-based B Fluid.

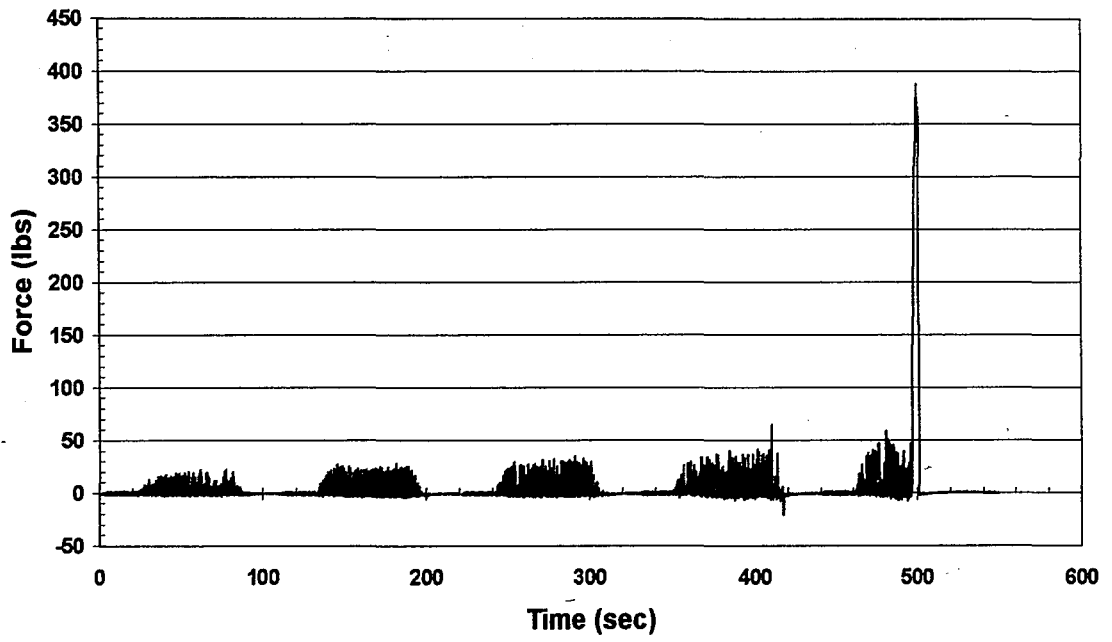


Figure 45: Normal force measurements for Wheel #1, Water-based C Fluid.

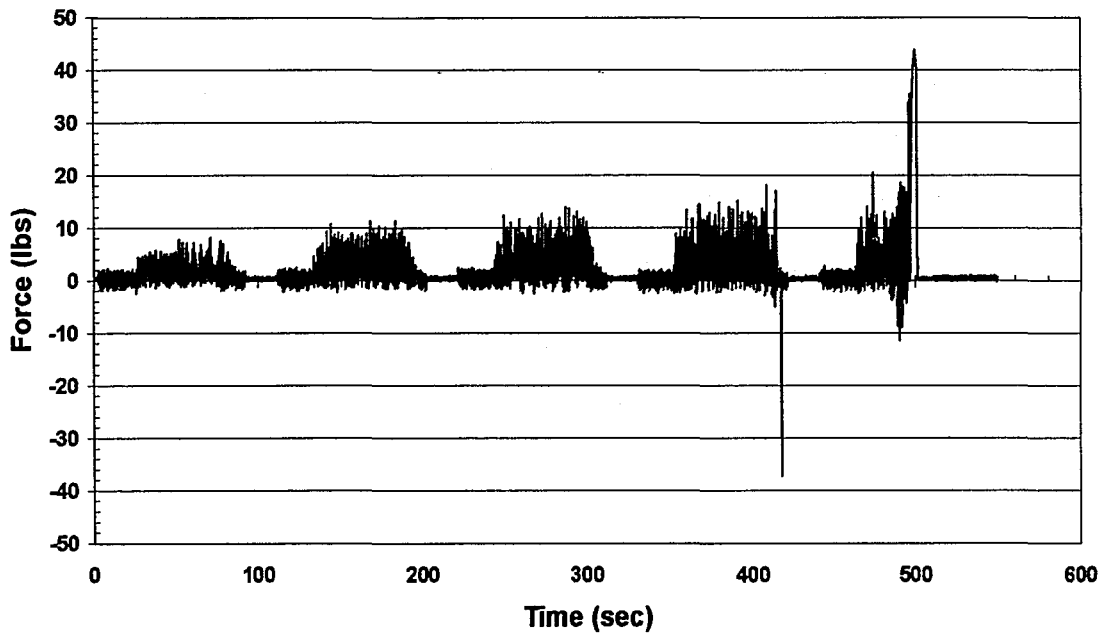


Figure 46: Tangential force measurements for Wheel #1, Water-based C Fluid.



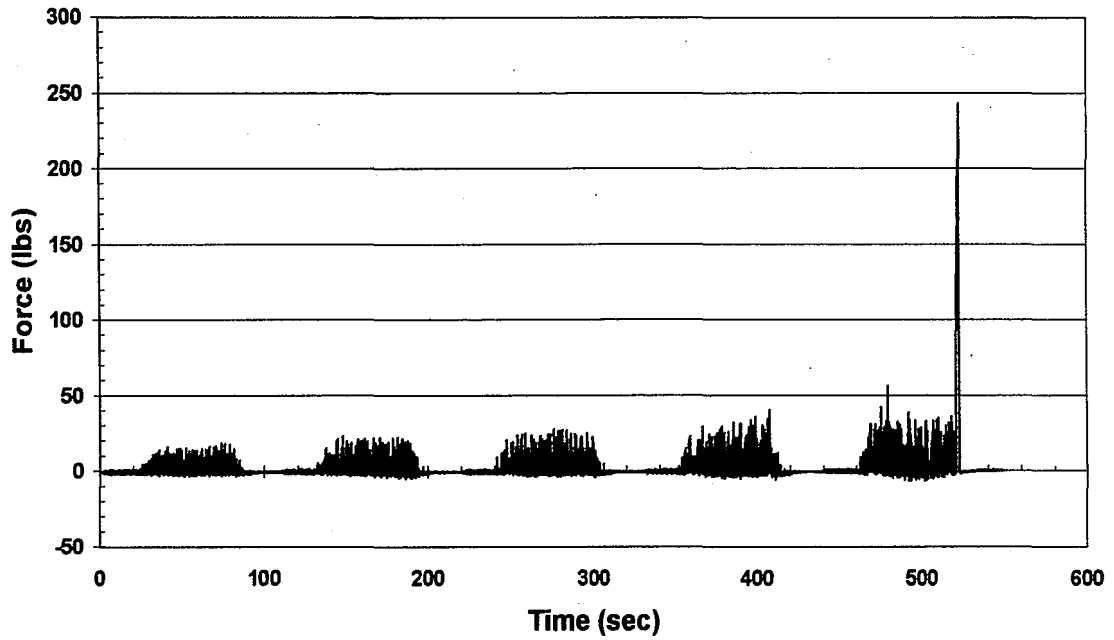


Figure 47: Normal force measurements for Wheel #2, Water-based C Fluid.

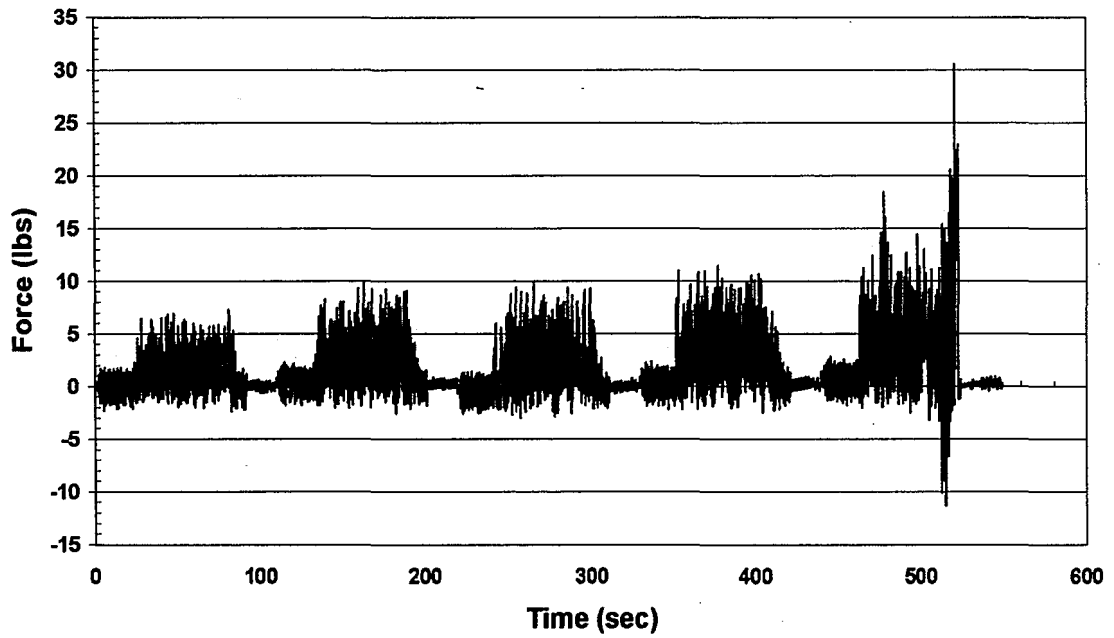


Figure 48: Tangential force measurements for Wheel #2, Water-based C Fluid.

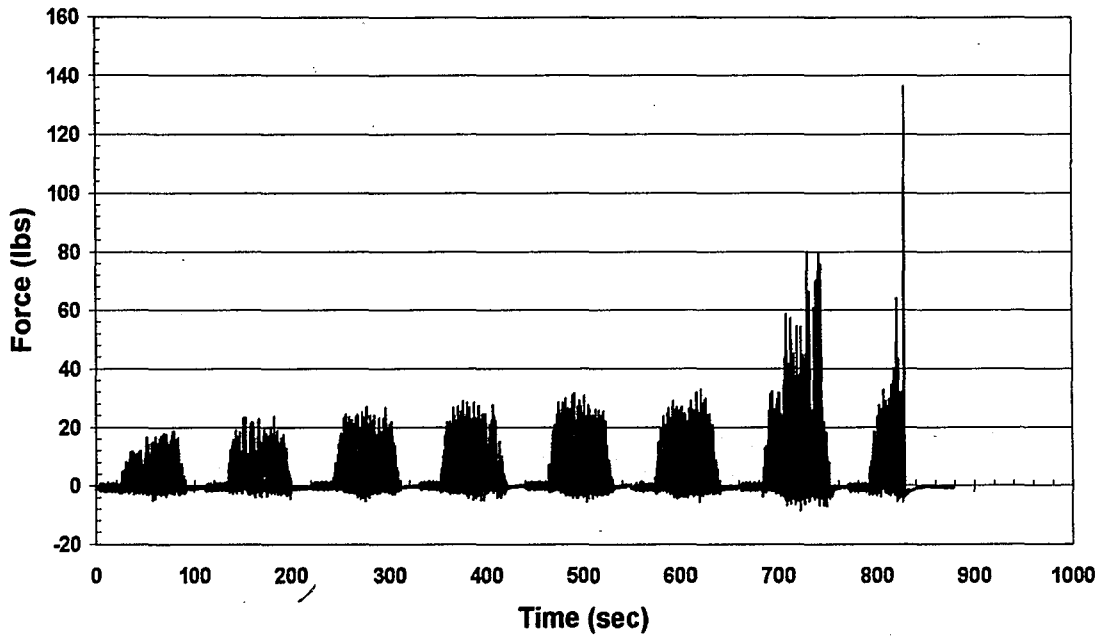


Figure 49: Normal force measurements for Wheel #3, Water-based C Fluid.

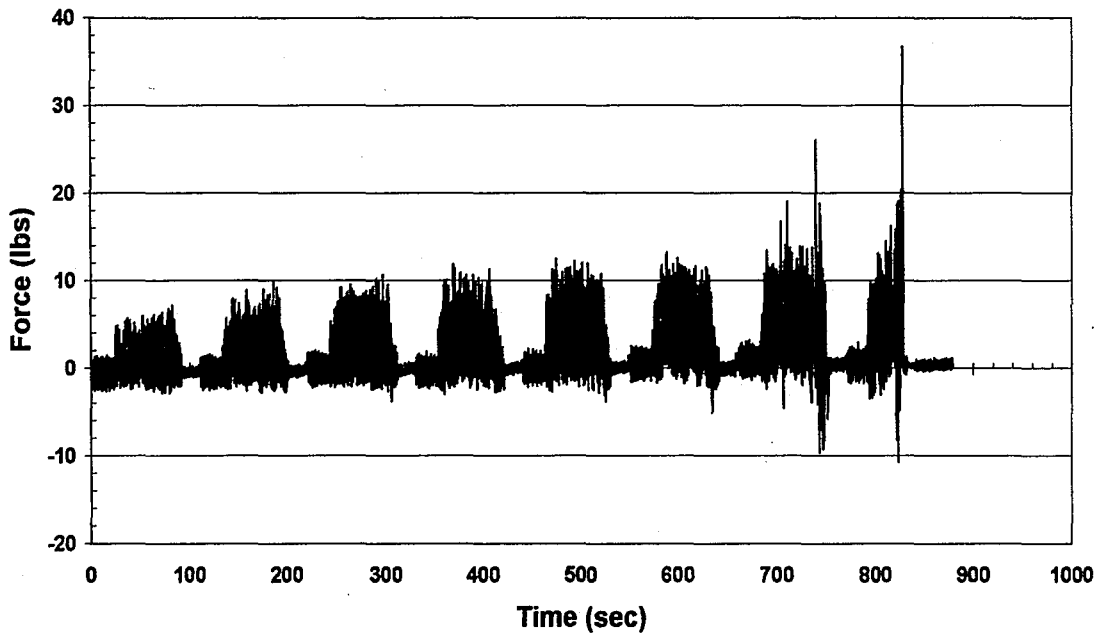


Figure 50: Tangential force measurements for Wheel #3, Water-based C Fluid.

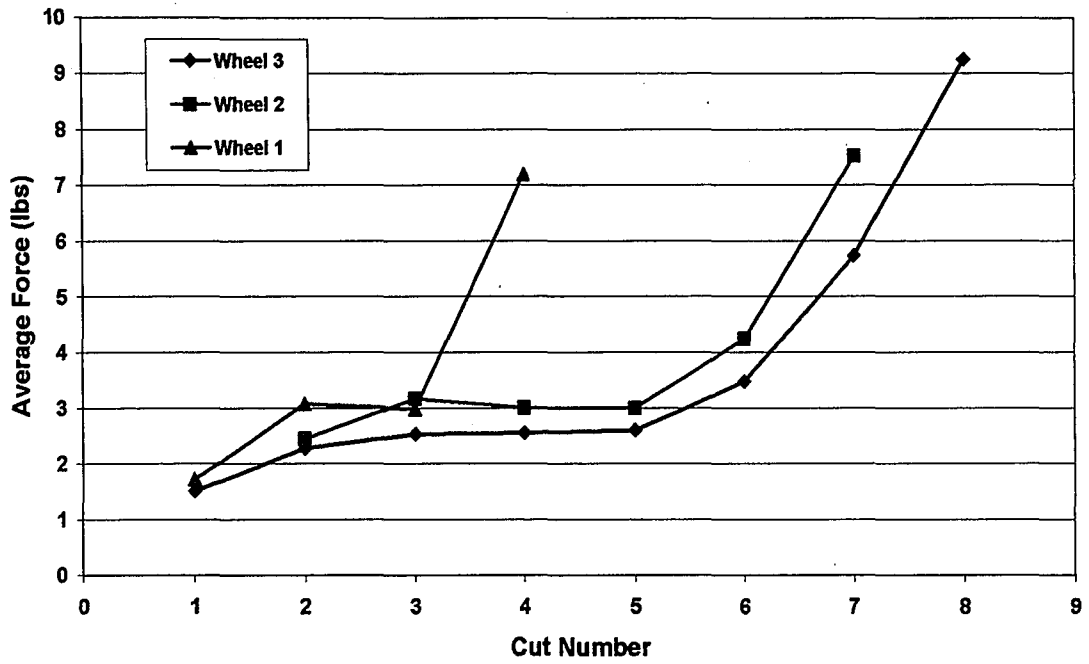


Figure 51: Comparison of the average normal force per cut using Water-based A Fluid.

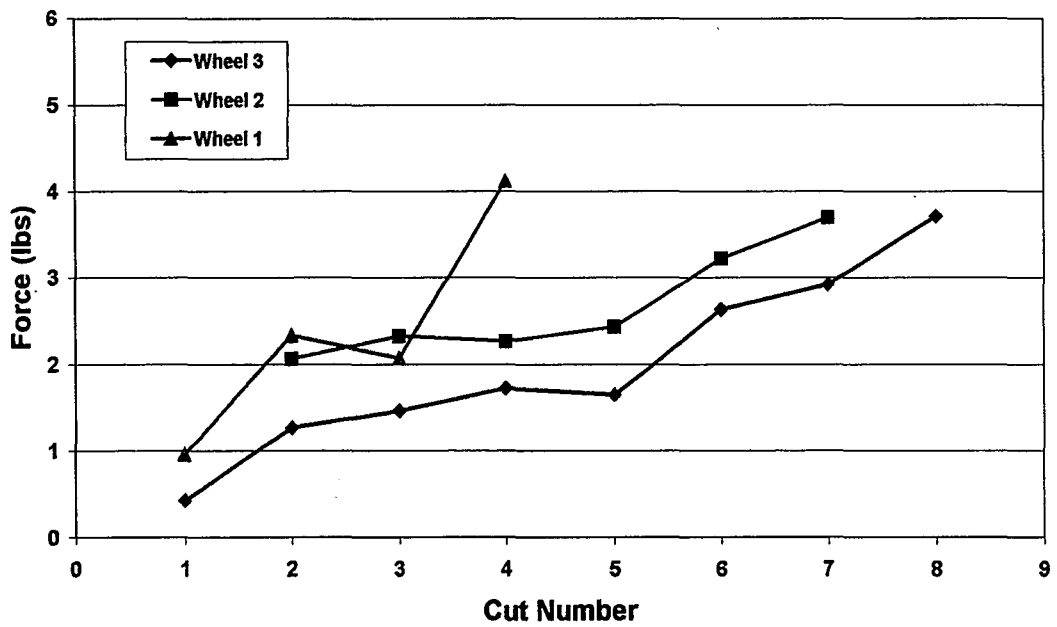


Figure 52: Comparison of the average tangential force per cut using Water-based A Fluid.

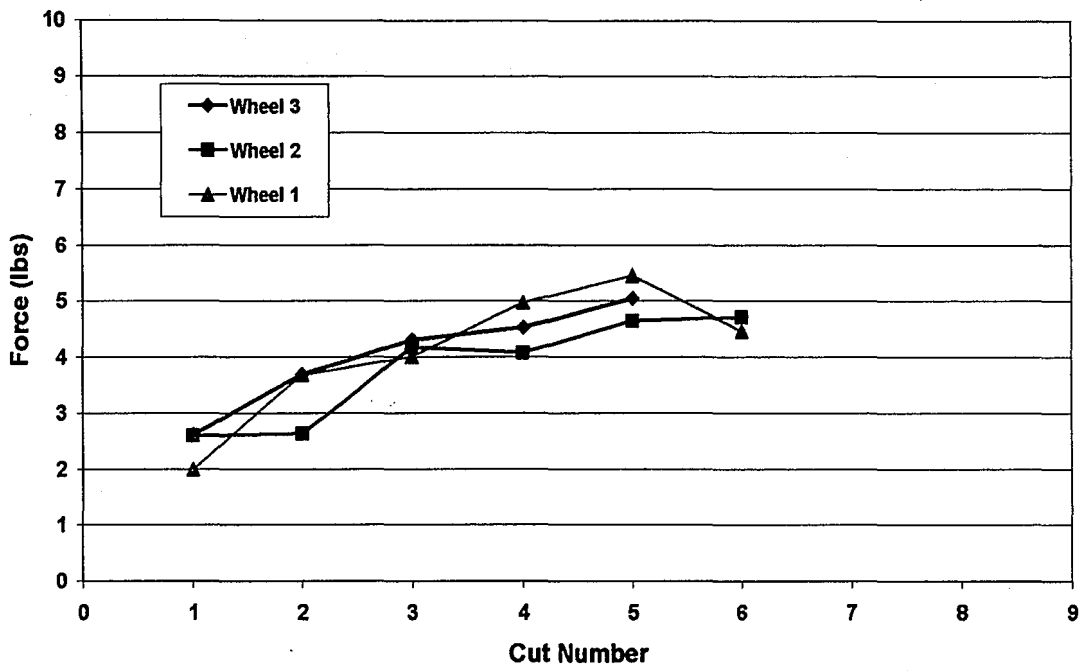


Figure 53: Comparison of the normal forces using Water-based B Fluid.

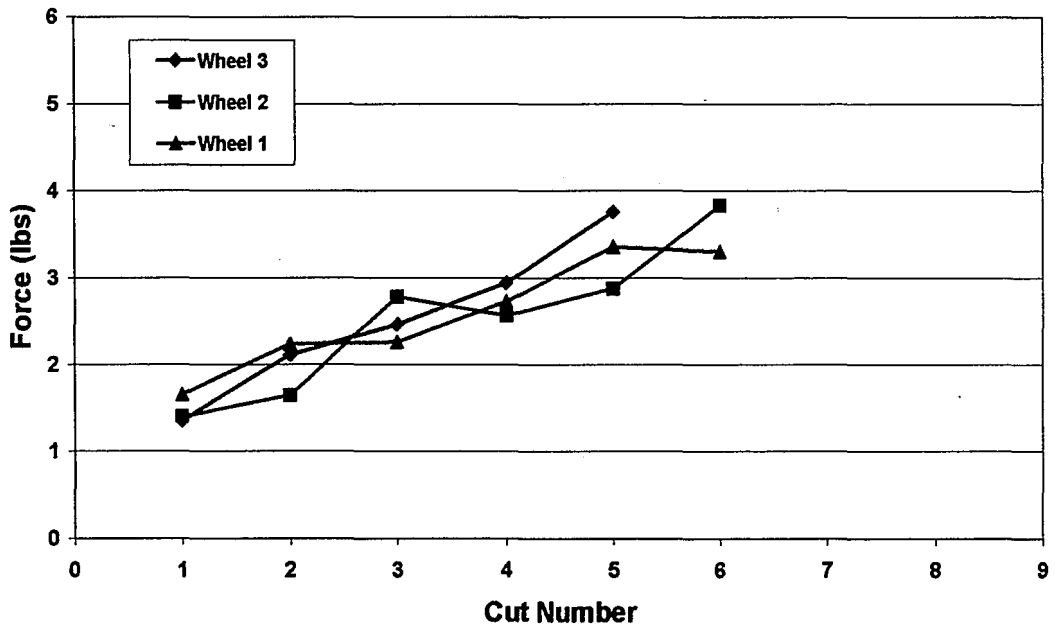


Figure 54: Comparison of the tangential forces using Water-based B Fluid.

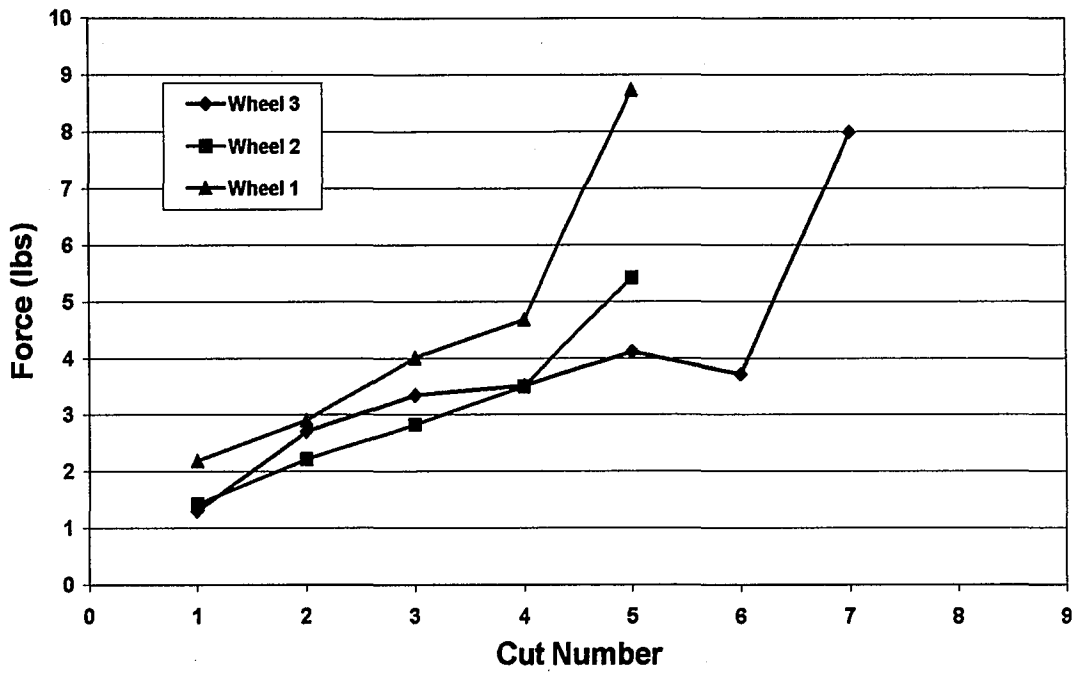


Figure 55: Comparison of the normal forces using Water-based C Fluid.

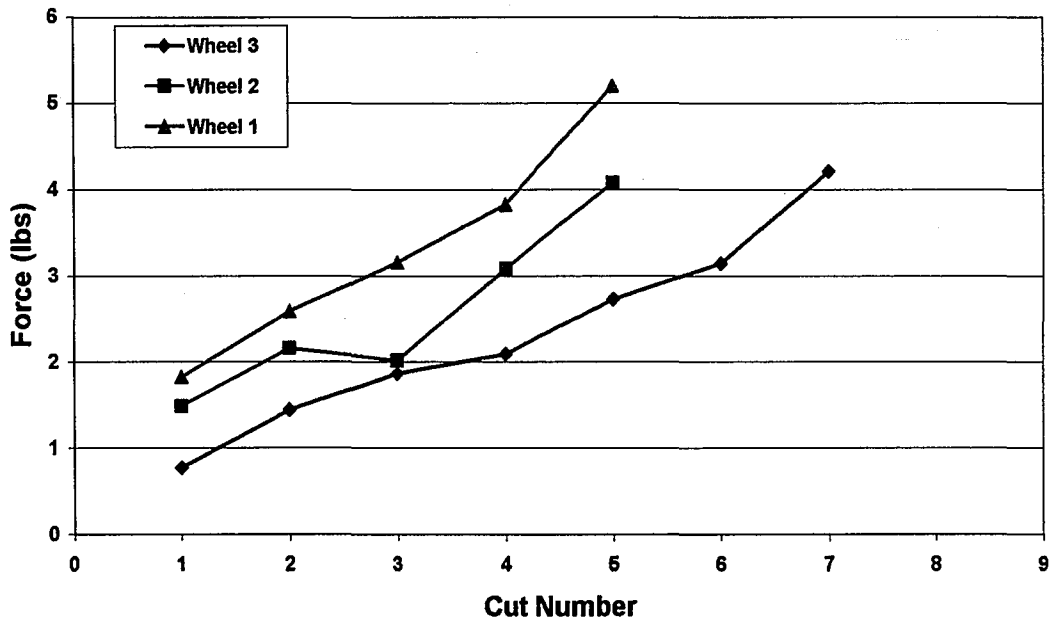


Figure 56: Comparison of the tangential forces using Water-based C Fluid.

4.6 Oil Baseline Fluid Trial:

After the water-based fluid trials, the Oil Baseline fluid (neat oil) was tested as the benchmark of performance for petroleum-based lubricating fluids. This trial was utilized to gauge the relative performance of the water-based fluids for this set of operational parameters, and to determine the failure mechanism of the electroplated CBN grinding wheel in oil coolant. Testing for the oil coolant was completed in the same manner as for the water-based fluids. Expectations were that grinding wheels used with the oil coolant would last considerably longer than with the water-based fluids. Those expectations were confirmed when the first grinding wheel completed 12,470 mm in grind length (120 passes) over four days of testing, without any indication that the wheel was approaching failure. The number of work blocks prepared for the gamut of tests was insufficient to continue with the fluid trial. After consideration of the cost to prepare additional work blocks and the absence of any indication that the wheel was about to fail, the Oil Baseline fluid trial was ended prior to reaching wheel failure. The grinding wheel, and the 16 work blocks and filter bags consumed during testing, were removed for subsequent analysis as in the previous water-based fluid trials.

Power measurements taken during the neat oil fluid test were recorded and plotted in the same manner as the water-based fluid trials. **Figure 57** shows the data from the four days of testing with the neat oil fluid. Trends in power consumption for each individual pass are the same as the water-based fluids. Periods of non-engagement had low power readings, with some peak value being obtained during full engagement. The first day of testing showed an increase in peak power

consumed from the first pass to the last pass. Decreases in peak power consumed from initial to final pass were observed on the second, third, and fourth day of testing. The difference in power readings between the first testing day and the other days of testing was due to oil temperature. During the first day, the oil was pumped through the system for several hours prior to the first pass. In subsequent testing days, oil was pumped through the system for only 30 minutes prior to testing. Heat was generated by the high pressure fluid pump, which had difficulty pumping the oil through the system. This heat slowly raised the temperature of the oil throughout the duration of the testing day. Warm oil was pumped through the system during the first testing day, without significant change in temperature. Cold oil was initially pumped through the system on the other testing days. As the oil rose in temperature, its viscosity decreased. As the viscosity of the oil decreased, the power required to spin the grinding wheel against the force of the scrubber jet decreased.

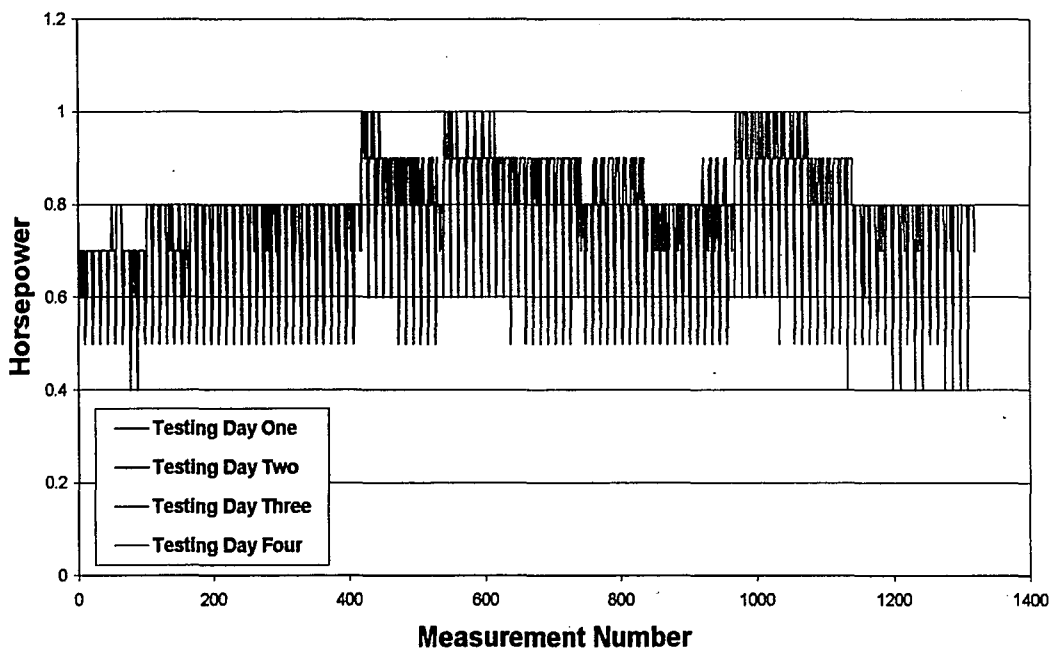


Figure 57: Power measurements for the four days of testing with neat oil.

Force measurements were recorded and manipulated in the same manner as was done for each of the water-based fluid trials. Data from each groove (all 16 work blocks) spread over the four testing days was put into a master plot. The plot (see **Figure 58**) shows the trends in tangential and normal forces throughout the test life of the wheel in the oil coolant. Dots mark the initial passes on new work blocks. Forces, particularly the normal force, typically show an increase in force recorded from the first pass to the last pass on a work block. This trend is attributed to the increase in cut depth (due to the table being slightly off-level) from the initial pass to the final pass in each block. Changes in tangential force are small when compared to the rapid increase that was observed in the water-based fluid trials. **Figure 59** shows a comparison between the tangential force readings of the third wheel tested for each water-based fluid and the wheel tested in the neat oil fluid. Clearly, by extending the trend of force readings, the neat oil fluid trial could have continued for a significant time before wheel failure.

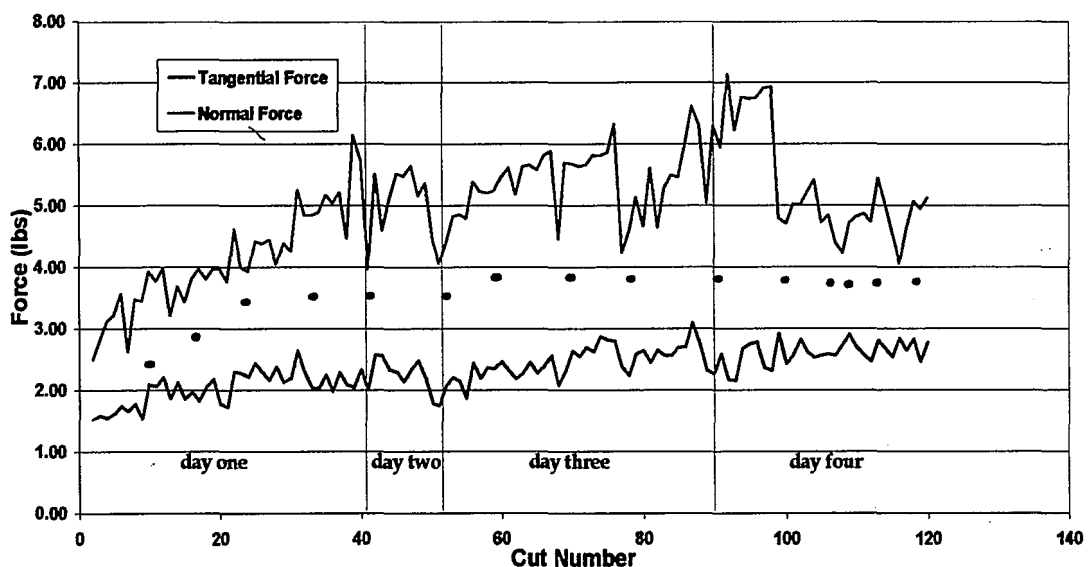


Figure 58: Plot of corrected average force per cut for the neat oil fluid trial.

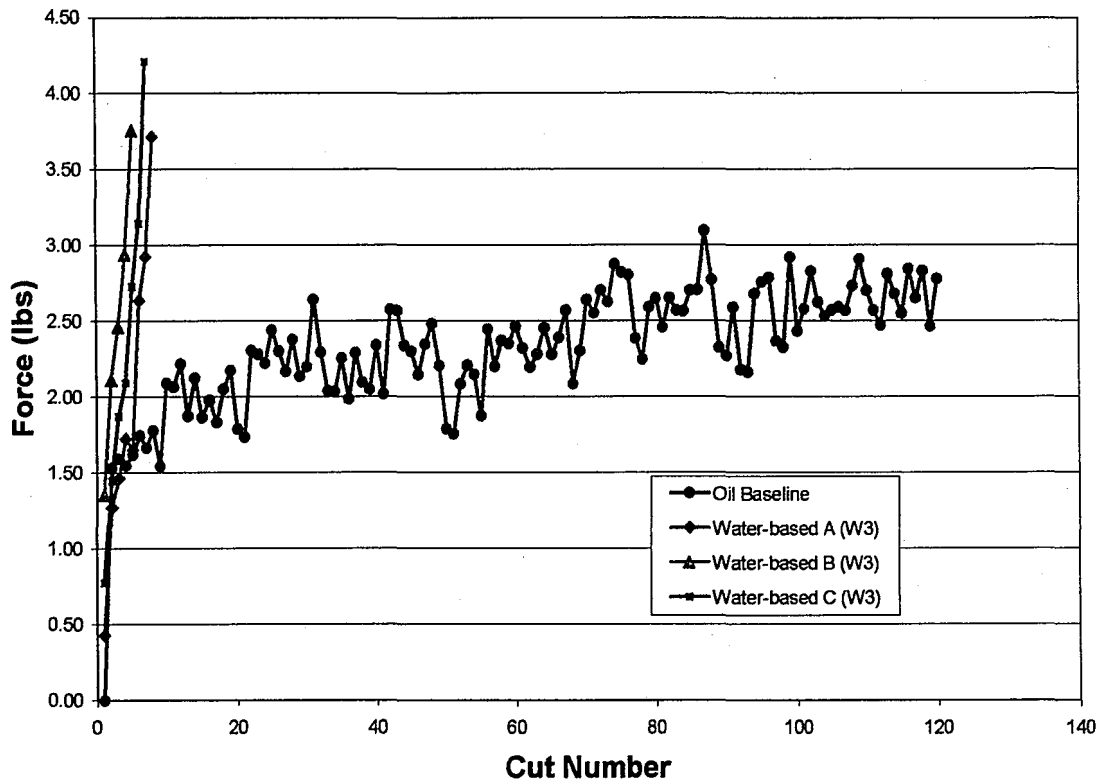


Figure 59: Comparison of average tangential force per cut between the neat oil fluid and the water-based fluids.

4.7 Grinding Swarf:

Grinding swarf, the debris captured in the mesh filter bags from the fluid trial grinding tests, was initially examined with an Olympus SZH10 Research Stereoscope. The swarf was comprised of grinding chips, abrasive grains removed from the wheel surface, and wheel deposits cleaned off by the scrubber jet. Grinding chips and wheel deposits were the focus of the analysis. Abrasive grains were present in all filter bags collected. Wheel deposits were found, but were rare. Grinding chips were the most prevalent, being clustered within the folds and bottom crease of the filter bags, and caught to a lesser degree within the fibers of the mesh bag.

Stereoscope images of the swarf collected from the dry machining test trials with the M509 alloy work blocks provided a working context for deposit formation.

Chips were small and spiral-shaped (see **Figure 60**). Clusters of chips were frequent, where the spiral morphology enabled them to easily tangle together. One section of material recovered was identified as a wheel deposit that had spalled off (see **Figure 61**). Several CBN abrasive grains were discovered embedded in the underside of the deposit, with one clear imprint of an abrasive grain that was either retained in the grinding wheel or had fallen out of the deposit once it was removed from the wheel surface. Parallel tracks on the reverse side (facing away from wheel surface) indicate the direction of grinding wheel rotation. Another material deposit recovered in the swarf also showed interesting features (see **Figure 62**). Smeared metal with tracks running in parallel directions, indicative of material deposits on the surface of the grinding wheel, had also been removed from the wheel. This monolithic deposit had a periphery that was comprised of grinding chips, evidence that the deposit was formed through the build-up of individual grinding chips.

Chips found in the filter bags from the fluid trials were similar. Patterns of accumulation in the bags were sometimes different. The Water-based A fluid, Water-based C fluid, and the Oil Baseline fluid filter bags contained finely dispersed chips throughout the bag. Water-based B fluid was noticeably different. Chips were held together in very large clusters, sometimes centimeters in length, which could be grasped in hand and removed from the bags. These clusters were comprised of long spiral chips that clung together with the lubricating fluid to form spongy masses (see **Figure 63**). Grinding chips from the Water-based B fluid trial could also be recovered by removing the patches that adhered to the interior of the grinding

chamber. Fluid behavior, in this respect, was noticeably different than the other water-based fluids and the neat oil.

Scanning electron microscopy was used to study the grinding chips at higher magnification. Chips from each fluid were examined for differences in morphology. Images of chips recovered from the Water-based B fluid are shown in **Figure 64**, illustrating the differences in size and shape. **Figure 65** shows the two distinct sides of the grinding chip that are present: the serrated side and the smooth, flat side which flows across the rake face of the abrasive grain. **Figure 66** shows images of the serrated face of the chips for each fluid type. Chips could not be distinguished from their respective fluid trial based on morphology of the individual chip.

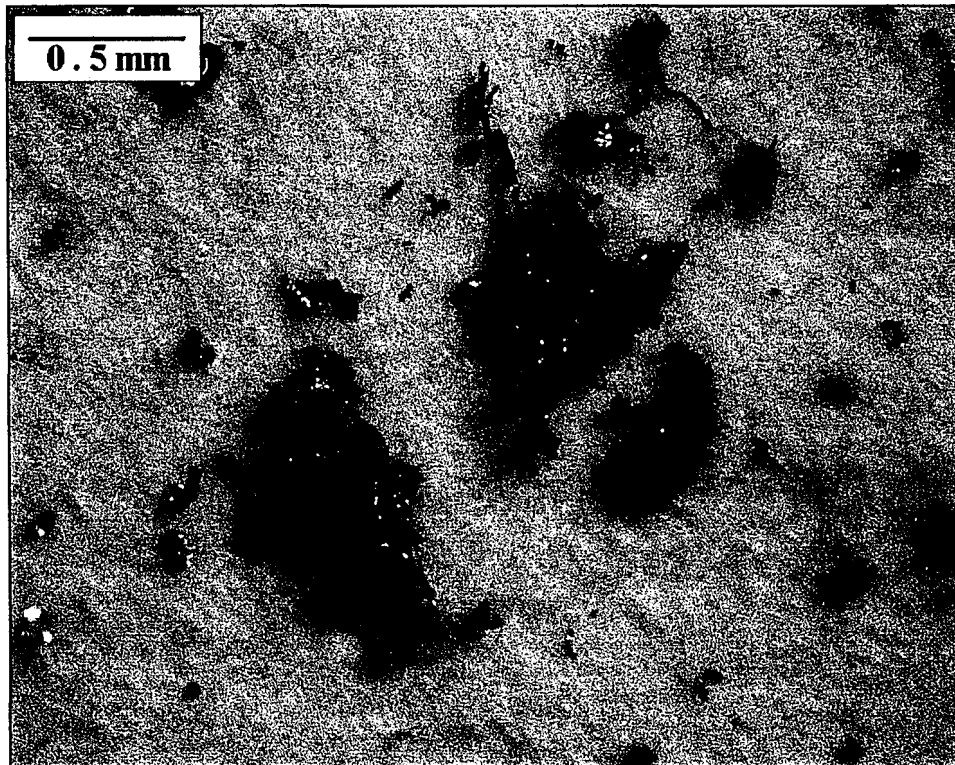


Figure 60: Grinding chips recovered from test trials of the grinding system with blocks of M509 alloy.

chamber. Fluid behavior, in this respect, was noticeably different than the other water-based fluids and the neat oil.

Scanning electron microscopy was used to study the grinding chips at higher magnification. Chips from each fluid were examined for differences in morphology. Images of chips recovered from the Water-based B fluid are shown in **Figure 64**, illustrating the differences in size and shape. **Figure 65** shows the two distinct sides of the grinding chip that are present: the serrated side and the smooth, flat side which flows across the rake face of the abrasive grain. **Figure 66** shows images of the serrated face of the chips for each fluid type. Chips could not be distinguished from their respective fluid trial based on morphology of the individual chip.

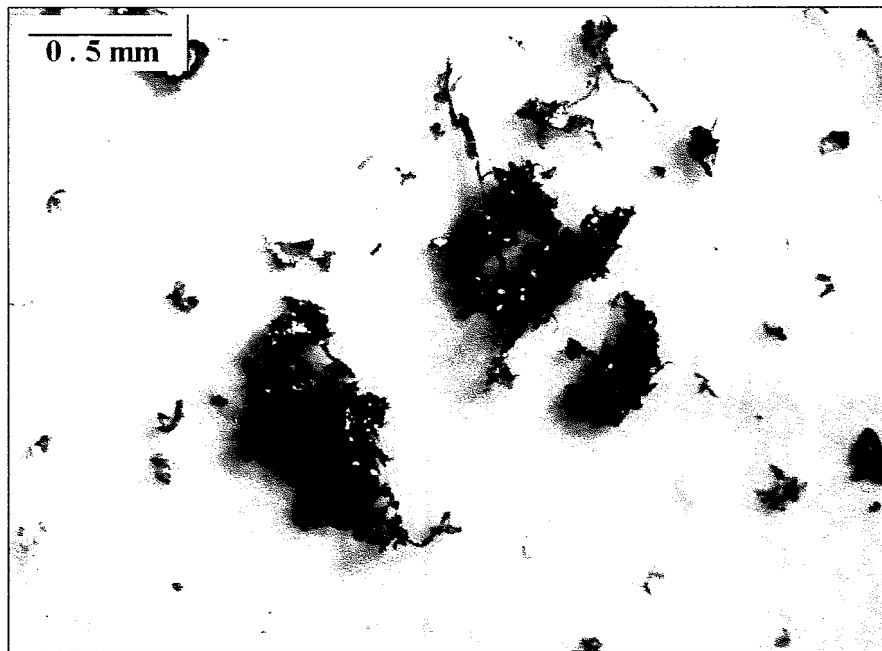
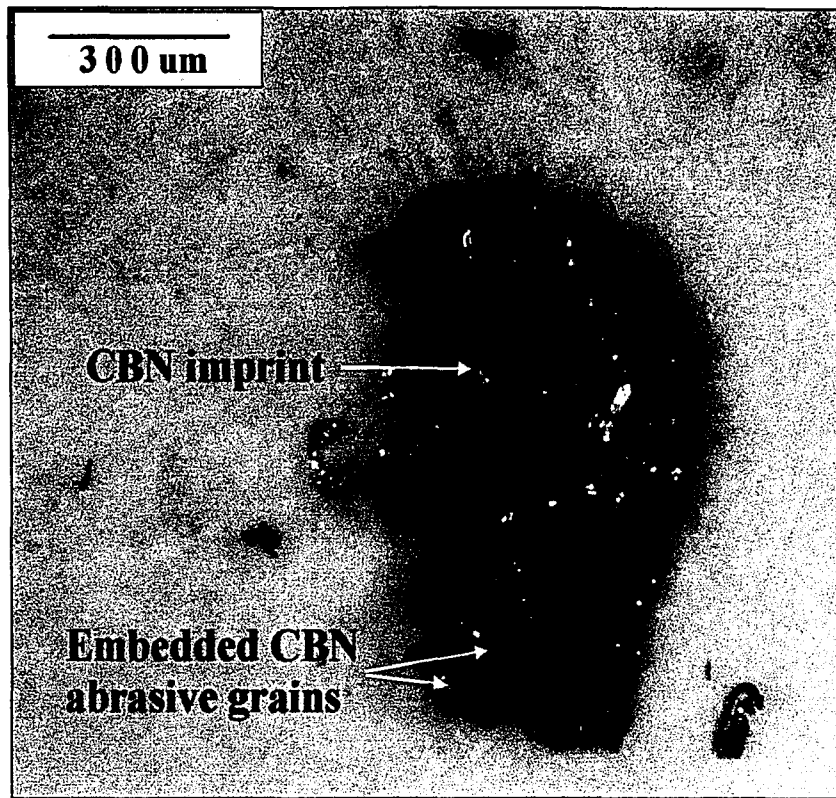
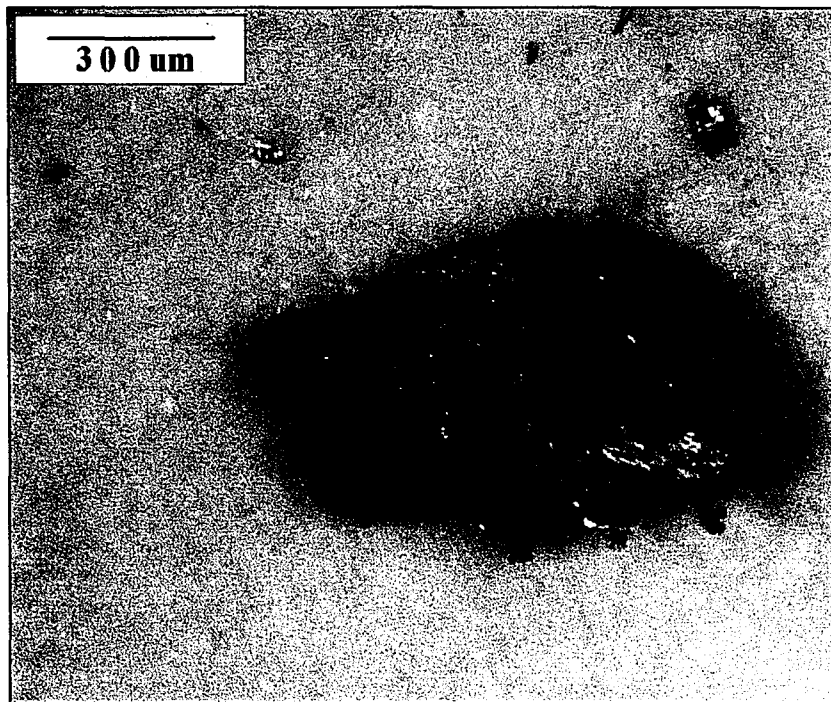


Figure 60: Grinding chips recovered from test trials of the grinding system with blocks of M509 alloy.

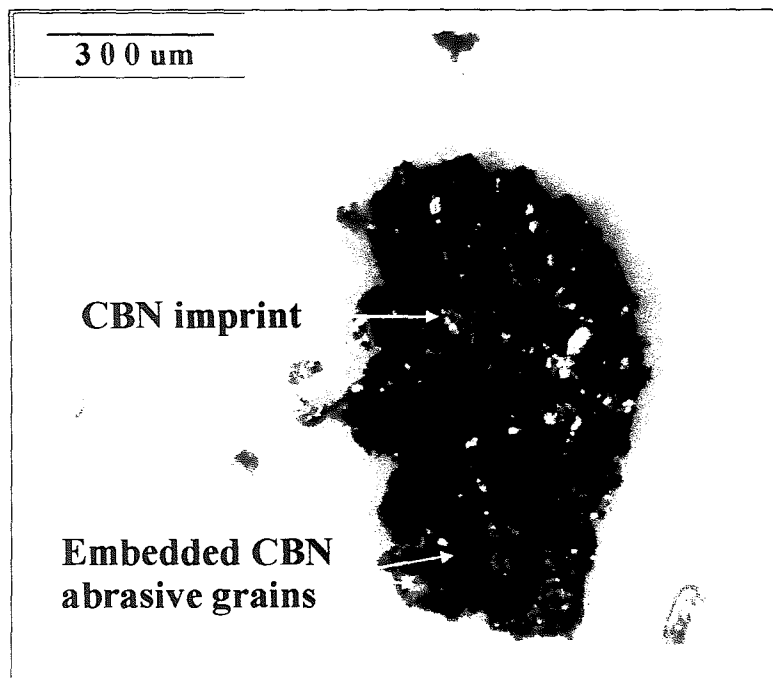


(a)

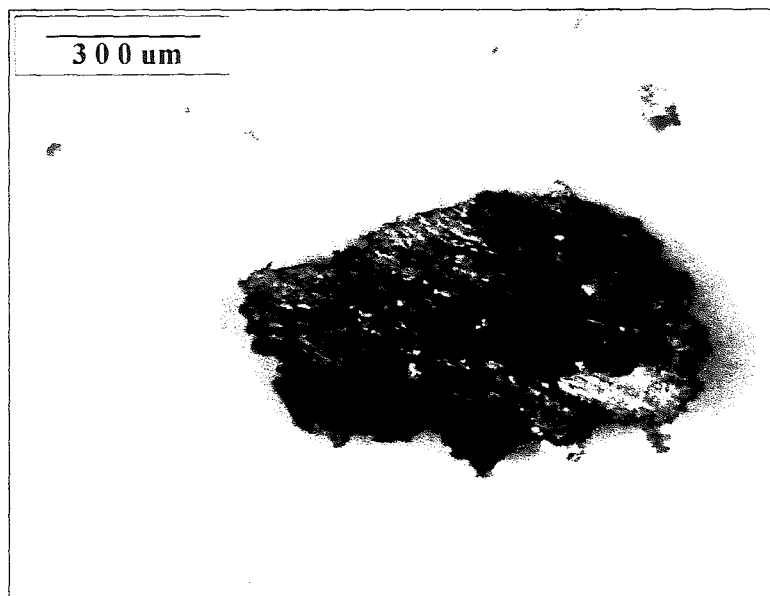


(b)

Figure 61: Wheel deposit from dry machining tests with M509, showing the underside (a), and top side (b), of the deposit.



(a)



(b)

Figure 61: Wheel deposit from dry machining tests with M509, showing the underside (a), and topside (b), of the deposit.

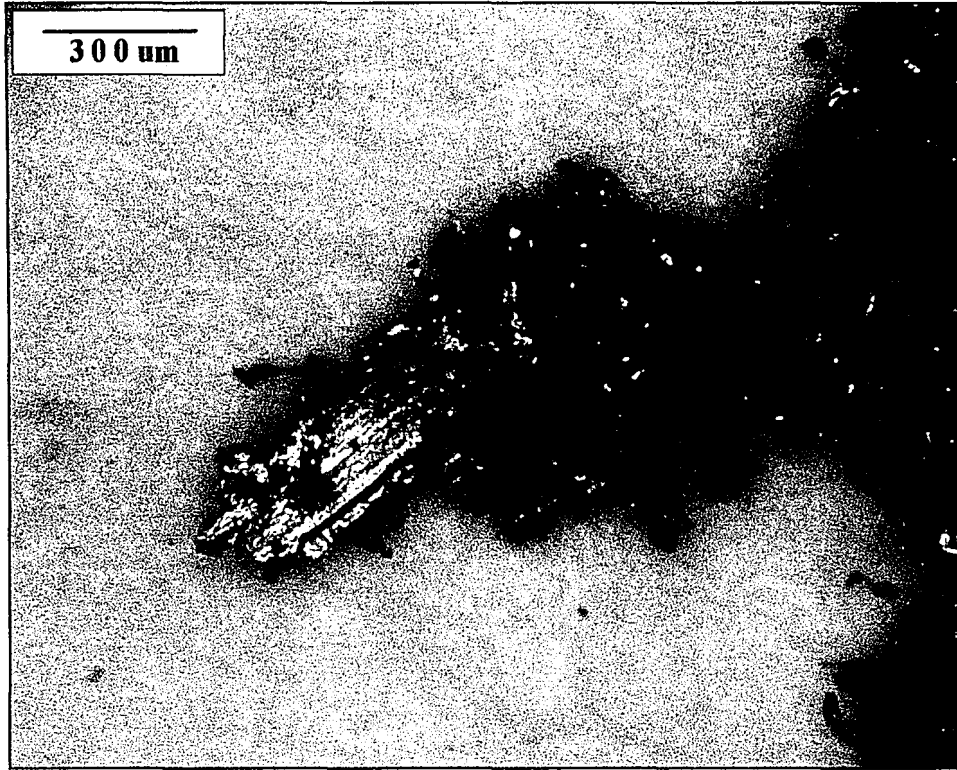


Figure 62: Smeared deposit of M509 material, comprised of grinding chips shown extending from all sides of the deposit's perimeter.

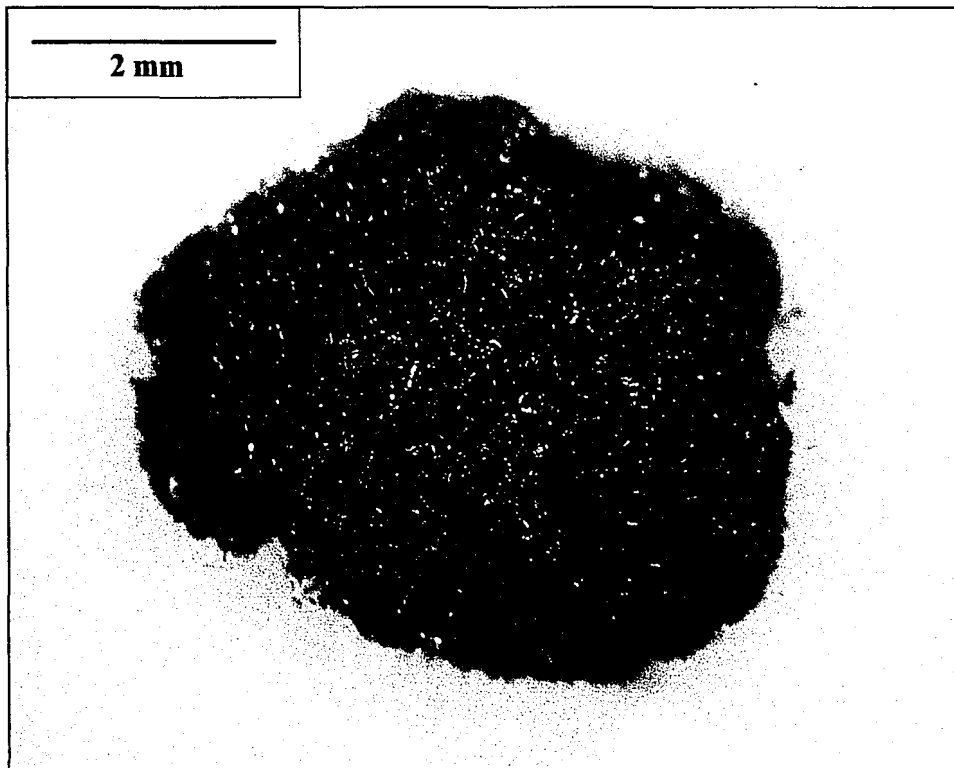


Figure 63: Clustered mass of grinding chips from the Water-based B fluid trial.

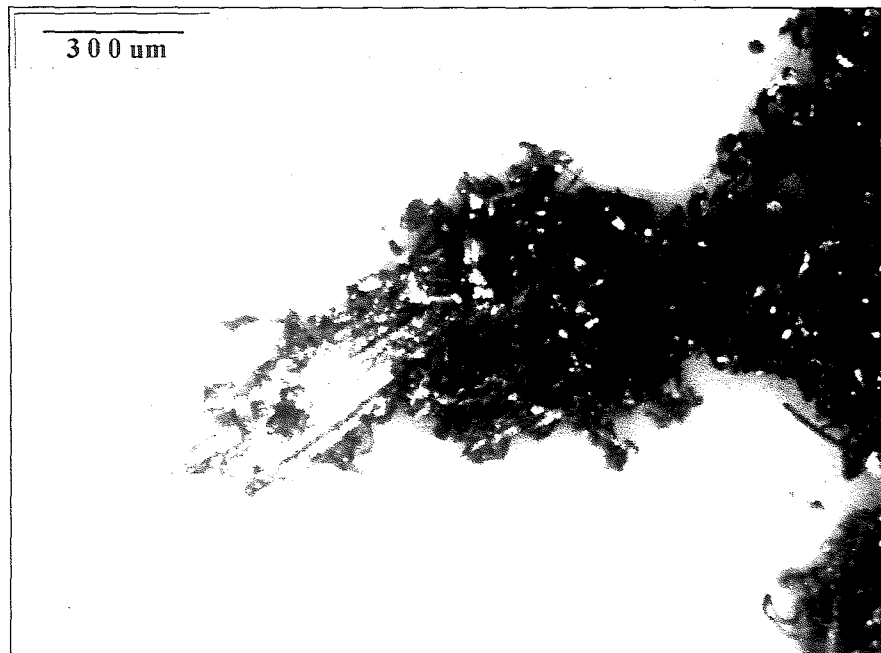


Figure 62: Smeared deposit of M509 material, comprised of grinding chips shown extending from all sides of the deposit's perimeter.

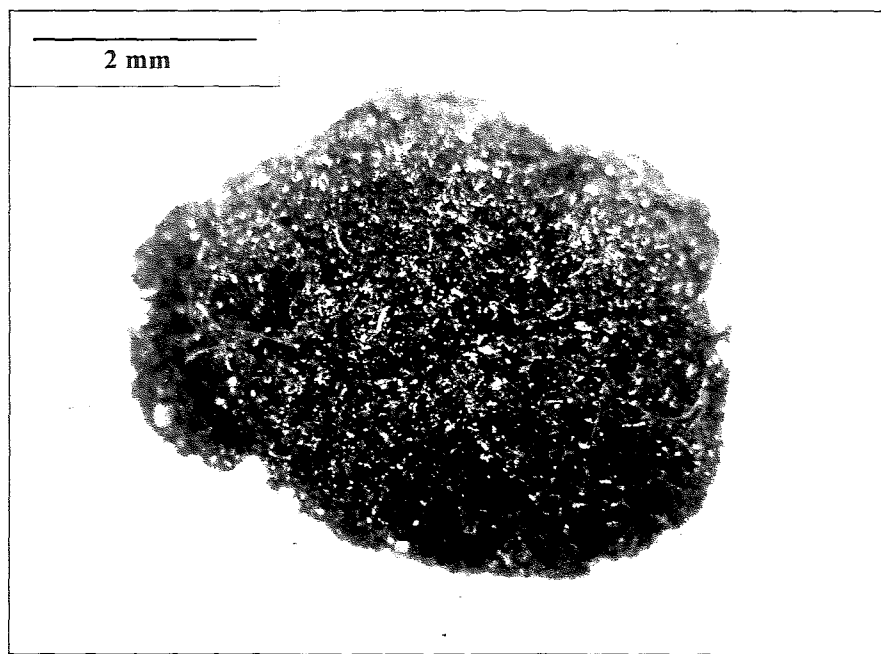


Figure 63: Clustered mass of grinding chips from the Water-based B fluid trial.

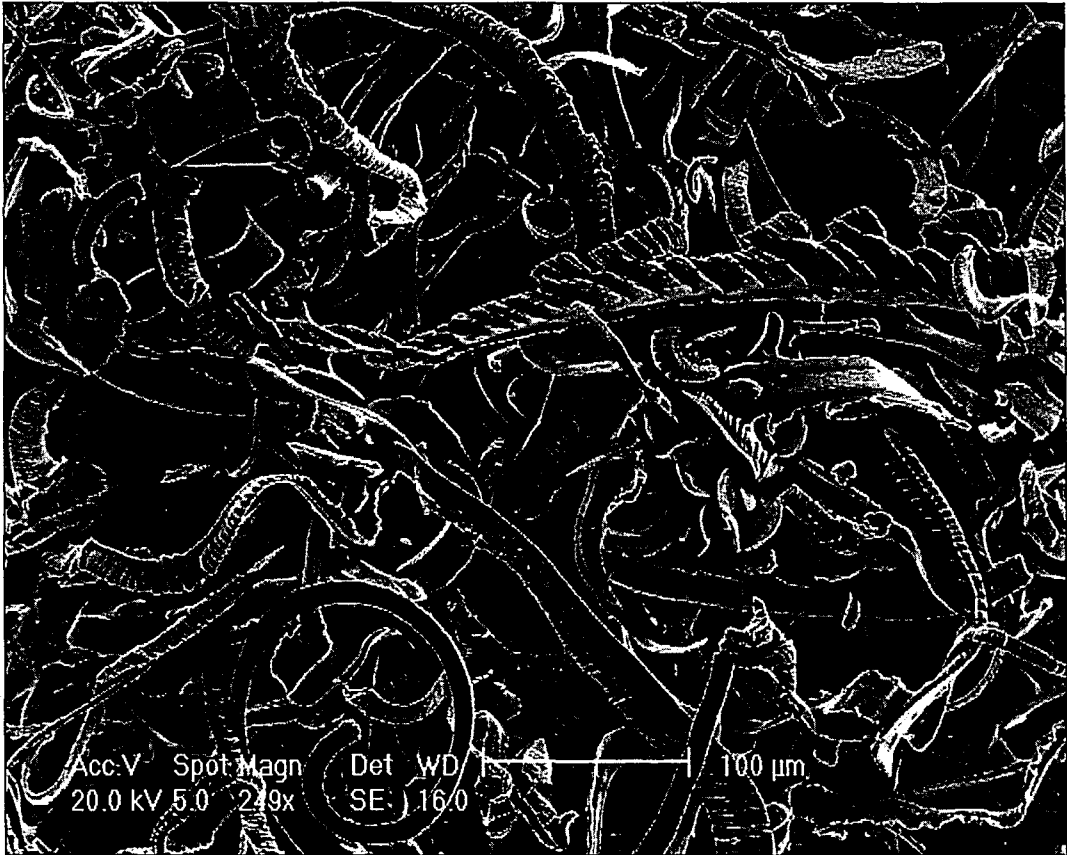
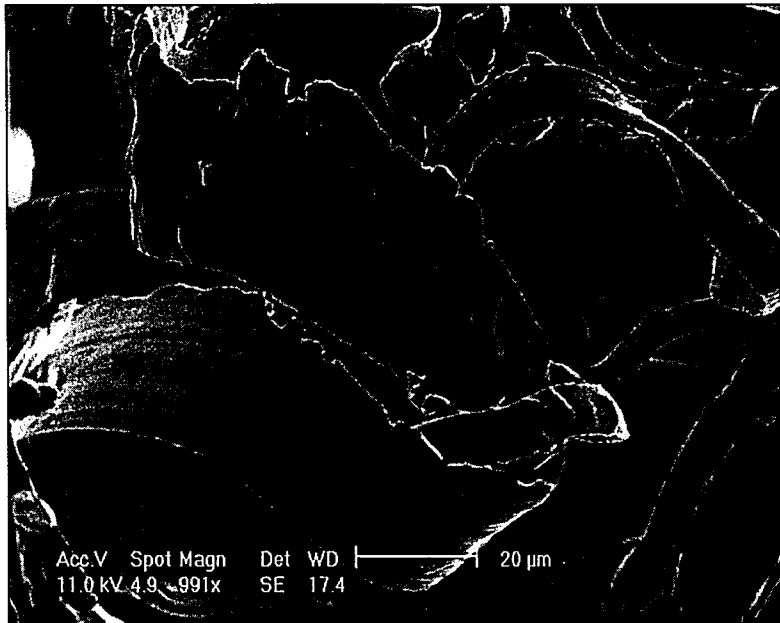


Figure 64: Collection of grinding chips with various shapes and sizes.



Figure 64: Collection of grinding chips with various shapes and sizes.

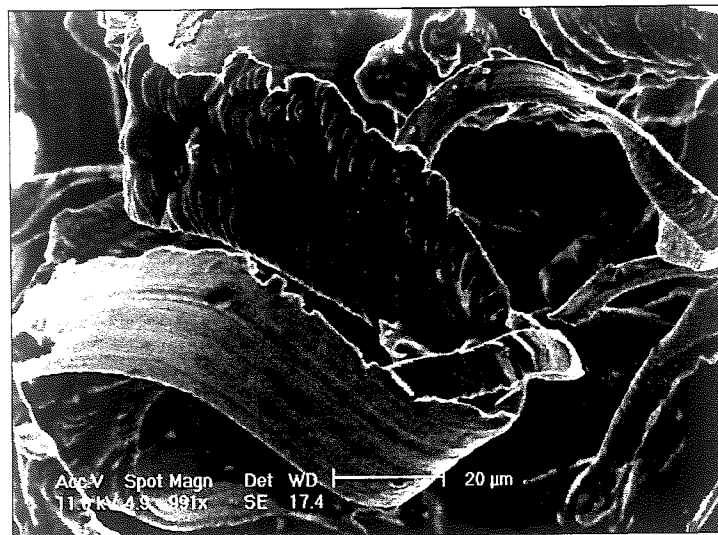


(a)

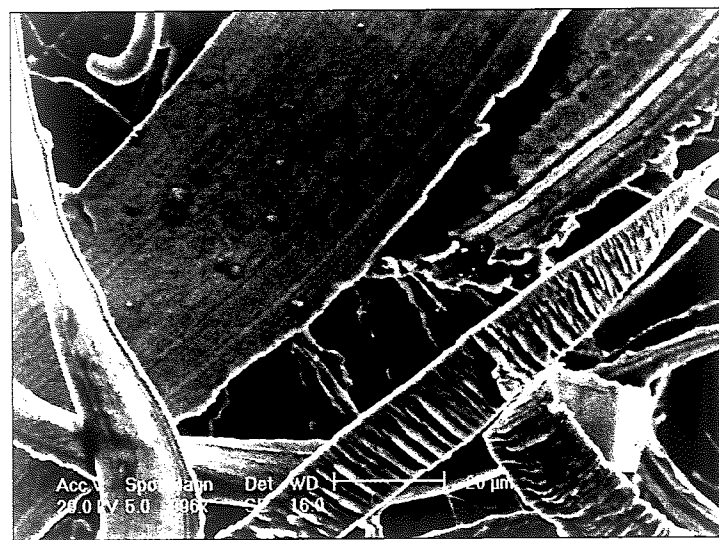


(b)

Figure 65: Serrated and smooth sides of grinding chips.



(a)



(b)

Figure 65: Serrated and smooth sides of grinding chips.

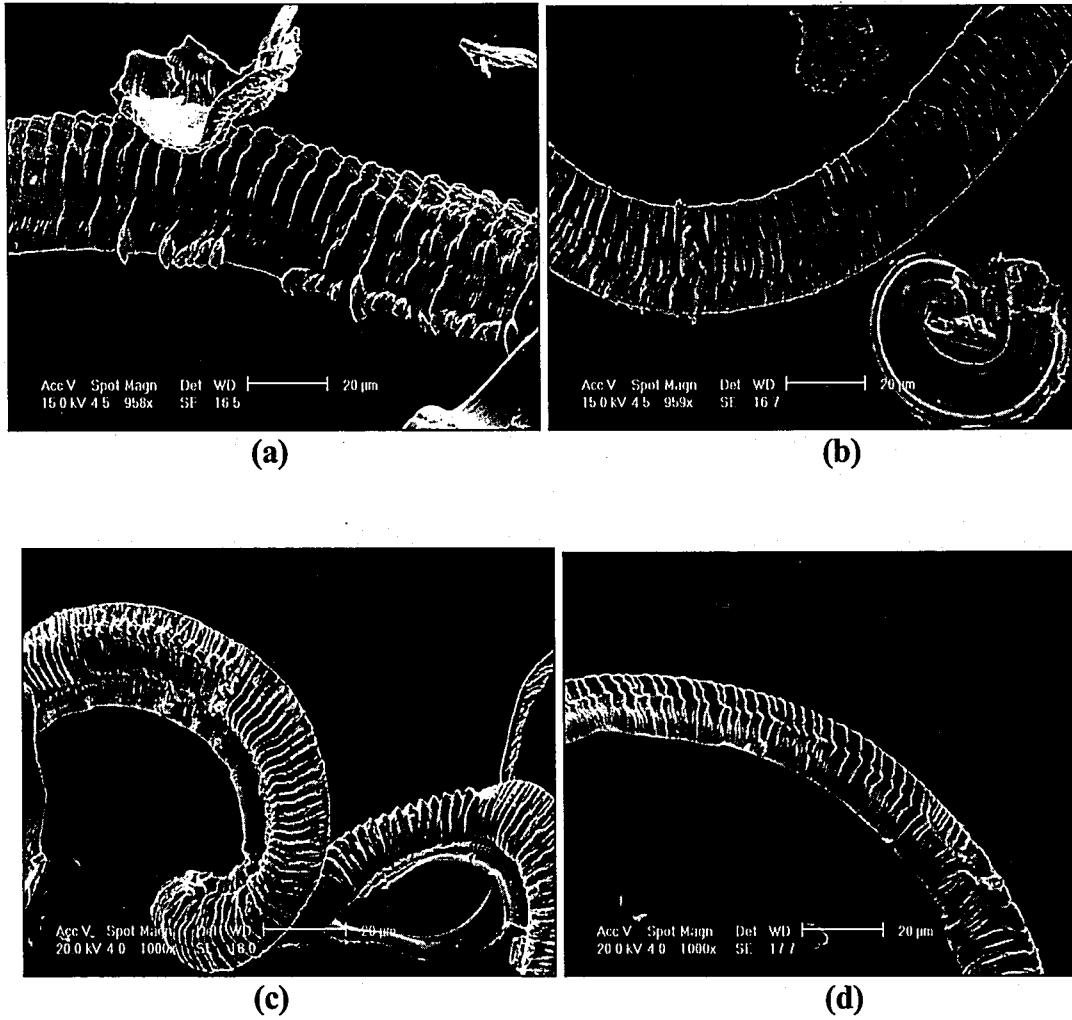


Figure 66: Curled chips with serration morphology visible for (a) Water-based A (b) Water-based B, (c) Water-based C, and (d) Oil Baseline fluids.

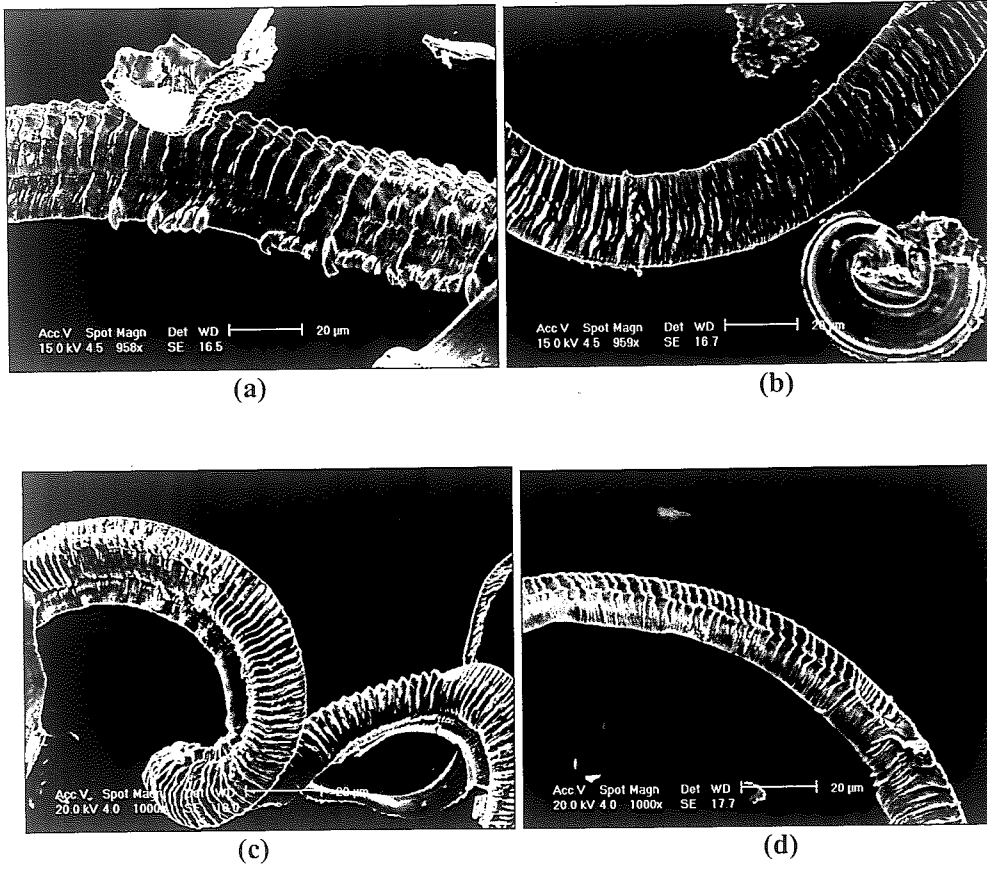


Figure 66: Curled chips with serration morphology visible for (a) Water-based A (b) Water-based B, (c) Water-based C, and (d) Oil Baseline fluids.

4.8 Grinding Wheels:

Grinding wheels were analyzed for all the fluid trials (water-based and oil) to determine the cause of failure (in the case of the water-based fluid trials) and to determine if wear existed on the wheel used with the oil coolant. Initial observations were made using an optical stereoscope. The surfaces of the grinding wheels used in the water-based fluid trials were loaded with alloy material of various amounts. Deposits were small in some areas, just covering a couple of abrasive grains, and large in others with deposits coating dozens of grains. Examples of these deposits are shown in **Figures 67** and **68**. Wheel loading was common to the wheels used in the water-based fluid trials, but was not observed on the grinding wheel run in the neat oil coolant.

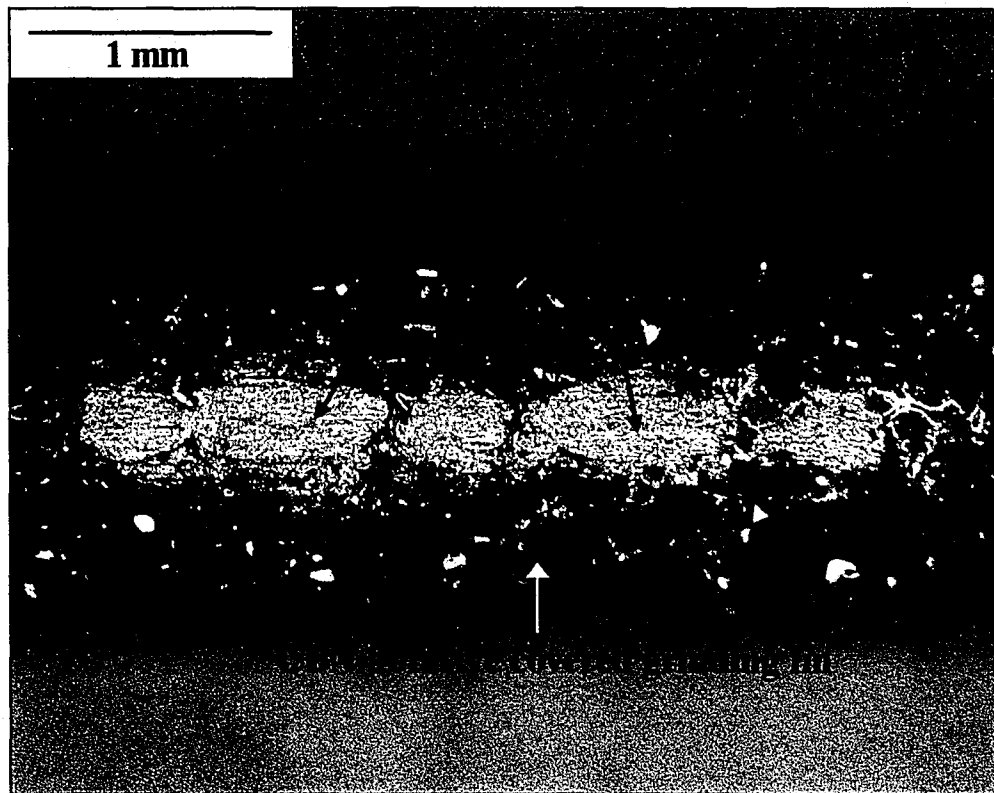


Figure 67: Large wheel deposit on the grinding wheel surface.

4.8 Grinding Wheels:

Grinding wheels were analyzed for all the fluid trials (water-based and oil) to determine the cause of failure (in the case of the water-based fluid trials) and to determine if wear existed on the wheel used with the oil coolant. Initial observations were made using an optical stereoscope. The surfaces of the grinding wheels used in the water-based fluid trials were loaded with alloy material of various amounts. Deposits were small in some areas, just covering a couple of abrasive grains, and large in others with deposits coating dozens of grains. Examples of these deposits are shown in Figures 67 and 68. Wheel loading was common to the wheels used in the water-based fluid trials, but was not observed on the grinding wheel run in the neat oil coolant.

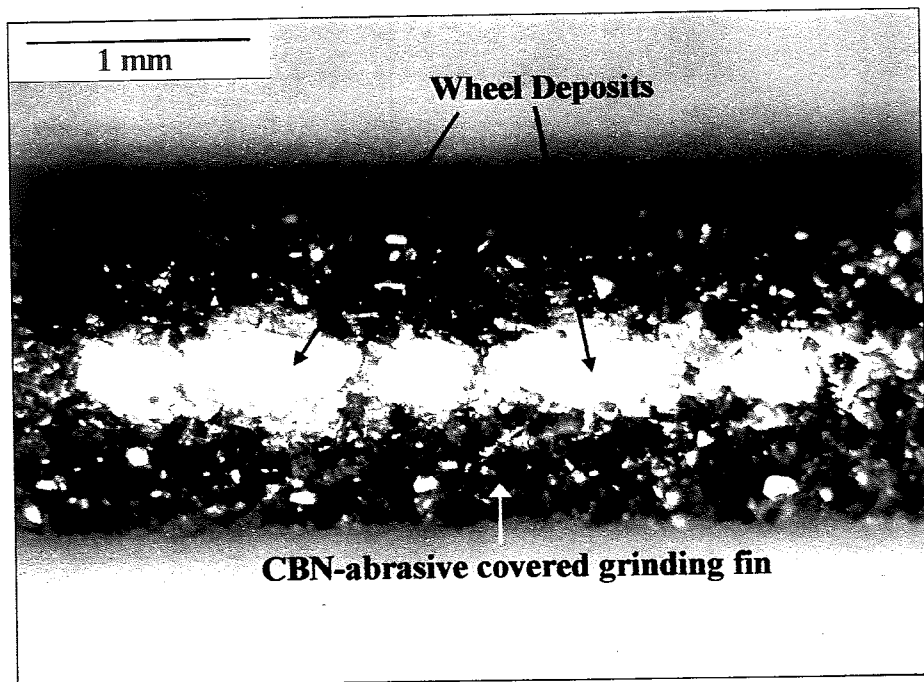


Figure 67: Large wheel deposit on the grinding wheel surface.

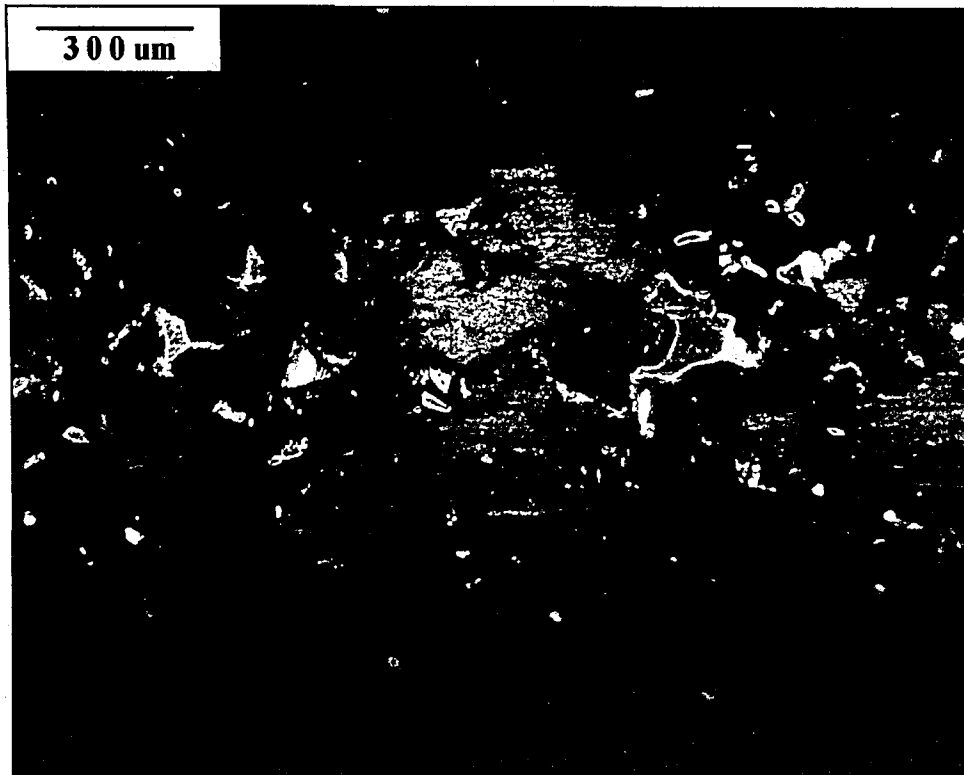


Figure 68: Image of a deposit showing grinding tracks in the direction of rotation.

Higher magnification was required for more in-depth assessment of the surfaces of the wheels. Grinding wheels were therefore sectioned to prepare samples for SEM and LOM analysis. Specimens from each wheel used in the water-based fluid testing were examined to determine the mechanism of deposition. Images from the investigation of the grinding wheels used in the water-based fluid trials are shown below (Figures 69-82). Figure 69 is an image of a small deposit, encapsulating one single abrasive grain. Chip adhesion to the abrasive grain is shown in Figure 70. Figures 71 and 72 show the deposit intimately adhering to the rake face of the abrasive grain; the self-supporting tail of the deposit hanging over the non-cutting face of the abrasive grain is shown in Figures 73 and 74. Material flow past the non-cutting face can be seen in Figure 75, and the flow of material over an adjacent grain

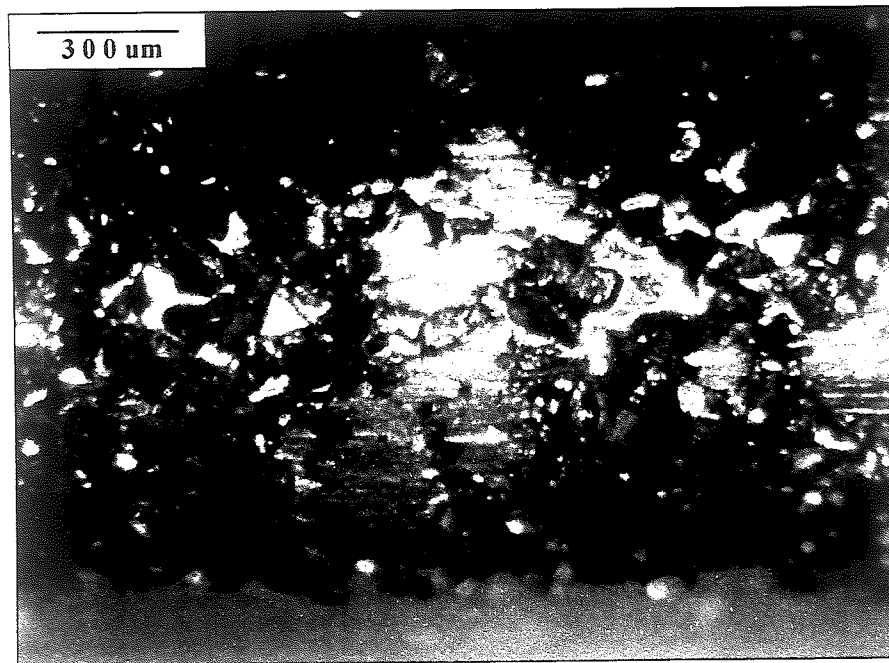


Figure 68: Image of a deposit showing grinding tracks in the direction of rotation.

Higher magnification was required for more in-depth assessment of the surfaces of the wheels. Grinding wheels were therefore sectioned to prepare samples for SEM and LOM analysis. Specimens from each wheel used in the water-based fluid testing were examined to determine the mechanism of deposition. Images from the investigation of the grinding wheels used in the water-based fluid trials are shown below (Figures 69-82). **Figure 69** is an image of a small deposit, encapsulating one single abrasive grain. Chip adhesion to the abrasive grain is shown in **Figure 70**. **Figures 71** and **72** show the deposit intimately adhering to the rake face of the abrasive grain; the self-supporting tail of the deposit hanging over the non-cutting face of the abrasive grain is shown in **Figures 73** and **74**. Material flow past the non-cutting face can be seen in **Figure 75**, and the flow of material over an adjacent grain

as the deposit builds is shown in **Figure 76**. **Figure 77** shows the direction of material flow on the rake face of the cutting grain as the deposit grows to a significant size. The layered morphology of the deposit is shown clearly in **Figure 78**. A profile view of a medium-sized deposit is shown in **Figure 79**. An example of the chips visible from the underside of the wheel deposits is shown in **Figure 80**. Cross-sectioned samples analyzed with LOM confirm that the underside of the deposits retains the chip morphology, without direct contact with lower height abrasive grains or the electroplated bond matrix. Examples of the underside morphology are shown in **Figures 81 and 82**.

Examination of the grinding wheel used in the Oil Baseline fluid study confirmed the absence of adhering material, as determined using the stereoscope. Inspection of the wheel surface proved that it was clean (see **Figures 83 and 84**), other than oil residue from the operation. Sharp grains like those seen in **Figure 85** were observed, indicating the grinding operation did not severely tax the cutting edges of the abrasive grains. No signs of wear were visible from inspection of the wheel.

A new grinding wheel was sectioned and analyzed to compare with the results from the examination of wheels used in the fluid trials. Abrasive grains on the new wheel had the same morphology as those observed on the other wheels. Initial conditions of the grinding wheel were characterized by features such as abrasive grain pullout in regions and over-plating in others (see **Figures 86 and 87**). Since it was impossible to examine the wheels used in the fluid trials at this magnification prior to

testing, it must be assumed that the starting condition of those wheels contained such manufacturing errors as well.



Figure 69: Encapsulation of a single CBN grain by adhering material.

testing, it must be assumed that the starting condition of those wheels contained such manufacturing errors as well.

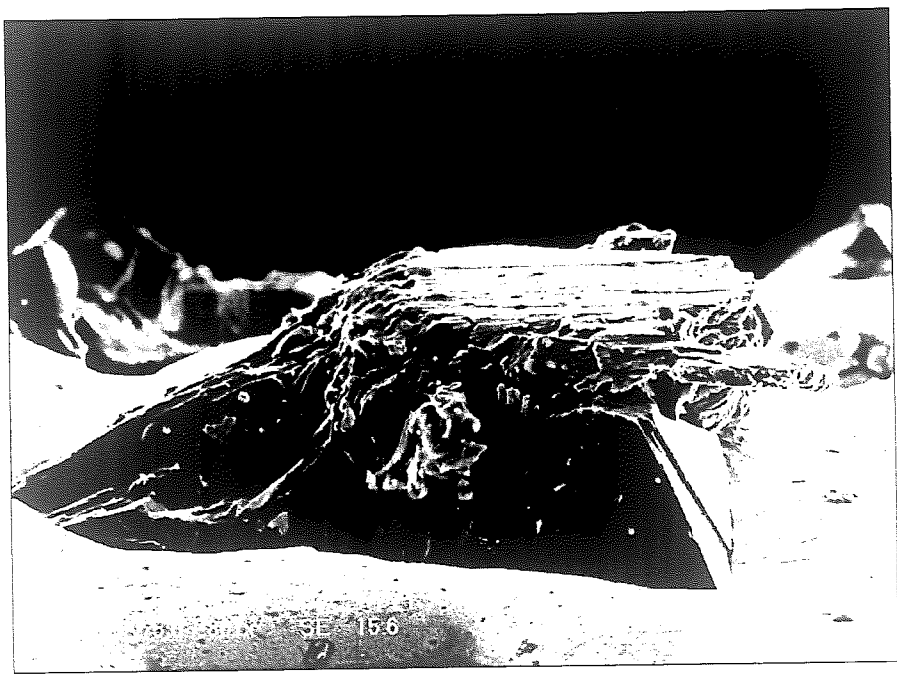


Figure 69: Encapsulation of a single CBN grain by adhering material.

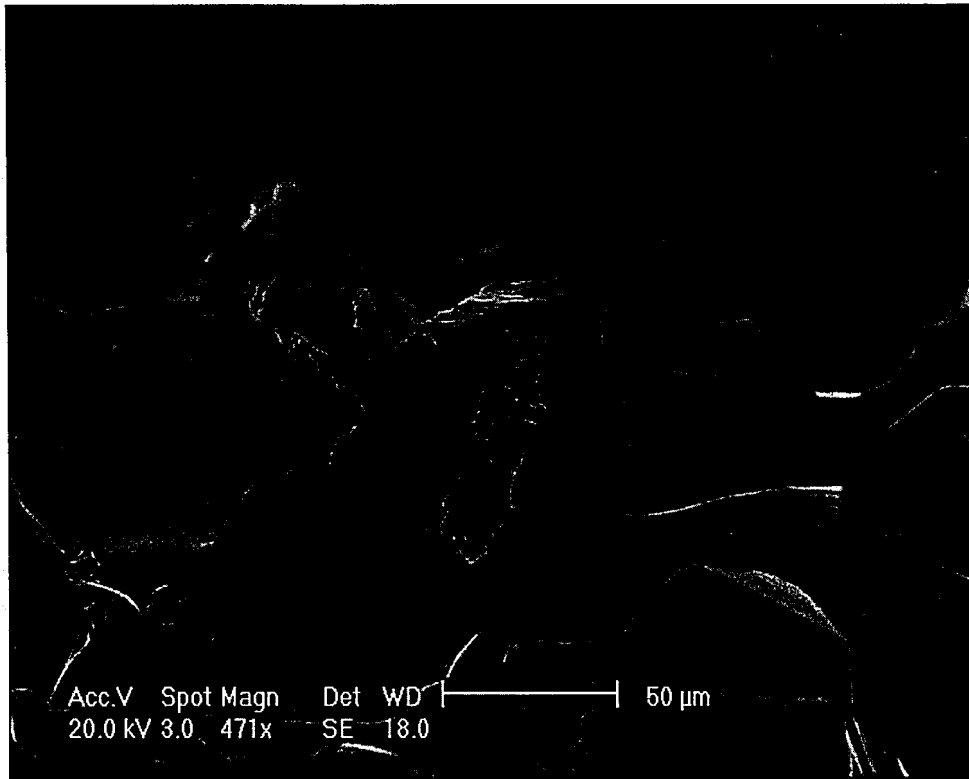


Figure 70: Chip adhesion on a single CBN abrasive grain.

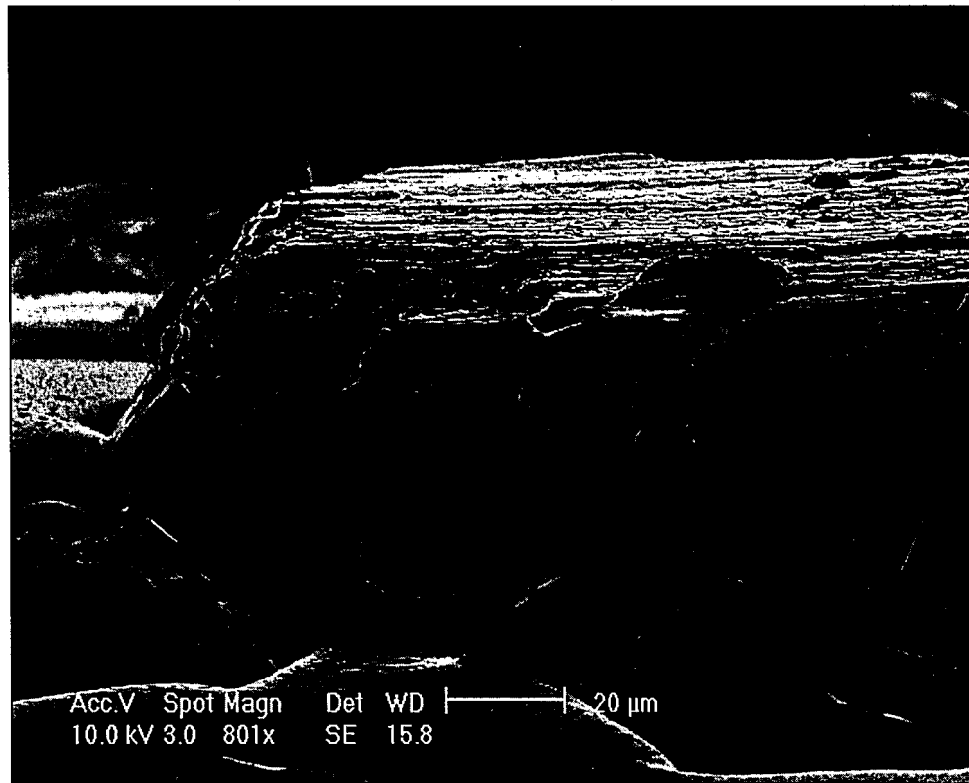


Figure 71: Deposit build-up at the abrasive grain's rake face.

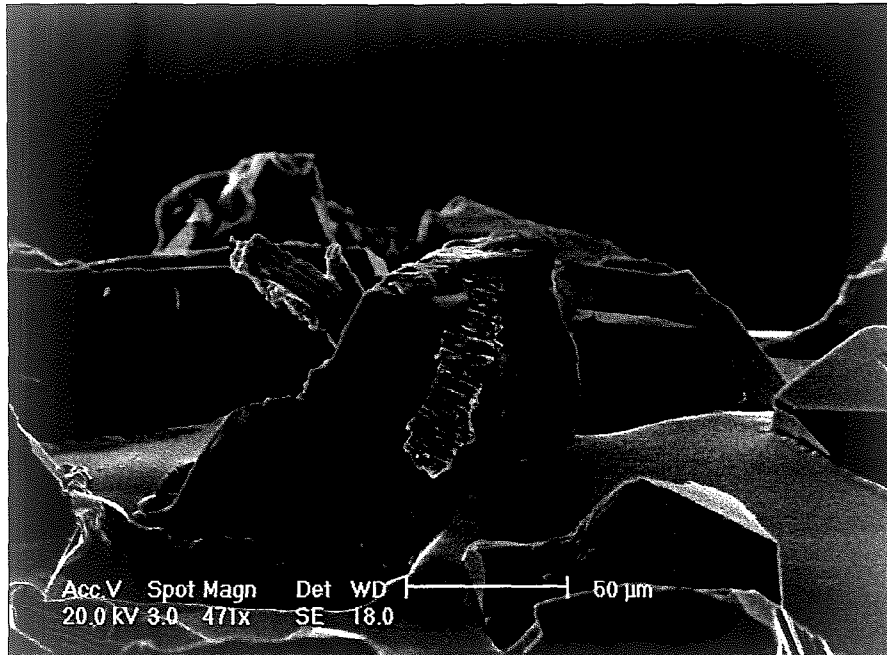


Figure 70: Chip adhesion on a single CBN abrasive grain.

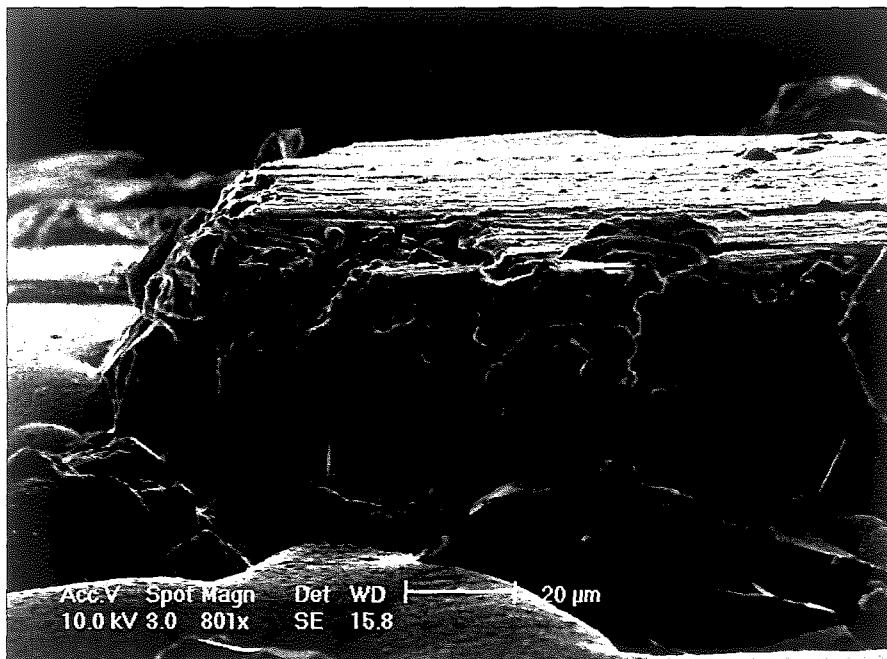


Figure 71: Deposit build-up at the abrasive grain's rake face.

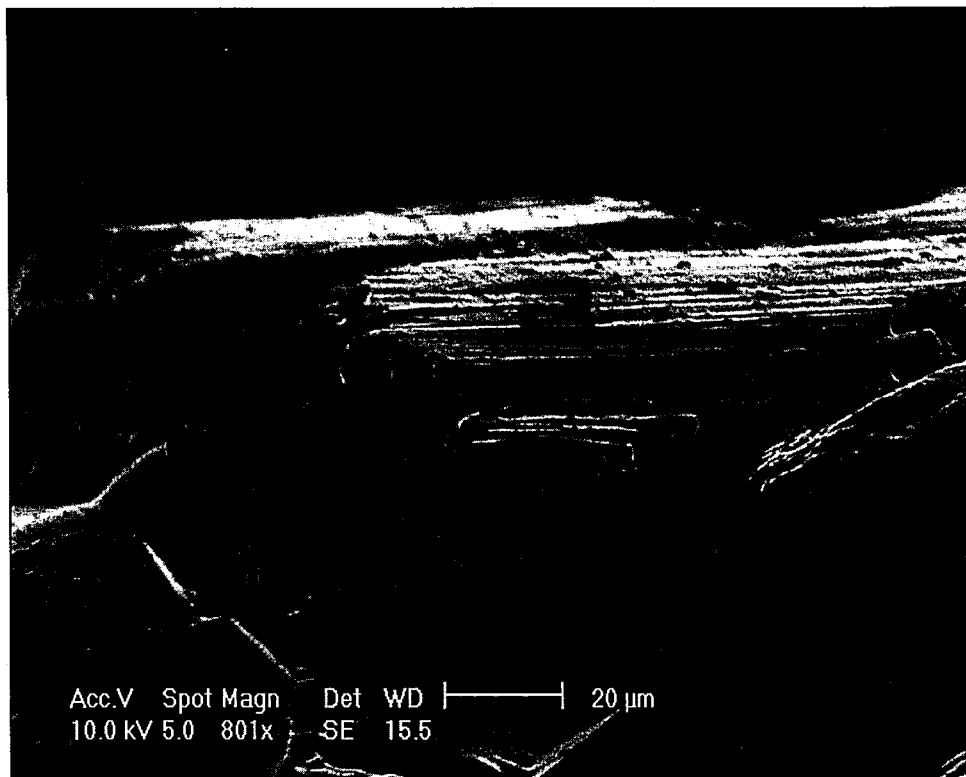


Figure 72: Intimate contact of the deposit at the rake face; track lines visible on top.

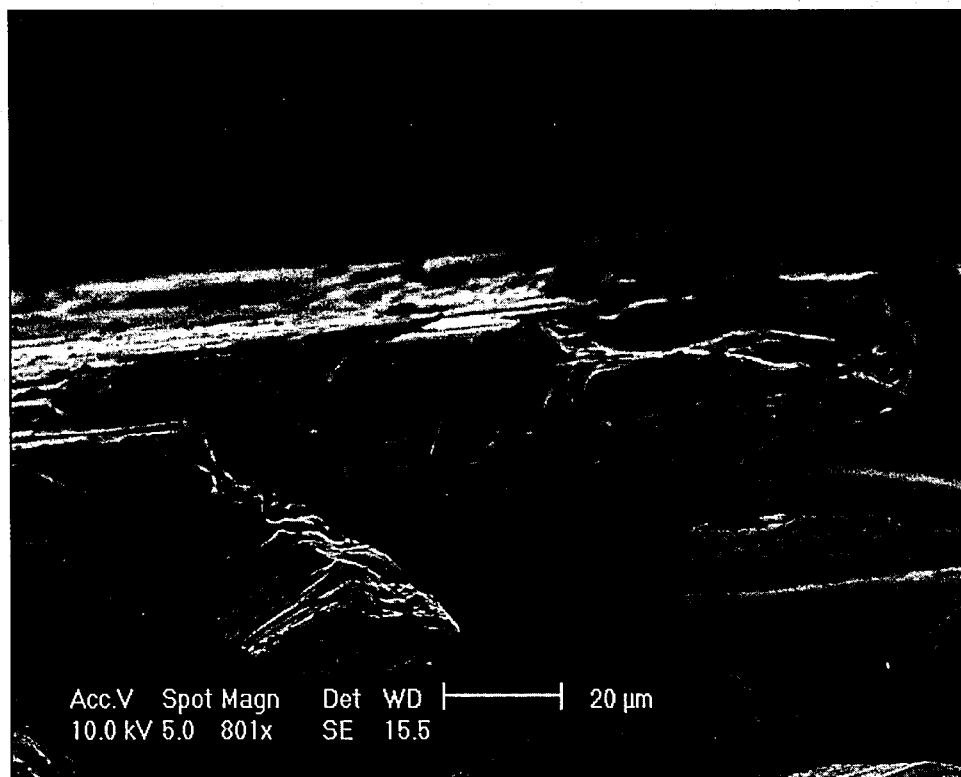


Figure 73: Self-supporting, trailing edge of a wheel deposit with chip morphology.

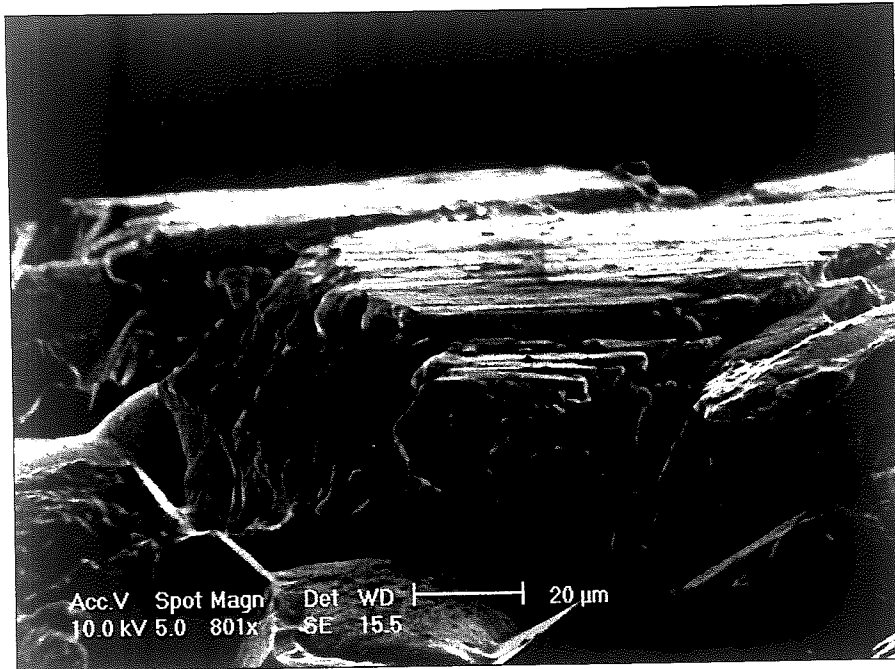


Figure 72: Intimate contact of the deposit at the rake face; track lines visible on top.

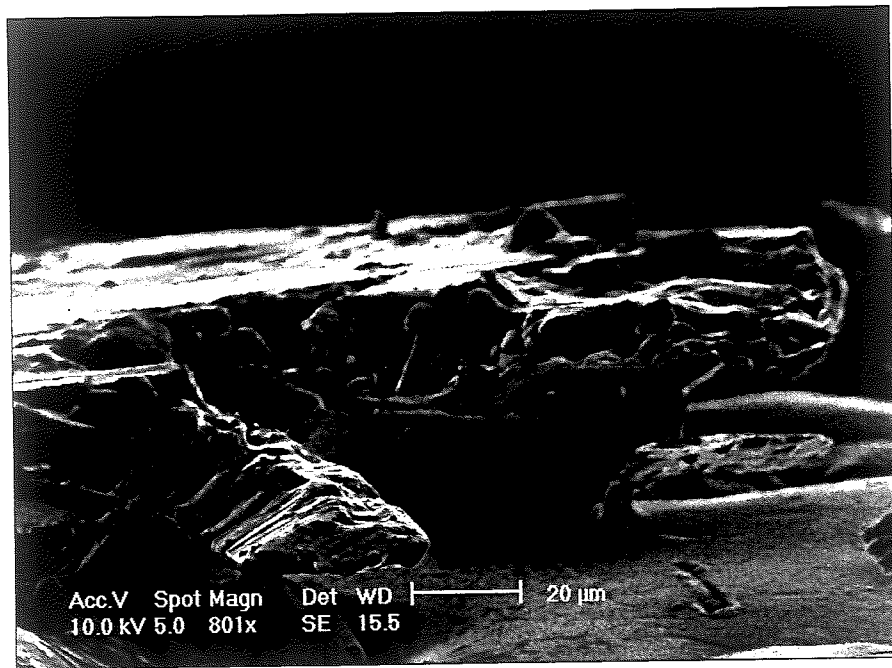


Figure 73: Self-supporting, trailing edge of a wheel deposit with chip morphology.

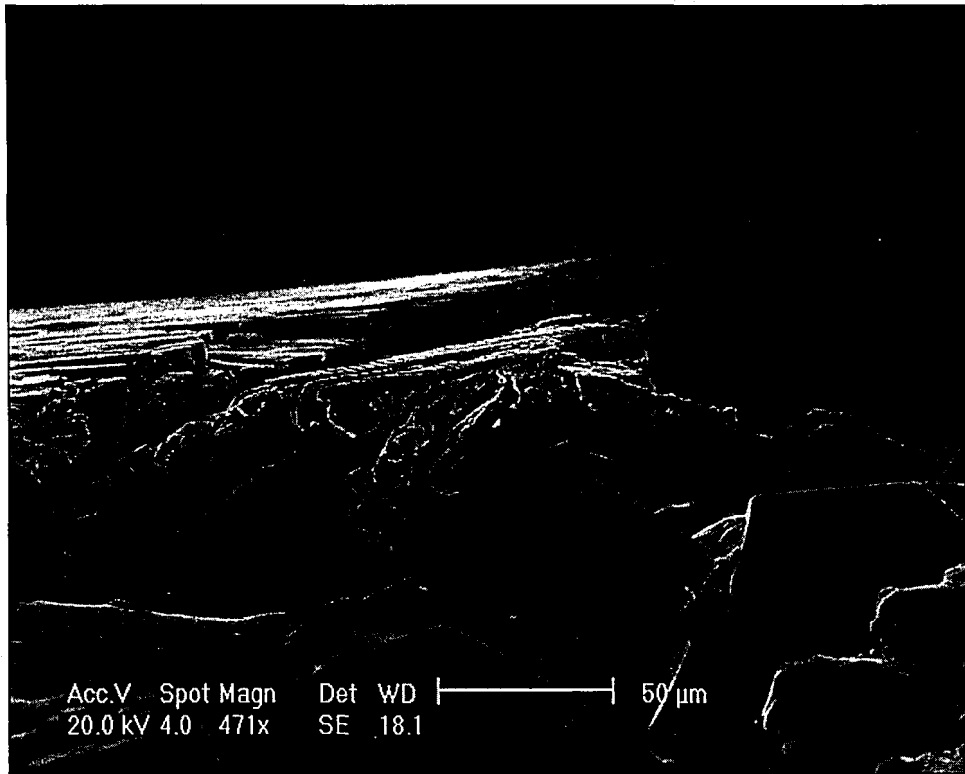


Figure 74: Deposit tail is not resting on abrasive grains or wheel bond.

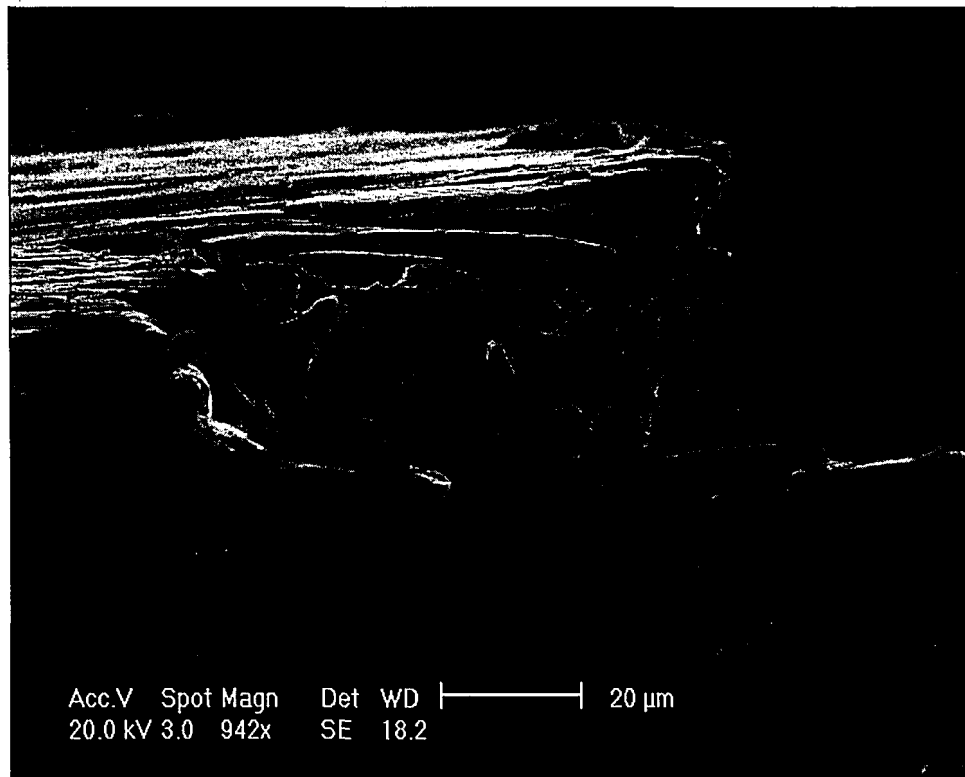


Figure 75: Material flow over the non-cutting face of the CBN grain.

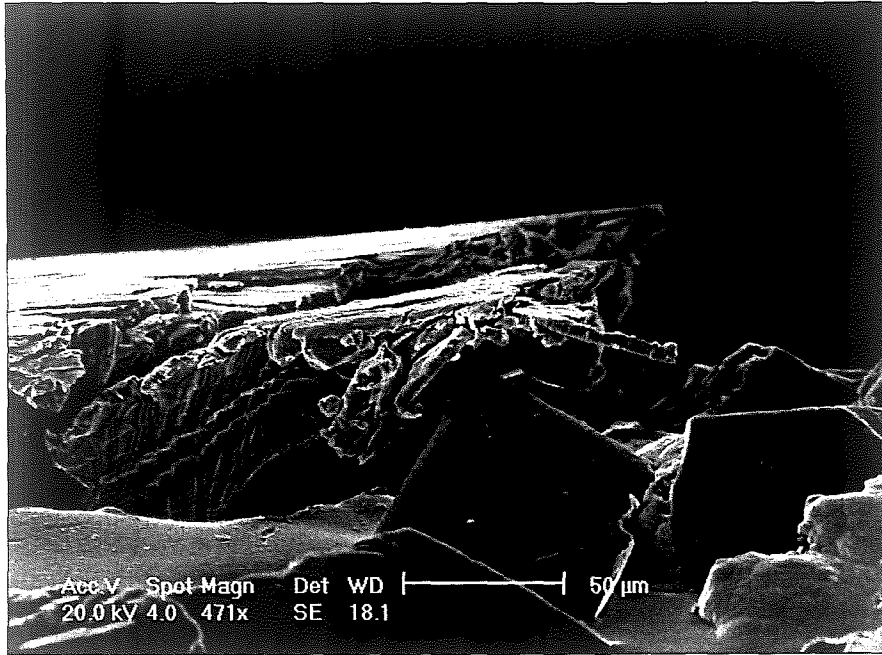


Figure 74: Deposit tail is not resting on abrasive grains or wheel bond.

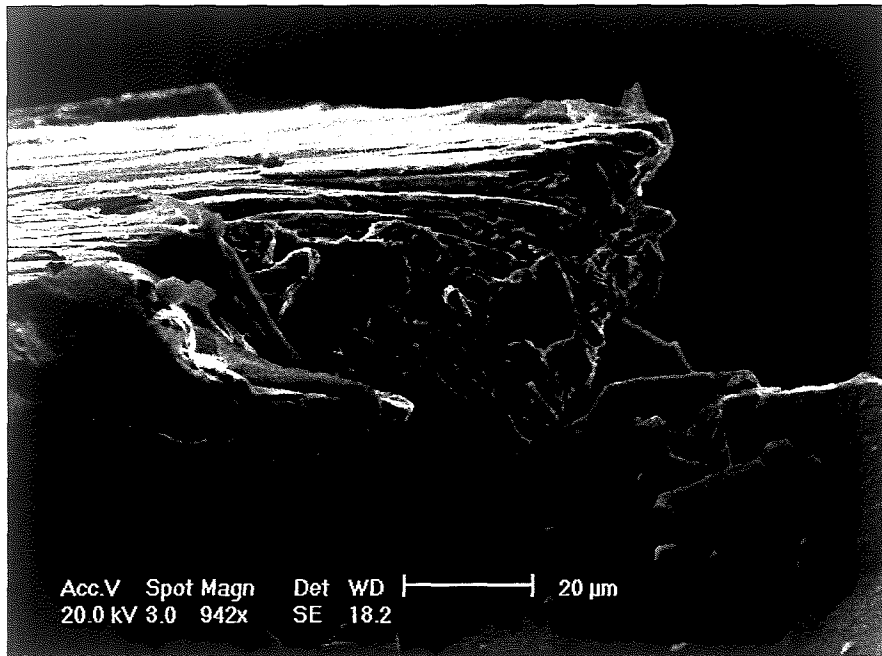


Figure 75: Material flow over the non-cutting face of the CBN grain.

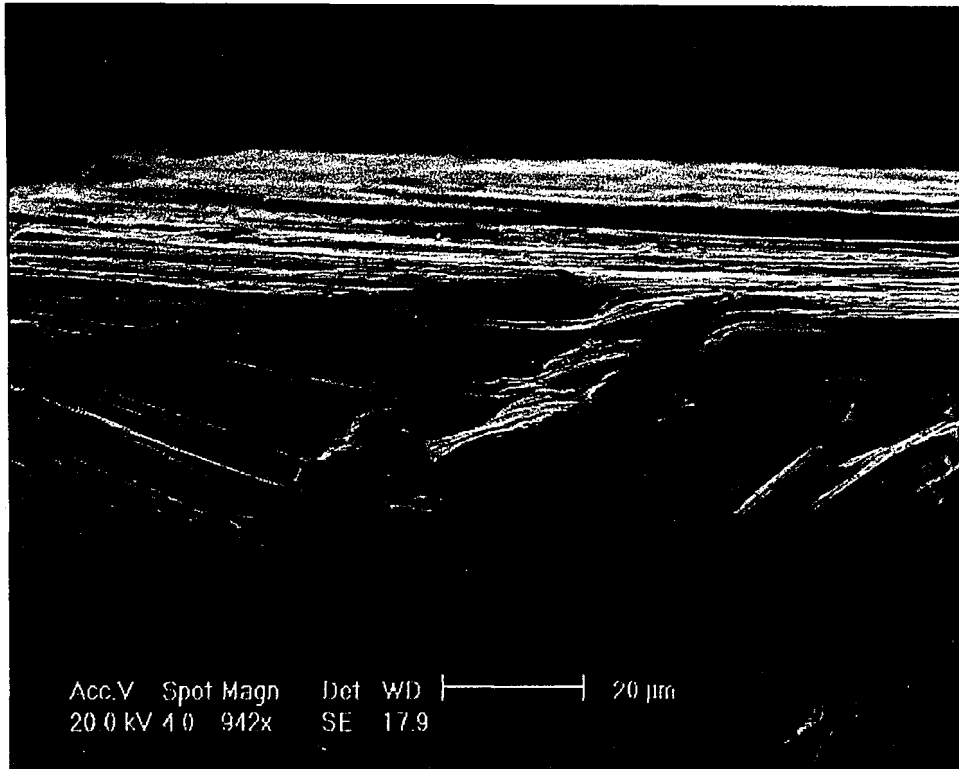


Figure 76: Material flow over grains encapsulated in a large deposit.



Figure 77: Build-up at the rake face showing the direction of material flow.

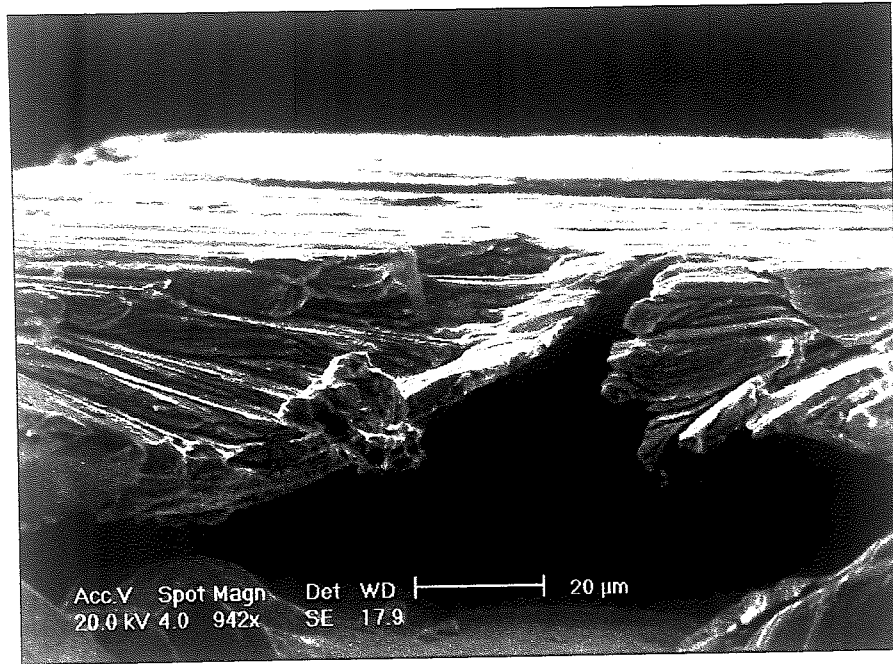


Figure 76: Material flow over grains encapsulated in a large deposit.

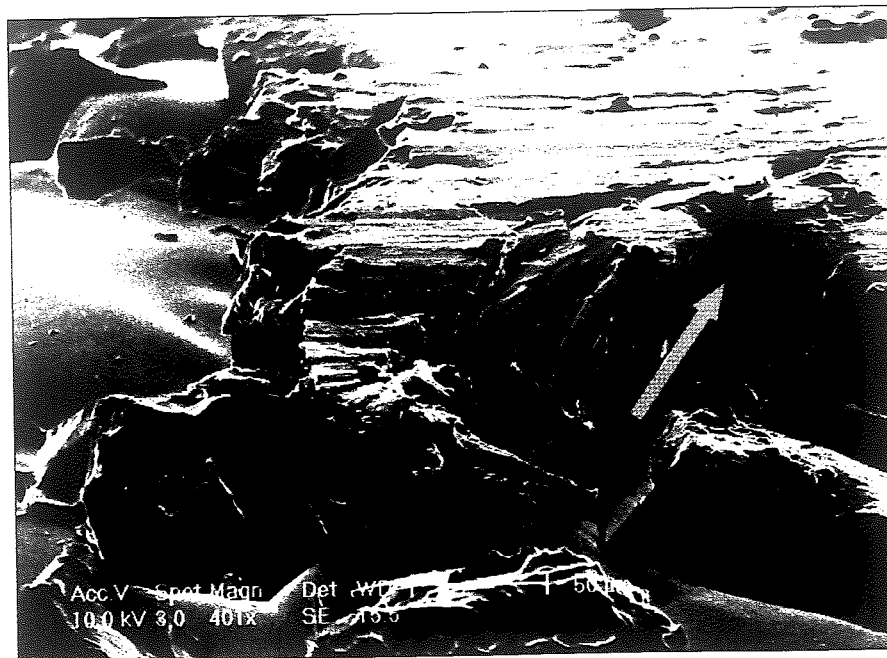


Figure 77: Build-up at the rake face showing the direction of material flow.

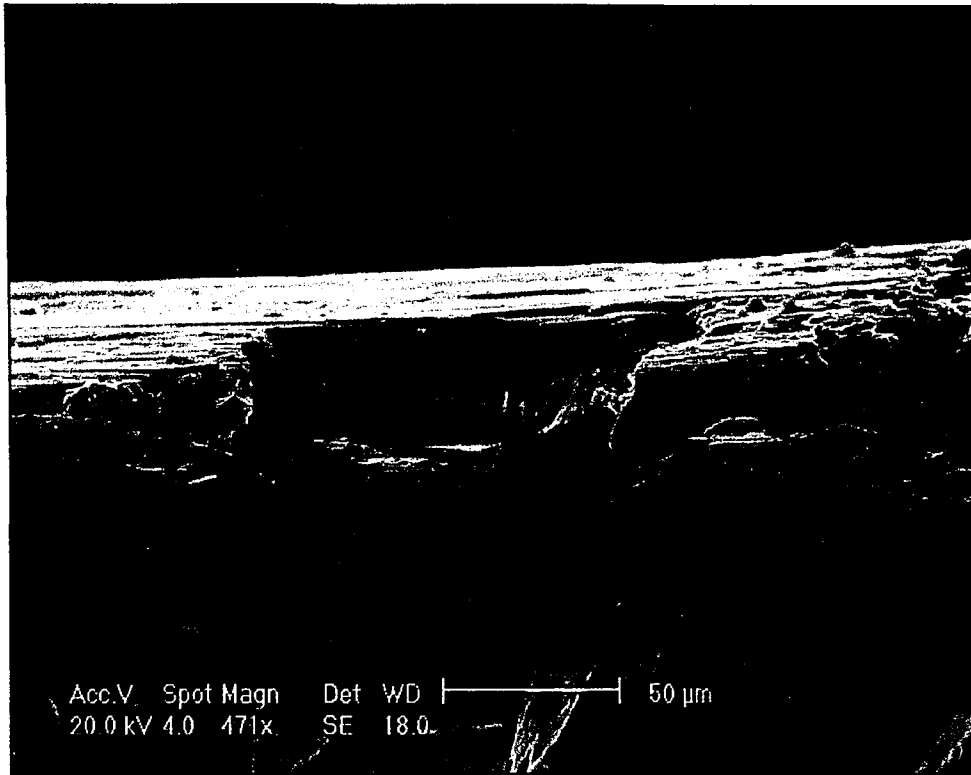


Figure 78: Layered morphology of the deposit visible.

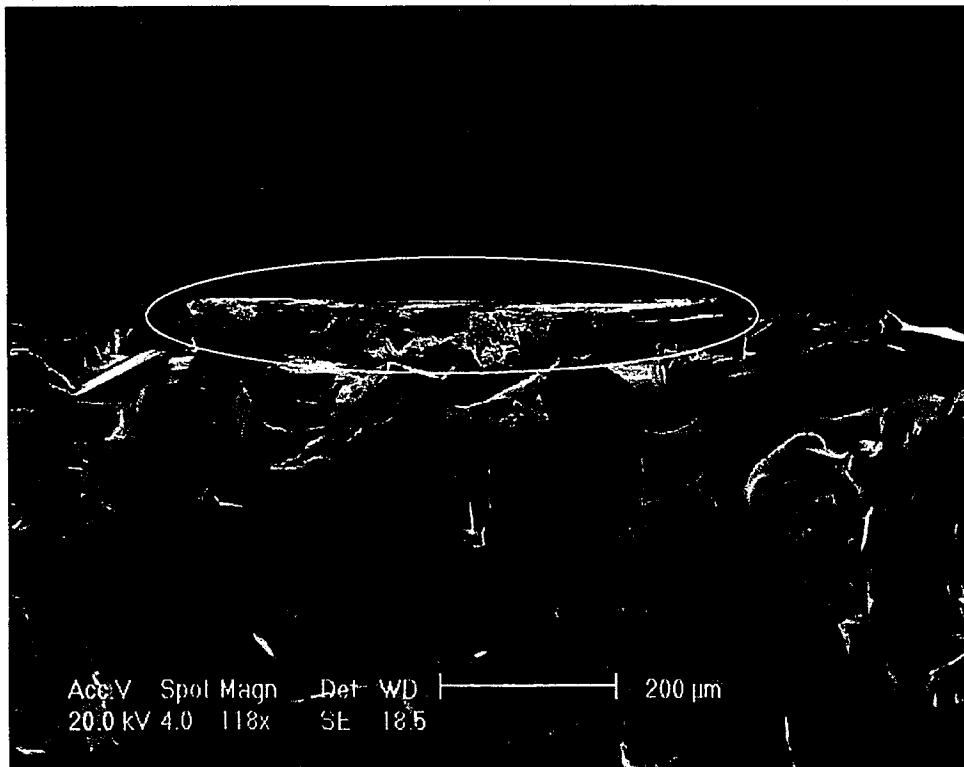


Figure 79: Profile view of a medium-sized wheel deposit.

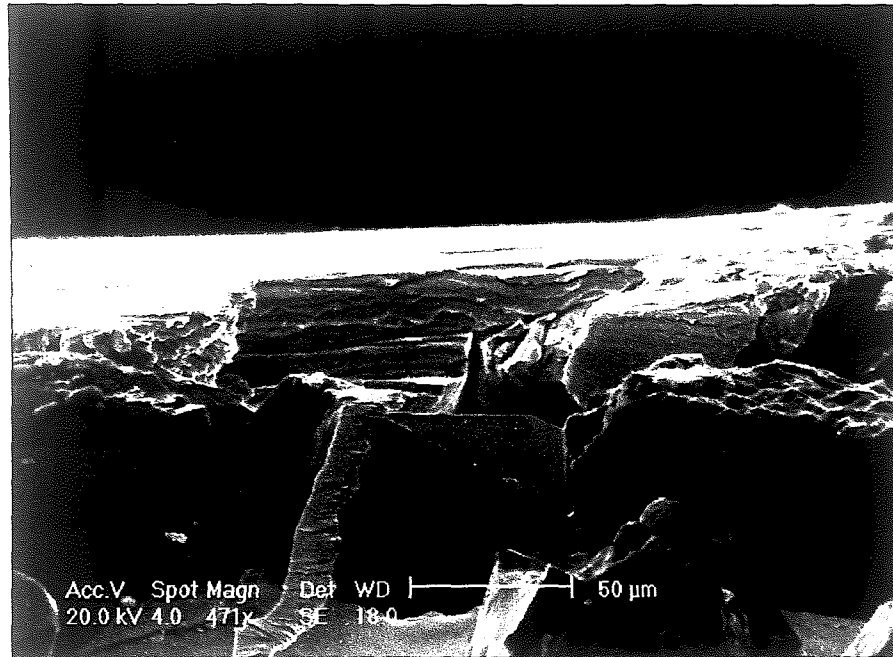


Figure 78: Layered morphology of the deposit visible.

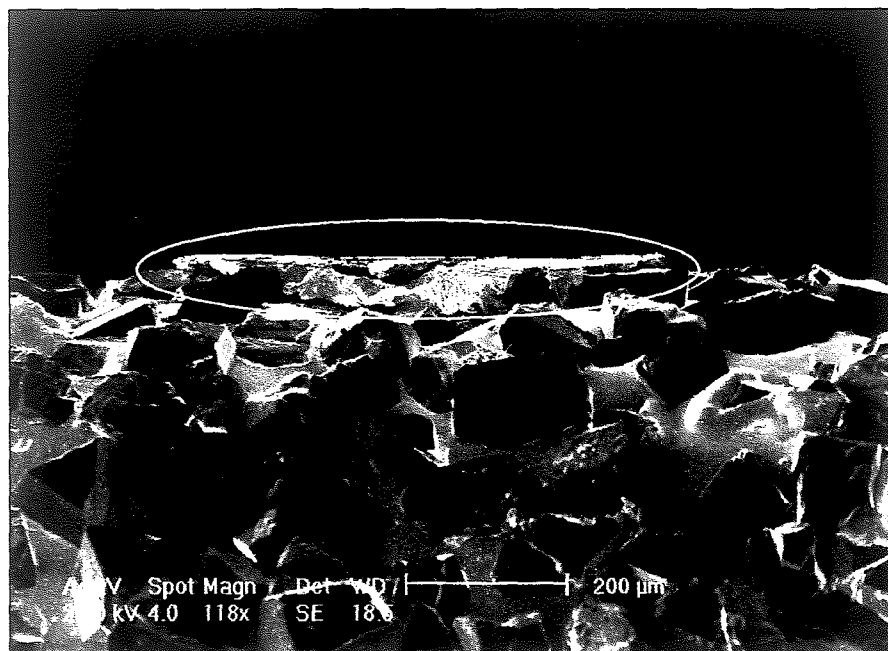


Figure 79: Profile view of a medium-sized wheel deposit.

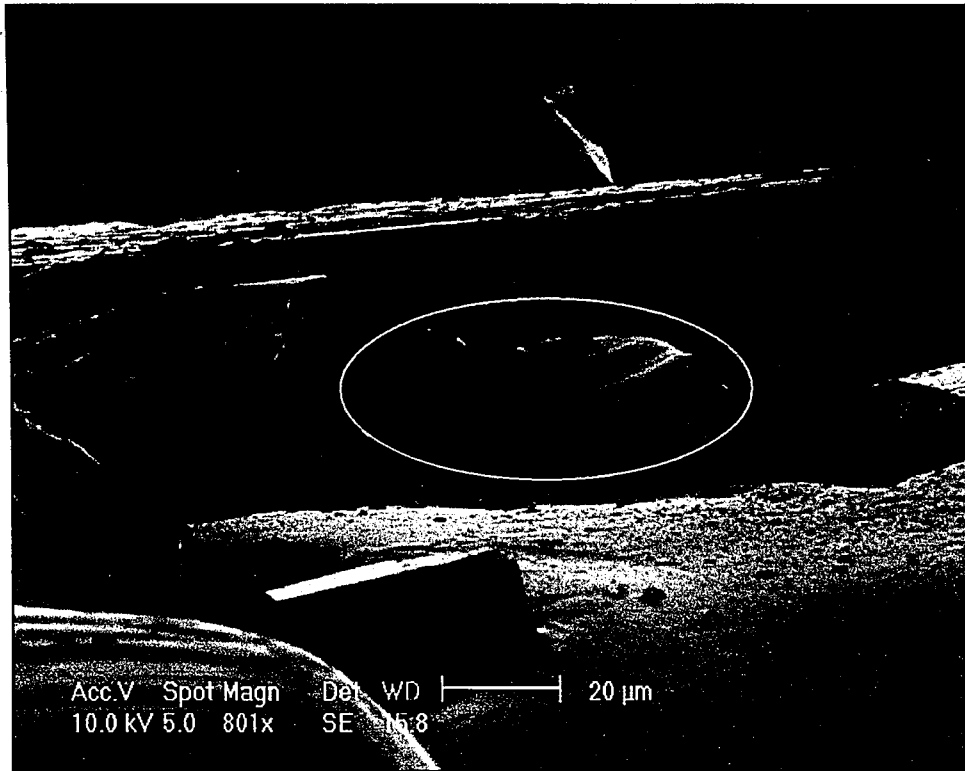


Figure 80: Grinding chip visibly coming from the deposit.

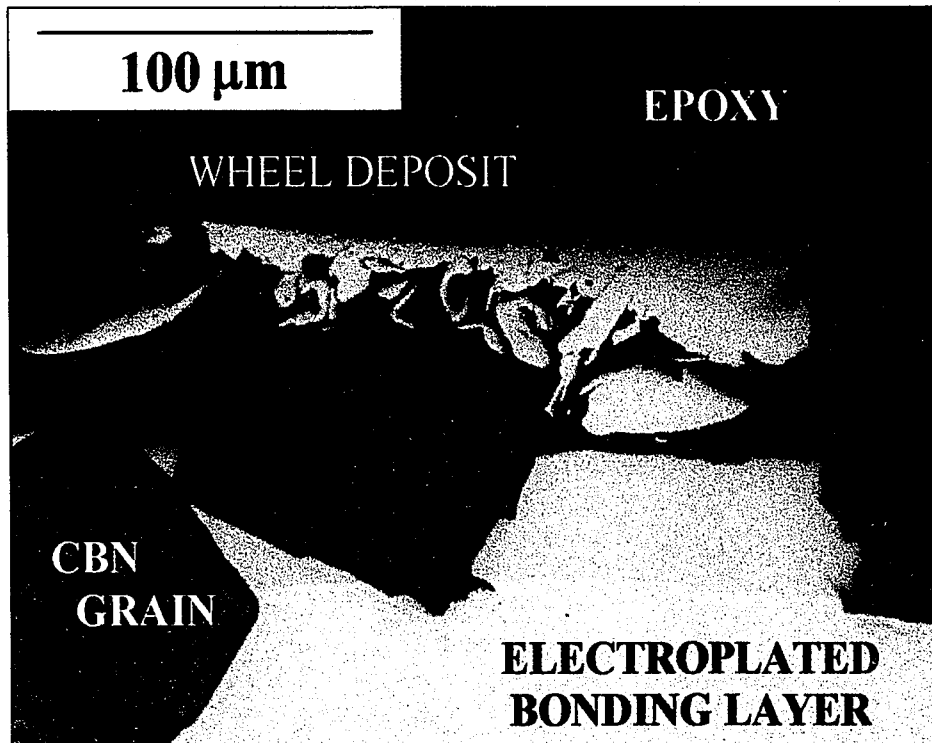


Figure 81: Chip morphology in the underside of deposit without direct contact with lower height CBN abrasive grains.

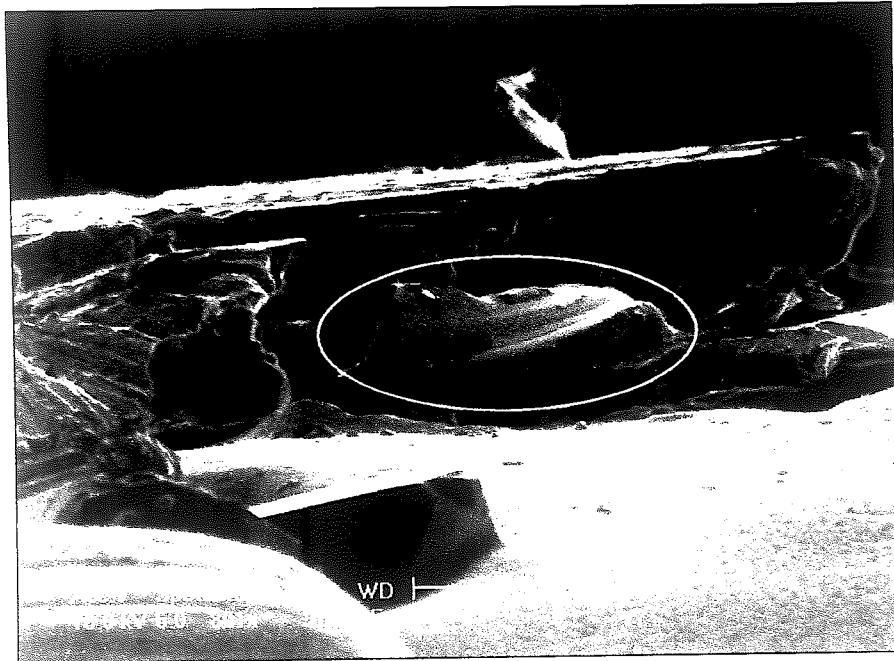


Figure 80: Grinding chip visibly coming from the deposit.

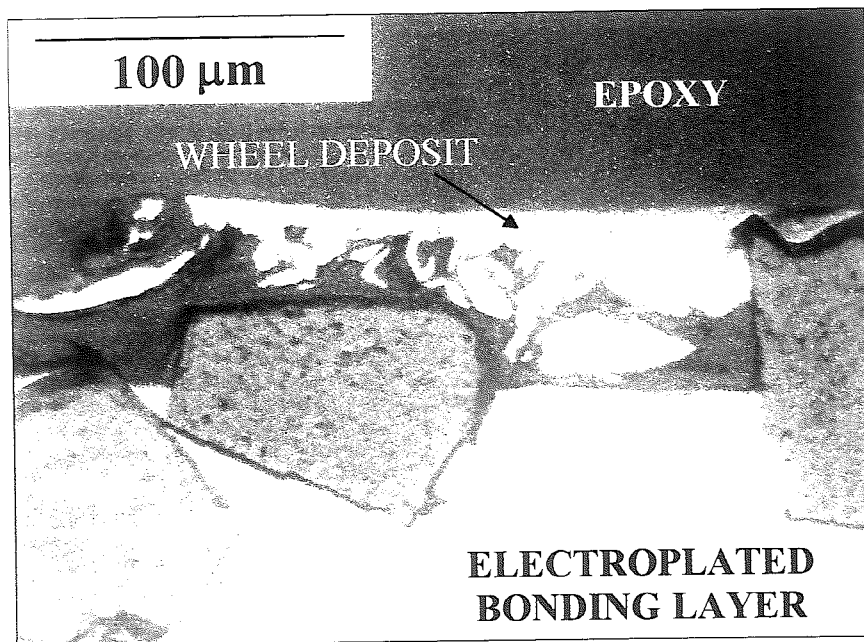


Figure 81: Chip morphology in the underside of deposit without direct contact with lower height CBN abrasive grains.

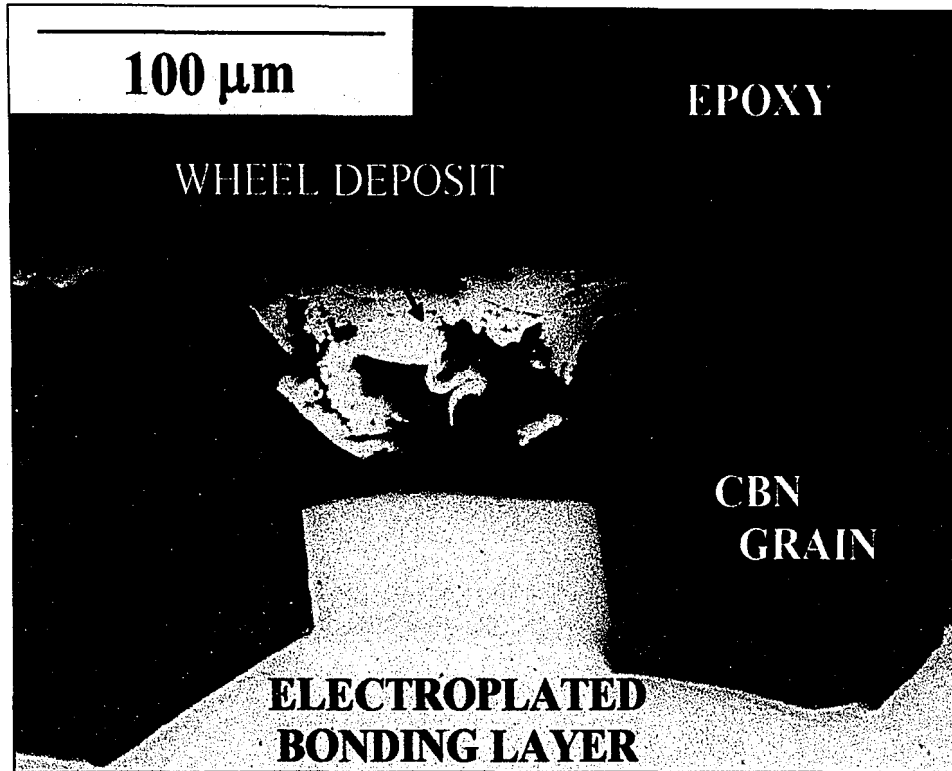


Figure 82: Wheel deposit with chip morphology on the underside, no damage to the CBN electroplated matrix layer is visible.

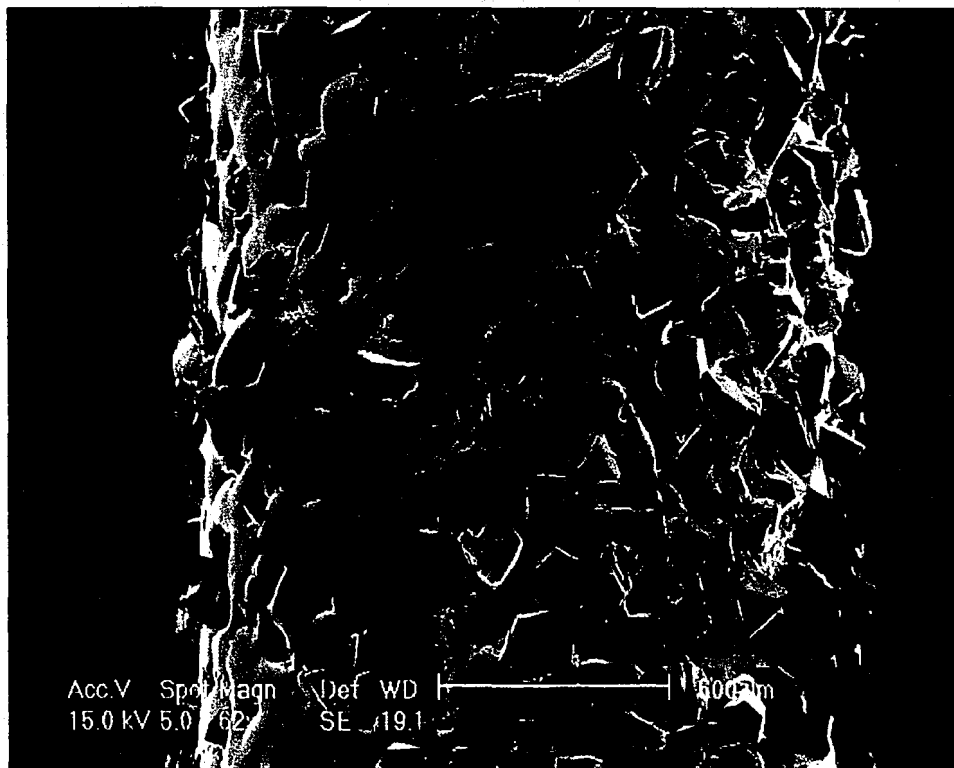


Figure 83: Grinding wheel used in the neat oil study shows no signs of loading.

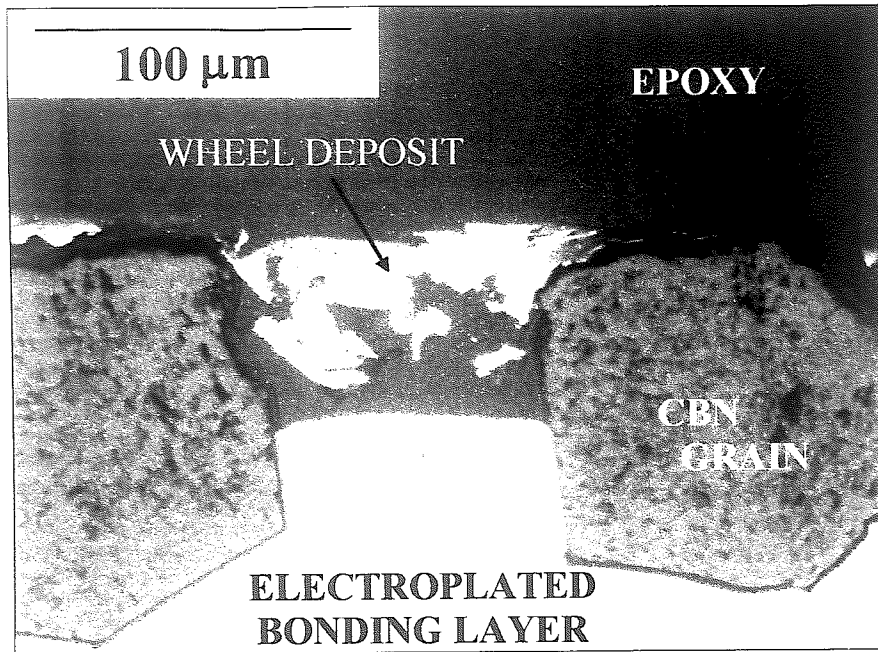


Figure 82: Wheel deposit with chip morphology on the underside, no damage to the CBN electroplated matrix layer is visible.

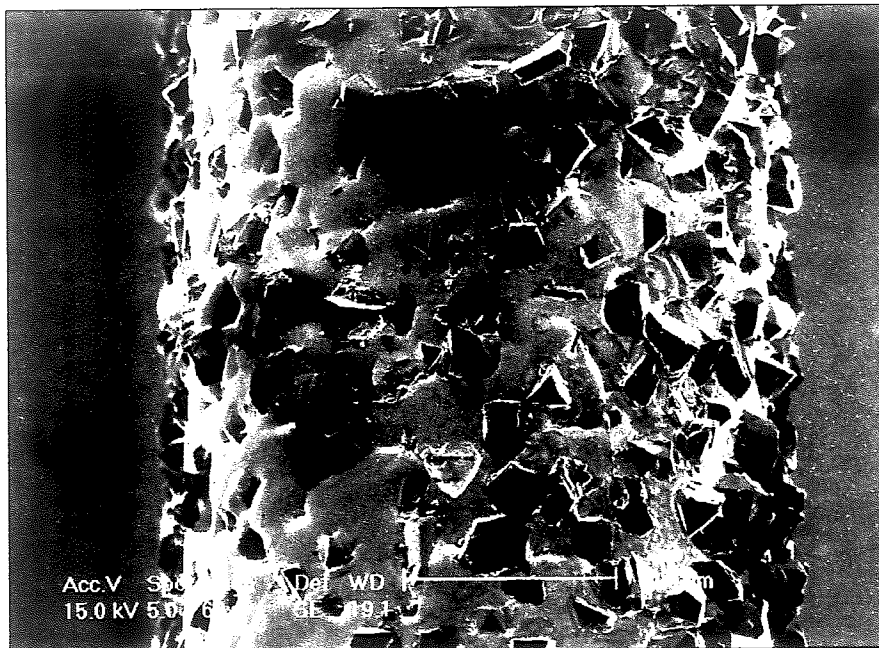


Figure 83: Grinding wheel used in the neat oil study shows no signs of loading.



Figure 84: Clear surface of the grinding wheel used in the oil fluid trial, some abrasive grains missing on the surface are circled.

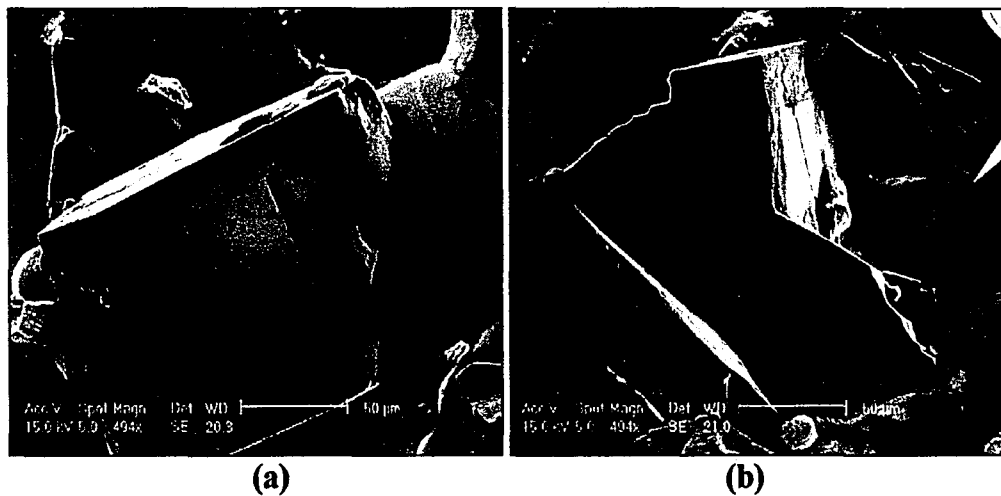


Figure 85: Sharp abrasive grains are observed on the surface of the wheel used with the oil, despite its completion of 120 grinding passes.

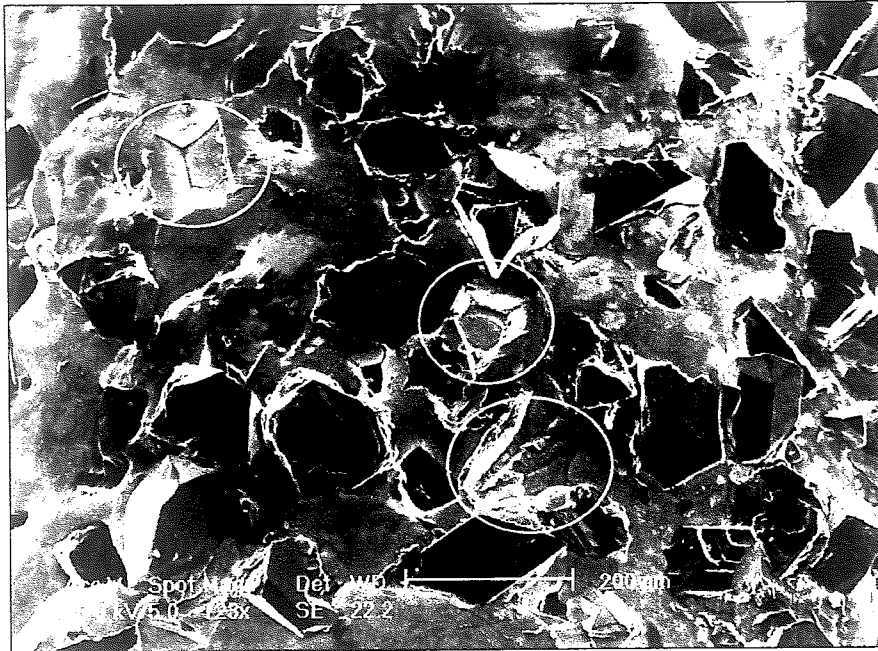


Figure 84: Clear surface of the grinding wheel used in the oil fluid trial, some abrasive grains missing on the surface are circled.

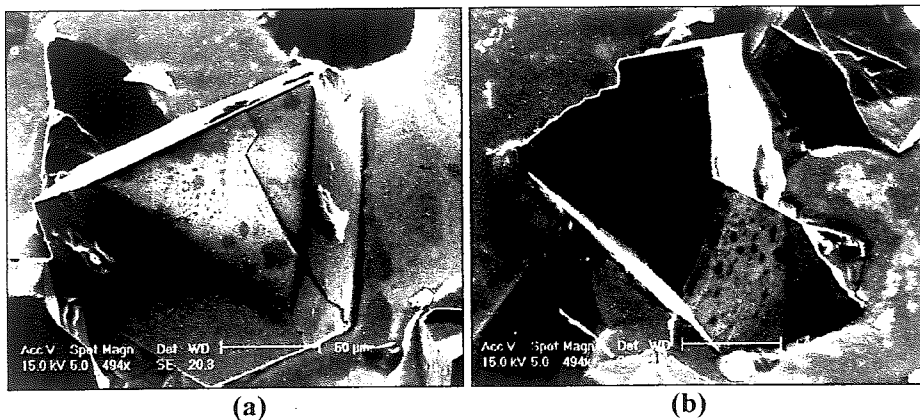


Figure 85: Sharp abrasive grains are observed on the surface of the wheel used with the oil, despite its completion of 120 grinding passes.

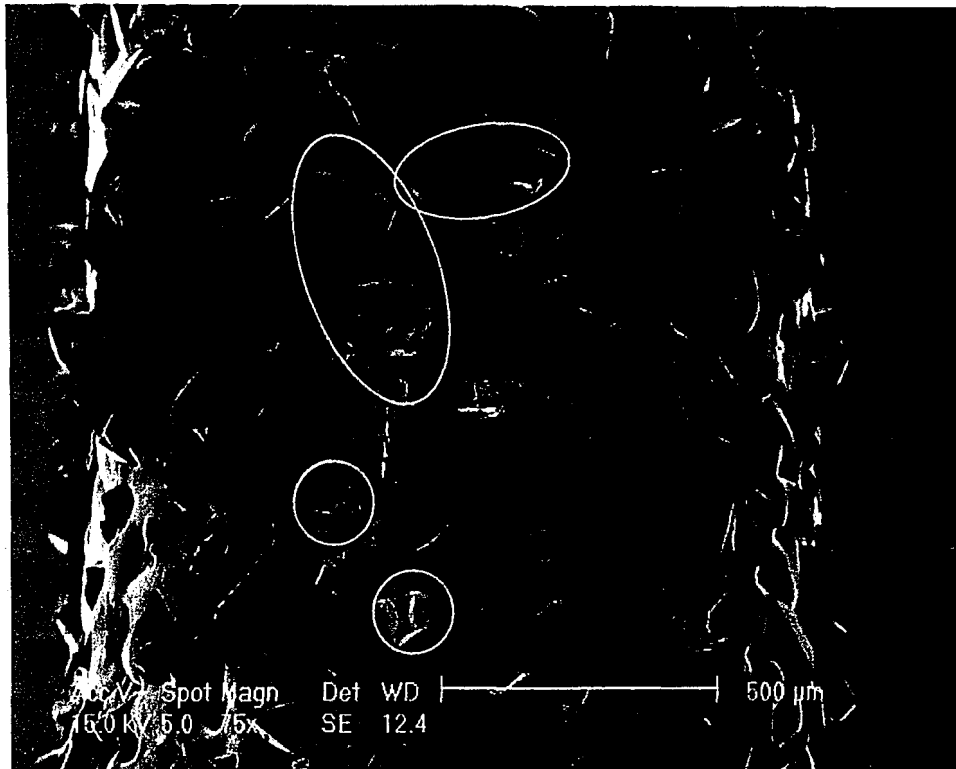


Figure 86: New wheel showing clean surface with regions (circled) where significant numbers of CBN grains are missing.

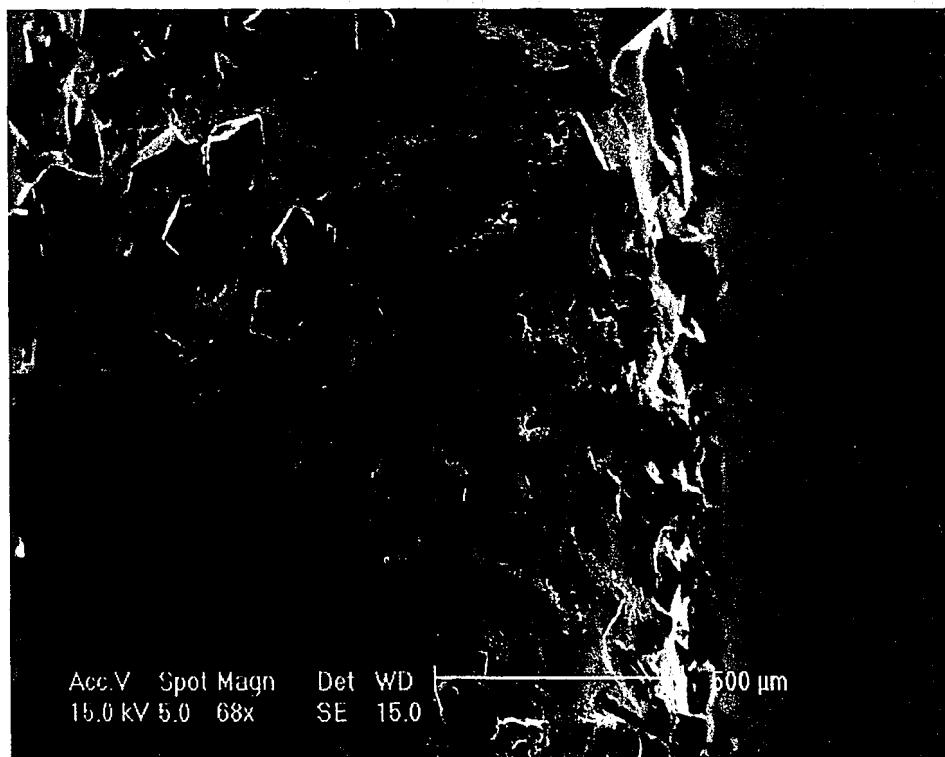


Figure 87: New wheel with a region of missing and/or overplated CBN grains.

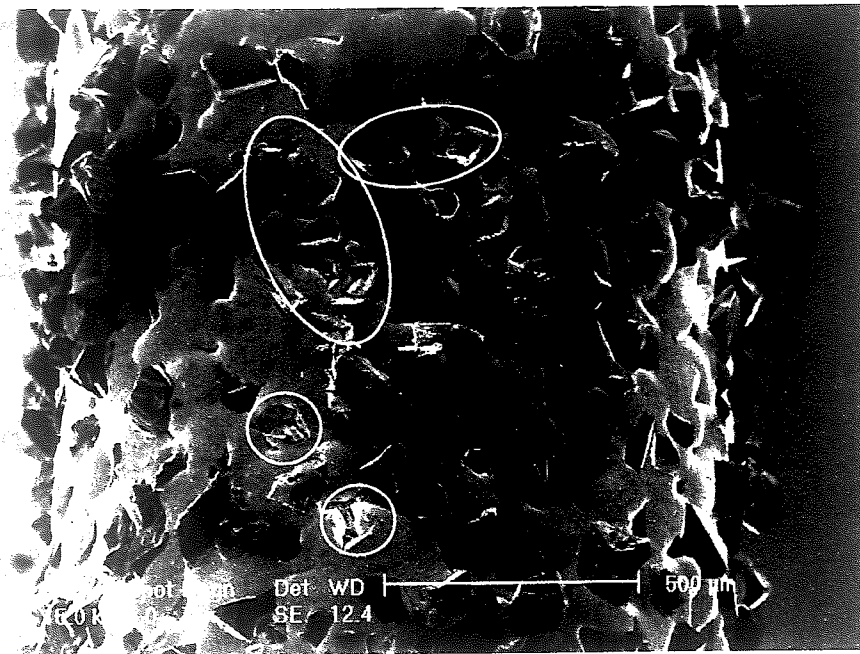


Figure 86: New wheel showing clean surface with regions (circled) where significant numbers of CBN grains are missing.

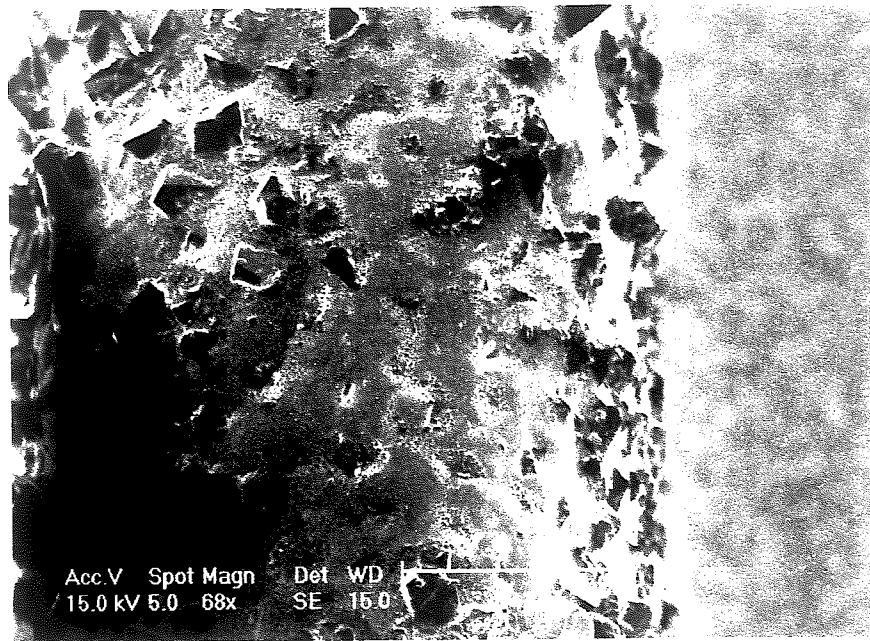


Figure 87: New wheel with a region of missing and/or overplated CBN grains.

4.9 CBN Abrasive Grains:

Samples of CBN 500 abrasive grains were obtained and used as references for the shape and surface structure of this abrasive material prior to grinding. SEM imaging of these particles revealed that the shape of individual particles varied considerably. Rough surface markings were observed on the faces of many abrasive grains. **Figures 2-4**, previously shown, illustrate this variation in shape and the nature of the visible surface roughness. **Figure 88** shows a high magnification image of the surface of a CBN grain. The ridges on the surface are spaced approximately 1-2 μm apart.

Without the ability to view and identify individual CBN grains at high magnification (ie. SEM imaging) prior to cutting, change in morphology due to grinding can not be ascertained. **Figure 89** shows a CBN grain from the control sample that could be construed as possessing a wear flat. **Figure 90** shows a CBN grain from the control sample that might appear to have been micro-fractured as a consequence of grinding. As a result of the inability to view the wheels at high magnification prior to grinding, determination of whether a CBN abrasive grain on the surface of a tested grinding wheel had developed a wear flat, fractured during cutting, or shown other visible signs of degradation were inconclusive.

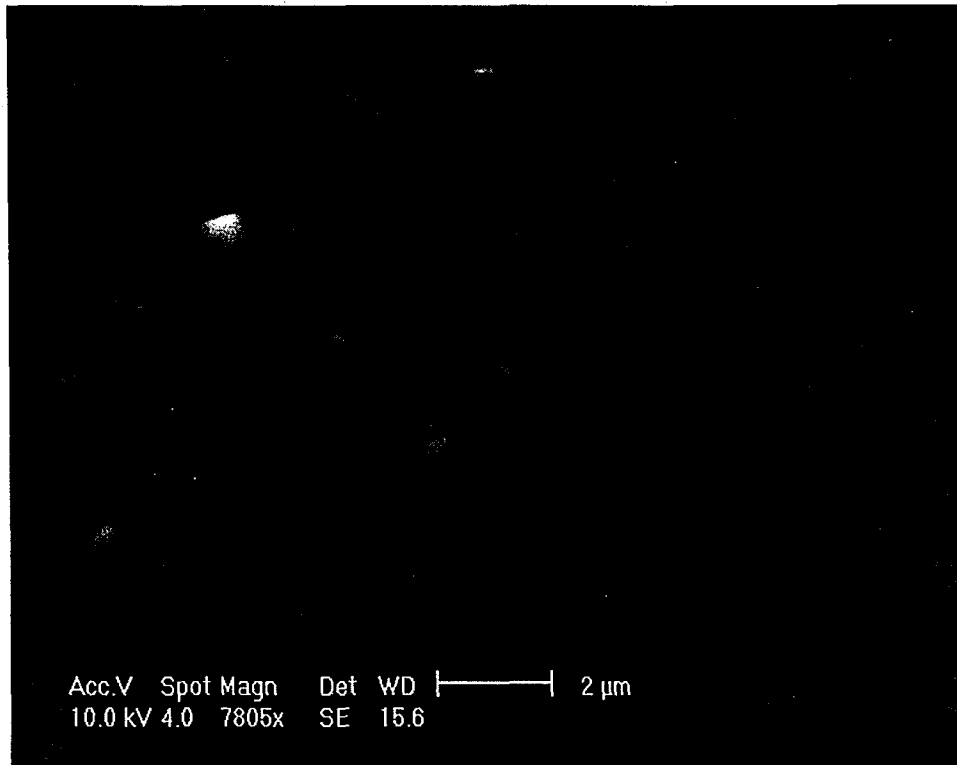


Figure 88: The surface of many CBN grains have finely spaced ridges.

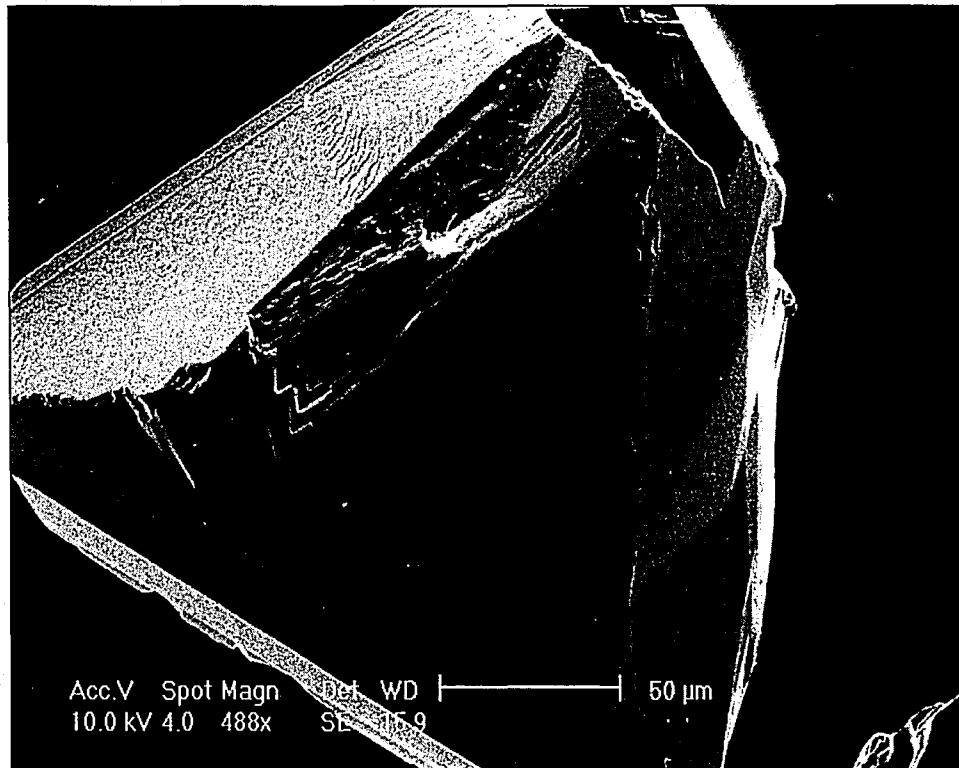


Figure 89: CBN control grain possessing what could appear to be a wear flat.

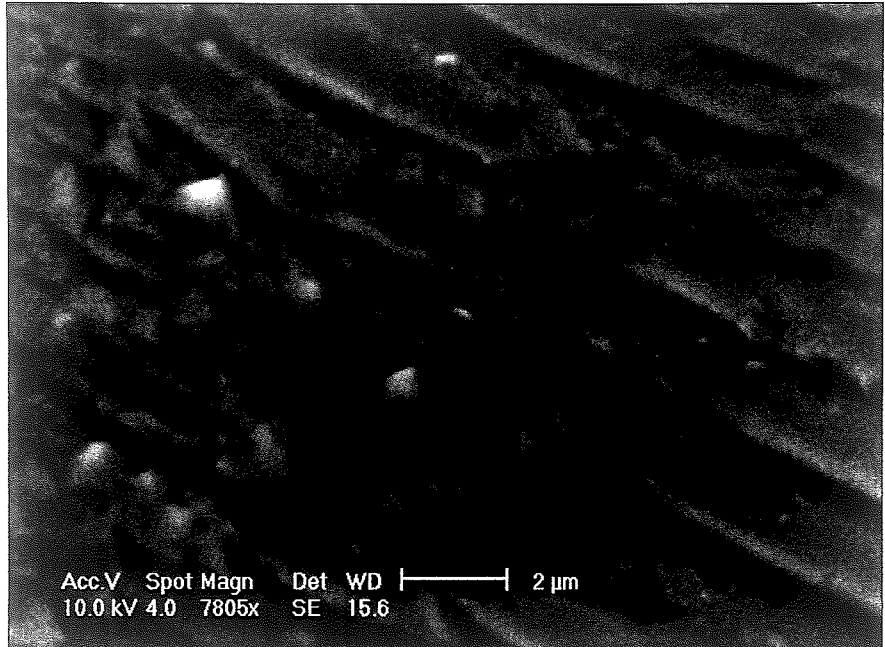


Figure 88: The surface of many CBN grains have finely spaced ridges.

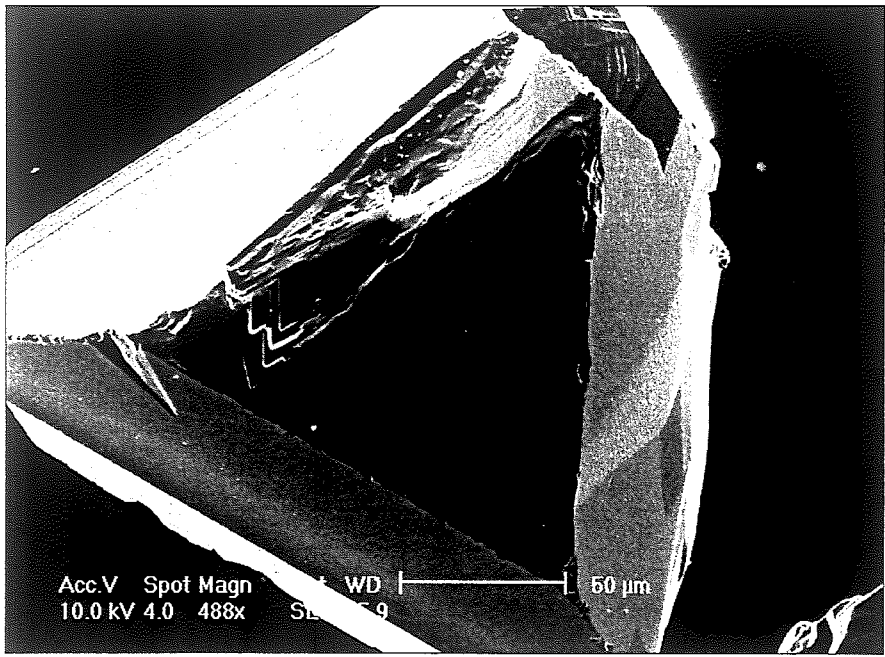


Figure 89: CBN control grain possessing what could appear to be a wear flat.



Figure 90: CBN control grain with a micro-fractured top surface.

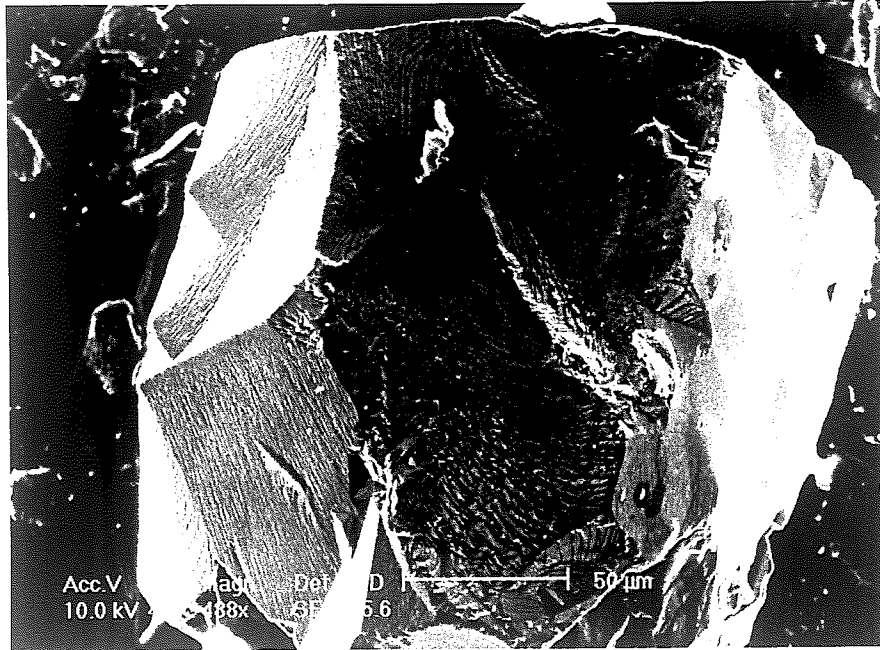


Figure 90: CBN control grain with a micro-fractured top surface.

5.0 DISCUSSION:

5.1 Foreword

Fluids serve an important role in most grinding operations, helping to reduce cutting temperatures, lubricate the wheel surface, and clear the grinding zone of grinding chips. The extent to which the grinding fluid will carry out each of these functions will vary with fluid make-up and operating conditions. Fluid performance may be evaluated independently in each of these aspects, or by assessing the efficiency of the operation as a whole. Experiments carried out in this research project were designed to gauge fluid performance based on the latter, through measurements of power, forces, and tool life as a function of fluid type. After the fluid performance trials were completed, specimens of the grinding wheels were prepared to analyze the mechanism of failure for each fluid. In this manner, the fluid's ability to effectively cool, lubricate, and clean the grinding wheel could be determined and the relevant performance properties of the fluid could be estimated.

5.2 Fluid Performance:

Fluid performance trials involved the testing of three electroplated CBN grinding wheels for each fluid type (one wheel in the case of the neat oil trial) in a groove-grinding experiment (system parameters in **Table VI**). Wheels were run until failure so that tool life could be measured in terms of total grind length, with power and force data characterizing changes in performance from the beginning to end of each wheel's life. System parameters were employed which closely matched the

operating conditions in radial slot grinding operations (with form grinding wheels) of segmented components for aerospace engine assemblies.

Grind length results of the water-based fluid trials are shown in **Table VII**. The variation in wheel performance for a given fluid was explained in terms of cut depth deviations between tests. Fluid performance was interpreted more clearly by plotting the wheel life against the average depth of cut the wheel experienced (see **Figure 21**). The statistical significance of one grinding wheel test for a specific value of cut depth is low; however, the data collected shows steady trends for the wheels tested in each fluid. As cut depth increased, the life of the grinding wheel decreased. The three data points for each fluid provide a rough estimate of performance (trend lines in **Figure 21**) for a specified depth of cut under the operating conditions of the experiment. If these trend lines are accepted as valid performance indicators for the operating conditions of the experiment, then for an average cut depth chosen to be 1.22mm (mid-range of experimental data), the Water-based C fluid would be the best water-based fluid performer, followed by the Water-based B fluid, and lastly the Water-based A fluid. Contrasting the performance of the water-based fluids was the tool life obtained in the Oil Baseline fluid trial. One grinding wheel successfully completed 12,470mm in grind length without reaching (or approaching) failure. Grind length achieved with the water-based fluids averaged fewer than 600mm at failure.

Power measurements from the beginning to end of each test showed an increase in power consumed for all water-based fluid trials (**Figures 22–30**). This confirmed that the effective cutting ability of the wheel decreased as the test

progressed for these water-based fluids. Power data from the neat oil trial (**Figure 57**) showed a small increase in power consumption at the beginning of the fluid trial. Ignoring the initial increases in power consumption at the beginning of the last three testing days (associated with the higher viscosity of cool oil), the peak power measured during each pass leveled off at 597 W (0.8 hp), even after 120 passes. This was an indication that the effective cutting ability of the grinding wheel used with the oil fluid had not been significantly decreased.

Force measurements were complimentary to the data collected by the power monitoring system. Force measurements from the water-based fluid trials (shown in **Figures 33 – 56**) indicated ~~the~~ normal and tangential forces increased from the beginning to end of the fluid trials. Both forces corresponded to the cutting and thrust forces that the grinding wheel experienced. As the effective cutting ability of a wheel is decreased due to wear and/or loading, it is expected that these forces would increase. These increases would continue until wheel failure, the point at which the impedance to wheel rotation (corresponding to tangential force measurements) reached a value that could no longer be sustained by the grinding machine. Force measurements for the oil fluid test (**Figures 58 and 59**) also showed increases in cutting forces, but to a lesser degree. The rate of increase was generally highest in the beginning, before reaching what would appear to be steady state conditions for the effective cutting ability of the tool in oil. **Figure 59** clearly shows the substantial difference in tangential force between the third wheel tested in each of the water-based fluid trials and the wheel tested in the oil trial. Indications are that the wheel

tested in oil would continue to grind effectively and have a considerably longer tool life in comparison to the water-based fluids.

5.3 Improvements to the Grinding Tests:

Legitimizing the performance tests for these fluids requires modifications to the current experimental design. Foremost, consistency in the depth of cut (as determined using the optical profilometer system) between the grinding wheels tested must be accomplished for all experiments performed. In order to achieve a constant depth of cut for a given pass, between passes on a given work block, and between the different work blocks tested, requires that improvements to several parts of the experiment must be performed.

Reinforcing the machine armature to increase its rigidity and stiffness will reduce spindle deflection during the grinding pass. Utilizing material stock with a geometry that allows cubic work blocks of constant size to be prepared will enable one method to be used for securing the blocks for testing. Both of these measures will improve the accuracy and consistency of each individual groove depth from the entry side to exit side. Leveling the dynamometer/feed-table support structure is critical. If leveling can not be completed to the precision level required ($\pm 0.01\text{mm}$), then the degree of variation must be characterized so that changes in machine settings between passes can accommodate and correct the problem. This improvement will stabilize the cut depth for all passes on a given work block. Changes in the procedure for setting the cut depth are required in order to achieve comparable values between tests. Visual confirmation of surface contact between the rotating grinding wheel and work block lacks the precision necessary to maintain

equivalent cut depths for each wheel. A new initialization procedure combined with using work blocks of constant geometry will allow the groove depth to be consistent between the different work blocks.

Fluid trials should also employ a greater number of grinding wheels to provide statistical significance to the tests. Abrasive Technology Inc.'s electroplated CBN grinding wheels (specifications similar to the wheels used in this experiment) have variation in wheel life of around 10% based on industrial use. To account for this manufacturing variability, a maximum error of estimate (E) could be used to determine the requisite number of tests with 95% confidence such that E is equal to (or less than) one-half of the tool life variance. Solving the maximum error of estimate equation

$$E = z_{\alpha/2} * \frac{\sigma}{\sqrt{n}}$$

for n (the number of tests) and assuming a normal distribution in test results, variance equal to 10%, E equal to half the variance, and 95% confidence in the error estimate being required ($z_{\alpha/2} = 1.96$), the number of wheels tested per fluid would need to be 16. Therefore, three wheels per fluid trial do not provide sufficient test data for performance evaluation.

5.4 Analysis of Failure:

Prior to developing an experimental plan and research project, it was known that electroplated CBN grinding wheels used with water-based lubricating fluids had shortened life-times in comparison to the same (or equivalent) industrial operation

using petroleum oil lubricating fluid. This debit in performance was reasoned to be due to loading of the grinding wheel surface, in combination with accelerated wear, fracture, and pullout of the abrasive grains. One previous research project involving wear of electroplated CBN wheels during creep-feed grinding found that wheel wear in oil was primarily due to chipping (microfracture), while wear in a 10% emulsion fluid was due to wear flat formation with localized microfracture and loading [40].

Tool wear reflects the process conditions, work material, and tool material employed in the operation. Wheel loading was recognized as a significant problem in tool life and performance for slot grinding operations of segmented engine components using electroplated CBN grinding wheels with water-based fluids [41]. Some previous research projects using industrial scale grinding machines had not been able to characterize the nature of adhesion wear taking place [42]. These more powerful machines had continued to grind even after the abrasive grains were stripped from the surface of the wheel, preventing subsequent analysis of wheel wear. Use of a laboratory-scale grinding machine has allowed tests to be performed with good sensitivity to changes in wheel condition. As wheel wear occurred, the effective cutting ability of the wheel was reduced until the forces on the wheel exceeded the capacity of the 1.5hp spindle motor. Wheels subsequently analyzed after testing provided evidence of the progression of wheel wear that might otherwise be destroyed using industrial-scale machines.

Grinding wheels used in the water-based fluid trials were loaded with the nickel-based superalloy material, while the wheel used in the neat oil showed no visible indications of wheel wear. Examination of the grinding swarf and surface of

the grinding wheels allowed a mechanism of chip formation and deposition to be determined. This model of wheel loading was then used to estimate the properties of lubricating fluids that may be responsible for differences in performance between water-based and oil-based fluids.

5.5 Grinding Swarf:

Swarf collected from the experiments contained grinding chips, abrasive grains, and clusters / deposits of the alloy. The presence of loose CBN abrasive grains in the swarf is evidence of grain pullout during grinding. Pullout may be a result of the abrasive material being held weakly in the electroplated bond or wheel loading and high grinding forces near the end of the wheel's life causing grit removal. Chips and deposits examined with the stereoscope showed the size and nature of clustering for the chips, as well as the morphology of both sides of wheel deposits. Initial observations indicated that deposits that spall off the wheel surface may pull some CBN grains out of the wheel surface (**Figure 61**). Deposits were also macroscopically observed to be comprised of grinding chips. **Figure 62** is an example of a continuous deposit with chips extending from all edges of its perimeter. The nature of this deposit suggested that its growth occurred by the accumulation of individual chips at its exterior.

Examination of the chips at higher magnification (**Figures 64 – 66**) revealed the mode of chip formation was shear-localized. High speed machining operations of nickel-based superalloys typically have chips with this geometry. The ridges are caused by distinct bands of high shear strain adjacent to sloping segments of low

strain. Knowledge of this chip geometry allowed the smooth surface of the chips to be identified as the side that slid against the rake face of the abrasive grain, while the ridged side was identified as the free-surface of the chip during formation.

5.6 Grinding Wheel Loading:

Individual abrasive grains on the grinding wheel surface serve as the cutting tools for chip formation and material removal. **Figure 91** shows a magnified, cross-sectioned schematic of three CBN grains on an electroplated wheel and how they might be oriented for cutting. In the upgrinding mode, these grains will rotate into the work block feeding against the wheel rotation, with chip flow in the manner described in **Figure 7**. Chip formation during the arc of cut would occur as schematically depicted in **Figure 92**. The surface of the work material would appear to be parallel to the wheel surface at this scale. In **Figure 92**, the right-most CBN grain is responsible for cutting and chip formation, as certain grains would inevitably cut while others would not. Grinding operations utilizing fluids would have some amount of the fluid entrained on the wheel surface and within the cutting zone, but it has been left out of the schematic for clarity. Chips are shown to break apart into small chips in the schematic; however, the chips analyzed from the experiments were much longer than is illustrated, having curled and continuous lengths that spanned 100's of microns (see **Figures 64 – 66**).

Chip flow across the tool surface (rake face of the CBN cutting grain) forced uncontaminated and unoxidized metal into direct contact with the CBN grain, promoting adhesion and bonding. This continuous chip flow at high speeds can result

in seizure between the chip and grain due to increased temperatures and high cutting forces. Chip adhesion to the CBN grains after exiting from the work block is schematically illustrated in Figure 92(d).

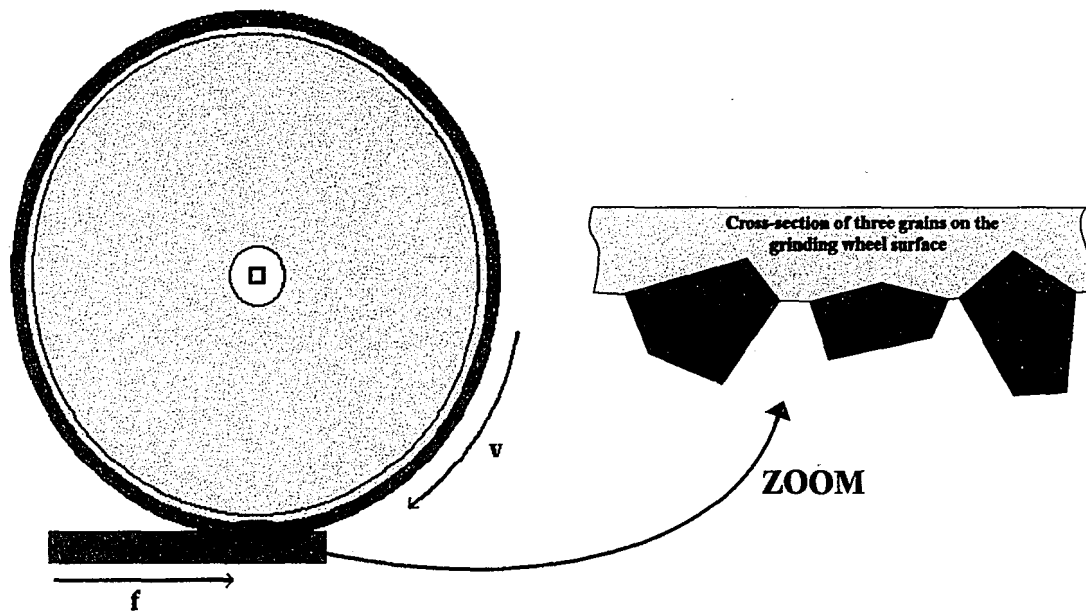


Figure 91: Schematic cross-section of three CBN abrasive grains on the wheel surface that function as cutting tools in grinding.

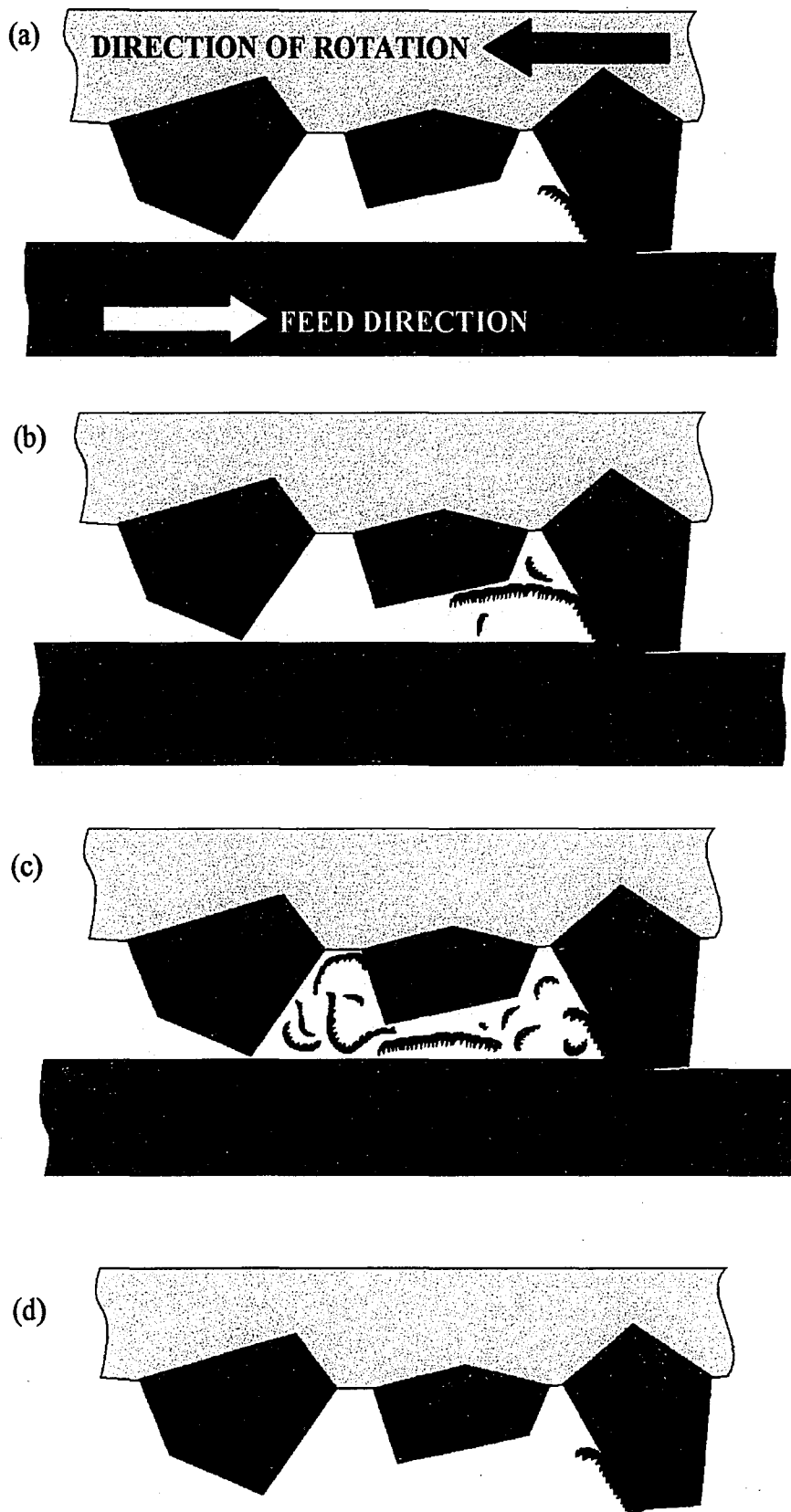


Figure 92: Schematic of cutting action displaying chip formation (a) – (c) and chip adhesion to the rake face of the cutting grain after it exits the work block (d).

Chips adhering to the rake face of the abrasive grain may not be removed from the wheel surface by the scrubber jet. This could be a function of the geometry of the CBN rake face (cutting surface) in relation to the direction of fluid spray. Figure 93 shows how the nozzle layout used in the experiment could allow high-pressure fluid to press the chip onto the grain rather than remove it from the wheel. If an adhering chip is not removed on its first rotation, it will be mechanically pressed onto the grain by the work block on subsequent rotations, making it more difficult for the scrubber jet to remove.

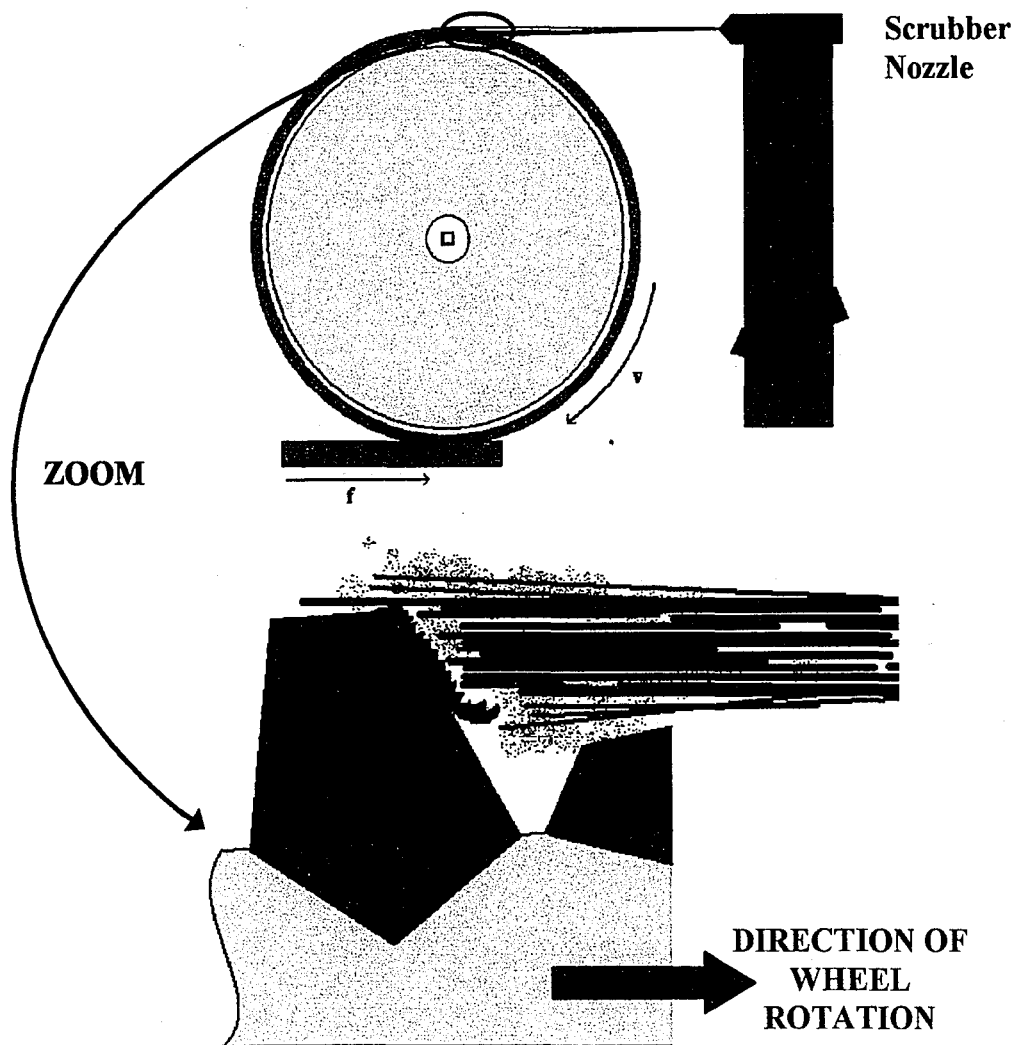


Figure 93: Illustration of scrubber jet spray against the individual cutting grains.

Chips adhering to CBN grains will grow and form deposits as the wheel continues to grind. Growth of the deposits will occur as schematically illustrated in **Figures 94 - 99**. In **Figure 94**, an adhering chip that was not removed by the scrubber jet remains on the CBN grain rake face. Successive rotations of the wheel during grinding cause the chip to be mechanically pressed into and formed across the rake face and clearance face of the CBN grain, as shown in **Figure 95**. The effective 'sharpness' of the CBN grain is reduced by the chip deposit smeared across the rake face and clearance face, as experimentally observed in **Figures 71 and 72**. Subsequent cutting by this abrasive grain would result in growth of the deposit. As stated earlier, deposit growth occurs through the accumulation of chips into the deposit body (see **Figures 62 and 80**).

Adhering material would cover the abrasive grain, schematically illustrated in **Figure 96**. These individual deposits would appear like those observed on the wheels tested in the water-based fluids (see **Figure 69**). Self-supporting tails observed on the trailing edge of the deposits (see **Figures 73 and 74**) indicate the deposit's rigidity during formation. These tails are not intimately contacting the wheel surface, such that the chips comprising the deposits interact exclusively with the CBN grain, the work block, and other grinding chips once deposited on the wheel surface. After covering a single abrasive grain, deposit growth would continue as schematically illustrated in **Figure 97**. Build-up on the clearance face would continue as chips adhere to the nickel-alloy already present on the CBN grain. Material flow past the rear face of the cutting CBN grain would fill the gap between it and an adjacent CBN grain, as experimentally observed in **Figure 75**.

Growth would then proceed as the deposit bridges to adjacent grains on the wheel. This process allows the deposit to continue accumulating chips into its body while the deposit insidiously spreads across the wheel, prematurely ending the life of the grinding wheel. This bridging is illustrated in **Figure 98**, with cross-sectioned LOM images showing the in-situ morphology of the deposit's underbelly (see **Figures 81 and 82**). Continued growth will inevitably involve repetition of these processes on other CBN cutting grains, which eventually grow together to form larger deposits. These aggregated masses are in adherence with the top part of the rake face and clearance face of the CBN grains, as observed in **Figures 76 and 77**. Deposits are comprised of compacted chips that form layered deposits (see **Figure 78**) through chip-to-chip adhesion. These larger deposits, like those shown in **Figures 67 and 79**, grow until the wheel surface is sufficiently loaded to impede wheel rotation and cause seizure during grinding.

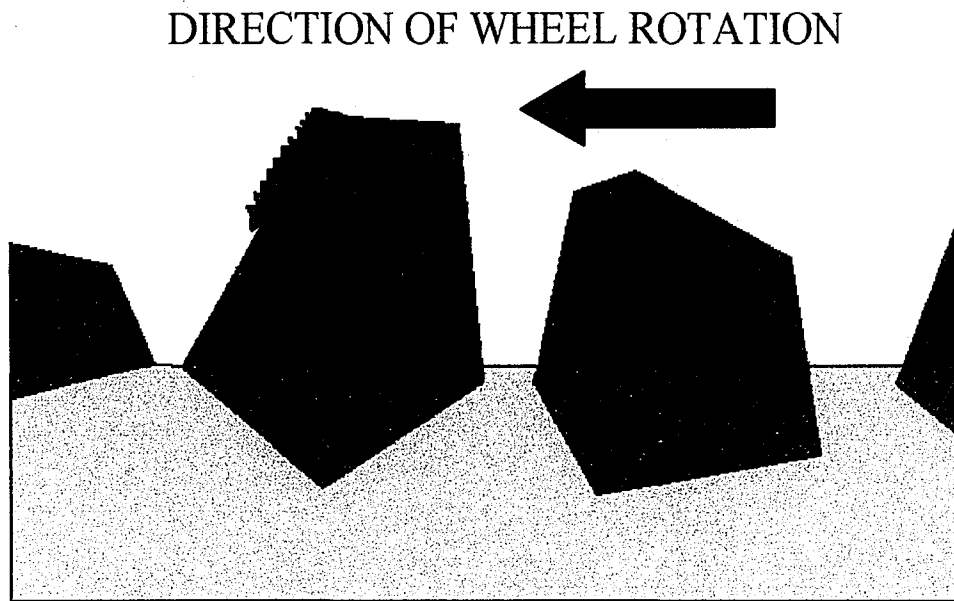


Figure 94: Adhesion of a grinding chip on the cutting face of a CBN grain.

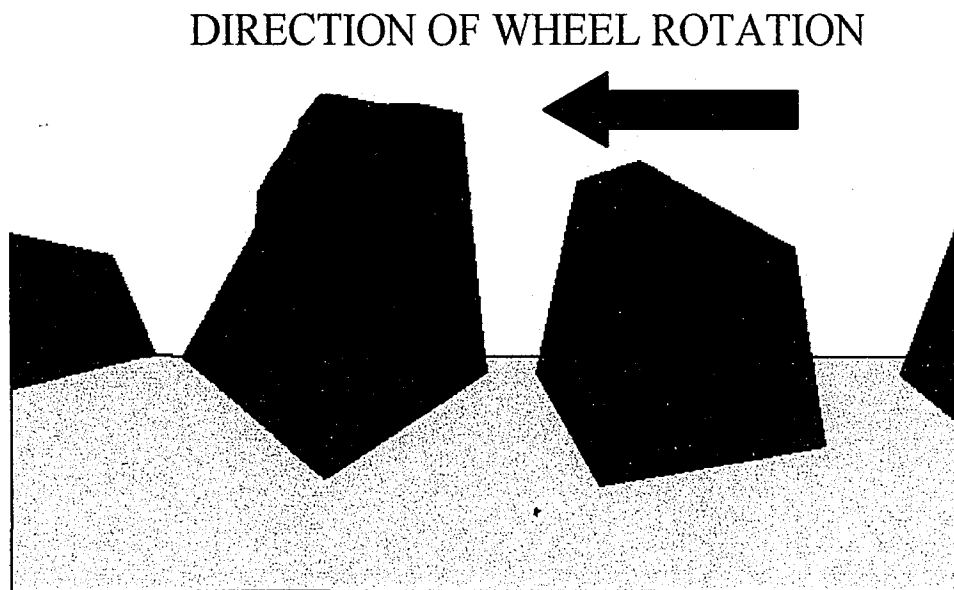


Figure 95: Deformation of adhering chips onto the cutting face and across the clearance face of the CBN grain.

DIRECTION OF WHEEL ROTATION

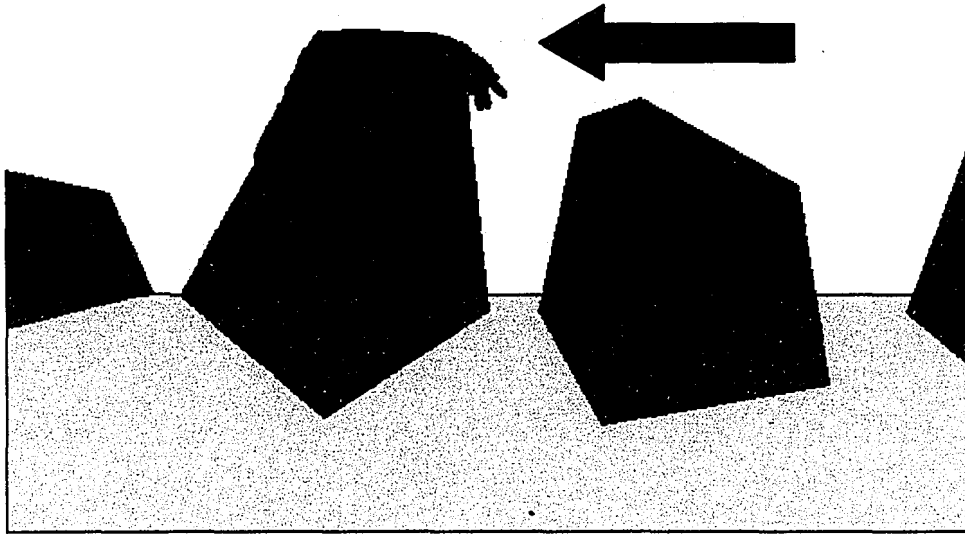


Figure 96: Deposit growth begins with buildup on the clearance face of the CBN grain.

DIRECTION OF WHEEL ROTATION

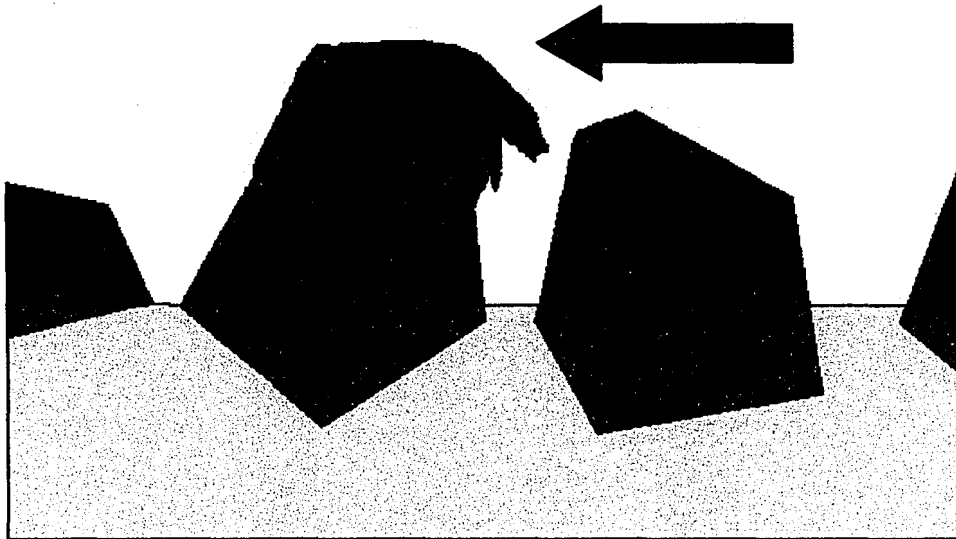


Figure 97: Continued growth leads the deposit to flow along the backside of the CBN grain and form self-supporting tails.

DIRECTION OF WHEEL ROTATION

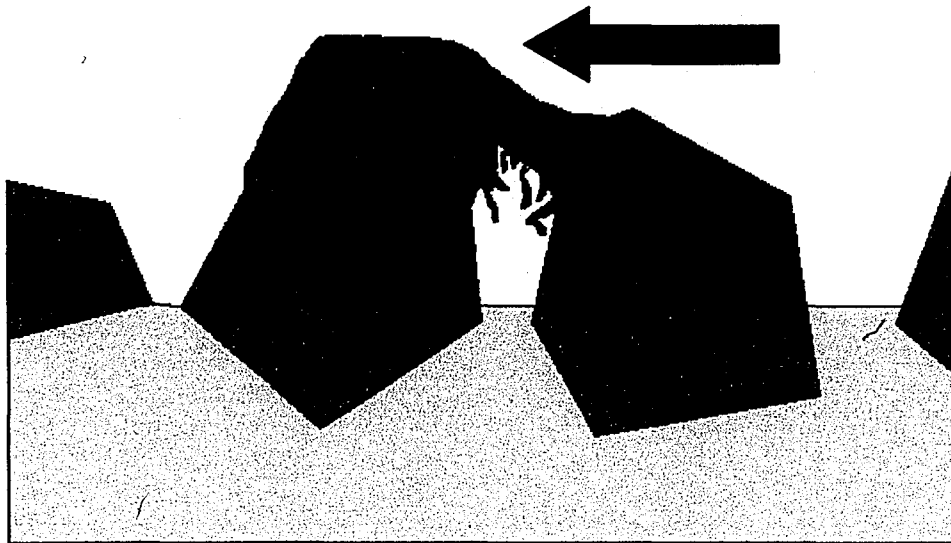


Figure 98: Bridging to adjacent grains occurs when the trailing edge of the deposit grows to a significant size.

DIRECTION OF WHEEL ROTATION

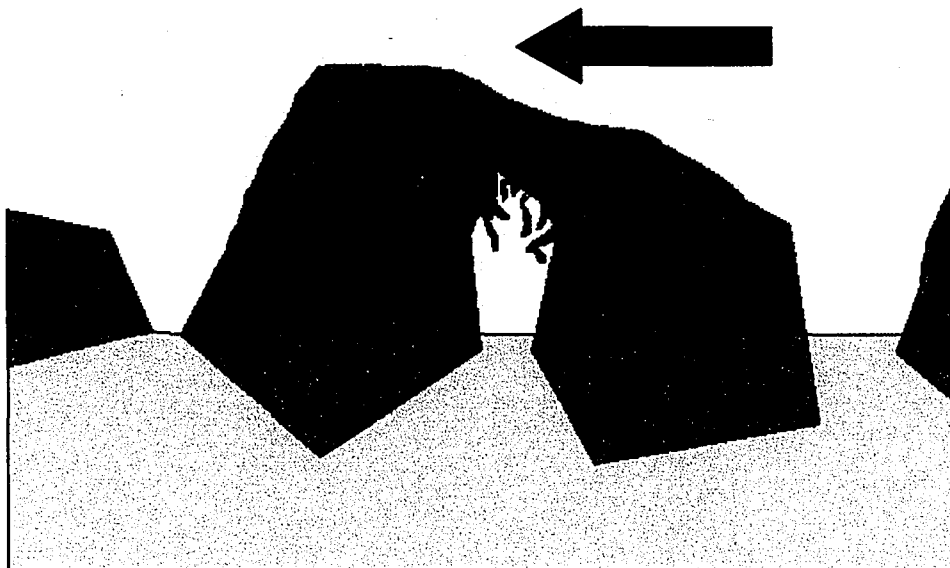


Figure 99: Deposit growth continues laterally around the sides of the CBN grain, with continued adherence and growth on adjacent grains.

5.7 Fluid Effects:

Wheels tested in the water-based fluids were observed to suffer from wheel loading, while the wheel tested in the petroleum oil showed no signs of wheel loading or worn grains (**Figures 83 - 85**). The failure mechanism for this wheel can not be predicted from the singular test performed. Power measurements and force measurements indicate that the test would have continued for a significant time longer than when the test was ended. Changes in condition of individual grains can not be determined without having documented the initial geometry and shape prior to cutting. Attritious wear and grain pull-out may have occurred, but no conclusive experimental evidence can be derived without a comparative starting condition. This was not feasible given the size of the grinding wheels, as they could not be prepared for high magnification observation using the SEM without first being destroyed.

Comparison of the tested wheels with a new wheel indicates that CBN grain pull-out could have been present prior to testing (**Figure 87**), along with other defects such as overplating (**Figure 88**). Determining the nature of wear of individual CBN abrasives was abandoned due to the subjectivity of each conclusion. CBN grains used as control specimens were analyzed to show the variability in shape and morphology prior to use. **Figures 89 and 90** show examples of how grains not used for grinding might appear to have formed a wear flat or been micro-fractured based on the initial morphology.

Clearly the presence of deposits on the wheels tested in the water-based fluid trials and the absence of such deposits on the wheel tested in the neat oil, along with the tool life measurements for each trial, provides evidence of distinct differences in

fluid performance. Wheel loading initiated with chip seizure on the cutting face of an abrasive grain and blossomed through chip-to-chip adhesion to form larger deposits. Definitive boundaries and chip morphologies present in the deposits indicated that growth occurred as a result of mechanical deformation and interlocking of adhering chips. Melting of the work block followed by solidification on the wheel surface had been eliminated as a possibility.

Chip adhesion must therefore be directly related to the bulk properties of the grinding fluid (water-based vs. oil-based). Wear flat formation, schematically shown in **Figure 100**, when water-based fluids are used may be accelerated due to hydrolytic wear, as previously discussed. If wear flat formation is occurring in the water-based fluid trials, then temperature increases in the CBN grains (see **Figure 101**) could be responsible for diffusional bonding or localized melting of the chip's skin in contact with the grain surface. Wear flat formation could be neither confirmed nor refuted without predicating the assessment on observations of the initial conditions of the grains. The oil's ability to effectively coat the CBN grain and provide a boundary layer to prevent chip adhesion is another strong possibility. Water-based fluids may suffer from film boiling and may not adequately coat and contaminate the CBN and work piece surface like the oil fluid, leading to the higher likelihood for wheel loading with water-based fluids. Water-based fluids also have lower viscosity, which may not afford the same wedging pressure during chip formation (fluid acting as a chip breaker) as the oil fluid.

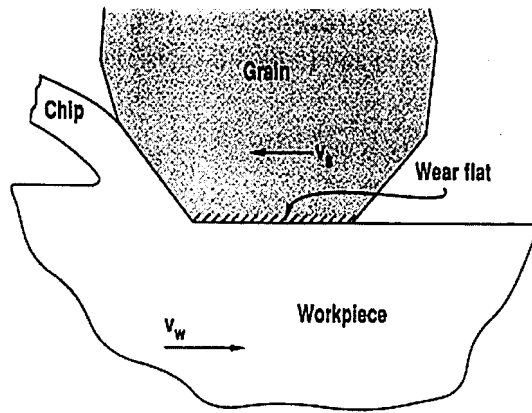


Figure 100: Illustration of a wear flat (clearance angle = 0°) sliding along the work piece surface. Ref. [5]

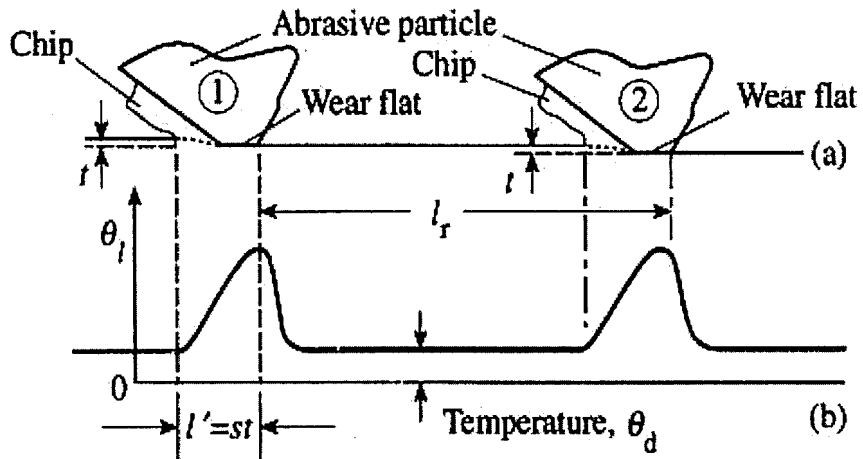


Figure 101: Temperature increases associated with frictional rubbing of wear flats. Ref. [6]

5.8 Preventative Measures:

Wheel loading may be prevented from similar operations using water-based fluids. Based on the mechanism of deposition described, avoiding the initial chip adherence is critical in preventing wheel loading. If the CBN grinding problems associated with water-based fluids such as hydrolytic wear and viscosity issues can not be resolved, then a more productive method of chip removal by the scrubber jet should be employed. Scrubber nozzle layouts like the one used in this experiment do not adequately remove material from the wheel surface. A design which would allow the high-pressure fluid stream to shear the adhering material off of the abrasive grain would be more effective. **Figure 102** shows possible directions for fluid flow (A and B) that could shear off chips based on the geometry of the CBN grains and mechanism of deposition described above. Stream A would scrape chips off without pressing them into the grain face, while Stream B would augment the wedging action of the fluid during chip formation. The improved nozzle layout is illustrated in **Figure 103** for the specific grinding operation used in the experiment.

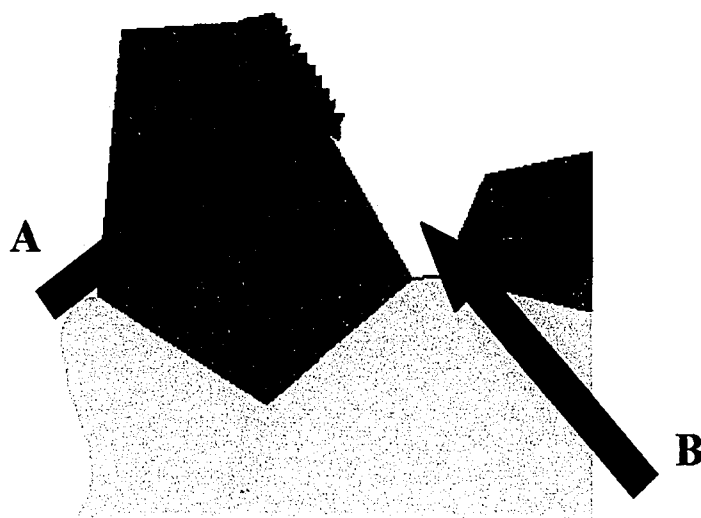


Figure 102: Fluid directions that would be more effective in wheel cleaning.

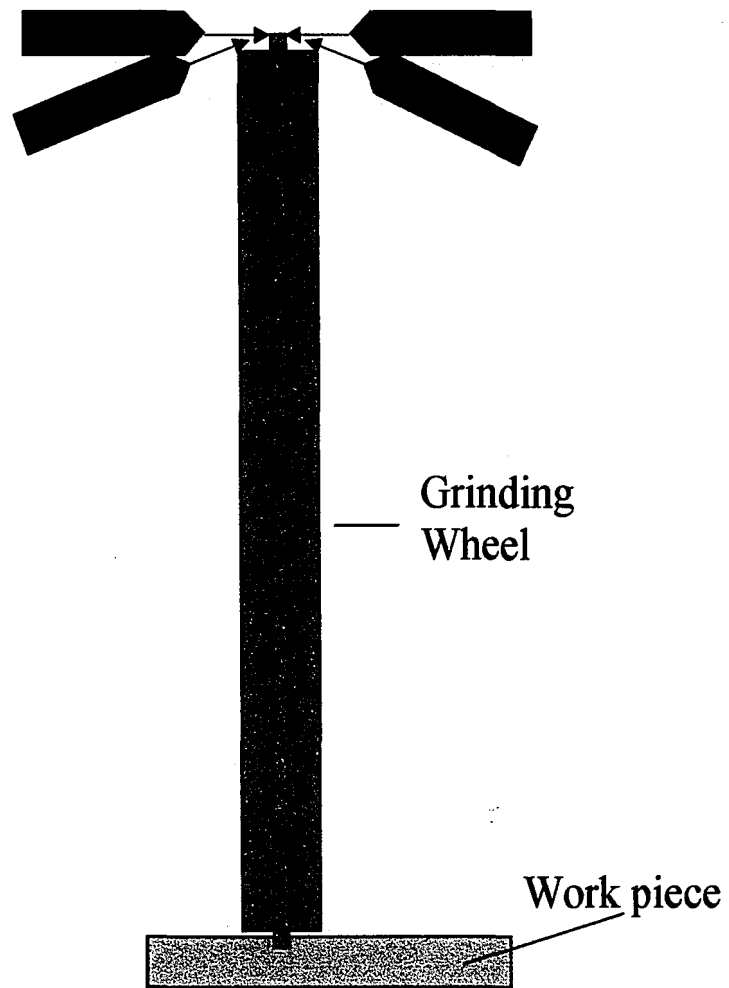


Figure 103: Scrubber nozzles would be oriented as shown on both sides of the wheel for high pressure fluid delivery that is effective in wheel cleaning.

6.0 CONCLUSIONS

- Performance of the water-based lubricants was gauged by wheel life. Results, accounting for variation in cut depth, indicate the Water-based C fluid performed the best at a cut depth of 1.22 mm. Water-based B was the second best performer, followed by Water-based A, at this cut depth.
- The neat oil (Oil Baseline fluid) significantly outperformed the water-based fluids in the grinding tests. Wheels used with the water-based fluids averaged about 600 mm in grind length at failure. The wheel tested in the neat oil lasted 12,470 mm without reaching failure.
- The grinding machine's sensitivity to increases in forces that impede wheel rotation allowed the tests to detect small changes in wheel condition, which represented the onset of wheel loading.
- Increasing measurements of power indicate the effective cutting ability of the electroplated CBN wheels used in the water-based fluid trials decreased as the tests progressed. Measurements of power in the neat oil fluid trial were roughly equivalent in the beginning and end of the test, indicating the effective cutting ability of this wheel was not reduced.
- Tangential and normal force measurements increased significantly and at a much higher rate in the water-based fluid trials when compared to the wheel tested in the neat oil fluid trial. These measurements compliment the power measurements, providing positive indication of wheel wear for the water-

based fluids and evidence that little wear or reduction in cutting ability was experienced by the wheel used in the neat oil fluid trial.

- Increasing the number of wheels tested and completing the listed improvements to the test equipment would allow trials to be executed which more clearly distinguish the difference in performance of the water-based lubricating fluids.
- Wheel loading was observed on the wheels tested with the water-based fluids, not the wheel tested in the neat oil fluid trial. This was deemed to be the cause of failure for the water-based fluid trials and what was responsible for the debit in performance when compared to the straight petroleum oil fluid.
- Grain pullout was observed, but not confirmed to be a result of grinding. Missing abrasive grains were observed on brand new wheels as well as those used in the tests. New wheels were observed to have heterogeneous distributions of grains as well as regions of overplating.
- Chips were observed to have a shear-localized (serrated) morphology, consistent with chips normally obtained in high-speed machining operations of nickel-based superalloys.
- Wheel loading was concluded to occur through a process of chip adhesion on the rake face of the cutting grain, deformation of adhering chips onto the rake face and clearance face, continued buildup through chip-to-chip adhesion, followed by deposit bridging and growth. This process would continue in multiple locations on the wheel surface until cutting forces reached a point where the grinding machine could no longer sustain the operation.

- Changes in the morphology of individual CBN grains on the wheel surface could not be determined. A 10-inch wheel diameter prevented high magnification imaging and analysis of wear using the SEM. This prevented a conclusive determination of whether attritious wear, microfracture, and grain pullout was present or a result of the tests performed.
- It has been suggested that chip adhesion, and ultimately wheel loading, are related to hydrolytic wear and possible wear flat formation. The petroleum oil's ability to coat and contaminate the wheel surface, along with its higher viscosity, may also be responsible for the marked difference in performance between the water-based fluids and the oil fluid.
- If it is assumed that hydrolytic wear is responsible for the debit in performance, an inherent property of a water-based lubricant, than the proposed change to nozzle design would help reduce this difference in performance. Accurate placement of the scrubber nozzles will be more effective in removing chips adhering to the rake face of the abrasive grains. This measure would not eliminate the cause(s) of wheel loading, but might help to reduce or eliminate the rapid deterioration of the wheel surface due to adhesive wear.

APPENDIX

Fluid Name	Fluid Type	General Description
Oil Baseline	Neat Oil	Straight oil coolant used for heavy duty grinding and machining for a variety of materials. Has excellent lubricity and provides extensive life for machining and grinding tools. Poses a fire hazard.
Water-based A	Emulsion	Micro-emulsion used for heavy duty grinding and machining. Clean, low foaming fluid with good corrosion protection, designed for machining cast aluminum, but contains non-sulfurized, non-chlorinated EP additives for machining Fe- and Ni- base alloys
Water-based B	Solution Synthetic	Water-based synthetic used for heavy duty grinding and machining. Operator friendly fluid with good corrosion protection that is suitable for use on steel and cast iron. Safe for use with aluminum and magnesium aerospace alloys.
Water-based C	Solution Synthetic	Water-based synthetic used for heavy duty grinding and machining. Operator friendly fluid with good corrosion protection suitable for use on steel and cast iron. Experimental fluid.

Fluid Name:	Oil Baseline	Water-based A*	Water-based B*	Water-based C*
Flash Point	176.65°C	N/A	N/A	N/A
Boiling Point	N/A	100°C	>100°C	>100°C
Solution pH	N/A	9.1	8.5	8.6

*Water-based fluid properties are for a 5% solution in distilled water.

REFERENCES:

1. Salmon, S.C., *Modern Grinding Process Technology*. 1992, New York: McGraw Hill Inc.
2. Groover, M.P., *Fundamentals of Modern Manufacturing: Materials, Processes, and Systems*. 2nd ed. 2002, New York: John Wiley & Sons, Inc.
3. Konig, W., K. Yegenoglu, and B. Stuckenhof, *Lower Grinding Costs and Better Workpiece Quality by High Performance Grinding with CBN Wheels*. Gear Technology, 1986: p. 1.
4. *Tool Materials*. ASM Specialty Handbook, ed. J.R. Davis. 1995, Materials Park, OH: ASM International.
5. Malkin, S., *Grinding Technology: Theory and Applications of Machining with Abrasives*. Ellis Horwood Series in Mechanical Engineering, ed. J.M. Alexander. 1989, Chichester: Ellis Horwood Limited.
6. Shaw, M.C., *Principles of Abrasive Processing*. Oxford Series on Advanced Manufacturing, ed. M.C.S. J.R. Crookall, Nam P. Suh. 1996, Oxford: Oxford University Press.
7. German, R.M., *Powder Metallurgy Science*. 2nd ed. 1994, Princeton: Metal Powder Industries Federation.
8. Love, M., *Personal Communication*, F.C.G. Jr., Editor. April 10, 2002, Abrasive Technology Inc.
9. Heywood, J., *Grinding Wheels and Their Uses*. 1938, Cleveland: Penton Publishing Co.
10. Ault, W., *Types of Grinding Wheels*, in *Handbook of Modern Grinding Technology*, R.I. King and R.S. Hahn, Editors. 1986, Chapman and Hall: New York.
11. McKee, R.L., *Machining with Abrasives*. 1982, New York: Van Nostrand Reinhold Company.
12. Elliot, S., *The Physics and Chemistry of Solids*. 1998, Chichester: John Wiley & Sons.
13. Komanduri, R., *Tool Materials*, in *Kirk-Othmer Encyclopedia of Chemical Technology*. 1997, John Wiley & Sons.
14. Markel, E.J. and M.E.L. II, *Nitrides*. 1996, Kirk-Othmer Encyclopedia of Chemical Technology, John Wiley & Sons, Inc.
15. *Borazon* CBN Product Selection Guide*. 2001, GE Superabrasives.
16. *Manufacturing with Materials*. Materials in Action Series, ed. L. Edwards and M. Endean. 1990, Oxford: Butterworth - Heinemann Ltd.
17. Trent, E.M., Wright, P.K., *Metal Cutting*. 4th ed. 2000, Boston: Butterworth-Heinemann.
18. Merchant, M.E., *Mechanics of the Metal Cutting Process. II. Plasticity Conditions in Orthogonal Cutting*. Journal of Applied Physics, 1945. **16**: p. 318-324.
19. *Cutting and Grinding Fluids: Selection and Application*. 2nd ed, ed. R.P. Jeffrey D. Silliman. 1992, Dearborn, Michigan: Society of Manufacturing Engineers.

20. Trigger, K.J., in *International Research in Production Engineering*. 1963, ASME: NY. p. 95.
21. Guo, C. and S. Malkin, *Inverse Heat Transfer Analysis of Grinding, Part 1: Methods*. ASME Journal of Engineering for Industry, 1996. **118**: p. 137-142.
22. Carius, A.C. *Effects of Grinding Fluid Type and Delivery on CBN Wheel Performance*. in *SME Modern Grinding Technology Conference*. 1989. Novi, Michigan.
23. Bennet Jr., B.G., *Effects of Coolants and Application in Using Vitrified CBN Grinding Wheels*. The Carbide and Tool Journal, 1987. **19**(2): p. 23-26.
24. Engineer, F., C. Guo, and S. Malkin, *Experimental Measurement of Fluid Flow Through the Grinding Zone*. ASME Journal of Engineering for Industry, 1992. **114**: p. 61-66.
25. Guo, C. and S. Malkin, *Analysis of Fluid Flow through the Grinding Zone*. ASME Journal of Engineering for Industry, 1992. **114**: p. 427-434.
26. Lorincz, J., *A World of Choice in Metalworking Fluids*. Tooling and Production, 2001: p. 52-57.
27. Drozda, T.J., Wicks, C., *Tool and Manufacturing Engineers Handbook: Machining*. 4th ed. Vol. I. 1983, Dearborn, Michigan: Society of Manufacturing Engineers.
28. Hitchiner, M.P. *Technological Advances in Creep Feed Grinding of Aerospace Alloys with CBN*. in *3rd International Machining and Grinding Conference*. 1999. Cincinnati, Ohio.
29. Harpster, A. *Grinding Superalloys with Plated CBN Wheels*. in *SME Superabrasives Conference*. 1991. Chicago, Illinois.
30. Miyoshi, K. and D.H. Buckley, *Tribological Properties of Silicon Carbide in the Metal Removal Process*. Wear, 1982. **82**: p. 197-211.
31. Broskea, T.J., *Analyzing PCBN Tool Wear*. Modern Machine Shop, 2001: p. 86-93.
32. Hitchiner, M.P. and J. Wilks, *The Wear of Diamond and CBN Grits during Grinding*. Advances in Ultrahard Materials Application Technology, 1983. **2**: p. 100-111.
33. Stokes, R.J. and T.J. Valentine, *Wear Mechanisms of ABN [CBN] Abrasives*. Industrial Diamond Review, 1984. **44**: p. 34-44.
34. Srivistava, A.K., K.S. Ram, and G.K. Lal, *A Simple Analysis for Evaluating Grinding Wheel Loading*. International Journal of Machine Tools and Manufacture (Design, Review, & Application), 1988. **28**(2): p. 181-190.
35. Yossifon, S. and C. Rubenstein, *Wheel Wear When Grinding Workpieces Exhibiting High Adhesion*. International Journal of Machine Tools and Manufacture (Design, Research, & Application), 1982. **22**(3): p. 159-176.
36. Nagaraj, A.P. and A.K. Chattopadhyay, *On Some Aspects of Wheel Loading*. Wear, 1989. **135**: p. 41-52.
37. Kumar, K.V. and M.C. Shaw, *Metal Transfer and Wear in Fine Grinding*. Wear, 1982. **82**: p. 257-270.

38. Yossifon, S. and C. Rubenstein, *The Grinding of Workpiece Materials Exhibiting High Adhesion, Part 2: Forces*. ASME Journal of Engineering for Industry, 1981. **103**: p. 156-164.
39. Duwell, E.J., R.J. Cosmano, and G.R. Abrahamson. *Influence of Chemically Active Water Base Grinding Fluids on the Dynamics of Grinding*. in *1985 SME Manufacturing Engineering Transactions: 13th NAMRC North American Manufacturing Research Conference Proceedings*. 1985. University of California-Berkely, Berkely, CA: North American Manufacturing Research Institution of SME.
40. Ramanan, N.V., *Wear of a Cubic Boron Nitride Electroplated Wheel During Creep-Feed Grinding of a Ni-Base Superalloy Using an Emulsion*, M.S. Thesis. 1998, University of Connecticut.
41. Guptil, E., *Personal Communication*, F.C.G. Jr., Editor. June 4, 2002, Pratt & Whitney.
42. Caglar, M., *Personal Communication*, F.C.G. Jr., Editor. December 2002, Quaker Chemical Corporation.

CURRICULUM VITAE

Frank C. Gift Jr. was born August 29th, 1979 to Frank C. Gift Sr. and Anita Gift in Philadelphia, Pennsylvania. Frank graduated in 1997 as valedictorian from Palmyra High School in Palmyra, New Jersey. He continued his education at Lehigh University in Bethlehem, Pennsylvania with assistance of a Martindale Scholarship from the generous benefactor Harry Martindale. During his undergraduate tenure pursuing a B.S. degree from the engineering college, he was inducted into the Phi Eta Sigma Freshman Honorary Society, the Tau Beta Pi Engineering Honorary Society, and the Alpha Sigma Mu Materials Science and Engineering Honorary Society. He graduated Summa Cum Laude in 2001 with his B.S. degree in Materials Science and Engineering.

Frank continued on to pursue his M.S. degree in Materials Science and Engineering from Lehigh University starting June 2001. He was partially sponsored by the P.C. Rossin University Fellowship which provided funding for one year's tuition and a 9-month stipend. Frank has been researching metal machining and grinding for his M.S. degree, with particular focus on the aspect of adhesion wear of electroplated CBN grinding wheels.

**END OF
TITLE**